

RETROSPECTIVE ANALYSIS OF CRYOPRESERVED SAMPLES

Dissertation
Zur Erlangung des Grades
des Doktors der Naturwissenschaften
der Naturwissenschaftlich-Technischen Fakultät
der Universität des Saarlandes

von
Asger Kreiner

Saarbrücken
2020

Tag des Kolloquiums: 8.9.2020

Dekan: Prof. Dr. Guido Kickelbick

Berichterstatter: Prof. Dr. Heiko Zimmermann
Prof. Dr. Gregor Jung

Vorsitz: Prof. Franziska Lautenschläger

Akad. Mitarbeiter: Dr. Christoph Pauly

SUMMARY

The aim of cryopreservation is to arrest physiologic structure, information and function by lowering the temperature. It is commonly believed that a reduction of temperature significantly halt or decelerate any detrimental process at storage temperature. Yet little is known about the interference of the remaining slow processes in the sample on the biological material at low temperatures. Furthermore, there is a lack of methods to observe such processes at low temperatures and detect them retrospectively.

In this work, different optical microscopy methods was adapted to samples at temperatures down to $-180\text{ }^{\circ}\text{C}$, evaluated and utilized for the study of such slow processes and their relation to the conservation conditions. For some of these, namely devitrification and eutectic crystallization, chemical markers were identified by Raman spectroscopy. Other slow processes like recrystallization were investigated using fluorescence microcopy. These results may be the first steps into solid sample characterization for retrospective sample history analysis.

Using the insights of these investigations, several innovations for real life biobanking were derived, such as fiber-based quality assessment of stored cryopreserved samples, time-temperature-indicators using recrystallization kinetics and a prediction tool for medium stability against devitrification by means of calorimetry.

ZUSAMMENFASSUNG

Das Ziel der Kryokonservierung ist es, physiologische Strukturen, Information und Funktionen durch Temperaturerniedrigung zu erhalten. Es wird allgemein angenommen, dass eine Verringerung der Temperatur zersetzende Prozesse nahezu unendlich verlangsamt. Dabei ist noch wenig über die Wechselwirkung der verbleibenden langsamen Prozesse auf biologisches Material bei niedrigen Temperaturen bekannt und es fehlen Methoden um solche Prozesse bei niedrigen Temperaturen zu beobachten und rückblickend nachzuweisen.

In dieser Arbeit wurden verschiedene Methoden der optischen Mikroskopie an Probertemperaturen bis $-180\text{ }^{\circ}\text{C}$ angepasst, evaluiert und für die Untersuchung langsamer Prozesse und deren Beziehung zu den Konservierungsbedingungen angewandt. Für manche dieser Prozesse, Devitrifikation und eutektische Kristallisation, wurden chemische Marker mittels Raman-Spektroskopie identifiziert. Andere langsame Prozesse wie Rekristallisation wurden mittels Fluoreszenz-Mikroskopie untersucht. Diese Ergebnisse eröffnen den Zugang zur Charakterisierung von festen Proben zur retrospektiven Analyse der Probenhistorie.

Aufbauend auf diesen Ergebnissen wurden mehrere Innovationen für den praktischen Einsatz in Biobanken abgeleitet, unter anderem faserbasierte Qualitätskontrolle von kryokonservierten Proben während der Lagerung, Zeit-Temperatur-Indikatoren basierend auf Rekristallisations-Kinetik und eine Vorhersagemethode für die Stabilität des Mediums gegen Devitrifikation mittels Kalorimetrie.

ACKNOWLEDGEMENTS

Thank you to:

Fraunhofer IBMT and Universität des Saarlandes

Prof. Dr. Heiko Zimmermann and Prof. Dr. Gregor Jung

Frank Stracke, Iris Riemann, Ronan LeHarzig and Daniel Dörr

Manon Schmidt and Marie Billard

Michael Gepp and Stephanie Bur

Lutz Warzemann (Askion GmbH)

André Schulz and Benjamin Fischer

Christoph Pauly

Laura and my family

CONTENTS

1 INTRODUCTION	1
2 INTRODUCTION TO CRYOPRESERVATION	7
2.1 APPROACHES TO CRYOPRESERVATION	8
2.1.1 <i>Slow freezing approach</i>	10
2.1.2 <i>Vitrification approach</i>	15
2.2 SLOW PROCESSES IN SAMPLES AT LOW TEMPERATURES	19
2.2.1 <i>Acceleration of slow processes</i>	22
2.2.2 <i>Phase transitions</i>	27
2.2.3 <i>Recrystallization</i>	29
2.3 APPROACHES TO RETROSPECTIVE ANALYSIS	29
3 METHODS	33
3.1 CELL CULTURE	33
3.2 CRYOMICROSCOPY	34
3.2.1 <i>Sample cross-section imaging</i>	39
3.2.2 <i>Fluorescence microscope</i>	41
3.3 LASER SCANNING MICROSCOPY	42
3.3.1 <i>Two-photon fluorescence laser scanning microscopy</i>	43
3.3.2 <i>Raman laser scanning microscopy</i>	46
3.3.2.1 Raman scattering	47
3.3.2.2 Confocal Raman Cryomicroscopy	49
3.3.2.3 Analysis of Raman spectra	51
3.4 DIFFERENTIAL SCANNING CALORIMETRY	55
4 MACROSCOPIC DISTRIBUTION OF SAMPLE COMPOUNDS	59
4.1 STRUCTURE FORMATION PROCESS	59
4.2 ICE CRYSTAL MORPHOLOGY IN CRYOPRESERVED SAMPLES	64
4.2.1 <i>Typical structures found in cryopreserved samples</i>	64
4.2.2 <i>Influence of supercooling on the dendritic channel structure</i>	68
4.3 CROSS SECTIONS OF CRYOPRESERVED CELL CULTURES	70
5 MICROSCOPIC DISTRIBUTION OF SAMPLE COMPOUNDS	75
5.1 CONFOCAL RAMAN MICROSCOPY	75
5.2 CHEMICAL MARKERS FOR RETROSPECTIVE ANALYSIS	79
5.3 SPATIAL DISTRIBUTION OF HYDROHALITE FROZEN CELL CULTURES	81
5.3.1 <i>Methods for spatial distribution measurements</i>	81
5.3.2 <i>CRM image analysis</i>	83
5.3.3 <i>Types of hydrohalite formation</i>	84
5.3.4 <i>Statistics of hydrohalite distribution in murine fibroblasts</i>	90
5.3.5 <i>Spatial distribution of hydrohalite in IPS cell colonies</i>	90
5.4 INFLUENCE OF DMSO ON HYDROHALITE CRYSTALLIZATION	95

5.4.1 CRM of hydrohalite in a DMSO solution	97
5.4.2 Temperature-dependence of hydrohalite crystallization.....	99
5.4.3 Murine fibroblast cells frozen in PBS with DMSO as CPA	103
5.4.4 IPS cell colonies	105
5.5 FIBER BASED RAMAN SPECTROSCOPY OF CRYOPRESERVED SAMPLES	107
5.5.1 Experimental Raman probe setup.....	107
5.5.2 Fiber-based Raman cryospectroscopy	109
5.6 RAMAN SPECTROSCOPY IN RETROSPECTIVE ANALYSIS.....	112
6 STRUCTURAL KINETICS AT ELEVATED TEMPERATURES	115
6.1 INTRODUCTION	115
6.2 STRUCTURAL DYNAMICS IN SLOWLY FROZEN MEDIA	117
6.2.1 Experimental setup	119
6.2.2 Fluorescence image analysis.....	120
6.2.3 Recrystallization in slowly frozen media	122
6.2.4 Retrospective analysis based on recrystallization.....	131
6.2.5 Application of recrystallization kinetics as a TTI.....	133
6.3 KINETICS OF DEVITRIFICATION.....	135
6.3.1 Johnson-Mehl-Avrami-Kolmogorov model for devitrification	137
6.3.2 Methods for devitrification measurements	139
6.3.3 Measurements of devitrification kinetics.....	145
6.3.4 Discussion of the DSC measurements and the JMAK model.....	152
6.3.5 DSC as an evaluation tool in biobanking.....	160
6.4 RECRYSTALLIZATION AND DEVITRIFICATION: PARALLELS AND DIFFERENCES.....	162
7 CONCLUSION AND OUTLOOK.....	165
8 REFERENCES	169

LIST OF ABBREVIATIONS AND ACRONYMS

CPA: Cryoprotective agent
CRM: Confocal Raman Microscopy
DMEM: Dulbecco Modified Eagle Medium
FWHM: Full width at half maximum
hESC: Human embryonic stem cells
IPS: Induced pluripotent stem cell
JMAK model: Johnson-Mehl-Avrami-Kolmogorov model
LN2: Liquid nitrogen
NA: Numerical aperture
NIR: Near-infrared
PBS: Phosphate buffered saline
TM: Transmission imaging
VTF model: Vogel-Tammann-Fulcher model
TTT: Time-temperature-transition

1 INTRODUCTION

The aim of cryopreservation is to preserve biological material and store it for later use while maintaining the biological function and characteristics [1]. This is done through a cooling process that aims at stopping all biological, chemical and physical processes so that the given sample can be stored virtually indefinitely. The field of cryopreservation was introduced in the 1930s by Luyet [2], [3] where he investigated vitrification of simple biological samples, i.e. rapid cooling of samples without ice crystallization. Cryopreservation started to gain interest through the discovery that cells could survive freezing and be revitalized through the addition of glycerol as so-called cryoprotective agent (CPA) in 1949 [4]. Today, cryopreserved samples are stored in biobanks; a term coined in the 1990s [5] and defined as a repository of biological material and associated data [6]. Biobanks has been growing significantly in the last decade both in terms of collection sizes as well revenue generated. A study from 2008 estimates that 270 million biological specimens are stored in the US alone and that this collection grows with 20 million samples per year [7], [8]. The revenue from biobanks was reported to 24.4 billion USD in 2013 and is expected to experience strong growth until 2023 [9]. Biobanks play an important role in both academic as well as commercial research since they provide a collection of biological samples with corresponding data and can be withdrawn from the biobank at any point in time for investigation. Such specimens can be used both in the research on the causes and treatment of many illnesses but also as a diagnostic and therapeutic tool [10].

The last decade has seen rapid development in the field of personalized medicine [11] that aims at personalizing treatment to each patient and thereby increasing its effectivity. Here biobanks have been identified as playing a key role [12]. They allow for the storage of personalized cellular samples that can be thawed at the appropriate time and applied for therapeutic uses [13], [14]. This requires that the revitalized cells survive the cryopreservation process with unimpaired biofunctionality [15], which is particular important for stem cells [16], [17]. The cryopreservation should thus ensure that the samples retain a high quality throughout the preservation process [18]. This poses high requirements on the employed cryopreservation protocol and CPAs used. The temperature profile used for the cryopreservation, i.e. cooling rate [19], storage temperature [20] and heating rate [21], play a major role in post-thaw viability of preserved cells. The CPA chosen can also exhibit cytotoxic effects and thus play a role on post-thaw viability and functionality [22]. This includes the common CPA Dimethyl Sulphoxide (DMSO) that has been in use since the 1950s [23]. Stem cells are particularly sensitive to the cryopreservation process [24]. The introduction of induced pluripotent stem cells for therapeutic use has further forced the development of

serum-free cryopreservation protocols to optimize viability and decrease cell differentiation [25], [26].

With state of the art methods, it is possible to store many different cell lines for extended periods of time with very low loss rates. A new cryopreservation protocol has been developed for each cell line. This encompasses both complex temperature profiles and preservation media. The deciding criteria for the given protocol are post-thaw viability and biofunctionality. This is an empirical and iterative development that is very resource intensive and not suitable for sample types of limited quantity [27]. It can be challenging to distinguish between different effects during preservation that influence the success rate, since the protocol is evaluated as a whole. This further implies that quality control in biobanks relies on thawing samples and reviewing biomarkers for the given sample type [28]. The most dangerous periods of a cryopreservation process are during freezing and thawing of the sample. A sample can thus not be refrozen and has to be used or discarded upon thawing. An optimal approach to the assessment of sample quality would thus be to perform non-contact measurements on the sample during storage. A quality control could then be performed on valuable, sensitive and limited samples without discarding them. Such a quality control would also allow bad samples to be discarded so that they do not take up precious storage space. With the increasing amount of stored samples this would optimize the utilization of storage space in biobanks and ensure that all stored samples are of high quality.

Liquid water constitutes a crucial part in living cells. The solidification of water in a freezing process as during cryopreservation thus poses challenges to the viability of cells. It is commonly known that intracellular ice crystal formation has lethal consequences for the cell [29]. The solubility of many compounds, such as electrolytes, CPAs or others, is much lower in ice as compared to liquid. This means that when ice crystallizes, the surrounding medium changes greatly in its composition and influences

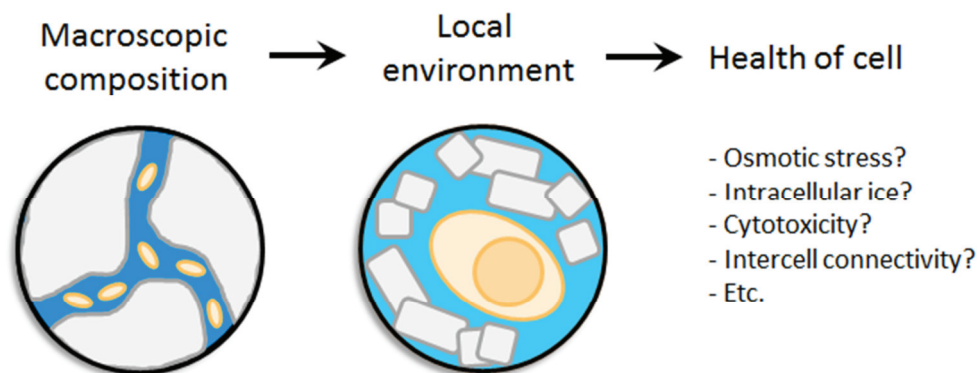


Figure 1.1 The health of a cell during cryopreservation is governed by the local chemical and physical environment. The local environment is in turn governed by macroscopic characteristics.

a cell profoundly. The health of a cell during cryopreservation is thus to a large extent governed by the chemical and physical environment inside the cell as well as in immediate proximity to the cell. This local environment is in turn governed by macroscopic properties of the sample such as temperature, initial chemical composition, phase composition, cooling rate, cell density etc. This has been outlined in Figure 1.1. Many of the macroscopic characteristics of a cryopreserved sample are expressed through the solid states that are formed in a given sample. This could for instance be the amount, size and shapes of ice crystals or the formation of a glassy phase between the ice crystals.

As an example hereof let us consider two identical samples. The outcome of a cryopreservation process may differ for the samples if storage conditions are identical but there are differences in the freezing and thawing of the samples. Differences can also occur if freezing and thawing are identical but the samples are not stored under identical conditions. This is a result of different macroscopic characteristics that lead to differences in the solid states that are formed in the samples during the cryopreservation process. Understanding the formation of the solid states during freezing as well as their influence on the biological state of the cells contained in the sample can increase the understanding of the cryopreservation process. This further aids knowledge-driven development of cryopreservation protocols that can possibly deliver results better and faster than an iterative approach to cryopreservation.

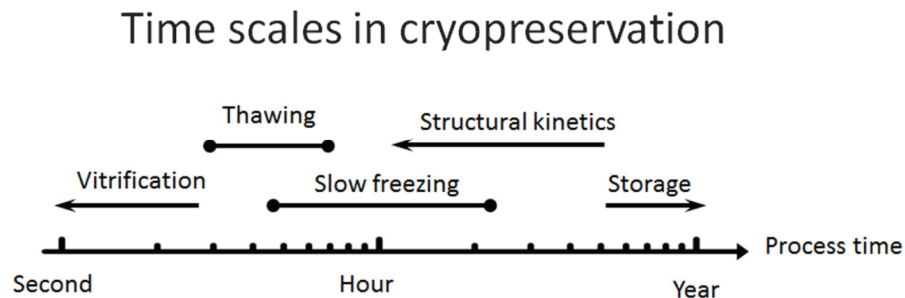


Figure 1.2 Time scales encountered in cryopreservation. The time scales encountered vary from seconds all the way up to decades.

One major challenge in the study of cryopreservation is that the processes encountered occur on vastly different time-scales as depicted in Figure 1.2. The time scales range from seconds seen in vitrification of samples to decade-long storage of samples. The outcome of a given cryopreservation is dependent on all processes that are encountered and any damaging effects accumulate over the entire lifespan of a sample. To understand the outcome, each process should be investigated separately using model experiments in order to be able to design an experiment with a reasonable time frame investigating effects that occur on similar time scales. This would also allow for a separation of the effects encountered during cryopreservation.

Many studies currently performed that investigate such part processes use cryomicroscopy imaging techniques that allow for conventional transmission and fluorescence imaging of cells during freezing in a low-temperature microscopy chamber. These methods are primarily used to study cell morphology [30] or intracellular ice formation [30], [31]. Transmission imaging does, however, have limitations in that penetration depth into a sample is limited due to scattering of light [32] and that physico-chemical processes cannot be investigated. Further insights, besides morphological and topological information, are required to improve on cryopreservation protocols in particular for more complex sample types. One such method has recently been introduced to the field of cryobiology [33]. Confocal Raman microscopy can effectively deliver chemical imaging of cryopreserved samples which is a major step forward in cryomicroscopy.

The aim of this work is to identify and establish methods that investigate cryopreserved samples in a manner, such that conclusions on what processes have occurred during the cryopreservation process and the state of the sample in a retrospective manner. Such a retrospective analysis should rely on macroscopic measurements that are conducted in a non-contact manner and that can be implemented in a low-temperature environment. This study is a start to look into these processes as a whole and investigating their influence on the storage state. This should be done while keeping in mind possible applications leveraging this knowledge for biobanks.

Through the application of Raman microscopy, chemical markers that convey information on the state of the sample can be identified and exploited to detect lethal effects that can occur during cryopreservation. This will allow for Raman spectroscopy studies of samples in storage and thus a retrospective analysis on the state of the sample. This offers a new perspective on how quality control can be performed in a biobank. The Raman microscopy study can furthermore be used to gain further insights into the local chemical and physical environment in and around cells during the cryopreservation process. This study will focus on cell suspensions, cell colonies and media used to cryopreserve these.

This study will furthermore investigate the effect of suboptimal storage conditions on samples. In particular, the response of media to temperatures over the typical storage temperatures, i.e. the glass transition temperature, will be studied. For slowly frozen samples, this results in recrystallization whereas ice can nucleate and grow in vitrified samples. When the temperature is high enough in a slowly frozen sample, ice crystals can fuse to minimize the surface energy in a process called recrystallization. The temporal development of ice crystals under isothermal conditions will be studied using fluorescence microscopy. Recrystallization plays a role in the resulting ice crystal structure during freezing and has an influence on the outcome of a cryopreservation process [34]. Recrystallization may also provide the key to develop a time-temperature

indicator as a direct proof of an unbroken cold-chain for cryopreserved samples and thus improve on quality control in biobanks.

Devitrification is the process where ice crystals nucleate and grow in vitrified samples. Through the application of differential scanning calorimetry, the ice crystal growth rates can be measured during devitrification and analyzed for various vitrification media. Such characterization of vitrification media can be used to predict how a sample will respond to unforeseen temperature elevations and thus deliver a different perspective on the development of cryopreservation protocols since both the choice of CPA and concentration have a major impact on the stability of the vitrified state. Such insights can furthermore be used to formulate best practice handling protocols for cryopreserved samples.

2 INTRODUCTION TO CRYOPRESERVATION

This chapter aims at providing all background information required for a complete understanding of the processes and structures found in cryopreserved samples that will be studied in this thesis. It is therefore important to understand the general approaches to cryopreservation since different methods results in vastly different sample types each with its advantages and challenges. The approaches to cryopreservation will be presented and discussed in section 2.1. Relaxation processes are a sign that a sample is unstable and is subject to ageing, an issue in cryopreservation that can lead to a degradation of the sample quality. A general discussion of relaxation processes will be given in section 2.2 Retrospective analysis aims at studying such processes after they have occurred and identifying them in stored samples. In section 2.3, general aspects of retrospective analysis are presented along with two different approaches to this topic.

Cryobiology considers the effects on biological material when they are exposed to sub-zero temperatures. One of the most essential components to cells and their functionality is water. The biological functionality, vitality and several other characteristics of living matter are significantly impacted during cryopreservation since water can crystallize and thereby fundamentally change the physical and chemical state in and around the biological material. When studying cryobiology it is therefore important to understand the processes that occur during a freeze-storage-thaw cycle and their effect on the biological state of a cell. The main applications of cryobiology can generally be divided into two groups. First of all it is understood that freezing can cause damage to biological material. This is actively used in cryosurgery where low temperatures are used to kill unwanted tissue such as malignant tumors [35], [36]. Here, the main purpose is to find ways to efficiently destroy some material through exposure to very low temperatures leaving the surrounding material unaffected. The study of cryobiology can also be used to preserve biological material in extended periods of years or even decades with a subsequent revitalization [37]. This is called cryopreservation and the main area of focus here is to cause as little damage as possible in the biological samples so that their vitality and functionality is unaffected by the exposure to low temperatures. When cells are cooled all chemical and physical processes are slowed including metabolism. If the temperature is low enough, metabolism can be halted thereby stopping the biological clock. Cryopreserved cells do therefore not age and can be stored virtually indefinitely. There currently exists

samples that have been stored for decades [6], [38], [39]. These should in principle exhibit the same characteristics compared to samples recently frozen if they are frozen and thawed in the same manner and that the storage conditions have been stable at sufficiently low temperatures.

The field of cryobiology started when Polge et al. succeeded in freezing spermatozoa to -79°C and subsequently reviving them [4]. In their study glycerol was used as an agent to protect the cells. Further studies by Lovelock described the hemolysis of red blood cells when frozen [40] and the role of cryoprotective agents (CPA) for a successful cryopreservation process [41]. By understanding the mechanisms that damage cells, precautions can be made to avoid them. It is therefore essential to study both the lethal effects when exposing cells to sub-zero temperatures as well as the protective mechanisms that different preservation strategies offer. In addition, cells usually undergo significant changes during the freezing process and need to recover. The cells furthermore need to be transferred to a normal cell medium.

The cryopreservation process can typically be divided into five distinct steps:

1. Preparation of the sample.
2. Cooling of the sample until the storage temperature is reached.
3. Storage of the sample.
4. Thawing of the sample to room temperature.
5. Recovery of the biological material.

Each cell line is different and a specific cryopreservation protocol has to be tailored to it where each of the five steps is optimized. The most common parameter that is optimized is the post-thaw vitality of the cells. For many other applications also criteria such as functionality or in the case of stem cells differentiation are important. Current research focuses on optimizing the preservation process [42], [43]. This is done using very different approaches such as understanding lethal mechanisms, optimizing current preservation protocols or automation in biobanks to increase throughput. Particular interest is given to preservation of stem cells since among other applications focused more on research applications they offer the attractive prospect of personalized medicine with the advent of induced pluripotent stem cells.

2.1 Approaches to cryopreservation

There are two fundamental different approaches in order to preserve cell cultures at cryogenic temperatures. They mainly differ in their freezing protocol, but due to the different characteristics of the resulting samples, also the sample media composition and sample container need to be adapted in order to optimize different aspects of the cryopreservation. The more common approach is the ‘slowly frozen’ approach where samples are frozen slowly at a cooling rate of the order of $1^{\circ}\text{C}/\text{min}$. The other approach is the so-called ‘vitrification’ approach. Here the samples are often plunged

into liquid nitrogen in order to achieve very fast cooling rates above 200 °C/min [44] or even over 10,000 °C/min for low-volume samples [21], [45]. The term vitrification or vitrified in cryobiology is only used for samples where the entire volume can be considered vitrified. Even though also parts of a slowly frozen sample form an amorphous phase and can be considered to be vitrified, the entire sample contains crystalline parts and is therefore not described as 'vitrified sample'. This terminology will be used in the following and the expression 'vitrified sample' always describes a sample that was subject to very fast freezing.

Even though these approaches have significant differences in their biological, chemical and physical aspects they in principle use the same mechanism in order to preserve cells. The aim of both approaches is to immerse cells in a highly viscous glass but the path to achieve this state differs for the two approaches. When the aqueous phase inside and around the cell is turned into a high-viscosity glass, all chemical and biological processes are slowed to such a degree that they can be considered as completely stopped. This occurs when the aqueous phase is supercooled to a temperature below the glass transition temperature that is around -130 °C for aqueous mixtures. An effective storage of cryopreserved cell culture samples thus requires storage temperatures below -130 °C. Such samples are therefore often stored in liquid nitrogen freezer units.

For both approaches, a CPA is added to the cell culture medium in varying concentrations. The CPA alters ice formation and thus offers the protection required for cells to survive being frozen and subsequently thawed. There exists a wide range of usable CPAs [22] and many cryopreservation protocols using different CPA types and concentrations have been developed and tailored to each specific cell line. The CPAs can roughly be divided into membrane-permeating and non-permeating CPAs and they thus provide protection based on an intracellular or extracellular mechanism. By far the most common CPA is dimethyl sulphoxide or DMSO, which is why this particular CPA is the primary focus of this study. DMSO is a membrane-permeating CPA meaning that it will provide internal protection to cells. Aqueous solutions of DMSO can easily form a glass and thereby suppress intracellular ice formation. It has furthermore been reported that DMSO exhibits membrane stabilizing properties in a hyperosmotic environment [22]. The main disadvantage of using DMSO as CPA is its cytotoxicity especially compared to other CPAs such as for example saccharides and polysaccharides. The concentration of DMSO used for the slow freezing approach is typically below 10 % [22]. Concentrations over 40 % are being used for vitrification [22]. The trade-off between DMSO's ability to form a glass and its cytotoxicity might thus differ for both approaches.

Both approaches offer advantages and disadvantages and the choice of preservation method relies on the application and cell line in question. Here, both the slow freezing and the vitrification method are presented as a fundamental understanding of both approaches is required to understand the findings in of this thesis. Thereafter several

effects that can be lethal to cells during cryopreservation and their relation to the preserving mechanisms will be presented.

2.1.1 Slow freezing approach

The slowly frozen approach to cryopreservation is the more common one. This approach was first demonstrated by Polge et al. in 1949 where spermatozoa was revitalized after being frozen to -79°C [4]. This approach can, to a certain point, be characterized as an equilibrium approach where the sample is cooled slowly enough to be in thermodynamic equilibrium. This approach relies on the formation of ice crystals and the resulting increase of CPA concentration between the ice crystals providing a suitable environment for cells to survive the cryopreservation procedure. When a sample is cooled slowly, ice crystals will start to form and grow. Between the ice crystals, so-called dendritic channels are formed, primarily due to the addition of CPAs such as DMSO to the medium. Using a sufficiently low cooling rate means that the number of ice nuclei formed is low compared to the ice crystal growth rate. This in turn means that most ice nuclei will form outside cells. As a result the vast majority of cells in the sample will be located in the dendritic channels since extracellular ice crystal growth does not penetrate intact cellular membranes.

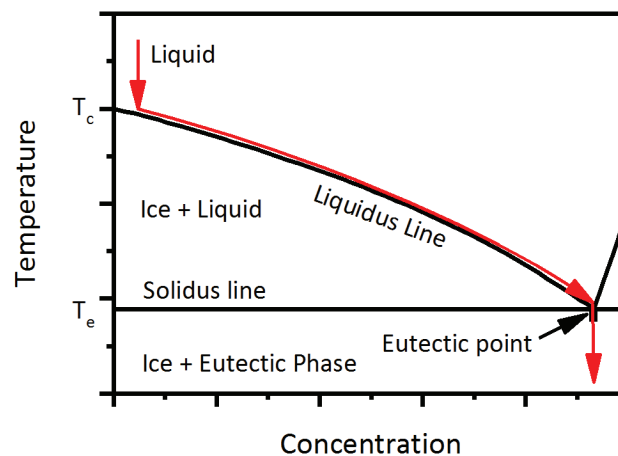


Figure 2.1 Schematic path through a binary phase diagram for a slowly frozen sample. T_c denotes the crystallization temperature and T_e the eutectic temperature.

A phase diagram such as the one in Figure 2.1 describes the chemical composition in the dendritic channels at given temperatures and thus the environment the cells in the sample experience during freezing. Phase diagrams can only describe samples in equilibrium and thus only when low cooling rates are employed. The macroscopic physical and chemical state of a slowly frozen sample can be described by a path through the phase diagram. When ice starts to form, the remaining liquid will concentrate and the liquidus line describes its crystallization temperatures at varying

concentrations. The medium in the dendritic channels concentrates as ice starts to grow due to the low solubility of electrolytes and other chemical compounds in ice. Due to its concentration dependency the crystallization temperature in the dendritic channels further decreases.

The initial concentration of the sample C_0 and the concentration C_T in the non-crystallized parts of the sample at temperature T can be used to calculate the amount of ice in the sample. The fraction of the sample forming ice f_{ice} and the fraction of the non-crystallized part of the sample f_{liq} can be calculated using the lever rule [46]:

$$f_{ice} = \frac{C_T - C_0}{C_T} \quad (2.1)$$

$$f_{liq} = \frac{C_0}{C_T} \quad (2.2)$$

These equations are only valid for temperatures between the eutectic and the crystallization temperature. The eutectic temperature describes the minimum equilibrium temperature where the dendritic channels are still liquid. When the sample is cooled below the eutectic temperature two different scenarios can occur. Without the addition of CPAs the sample completely solidifies through eutectic crystallization since from a thermodynamic point of view the remaining liquid is just ordinary brine in a concentrated form with an eutectic temperature of approximately -21 °C. In the presence of CPA in the medium the sample leaves the equilibrium state and the phase diagram cannot further describe the chemical state of the sample. The viscosity of the remaining liquid increases thereby preventing eutectic crystallization. The medium inside the dendritic channels eventually turns into a glass providing the preserving feature of this process. Any cells in the dendritic channels can thus be preserved for later thawing and revitalization. If the sample reaches temperatures well below -130 °C without a eutectic crystallization all chemical and biological processes are completely stopped and the sample can then be stored in a liquid nitrogen freezer unit.

The effects of the slow freezing approach on a cell are sketched in Figure 2.2. The crystallization of ice in such samples has two consequences that both are very important to consider for the preservation nature of this process. The first consequence is that the CPA concentration in the dendritic channels is increasing as previously mentioned which essentially provides the preservation feature of this process. The second and equally important effect is that the concentration of electrolytes is increasing in the direct surroundings of the cells. This leads to osmotic dehydration of the cells during the cooling process depends on three parameters: Cooling rate, membrane diffusion characteristics and the share of osmotic active water. A lower cooling rates leads to longer exposure times of the electrolyte concentrations at each temperature during cooling. This means that a cell will dehydrate more if the sample is exposed to lower cooling rates compared to high

cooling rates. The cell membrane diffusion characteristics have a major impact on the dehydration where higher permeability leads to a larger amount of water escaping the cell. This also explains why the dehydration differs between cell types. However, a part of the intracellular water does not take part in the osmotic exchange since the water molecules are strongly bound to biomolecules such as proteins. This can be considered osmotic inactive water. There exists an optimum dehydration level during cryopreservation as too little dehydration increases the risk of intracellular ice formation whereas too much dehydration eventually is lethal. The resulting optimum cooling rate is dependent on the cell type due to the membrane diffusion characteristic and cell volumes for the particular cell type.

The slow freezing approach possesses several advantages over the vitrification approach that have made it the primary method for cryopreservation for a broad range of cell types. The technical requirements are lower since low cooling rates on the order of 1-10 °C/min are relatively easier to control and maintain compared to the high cooling rates required for vitrification. The second main advantage of this method is that only relatively low CPA concentrations are required in order to achieve a successful preservation. Many CPAs are cytotoxic but the harmful effects of CPAs are less pronounced at lower temperatures. Their detrimental effects are also strongly dependent on their concentration. Since the CPA concentration in direct vicinity of the cells is increased gradually during ice crystal growth, the cells are only exposed to high CPA concentrations at low temperatures. In the slow freezing approach the relatively

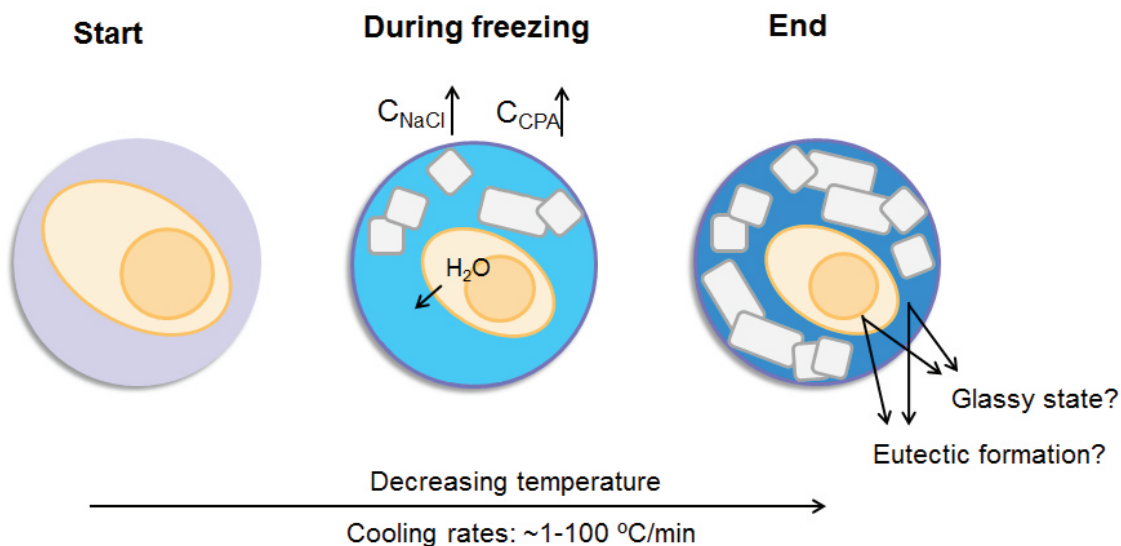


Figure 2.2 Here a cell is sketched during slow freezing. The concentration of osmolytes and CPA increases when ice starts to crystallize. This increase induces a flux of water out of the cell due to osmotic forces. The amount of water flowing out of the cell is depending on cell type and cryopreservation protocol but can be rather significant (>70 % of cell volume). The increase of CPA can result in the formation of a glassy state.

low CPA concentrations that are initially added to the sample only poses a moderate risk to the cells. Additional measures can be taken to reduce this risk further as for example adding the CPA only at temperatures below 4 °C. Different CPAs exhibit different levels of cytotoxicity to different types of cells. They should thus be chosen accordingly while keeping in mind the amount of protection the given CPA offers. The slow freezing approach also offers the potential for high-throughput cryopreservation as vessels with a relatively large volume can be employed for a simultaneous cooling of a high number of cells. Today many applications and studies require a high quantity of cells and here a high throughput is essential in the cryopreservation process. The high throughput is furthermore enhanced by the possibility for an automated and standardized freezing and thawing process.

The slow freezing approach does, however, also possess some disadvantages that make it unfavorable compared to the vitrification approach in some cases. The preservation protocol cannot always be optimized to such a degree that the disadvantages are only minor and can in practice be disregarded. The main problem with the slow freezing approach is the crystallization of ice and the formation of dendritic channels. The cells are located in a changing chemical and physical environment in the dendritic channels as the temperature is lowered. This means that the cells will dehydrate and are not in their natural hydrated isotonic equilibrium during storage. This can lead to lowered cell viability in particular when very low cooling rates are employed. The cells furthermore have to recover post thaw to regain the equilibrium state. Some cell lines like for example oocytes and stem cells are particular sensitive to dehydration which is why the vitrification approach is almost exclusively used for these. Another detrimental effect of ice crystallization is that it can potentially destroy cell-cell contacts. This means that cellular constructs such as cell colonies, organoids and tissues cannot be preserved using the slow freezing approach since the cell-cell contact plays a vital role in the functionality and vitality of the sample in question. Crystallization of ice in the sample can also result in intracellular ice, which is commonly known to reduce cell viability.

The so-called 'two-factor hypothesis coined by P. Mazur describes the main lethal mechanism when slowly freezing cells [19]. This hypothesis describes the interplay between, water transport, dehydration, intracellular ice crystallization and their influence on the viability of the sample.

Ice crystal growth in a sample is limited by a low nucleation rate at slow cooling rates. Since the extracellular medium is order of magnitude larger than the biological matter the ice in the sample is primarily extracellular ice. The concentration of osmolytes in the immediate vicinity of a cell is increasing as ice nucleates and grows through the sample and thereby extracts water from the remaining medium. The cells are experiencing a strongly hypertonic environment, i.e. an electrolyte concentration higher than the osmotic neutral isotonic concentration. Through an osmotic response the cells will eventually dehydrate. If the dehydration is too strong or too prolonged without reaching the storage state it can lead to cell death. The cell death due to

dehydration is probably caused by denaturation of proteins and the cell membrane. If, on the other hand, a relatively high cooling rate is employed, in order to minimize the dehydration effects on the cells, the nucleation rate increases. With a high density of ice nuclei throughout the sample also the risk of intracellular ice crystallization increases. The ice nucleation rate increases with lower temperatures until a maximum is reached the so-called the homogeneous nucleation temperature that depends on the media composition. For pure water the homogeneous nucleation temperature is around -40°C [47], [48]. This risk of intracellular ice formation is furthermore enhanced when the sample becomes supercooled. Supercooling describes a non-equilibrium state in samples that are cooled too fast so that ice crystals do not start to nucleate when the freezing temperature is reached. At a lower temperature, very fast nucleation will eventually start in slowly frozen samples. As the cells in the sample cannot dehydrate due to extracellular ice formation in the case of supercooling, the higher amount of water still present in the cells at the onset of nucleation increases the probability that an ice crystal will nucleate intracellularly. It is commonly known that intracellular ice crystallization is detrimental to cell viability although the exact lethal mechanism has not been found. It has been speculated that intracellular ice crystallization destabilizes the membrane causing the cell to lyse on thawing. Another proposal is that recrystallization of smaller ice crystals into larger ones causes damage to the organelles of the cell [49]. Other explanations directly related to the effects of intracellular dehydration might also hold true.

An optimal cooling rate exists when taking into consideration that dehydration is pronounced at low cooling rates whereas intracellular ice formation is pronounced at high cooling rates. This is illustrated in Figure 2.3, where the optimal cooling rate is located where the two damaging effects are tapering off. When a cryopreservation

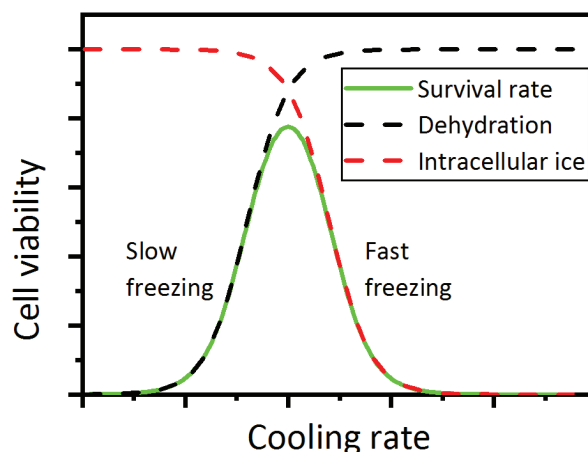


Figure 2.3 Graphic representation of the two factor hypothesis. Cell viability drops at slow cooling rates due to dehydration and at fast cooling rates due to formation of intracellular ice. There exists an optimal cooling rate where the combination of solution effects and intracellular ice crystallization is minimized.

protocol is developed, the cooling rate allows the cell to dehydrate in order to minimize the risk of intracellular ice formation but should not expose the cells to significant periods of dehydration. The optimal cooling rates depends on the particular cell characteristics such as volume and membrane diffusion properties but also on the cell media chosen since this governs the ice crystal growth rate as well as ice nucleation rate. The viability of various cell types exposed to increasing cooling rate supports this two factor hypothesis [19], [29], [50]. Further damage to cells during slow freezing can originate from mechanical interactions between extracellular ice crystals and the cellular membrane [51]. A study also shows that eutectic crystallization is harmful to cells [52]. Here the lethal mechanism is mostly unexplored and will be investigated in chapter 5.

2.1.2 Vitrification approach

The principle of vitrification of biological material by rapid cooling is generally considered to be introduced by Luyet in 1937 [2], [3]. It is as such not a new technique compared to the slowly freezing technique. The method was however only popularized by Fahy et al. in the early 1980s [53], [54] after the slowly freezing technique was already well established.

Vitrification is a non-equilibrium approach that relies on cooling a sample rapidly enough in order for it to directly vitrify without any ice crystallization. The glass transition is a second-order phase transition and implies a change in the heat capacity of the sample. The glass transition temperature can then be defined as the temperature at which half of the change in heat capacity related to the phase transition has occurred. Besides this thermodynamic definition of the glass transition temperature, purely phenomenological descriptions exist but when applied correctly all methods deliver the same result. It can for example be described as the temperature below which the viscosity is above 10^{13} Poise [55] or when the structural equilibration time is on the order of 100 s [56]. For aqueous mixtures the glass transition temperature is approximately -130 °C.

Figure 2.4 shows an example of a binary phase diagram of an aqueous mixture containing CPA. In order to vitrify the sample successfully the unstable region below the homogeneous nucleation temperature has to be avoided as this would always lead to the formation of ice in the sample. The CPA concentration thus needs to be high enough to avoid homogeneous nucleation. The other critical region in the phase diagram is the metastable state below the crystallization temperature. In contrast to the unstable region it cannot completely be avoided by adjusting the sample composition. Here, the cooling rates needs to be very high so that the sample is out of equilibrium and supercooling occurs. When the cooling rate is high enough the sample can be cooled below the glass transition temperature in a non-equilibrium state without any ice crystallization at all [57], [58]. This can be considered as complete supercooling and the vitrification process is depicted as arrows in Figure 2.4.

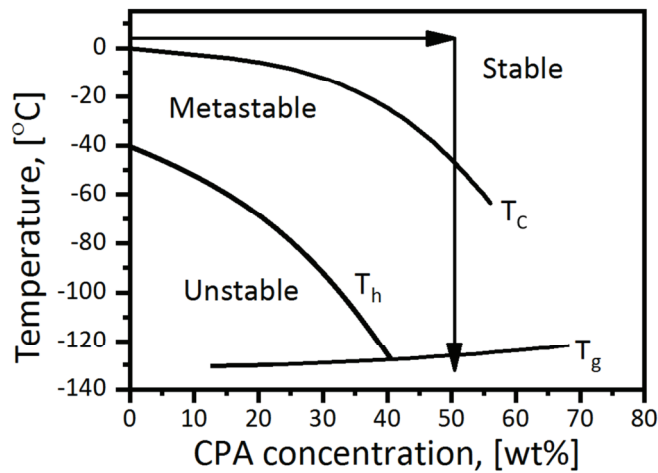


Figure 2.4 Typical vitrification procedure visualized in a phase diagram. First the concentration of the CPA is increased and the sample is subsequently cooled rapidly to below the glass transition temperature T_g . As soon as the sample is cooled below the crystallization temperature T_c it enters a metastable region that should be traversed within a short period. The region below the homogeneous nucleation temperature T_h is considered unstable and has to be avoided for vitrification. Figure inspired from [58].

The cooling rate required in order for a sample to vitrify, the critical cooling rate, depend on the chemical composition of the sample. In order for pure water to vitrify it has to be cooled at rates over 10^7 °C/s [59]. This is usually achieved by depositing water vapor or micro droplets on a very cold surface [60] and rather impractical from the perspective of cryopreservation. The relatively low heat conductivity furthermore hinders liquid water samples thicker than 1 μm to vitrify. For any practical application of vitrification, high concentrations of CPA are added in order to reduce the critical cooling rate to realistic values and low-volume samples are used to assure fast enough cooling also in the central parts of the sample.

Let us first consider adding high amounts of CPA to a sample. The advantage of high concentrations of CPA is two-fold. CPAs often have a higher viscosity than water, slowing down ice nuclei formation and increasing the possibility that the sample remains supercooled. High concentrations of CPA also lead to significant depressions of the freezing temperature and homogeneous nucleation temperature which shortens the time period that a sample will have to spend in a supercooled state. In effect, this leads to a significant reduction of the critical cooling rate for a given sample [58], [61]. For a sample containing over 42 wt% DMSO, the unstable region can be avoided the critical cooling rate is reduced to below 100 °C/min.

Low volume samples necessary as there is an internal limit to the cooling rate due to the relatively low heat conductivity of aqueous media. The limits on the cooling rate of the entire sample can be increased by minimizing the volume or thickness [26], [62]–[66]. This is a rather common method that has been utilized in a variety of ways and

optimized. Also the choice of container material and thickness plays a role in order to achieve high sample cooling rates.

The main advantage that the vitrification method offers over the slow freezing process is that ice crystallization is completely avoided. This has several positive consequences. When ice crystallization is generally avoided, intracellular ice crystallization is also avoided. It furthermore allows for cryopreservation of cell colonies without disturbances of the general structure of the colony where ice forming between cells would destroy cell-cell contact. Slowly freezing stem cell colonies can lead to differentiation and apoptosis [67]–[69]. It has furthermore been shown that using vitrification for stem cell colonies reduces mechanical and chemical stress [26]. Avoiding ice crystallization furthermore allows biological molecules and intracellular structures to remain in their natural hydrated state throughout the preservation or as B. Wowk states [58]:

“Vitrification is important to cryobiology because the natural state of liquid water inside living things is disordered. Maintaining the natural disorder of water molecules and dissolved solutes inside living things during the solidification process of cryopreservation is advantageous from the standpoint of minimally disturbing the system being preserved.”

This is a very important aspect especially for sensitive cell lines since the post-thaw recovery is facilitated when dehydration is avoided. Another advantage of the vitrification approach is that there exists no optimum cooling rate as long as the sample is cooled fast enough to achieve vitrification. When a method providing very fast cooling or heating rates has been developed and established, then it can directly be transferred to other cell lines or sample types without the need to individually adapt the cooling rate. As the sample container has a major impact on the sample cooling rate and since some sample types are not compatible with all containers, there are limits to the standardization of the vitrification process.

There are, however, also disadvantages of vitrification that have to be taken into consideration. CPAs often have cytotoxic effects that are enhanced by the high concentrations required. This is probably the most significant disadvantage of the vitrification approach. The cytotoxic effects decrease with decreasing temperature. The high concentrations of CPAs are therefore often first added to the sample at low temperatures around 4 °C or even gradually with the decreasing temperature. The latter method is called liquidus tracking where the CPA is gradually added so that the sample composition and temperature follows slightly above the liquidus line in the phase diagram thereby avoiding ice crystallization [70]–[73]. This means that the very high concentrations of CPA are first encountered at very low temperatures minimizing the cytotoxic effects. This is, however, a significantly more complex and time-consuming method than ordinary vitrification and also requires sealing of the sample

at cryogenic temperatures. The applicability of the liquidus tracking method is also limited by CPA diffusion in the sample. It should be kept in mind that diffusion times for CPA into cells or tissue can increase dramatically due to higher viscosity of the medium or decreased membrane diffusivity. Therefore, CPA cytotoxicity is also the main barrier to successful cryopreservation for tissue samples. Since the CPA has to be present in all parts of the tissue, long incubation times are required in order to achieve a high enough CPA concentration to ensure vitrification at the center of the tissue. This effect is even more pronounced in articular cartilage tissue where no vascular system can transport the CPA into the tissue [74].

Another disadvantage is the limitation of the sample size that is imposed by the very high cooling rates required for successful vitrification. Beier et al. [26] report that typically only 5-10 human embryonic stem cell colonies are preserved in a sample. When considering the large amount of biological material currently being preserved every day then it is clear that low volume samples are a disadvantage. As with most industrial endeavors, high efficiency and high throughput are also desired in biobanks and low volume samples are clearly disadvantageous. For specific cell lines and types it is, however, more efficient to use the vitrification method over the slowly freezing technique that allows for higher volumes, since it offers significantly higher survival rates. For some sensitive samples like stem cell colonies it is even the only method possible.

The main risk to vitrified samples is so-called devitrification [75], [76]. It describes the process of crystallization in a sample that was originally vitrified. Vitrified samples are in a non-equilibrium state and there are a driving force will force the sample towards equilibrium. As a result, ice will crystallize in the sample. This can happen if the sample temperature is increased above the glass transition temperature in a significant amount of time. During storage, this could happen through handling of the sample or withdrawal of a neighboring sample. Devitrification can also occur during thawing if the heating rate is too slow and the non-equilibrium state cannot be maintained until the sample temperature is above the crystallization temperature. Recent studies show that the heating rate plays a major role in the success of a cryopreservation process using the vitrification approach [21], [34], [45], [77], [78]. Devitrification as a process will be studied in great detail in section 6.3.

Another risk for vitrified samples is related to the change in density during a phase transition [79]. The density of water is 1.000 g/cm^3 in its liquid state, and $0.937 \pm 0.002 \text{ g/cm}^3$ in the low-density vitrified state. When a sample undergoes the phase transition to glass internal tension will occur. This tension increases with the cooling rate and can be considerable in vitrified samples. If this tension is too high then the glass can crack. Figure 2.5 presents an example of a vitrified sample that suffered damage due to internal tension resulting from fast cooling. A sample of murine fibroblast cells in phosphate buffered saline (PBS) was cooled with a cooling rate of approximately $240,000 \text{ }^\circ\text{C/min}$ of a low volume sample mounted under a microscope objective. The image recorded at $-155 \text{ }^\circ\text{C}$ shows that cracks appear in the medium.

Cracking of the glass can be harmful to cells through mechanical damage. While this is only a minor risk to cell suspension samples, it is a major risk for cell constructs such as colonies, organoids or tissue. Cracking of the vitrified state is dependent on cooling rates and medium composition as well as sample container material and topology. The very high cooling rates were achieved by directing liquid nitrogen under high pressure to the sample.

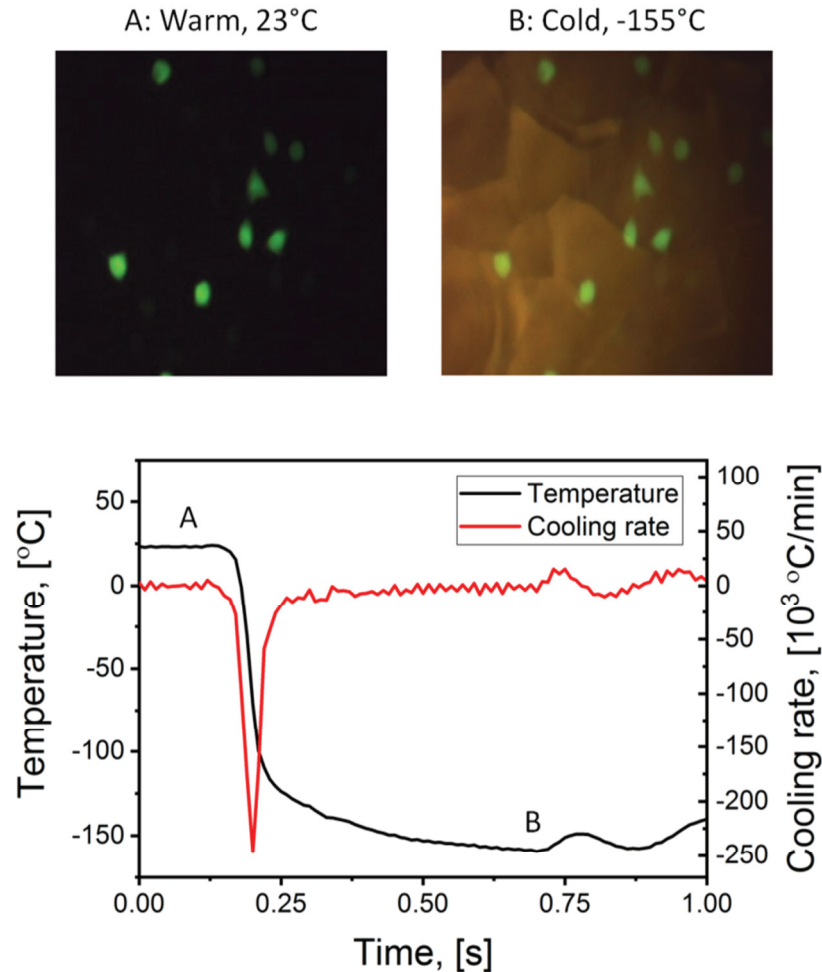


Figure 2.5 Murine fibroblasts stained with calcein green are rapidly frozen with a cooling rate of approximately 240,000 °C/min. The image recorded at -155 °C shows cracks in the medium due to a change in density.

2.2 Slow processes in samples at low temperatures

The aim of cryopreservation is to halt all chemical and biological processes by reducing the temperature. Whether all processes really have been stopped can be very difficult to verify due to high reduction of the process rate and time constraints. It will require very stable storage conditions and take years or even decades to test this assumption. The processes that can occur when a sample temperature is lowered below the freezing temperature are either of physical nature, such as cell dehydration, phase

transitions or recrystallization, or of biochemically triggered nature, such as metabolism or stem cell differentiation.

The cryopreservation of biological samples aims at stopping all biochemical processes. However, the direct detection of metabolism or other biological activities is very challenging, in particular when cryogenic temperatures slow down all dynamic processes extremely. To check whether a sample is stable and stored correctly, the more accessible physical processes are thus used as an indicator. When all physical processes are fully halted and when the sample is in a kind of immobilized solid state, it can be assumed that biochemical processes are halted as well or at least slowed down tremendously. The success of a cryopreservation can thus be monitored by checking the progress of physical processes such as cell dehydration, phase transitions or recrystallization.

A cryopreserved sample transitions to its solid storage state through physical processes. Phase transitions describe the formation of crystalline structures such as ice and precipitates, while recrystallization describes how ice crystals fuse and change shape in order to minimize their inherent surface energy. Both of these processes can occur during freezing and thawing of the sample, but little is known about their progress during storage. One of the major focus points of this study is to investigate these slow physical processes. Based on a detailed understanding of these processes, methods will be developed that allow for monitoring of cryopreserved samples during storage.

Physical processes describe a relaxation towards an equilibrium state. A sample can either be stable if it is in the global energy minimum, metastable if it is in a local energy minimum or unstable when it is not in an energy minimum. Relaxation thus describes a process where the sample is in an unstable or metastable state and transitions towards the equilibrium state. Cryopreserved samples are typically in a metastable state that can be stabilized by providing suitable environment conditions that hinder relaxation to the equilibrium state. A vitrified sample is a supercooled highly viscous liquid at a temperature far below the crystallization temperature and thus entirely out of equilibrium. If it was not for the high viscosity, ice would start to crystallize in order to bring the sample to an equilibrium state.

Figure 2.6 depicts the relaxation process from a metastable state where an energy barrier has to be overcome in order to bring the sample to an energetically more favorable state. The sample is initially in the metastable state with energy E_1 . Through a relaxation process, the sample can be brought to the stable or metastable state with lower energy E_2 . The energy difference $\Delta E = E_2 - E_1$ between the two states will be released during the relaxation process and can be considered the driving force of the process. Only when the energy difference is negative, the transition from E_1 to E_2 is possible without any external driver and the system is more likely to relax the larger ΔE is. The energy barrier is often referred to as the activation energy E_A . The higher the activation energy is the less likely it is for the process to spontaneously start. In the

case of cryopreserved samples that can best be described as large ensemble, where the energy provided for relaxation processes is thermal energy, high activation energy for a process translates into slow dynamics. When the temperature is reduced sufficiently, the activation energy for processes like recrystallization or ice crystal formation cannot be provided thermally any longer. This is the main reason why it is beneficial to reduce the temperature in order to effectively halt the relaxation in cryopreserved samples. A sample can, however, also be stabilized and become more robust against temperature fluctuations when the activation energy for all possible relaxation processes is increased. In the case of cryopreserved samples, viscosity is a crucial parameter in order to increase the energy barrier for the predominant relaxation processes such as ice formation and recrystallization. According to kinetic theory, the rate of relaxation is proportional to the probability that the system has enough energy to overcome the activation energy. The rate of relaxation $K(T)$ can be described with the following Arrhenius equation:

$$K(T) = K_0 \exp\left(-\frac{E_A}{RT}\right) \quad (2.3)$$

Here R and T denote the gas constant and temperature, respectively. The constant K_0 describes the process rate when unlimited energy is present in the system.

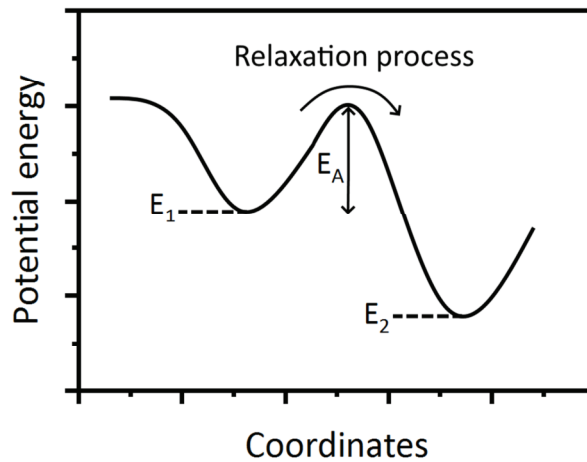


Figure 2.6 Schematic representation of the energy landscape. The system is initially located in energy state E_1 . Through a relaxation process it can overcome the energy barrier E_A to enter the energetically more favorable state E_2 .

The Arrhenius relation shows that relaxation is not completely halted even at very low temperatures. When a sample is stored at temperatures well below the glass transition temperature relaxation processes continue to proceed but at an extremely slow pace. Sample conditions change at the glass transition temperature resulting in for instance a change in the heat capacity and viscosity. Only extremely sensitive

measurements covering a large timespan can thus be used in order to test for these very slow relaxation processes at cryogenic temperatures.

2.2.1 Acceleration of slow processes

It would be advantageous if it were possible to accelerate these processes to a reasonable level. A direct measurement would then be possible and by an extrapolation of the results to typical storage conditions, the effect of slow processes on a cryopreserved sample can be investigated. Due to the temperature-dependence of relaxation processes, an elevation of the sample temperature can be used to accelerate them.

The effect of raising the temperature can also be seen in the perspective of Figure 2.6. The rate of relaxation is governed by the energy barrier. When raising the temperature, thermal energy is added to the system making it more likely that the system can overcome the energy barrier and enter an energetically more favorable state. This effectively increases the rate at which the relaxation occurs and the process is accelerated. This allows for an investigation of the process and its effects in a reduced timeframe. By repeating the measurements at multiple temperatures, important characteristics of the relaxation process can be extrapolated to a much broader temperature range. This measurement would provide detailed information on the parameters governing the relaxation process, namely the activation energy E_A and the asymptotic process rate at infinite temperature K_0 . Extrapolation to the storage conditions would then allow for a prediction of sample lifetimes. It is, however, not trivial to extrapolate to storage conditions since detailed knowledge on sample parameters would be required for both above and below the glass transition temperature. Such information can be extremely difficult to obtain. Care should further be taken when choosing a temperature regime to investigate the relaxation processes in.

When a relaxation process is accelerated through temperature, two fundamental aspects should be taken into considerations when choosing a suitable temperature range for the measurements. On the one hand, the temperature should be high enough so that the relaxation process proceeds fast enough so that it can be studied within a reasonable timeframe set by the experimental constraints of the measurement technique. On the other hand, the temperature should be low enough in order to keep the chemical and physical properties of the sample comparable to storage conditions. One example of how the temperature can be used to accelerate a relaxation process is devitrification of vitrified samples consisting of highly concentrated DMSO in water. A deliberate choice of temperature can tune the devitrification time between minutes and several hours while keeping the important characteristics of the sample constant. Such a time frame is ideal to study the devitrification kinetics.

A typical binary phase diagram for an aqueous solution is shown in Figure 2.7. A similar phase diagram is also found for more complex sample types where an additional CPA is considered and the ideas explained with this example can be generalized to other mixtures used for cryopreservation. Based the phase diagram, four distinct temperature regimes can be identified. In the following, they will be described from the perspective of a cryogenic sample that is heated above the storage temperature.

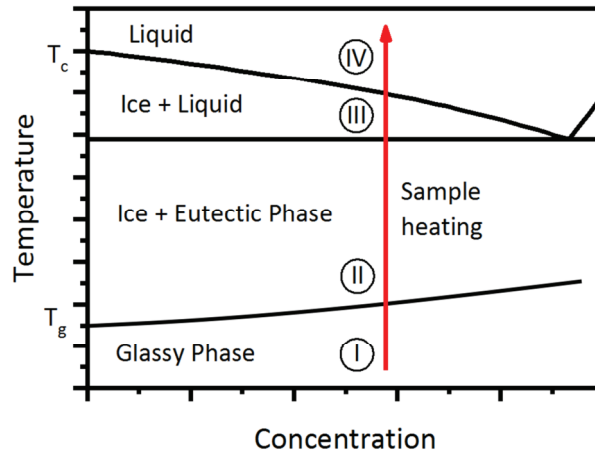


Figure 2.7 Typical binary phase diagram for an aqueous solution. Here four different temperature regimes are identified, with different relaxation dynamics.

The first regime is below the glass transition temperature of approximately $-130\text{ }^{\circ}\text{C}$. This could be considered as the storage temperature regime in the case of cryopreserved samples. Here, processes are very slow if not completely halted, making them difficult to investigate.

The second regime is between the glass transition temperature and the eutectic temperature. Here, the equilibrium state resembles that of the stored state but the viscosity and the amount of thermal energy available in the sample decrease and increase, respectively, with increasing temperature. Samples in a glassy state will devitrify, i.e. form ice crystals in this regime in order to bring the sample closer to its equilibrium state. In this region, the relaxation processes should thus be accelerated appropriately and can be investigated. For brine this region spans from approximately $-20\text{ }^{\circ}\text{C}$ to $-130\text{ }^{\circ}\text{C}$. In presence of a CPA, this regime is restricted to a smaller temperature range and reaches from approximately $-70\text{ }^{\circ}\text{C}$ to $-130\text{ }^{\circ}\text{C}$ for an aqueous mixture of DMSO.

The third regime is between the eutectic temperature and the crystallization temperature. When the sample is heated above the eutectic temperature, then the samples chemical equilibrium change and its characteristics change fundamentally. Here, ice can start to melt and eutectic crystallization cannot take place. This also affects relaxation processes like ice crystallization and recrystallization since the driving force behind has changed or even vanished. As example, a slowly frozen sample can be considered. When raising the sample temperature above the eutectic temperature, ice

will start to melt. This changes the CPA concentration of the dendritic channels between the ice crystals. This has a profound effect of the viscosity in the dendritic channels since viscosity is dependent on CPA concentration. The viscosity in the dendritic channels can thus no longer be described with an Arrhenius relation due to this concentration dependence.

The fourth temperature regime is above the crystallization temperature. Here, the sample is completely liquid and the processes observed at lower temperatures in the case of cryopreserved samples cannot take place. The processes occurring here are purely of biochemical nature. This temperature regime is thus not suitable for observing accelerated relaxation processes.

The transition points between these four regimes represent temperatures where the sample changes. This implies a profound change of the equilibrium conditions in the sample and extrapolating measurements across different regions can lead to erroneous conclusions. Care should thus be taken when using measurements of samples above the glass transition temperature in order to learn about the dynamics of relaxation processes at the storage temperature. In order to interpret the results correctly, all parameters that are affected by crossing the glass transition temperature need to be studied in detail. In the case of cryopreserved samples, viscosity and ice crystal nucleation and growth change fundamentally at the glass transition temperature and will be discussed in the following.

Both phase transitions and recrystallization are dependent on the diffusion characteristics of molecules in the liquid parts of the sample. Since diffusion is highly dependent on the viscosity in the sample, it is important to discuss the relation between the viscosity of a liquid and temperature in order to understand relaxation processes like recrystallization and crystal nucleation and growth. Above the glass transition temperature, viscosity changes gradually with temperature without disruptions at the eutectic or the crystallization temperature. This is, however, only valid if the sample composition is not changed and only hold true for supercooled liquids. In a sample heated above the eutectic temperature, ice can start to melt changing the chemical composition of the sample and thus also the viscosity. Viscosity therefore behaves differently from temperature regime to temperature regime.

Viscosity furthermore changes fundamentally at the glass transition temperature. This is particularly important since it makes extrapolation of measurement results obtained above the glass transition temperature to storage conditions difficult or even impossible. The viscosity η over a broad temperature range can be determined based on the Vogel-Tammann-Fulcher (VTF) model [58]:

$$\eta(T) = \eta_0 \exp\left(\frac{B}{T - T_0}\right) \quad (2.4)$$

Here η_0 is the viscosity at the high temperature limit, B is a temperature independent constant and T_0 is the low temperature limit and is sample specific.

Angell et al. have proposed a scale for liquids that describes the fragility of a glass spanning from strong glass formers to weak glass formers [56], [80], and. A strong glass is robust toward crystallization since the probability of nucleation is low at all temperatures whereas it is highly probable that crystallization will take place in a weak glass. A glass can be generated from a strong glass former almost independently of the cooling protocol whereas a certain cooling rate threshold has to be exceeded for weak glass formers. For a better overview of what make a liquid a strong or weak glass former some of their differences are listed in Table 2.1. The VTF model is related to the glass forming abilities of a liquid through the low temperature limit T_0 . Strong glass formers such as silica have a T_0 approaching $-273\text{ }^{\circ}\text{C}$ whereas it is close to the glass transition temperature for weak glass formers such as o-terphenyl [55]. The temperature dependent viscosities of a weak and a strong glass former are shown in Figure 2.8. From the VTF model it is evident that when T_0 is approaching $-273\text{ }^{\circ}\text{C}$, as for strong glass formers the viscosity exhibit an Arrhenius dependence. The viscosity is, however, clearly non-Arrhenian for weak glass formers over a broad temperature range. According to the VTF model, viscosity will diverge to infinity at T_0 . The VTF model cannot be applied below the glass transition temperature since it is only valid for liquids in equilibrium and glass is in this context a divergence from this equilibrium [58].

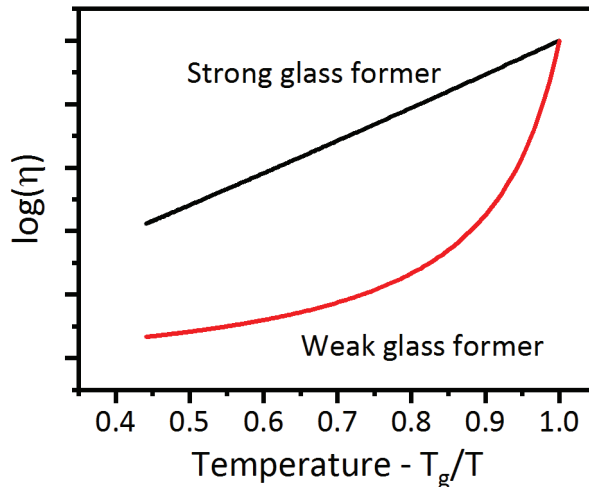


Figure 2.8 Viscosities of a strong and a weak glass former are presented according to the VTF model. The strong glass former is seen to exhibit an exponential correlation between viscosity and temperature, i.e. Arrhenius dependence, as opposed to weak glass formers.

Table 2.1 Characteristics that differ between strong and weak glass formers. ΔC_p denotes the change in heat capacity related to the glass transition.

	Weak glass former	Strong glass former
Nucleation	High probability	Low probability
Cooling rate	Exceeds critical rate	Normal cooling rate
Viscosity	Non-Arrhenius	Arrhenius
ΔC_p	Large ΔC_p	Small ΔC_p
Interactions	Non-directional van der Waals or Coulomb interactions	Directional covalent bonds

Viscosity is often also dependent on the concentration of various chemical compounds in the sample and CPA is often added to a preservation media with the intention to increase the viscosity in order to achieve a protective glassy state. Ice crystallization in the sample can further complicate the picture as it leads to rising CPA concentration in the non-crystallized part of the sample. The influence of the viscosity on the relaxation processes observed in cryopreserved samples is therefore difficult to determine.

The different relaxation processes related to ice crystal nucleation and growth, respectively, also scale completely different with temperature and have their respective maximal relaxation rates at very different temperatures. It has been shown that an aqueous mixture containing DMSO exhibits its maximal homogeneous nucleation rate close to the glass transition temperature whereas the ice crystal growth is fastest at -55 °C [81], [82]. Both of these are clearly of non-Arrhenian nature. It can thus not be expected that a relaxation process follows an Arrhenius relation over a broad temperature range and in particular not below the glass transition temperature. Measurements of relaxation processes performed at different temperatures above the glass transition temperature can thus not be used to predict the time scales of the same processes below the glass transition temperature in a quantitative manner.

Relaxation processes are, however, still accelerated at elevated temperatures and give relevant insights into the processes that can occur during freezing, storage and thawing of cryopreserved samples. Detailed information on the relaxation processes and their temperature dependence in the temperature regime above the glass transition temperature might still indicate what happens at storage conditions albeit at a significantly lower rate. Without prior knowledge, it will be nearly impossible to determine if a sample is unstable and how it will manifest. Such background information is paramount in retrospective analysis of cryopreserved samples since it serves as a database of events that a sample can experience and can thus be identified through suitable measurements. Acceleration of relaxation processes through temperature elevation gives, in other words, information that can be extrapolated to just above the glass transition temperature and bring qualitative statements on the

state of a given sample. With this knowledge established, it is then possible to determine whether a cryopreserved sample is unstable and how this would manifest. The relaxation processes of recrystallization and devitrification are the focus of chapter 6. Understanding the relaxation processes in a particular sample can bring a different perspective on the risk of repeated temperature elevations during its life time, for example due to sample handling, transport or extraction of a neighboring sample. In the following phase transitions and recrystallization will therefore be discussed in more detail.

2.2.2 Phase transitions

The phase transitions encountered in cryopreservation are ice crystallization in slowly frozen samples, eutectic crystallization, devitrification and melting. The glass transition is a second order phase transition from a liquid to a glass that implies the change of some of the properties, such as viscosity, thermal expansion coefficient and heat capacity. A second order phase transition is a continuous process that happens over a temperature range. The temperature range for the glass transition is dependent on the history of the sample, especially on the heating and cooling rates of the sample [83]. A glass can be viewed as a metastable configuration that is energetically favorable compared to the liquid state [56]. A crystalline state is the energetically preferred stable state due to the formation of a crystal lattice with strong bonds. The atomic or molecular configuration of the metastable glass state is, however, stable enough so that it can resist crystallization to a certain extent. Even above the glass transition temperature ice nucleation and ice crystal growth are rather slow processes.

Phase transitions describe relaxation processes where the physical state of the sample changes towards the energetically more favorable state. Let us consider the phase transition of water into ice. When the temperature is lower than the crystallization temperature, it is energetically favorable for water to crystallize. The crystallization event can in general be subdivided into two different processes that both have an impact on the overall crystallization rate. These are ice crystal nucleation and ice crystal growth.

Due to the formation of more stable bonds in ice crystals, the energy released during nucleation is proportional to the volume of the crystal or r^3 . There is, however, also an energy cost associated with the surface of the nucleus that is proportional to r^2 . As both contributions are always present simultaneously, a dynamic equilibrium will establish. This directly results in a threshold size of ice nuclei. The probability that a seed crystal will randomly self-assemble increases when the temperature is reduced. At lower temperatures water molecules have less energy to break the stable configuration of a crystal nucleus. The ice crystal seed will thus stay in a crystal configuration for a longer time and thus increase the probability that its size will exceed the threshold to a stable ice crystal. If the temperature is low enough ice will always form eventually. Nucleation can either happen randomly throughout the

sample in a homogeneous nucleation or locally triggered by an impurity in the sample denoted as heterogeneous nucleation. Heterogeneous nucleation has some temperature dependence that is dependent on the nucleator. Nucleators can promote ice crystal configuration in that they effectively reduce the energy cost crystal formation and can thus be seen as catalysts in this regard.

After ice nuclei have formed the complementary relaxation process of ice crystal growth can start as water diffuses towards the crystals. The ice crystal growth is also dependent on temperature and its dynamics is faster at higher temperatures. More energy is then present in the system and facilitates to overcome the activation energies associated with diffusion of water molecules toward the ice crystal surface as well as with binding on the surface, respectively.

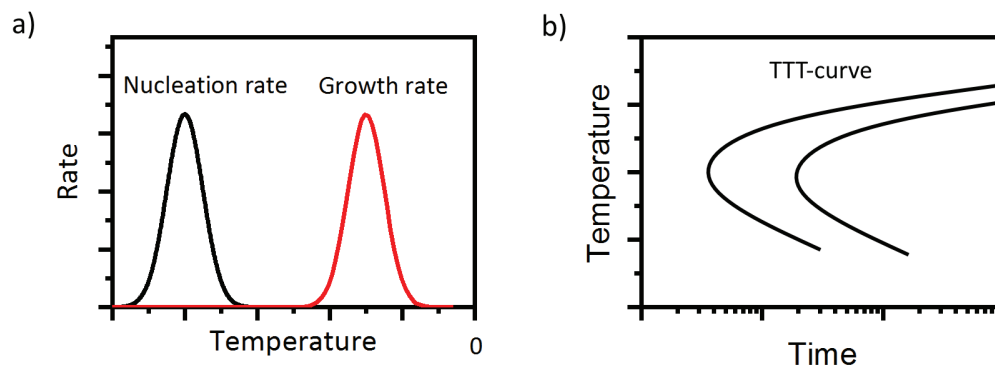


Figure 2.9 a) Graphical representation of the crystal nucleation and growth rate and how they can be separated in temperature. b) Example of TTT-curves for different crystallization fractions. These are representations of the time it takes for a given fraction of a sample to crystallize at various temperatures.

In general, ice crystal nucleation and ice crystal growth happen at different temperatures with nucleation having its maximal process rate at lower temperatures. For vitrified samples this implies that heating is actually the more critical part of the temperature protocol compared to freezing. In the rather extreme depiction in Figure 2.9a, freezing would be relatively unproblematic since ice crystals cannot grow at low at the lower temperatures required for nucleation. In the reverse heating process, the nucleation will start first. This implies that at the higher temperatures required for ice crystal growth, nuclei are present in the sample and allow for considerably ice formation. It is thus very important for a successful cryopreservation using the vitrification approach that the heating rate is high enough so that ice formation is avoided.

This crystallization process can also be described from a temporal perspective. A typical crystallization process is completed fastest at a certain temperature and will take longer in older or warmer samples. Such a crystallization process is often described through a so-called time-temperature-transformation curve. It describe the

time it takes for a specific fraction of the sample to crystallize at a given temperature [59]. An example of how such a TTT-curve is also shown in Figure 2.9b.

2.2.3 Recrystallization

Recrystallization takes place because there is an energy cost associated with the surface area of any crystal. When ice crystallizes, many nuclei are formed that grow simultaneously. When considering slowly frozen biological samples, a complex dendritic network is eventually formed during freezing where only very fine channels of liquid separate the different ice crystals. The total surface energy associated with the ice-liquid interface is much higher in a typical sample compared to a hypothetical sample with a single spherical ice crystal. Without changing the fraction of the sample in the crystalline state, the surface energy can only be reduced by lowering the surface to volume ratio of the ice crystals in the sample. Recrystallization describes the relaxation process where ice crystals minimize the total surface area and thus the surface energy. Different mechanisms are contributing to recrystallization. Each ice crystal individually can change its shape to a more spherical distribution. When in direct contact, ice crystals can fuse and form larger crystals out of two or more smaller ones. Even in absence of spatial proximity a net volume transfer from smaller to larger crystals is possible through diffusion. All these processes are more likely to happen when the sample temperature is raised. When more energy is present in the system it is more likely that water molecules can change position or transfer from one ice crystal to another. The activation energy for recrystallization is correlated to the diffusion characteristics between the ice crystals as well as the transition of water molecules into the ice crystal lattice. This process is independent of a change in the phase composition and the mass balance of the sample on a macroscopic level. In other words, recrystallization does not change overall amount of ice in a sample but alters the ice crystal morphology.

Recrystallization does, however, not only affect the morphology of the sample but also its thermodynamic properties. The so-called Kelvin effect states that average ice crystal size and morphology has an effect on the freezing point [84]. The reduction of the surface energy per volume during recrystallization leads to an increased freezing point. This change is very small and the thermodynamic consequences of recrystallization will not be considered in the following due to its negligible contribution.

2.3 Approaches to retrospective analysis

The aim of retrospective analysis is to learn about the history of a sample. Based on measurements of a sample at a given point in time, retrospective analysis allows deducing which events it has experienced in the past. Single measurements may reveal singular events but only in combination with further knowledge on the sample more

detailed information may be revealed. The more information that can be gathered concerning a single sample the more details of its history can be learned from retrospective analysis. If for example the sample composition and the freezing protocol are known in addition to measurements of the sample in its storage environment, events like supercooling or the true cooling rate experienced within the sample may be deduced. In some cases it is paramount to know the starting condition of a sample in order to draw the right conclusions. For example in the case that ice is detected in a cryopreserved sample, a meaningful conclusion can only be drawn when the freezing protocol is known. While the presence of ice would be a sign for devitrification and thus a detrimental damage in the case of a vitrified sample, no meaningful information on the quality of a slowly frozen sample could be retrieved from this measurement.

Retrospective analysis can generally be subdivided into a phenomenological and an analytical approach.

The phenomenological approach analyzes changes in the sample based on specific parameters that are tracked over time. In other words, a measurement is performed at one point in the sample lifetime. At a later time, this measurement is repeated and differences between these two measurements indicate that the sample has changed in some manner. Changes in before and after measurements indicate that the storage conditions of the given sample has not been stable enough to ensure a successful cryopreservation and the quality of the sample preservation is therefore endangered. In order to extract meaningful information from retrospective analysis, it is generally not necessary to identify the exact mechanism that drives changes in a sample. This is exploited in the phenomenological approach to retrospective analysis where only the general type of change in a sample is considered. If for example, chemical changes are detected in a sample, it is of little importance what exactly caused these changes as long as it is possible to estimate the consequences for the quality of the sample.

Phenomenological retrospective analysis uses a direct measurement of changes in the sample in order to derive more information on the changes in a sample between two points in time based on detailed understanding of possible processes in the sample. Changes in a light scattering experiment could, for instance, be used to deduce that the ice crystal structure has changed within the sample. This could then be traced back to nucleation of new ice crystals or recrystallization of existing ice crystals

This phenomenological approach provides the advantages that changes in the sample can directly be tracked and that little background information is required in order to perform the analysis and to determine whether the sample is unstable. The drawback of this method is that it can only detect changes in the sample that occurred during the observation period. It is thus not possible to identify quality issues related to the freezing protocol based on a phenomenological retrospective analysis or to detect historic event older samples have experienced.

In these cases, the analytical approach to retrospective analysis can be applied. Here, a single measurement is used to extract information on the sample history. To this end, the processes that could potentially occur in cryopreserved samples have to be known in more detail. The analytical retrospective analysis thus requires an extensive preliminary study but rewards with a truly retrospective tool that allows learning about historic changes in the sample in a single measurement. Examples of the parameters that can be used for a phenomenological analysis are:

1. Chemical composition
2. Cell composition
3. Degree of ice crystallization
4. Ice crystal size, distribution and morphology

Some chemical compounds can directly be correlated to specific events given that the sample composition and freezing protocol are known. For example ice in vitrified sample is a clear indicator that devitrification has occurred. Other compounds such as hydrohalite indicate that eutectic crystallization has occurred which will be investigated in detail in chapter 5. Examples of biological markers are the Amide I and III Raman signal related to CPA cytotoxicity [85], [86] or the Raman signal from DNA and RNA that drop upon stem cell differentiation [87]. A direct measurement of ice crystal size and distribution can reveal information on supercooling and ice crystal growth in the sample when coupled with detailed information on sample composition and freezing protocol. Since supercooling and ice crystal growth are directly linked to intracellular ice formation and thus the success of the cryopreservation process, this can provide a direct measurement of the sample quality. Examples of markers that can be used for an analytical retrospective analysis are:

1. Chemical compounds such as ice crystals, hydrohalite etc.
2. Biological markers, for instance for stem cell differentiation
3. Glassy phases and their distribution
4. Ice crystal size and distribution

When designing a measurement protocol for retrospective analysis purposes there are some requirements that it should fulfill. It should influence the sample as little as possible so that it does not take damage. All measurements should be performed at storage conditions or at least as close to storage conditions as possible. Only non-contact measurement methods can be applied that do not alter the sample through biological damage, mechanical manipulation or temperature variations. General optical methods are best suited here but high intensities, long exposure times or critical wavelength bands should be avoided especially when using lasers.

The experimental technique should furthermore provide information representing the entire sample since this remove or at least significantly reduces the risk of incorrect

conclusions derived from local anomalies. Macroscopic measurements that cover a large area or even the whole sample should be preferred for retrospective analysis. Microscopic measurements only cover a small area that constitutes the local environment in and around one or a few cells. Through multiple measurements with statistic distribution across the sample the measurement volumes would in this case constitute a representative region of the sample.

The development and implementation of technologies for retrospective analysis can move quality control in biobanks to the next level. If suitable protocols and testing methods are available, a high sample quality can be assured at all times. This would be a major innovation compared to the current situation where the sample quality basically is not known until a post thaw analysis has been performed. In combination with the result of post thaw analysis such retrospective analysis might further improve the understanding of the cryopreservation analysis and allow for a correlation of biological success criteria to a detailed chemical and physical history of a given sample. To this end it is paramount that all processes that might occur during cryopreservation are well studied and understood. Detailed background knowledge is the basis for any retrospective analysis.

This work aims at contributing to both the knowledge base and the experimental toolkit required for retrospective analysis of cryopreserved sample. To this end, crucial processes like eutectic crystallization, recrystallization and devitrification as well as their correlation with temperature variations will be studied in model systems. This study is complemented with developing suitable measurement techniques. Optical methods based on Raman scattering and fluorescence imaging are presented as non-contact technologies whereas calorimetry is demonstrated to be a valuable tool for the preliminary investigation of phase transitions. In order to allow for an application in common cryopreserved samples, specific measurement tools are developed that allow for operation at storage temperature. Based on the insights gained through these studies and the methods developed for non-contact measurements innovative applications for quality control in biobanks are proposed.

3 METHODS

In this chapter, general methods will be presented that will be used throughout the thesis. Later, specific methods will be presented as they become relevant. The first part of the chapter will briefly describe the cell lines used in this work and how they are cultured. The second part describes cryomicroscopy and how a cryostage can be applied in order to investigate frozen samples using microscopy techniques. Then, Laser Scanning Microscopy (LSM) is discussed in general while going into more detail on two photon fluorescence microscopy and Raman microscopy. Both two-photon fluorescence microscopy and Raman microscopy use LSM as a foundation but have two distinctly different excitation and signal detection methods. Finally differential scanning calorimetry (DSC) is introduced as a technology to study phase transitions in cryopreservation media.

3.1 Cell culture

Two cell types have been used in this work. A Murine fibroblast cell line (L929 cell line) was chosen since it is an established and robust cell type that is easy to handle and very well characterized. This cell line is thus ideal as a cell culture model for experiments where external parameters are investigated. Further experiments have been done using human induced pluripotent stem cell colonies (IPS colonies) since they have a high potential for use in therapeutic applications. Here, the cell line ER19-18 was used. IPS cells are generated by treating ordinary cells, for instance fibroblasts, with transcription factors and thereby inducing the pluripotent cell state. IPS cells can subsequently differentiate to any type of cell. This makes IPS cells very interesting in medical applications since cells from a single patient can be used to derive various other cell types required in different medical treatments where lost cells are to be replaced. This bypasses the need for the ethically problematic embryonic stem cells and is intrinsically a patient-matched treatment. Research in IPS cell colonies has received a lot of attention due to their usefulness in personalized medicine, regenerative medicine and tissue engineering. An important step toward the practical application of IPS cell colonies is the possibility to store them through a cryopreservation process. IPS cells are cultured as colonies which intrinsically have other requirements to cryopreservation protocols as for example the murine fibroblast culture due to the importance of cell-cell contact. The IPS cell colonies are furthermore very sensitive and fragile which pose extra challenges to the development of suitable cryopreservation protocols. This can give a different perspective on cryopreservation compared to the cell culture experiments with the more robust murine fibroblast cells

and are on the forefront of biomedical research. Cells were generously cultured and provided by Dr. Iris Riemann and Dr. Stephanie Bur (Fraunhofer IBMT). In the following a short overview will be given on how the cells were cultured.

Murine fibroblast cells – L929 cells

The murine fibroblast cells are cultured in 75 cm² culture flasks in a Dulbecco Modified Eagle Medium (DMEM) culture medium (DMEM F12, Gibco). The cells are passaged three times a week during culture. First, the excess culture medium is carefully removed and the cells are subsequently washed with 5 mL PBS. Then, 1 mL of a trypsin solution is added to the culture flask. The trypsin solution consists of 0.05 % Trypsin and 0.02 % Ethylenediaminetetraacetic acid in PBS. This detaches the cells from the cell culture flask. The trypsin solution is then carefully removed and the flask is filled with 15 mL culture medium and placed in an incubator.

In this work, several experiments have been carried out using adherent murine fibroblasts. This was done by first adding a coverslip to each well in a six well plate. Then, 1 mL of the cell suspension was added to each well directly after passage of the cells. Finally, 2 mL of the culture medium was added. The cells were then incubated a few days in order for the cells to adhere to the top side of the glass coverslip. The samples were used before a confluent cell layer had grown on the coverslip. The incubation time depended on the cell count in the cell suspension.

IPS cell colonies – ER19-18 cell colonies

The culture dishes used for the culture of the IPS cell colonies are coated with a 0.1 % gelatin solution. In order to avoid cell differentiation of the stem cells an inactivated mouse embryonic cell layer (PMEF) were grown in the culture dish. The IPS cell colonies were cultured on top of this PMEF layer. The culture medium is based on the DMEM, but have several additives required by the IPS cell colonies. A detailed description of the medium can be found in [26]. The IPS cell colonies were passaged approximately once a week onto a fresh layer of PMEF. The colonies were detached and transferred manually using a sterilized needle. Preparation of coverslips with adherent IPS cell colonies was similar to that of the murine fibroblasts. The only differences is the modified culture medium and that the colonies were manually transferred with a needle.

3.2 Cryomicroscopy

Cryobiological processes are often studied using microscopy techniques. The application of microscopy techniques to frozen samples is often referred to as cryomicroscopy. Cryomicroscopy poses extra requirements to the experimental method compared to traditional microscopy techniques. A cryostage is first of all required in order to program and simulate a desired temperature profile that the

sample should experience. In order to study all sides of cryopreservation, this should take place under observation through the objective of the microscope. Ideally such a cryostage should be able to simulate the entire temperature range between room temperature and storage conditions. Furthermore, cooling and heating rates should be precisely controlled between very slow rates below 1 °C/min as well as very fast freezing rates above 1000 °/min. In this manner, both the slow freezing and the vitrification approach can be investigated. This is often not realistic and common cryostages have been optimized for slowly frozen samples only. Further limitations are posed by the sample temperatures. The sample is often cold enough that water condensates on the sample from the surrounding atmosphere. This can significantly reduce both excitation efficiency and signal strength from the sample, hampering the imaging quality. There are two general methods to circumvent this problem, both with advantages and disadvantages. One approach is to keep the surrounding atmosphere completely dry by flushing with dry nitrogen. The advantage of this method is that all types of objectives can be employed, and air objectives suitable for operation at room temperature can thus be used. It does, however, require a constant and reliable stream of dry nitrogen. It can furthermore be difficult to troubleshoot this method if vapor condensation is detected in the setup. A more reliable method to remove water vapor from the sample is to use oil immersion objectives. This effectively removes any possibility of water condensation on the sample through the presence of another liquid. This method also comes with some disadvantages. The immersion oil becomes both very viscous and opaque at very low temperatures below -100 °C. This can potentially diminish the imaging capabilities of the microscope. The immersion oil furthermore creates a thermal bridge between the sample and the microscope objective. This can potentially increase the sample temperature compared to the programmed cryostage temperature and it can furthermore cool down the objective so far that water vapor condensation on the objective backside can become an issue. Typical containers used in cryopreservation are furthermore unsuitable for microscopy studies due to the curvature, opacity and thickness of the container wall. This should be compensated in a deliberate choice of sample container that allow for high quality and easy imaging.

In this study, a Linkam MDS600 cryostage is used. The cryostage and its working principle are shown in Figure 3.1. This cryostage is able to precisely simulate the temperature profiles that typically are employed for slowly frozen samples. This cryostage allows for imaging of cell culture samples sandwiched between two glass cover slips. The sample is placed on top of a hollow cylindrical silver block with a diameter of 20 mm. Liquid nitrogen is sucked through the silver block and thereby cooling the sample. Both a platinum resistance temperature sensor and an electric heating element are contained in the silver block. By controlling the nitrogen flow and counter heating from the heating element, the temperature of the silver block can be controlled with a precision of approximately 0.1 °C. This means that the temperature protocol typically experienced by a slowly frozen sample can be simulated in such a

cryostage. These temperature protocols can either be preprogrammed or manually controlled during the experiment. This cryostage is able to cool a sample with a cooling rate of up to 100 °C/min down to the boiling point of liquid nitrogen at -195.8 °C. However, the lowest typical operating temperature is however around -100 °C due to limitations of the microscopy methods employed. The cryostage can be used with optical applications that either use air objectives or oil immersion objectives. When an air objective is employed, a lid is mounted over the silver block and sample. The cryostage chamber is then flushed with the exhaust nitrogen from the liquid nitrogen pump to avoid water condensation and ice crystallization on the sample surface. It turned out that ice did still crystallize on the sample surface in some studies at low operating temperatures. This could either be caused by a leak in the cryostage chamber itself or the fact that the exhaust gases from the liquid nitrogen pump are not

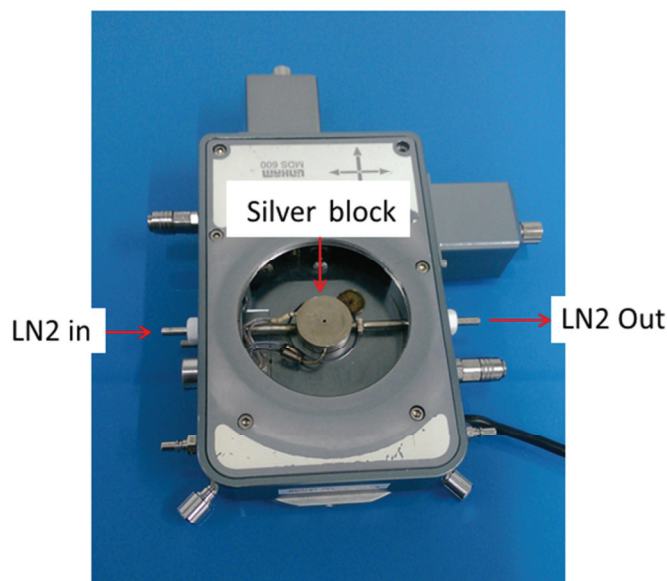
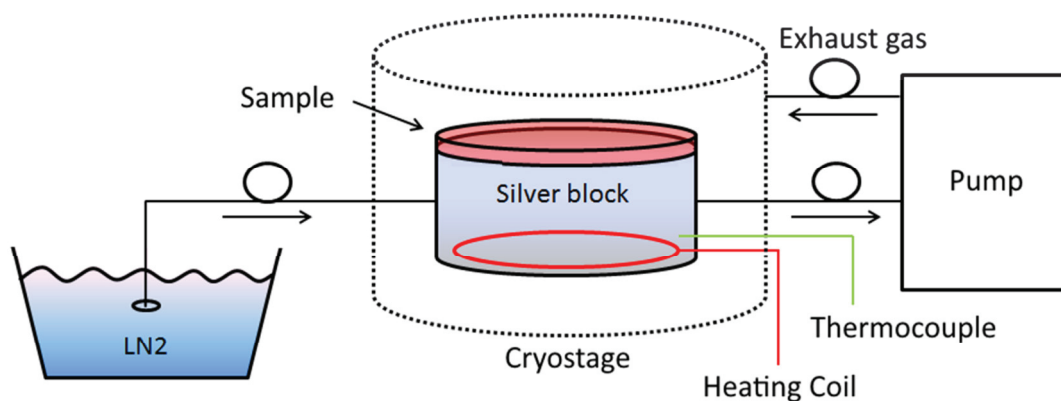


Figure 3.1 Schematic and image of the cryostage setup. Liquid nitrogen is pumped through a hollow silver block where the sample is located. The temperature is controlled by counter heating with an electric heating coil. Exhaust gas is lead back into the cryostage chamber to remove humidity from the sample. Optical access is from the top. Liquid nitrogen is taken in from the left and pumped through the silver block.

completely dry. Despite extensive search for the cause of this problem it was not possible to pinpoint the problem limiting the operating temperature in some cases. I will investigate and discuss this issue further for the experiment where it becomes a limiting factor in section 6.2. This issue does not occur when employing an oil immersion objective since the immersion oil between the sample and the objective prevents ice from crystallizing on the sample surface. The immersion oil does, however, become opaque at around $-100\text{ }^{\circ}\text{C}$ decreasing detecting efficiency which is critical in sensitive optical applications like Raman spectroscopy. The immersion oil also becomes very viscous at low temperatures. This can cause a detachment of the objective from the immersion oil when scanning the objective over relatively large distances. Whenever this occurs the experiment cannot be completed and needs to be repeated. Ideally, the operating temperature should be below the glass transition temperature. In practice, higher operating temperatures are often sufficient when taking into account the time scale of the processes taking place along with the time scale of the microscopy experiment. The dewar supplying the cryostage with liquid nitrogen can contain approximately two liters of liquid nitrogen. This allows for up to four hours of continuous operation depending on the cooling rates employed as well as the simulated storage temperature. The operation duration can be extended by refilling the supply dewar during the experiment but it is impractical to extend an experiment to run for more than one day. This is very short compared to the storage period that typical samples endure in a cryopreservation process long enough to perform numerous experiments on a given sample.

An aperture is located at the center of the silver block. This allows for transmission imaging by positioning a white light source beneath the cryostage. This is critical for the operation of microscopy applications since this allows for an efficient search of suitable locations to perform a given experiment. This furthermore eliminates the potential for reflections from the silver surface beneath the sample. The cryostage can be mounted on a XYZ-scanning stage.

Samples investigated in the cryostage were prepared in the same manner with one exception. Large volume samples investigated in the cryostage are prepared in a different manner which will be described in section 3.2.1. First, a droplet of $10\text{ }\mu\text{L}$ of water was pipetted onto the silver block. This serves two purposes: Better thermal contact to the silver block is established and the sample is kept in place on the silver block through capillary forces. A cover slip with a diameter of 18 mm or 20 mm is then placed on top. Then, $20\text{ }\mu\text{L}$ to $30\text{ }\mu\text{L}$ of the sample medium are pipetted onto the cover slip. The sample medium can for example be cell medium, PBS, water with or without added CPAs depending on the experiment currently being performed. In this work PBS has primarily been used. Then, another coverslip is placed on top. If the particular experiment aims at investigating cells then these are often adherent on this top cover slip, which typically has been incubated with the cells in a six-well plate. The coverslip is first picked up and placed on a piece of paper in order to dry the backside of the coverslip before being flipped and placed on the cryostage so that the cells are located

in the sample medium. The drying process of the backside is an important step. Water on this side will either mix with the immersion oil deteriorating the detection efficiency of the oil immersion objective or crystallize on the sample surface. Finally, the lid is placed on the cryostage or a drop of immersion oil is placed on top of the sample depending on the microscopy application employed. The sample is now ready for the application of a given temperature protocol.

This cryostage model does possess some disadvantages. The temperature sensor used to control the temperature is located within the silver block. This means that there can be a small discrepancy between the actual sample temperature and the measured silver block temperature. This effect is enhanced at the center of the aperture due to the increased distance to the silver block and also when employing oil immersion objectives due to the thermal contact to the microscope. This effect was investigated by placing an external thermocouple in a water droplet on a coverslip on the cryostage and comparing the temperatures in the silver block and the water droplet. The difference in temperatures was found to be small and could be taken into consideration based on this measurement series. It does, however, increase the uncertainty of the sample temperature to a few degrees. In addition, the aperture is relatively small ($\varnothing \approx 1.3$ mm) compared to the sample diameter ($\varnothing \approx 20$ mm). This means that in practice only a small portion of the sample can be used for microscopic investigations.

The cryostage is furthermore constructed in such a manner that only upright microscopes can be employed, whereas microscopy applications in biology often use inverted microscopes. This can be overcome by mounting an objective inverter on the microscope. This consists of a u-shape tube that can be mounted on the microscope in place of the objective. The microscope objective is then mounted in an upright manner

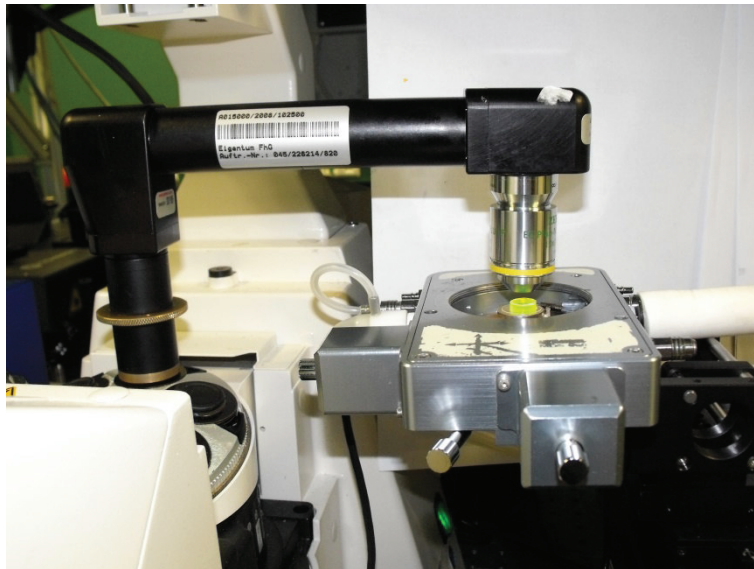


Figure 3.2 Microscope objective inverter. The inverter is mounted on the two-photon LSM microscope in order to image a sample located in the cryostage.

on the other side of the objective inverter. Mirrors in each corner then ensure that the light is directed from the objective to the microscope. This solution cannot be employed on all microscopes but was used for all experiments where the two-photon LSM was used. This objective inverter introduces more vibrations to the system due to the long arm making the setup more sensitive to mechanical distortions. The objective inverter (LSMtech) can be seen mounted on the two-photon LSM setup in Figure 3.2 as the black arm between the microscope and the cryostage.

When air objectives are used, the lid has to be mounted on the cryostage to prevent water condensation on the sample. This poses a limitation on the microscope objectives that can be utilized. The sample itself rather flat (below 350 μm including coverslips) and the distance between the silver block and the window of the lid is 4.5 mm. A suitable microscope objective thus needs to have a relatively high working distance of at least 5 mm. This excludes a broad range of objectives, especially high NA air objectives with high collection efficiencies.

The development of such a cryostage was an important improvement in cryomicroscopy since it allows for freezing with a defined temperature protocol without the need of either cooling the entire microscope along with the sample or relying on heat exchange with a cold substance such as dry ice [88].

3.2.1 Sample cross-section imaging

A new sample container was developed in order to study the structures formed in common cryotubes. Samples between two coverslips have a very low volume and thus show different structures found in larger samples. It was also not possible to directly cryotubes as sample containers for imaging purposes due to their thick and often opaque container wall as well as their unsuitable size and shape. For large volume samples, a new sample container was needed to closer imitate the conditions found in the cryotube center.

A slice approximately 1.5 mm to 2 mm thick was cut out of a cryotube and glued to a coverslip in order to create the sample chamber with a large volume. This would furthermore allow us to study a cross section of a cryotube. The sample chamber can be seen in Figure 3.3. This chamber has a volume of approximately 150 μL , significantly higher than the low volume configuration with two coverslips. After the given sample was loaded into the container, another coverslip is placed on top to close the system while providing optimal optical access to the top of the sample. The sample container fit in the cryostage with these dimensions and can be used to perform microscopy studies of a large volume using an air microscope objective. Oil immersion microscopy is not possible with this setup since this will induce high temperature gradients in the sample and potentially melt the top of the sample due to the relatively high thermal mass of such an objective.

It would be possible to freeze the sample using the cryostage but this would mean that the sample is cooled from the bottom. Therefore, it is more advantageous to freeze the sample in another manner and thus simulate the way a cryotube typically freezes

such that the sample chamber represents a slice from the middle of a standard cryotube. Cryotubes are commonly frozen by controlling the air temperature around the sample. For this purpose, a computer controlled rate freezer as shown in Figure 3.3 (Icecube 14S Sy-Lab) was employed. Here, the air temperature was controlled by adjusting the flow rate of cold nitrogen gas through the cryochamber. The flow of dry nitrogen also kept moisture from condensing on the sample. The sample was kept between two blocks of insulating Styrofoam as shown in Figure 3.3 to simulate that the sample chamber is a slice from the middle of a cryotube. After cooling the sample, typically to -80°C at $1^{\circ}\text{C}/\text{min}$, the sample was transferred to liquid nitrogen using precooled tweezers. This allowed for the transport to the microscope in a controlled environment. Here, the sample was placed on the precooled silver block in the cryostage and the lid was put in place immediately thereafter in order to minimize condensation on the sample.

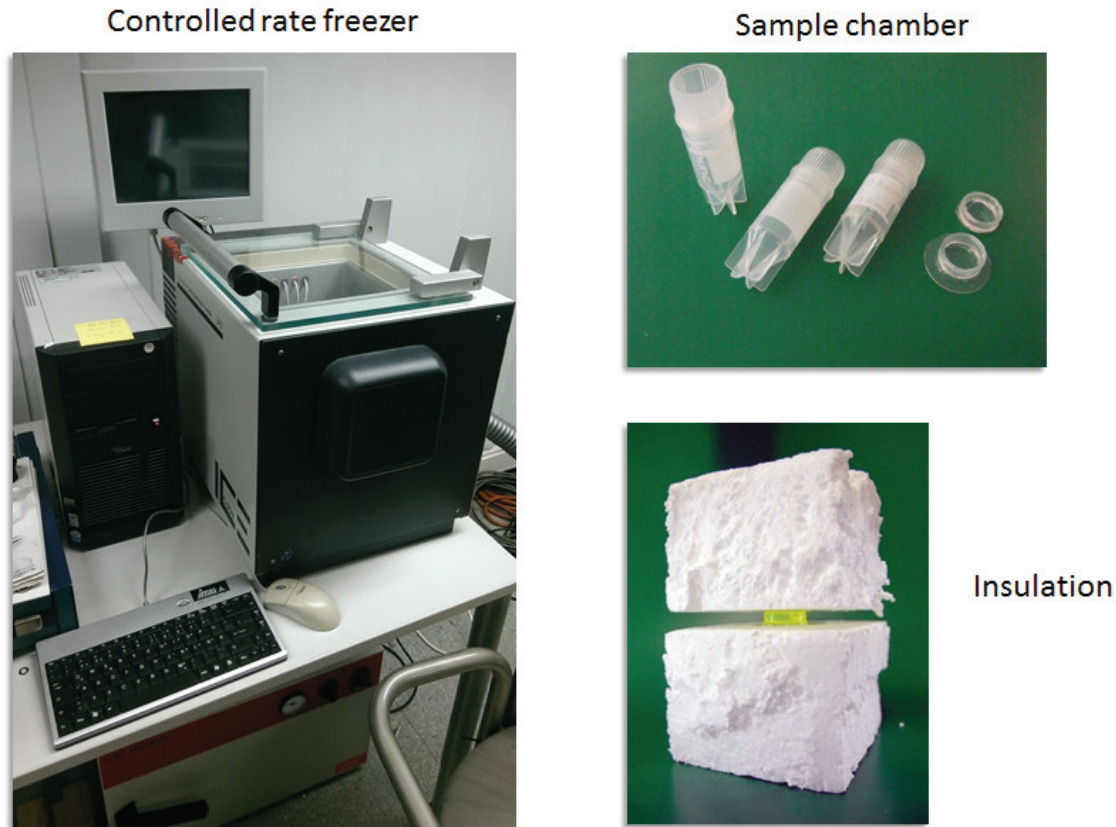


Figure 3.3 Images of the computer-controlled rate freezer and the sample chamber used to simulate freezing of a cross section of a cryotube.

3.2.2 Fluorescence microscope

A fluorescence microscope was built for investigation of standard samples and to study the recrystallization of ice crystals. The microscope was built in such a manner that it could image samples in a cryostage or placed in a freezing environment along with the investigated samples for long-term investigations of recrystallization. A schematic and an image of the setup are shown in Figure 3.4. Here, blue light is directed to the sample over a dichroic mirror where it can excite a fluorescent dye. The fluorescence light is collected using the same microscope objective and imaged using a CCD-camera. This allows for simple fluorescence imaging of the dendritic channel structure that arises in most cryopreserved samples. A blue LED (M470L2-C3, Thorlabs) which was collimated using a single lens, was used as an excitation light source. The light was directed towards the sample at a dichroic mirror (Di01-R405, Semrock). A 10x 0.10 NA microscope objective was used to focus the excitation light and collect the fluorescence signal. A CCD-camera (DFK 72AUC02, The Imaging Source) then collected the fluorescence light generating the images. The image size was determined using 6 μm fluorescent beads. Using the beads, the image area was found to be 325 μm x 430 μm . The microscope was mounted over the cryostage as shown in Figure 3.4. The cryostage was mounted on a manual XYZ translation stage in order to control the focal plane and imaging region of the objective with respect to the sample. Here, the lid on the cryostage was closed in order to inhibit water vapor condensation on the sample that hinders imaging. It turned out that the lid was not able to completely keep

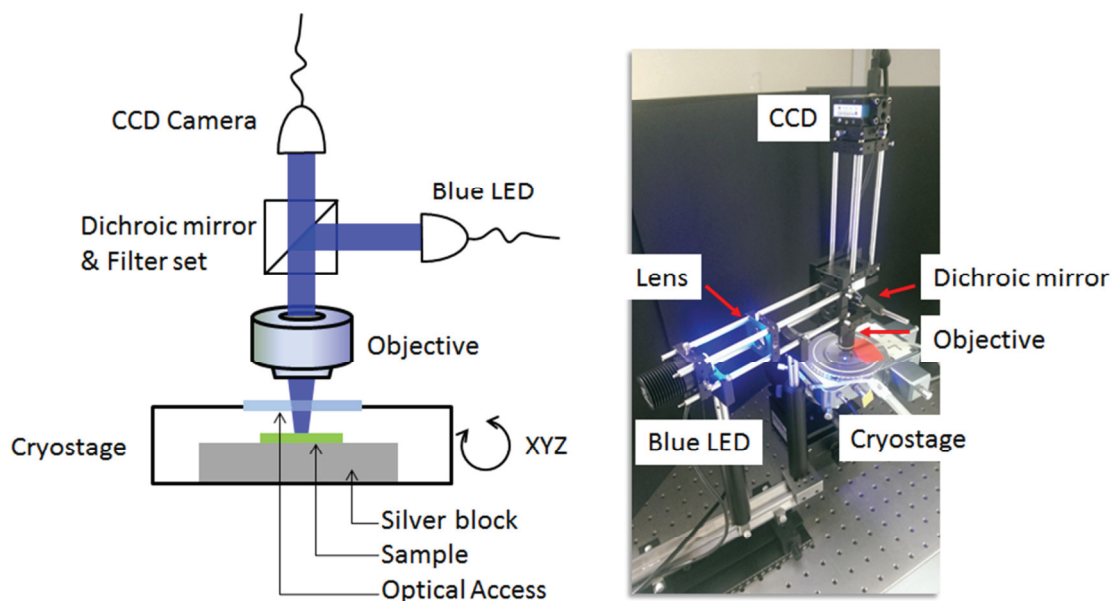


Figure 3.4 Schematic and image of the experimental setup to record fluorescence images of slowly frozen samples. Fluorescence is excited using a blue LED and the emitted light is collected with a CCD camera. The sample is located in a cryostage. This setup allows for measurement series of several hours keeping the sample at constant temperature.

out water from the cryostage despite the fact that the chamber was flushed with the dry nitrogen exhaust gas from the LN2 pump. This effect started around -50 °C and got significantly worse at lower temperature. Despite huge efforts it was not possible to locate and seal the chamber. This will be discussed further in section 6.2.3.

3.3 Laser Scanning Microscopy

The primary microscopy technique used in cryobiology is light transmission microscopy (TM). This is a simple microscope technique that enables the study of cells in a 2D-culture during the cryopreservation process. Using this technique, cell morphology and dehydration [30], [88]–[90], dendritic channel morphology [91] and intracellular ice crystallization [31], [92]–[94] have been studied. Fluorescence techniques have also been introduced [95]–[97] but these are similarly limited to only study morphological changes. The main obstacle for further development of cryomicroscopy is the microscopy chamber that imitates the conditions found during cryopreservation. Even the relatively advanced Linkam cryostages, such as the one described in section 3.2, impose several limitations on the microscope. This chamber has a silver block for cooling with only a small aperture in the center that restricts TM imaging to a small area. This silver block also produces unwanted reflections in some cases reducing the contrast unless the images are recorded at the small aperture. These cryochambers are furthermore limited to very flat samples, which introduce further supercooling to the freezing process.

A natural development to overcome these limitations and extract images of higher quality that also convey more information is to employ Laser Scanning Microscopy (LSM). LSM is a microscopy method where a laser is used as excitation source and scanned over the sample. At each spatial position, a signal is recorded and by combining the signals from all spatial positions, an image is generated. This provides several advantages over the TM imaging technique. Both the excitation laser and the detection signal use an optical path through the same microscope objective, which means that excitation and detection can be made on the same side of the sample contrary to TM where illumination and detection are on opposite sides of the sample. Depending on the choice of excitation laser, filter setup and detection optics, several different signal types can be measured providing more information than what would be possible with TM or standard fluorescence microscopy. This study utilizes two-photon fluorescence and Raman spectroscopy in a LSM configuration that will both be explained in detail. Using LSM does, however, require a significantly more complex microscopy setup due to the introduction of a laser that has to be scanned over the sample. This furthermore requires better optical filters in order to suppress the excitation laser in the measured signal. LSM is also an inherently slower microscopy technique compared to TM since the excitation laser needs to be scanned over the sample and a signal has to be recorded at every position.

In order to ensure high-quality imaging, it is furthermore required that the detection signal only originates from the focal volume. The laser can be scattered and excite a signal outside the focal volume reducing the spatial resolution of the imaging technique. This is particularly significant for cryomicroscopy due to the many scattering ice crystals. The spatial resolution is commonly increased by introducing a pinhole in the detection optical path and thereby making a confocal microscopy setup.

3.3.1 Two-photon fluorescence laser scanning microscopy

One method to image the dendritic channels formed in slowly frozen binary mixtures is to use fluorescence microscopy. Fluorescent dyes are generally not soluble in ice crystals. It is therefore simple to make the dendritic channels fluoresce whereas the ice crystals remain dark. There furthermore exist a wide range of dyes targeted at different parts of a cell. Fluorescence imaging is therefore a useful tool to investigate slowly frozen cell cultures. This gives detailed information on the crystal structures formed. Fluorescence imaging is a common and very important tool in microbiological studies.

A fluorescent dye can absorb photons whose energy exceeds the energy gap between the energy ground state and an excited state as depicted in Figure 3.5. A photon is emitted when the fluorescing molecule relaxes from the excited state to the ground state. The emitted photon's energy then corresponds to the energy difference between the energy levels and is dependent on the molecule. In between absorption and emission of a photon, a relaxation process takes place within the excited states under release of heat. Therefore, the absorption wavelength is usually shorter than the emission wavelength and the excitation and signal are thus spectrally distinguishable. This allows for excitation and signal collection through the same objective with subsequent omission of the excitation through a spectral filter.

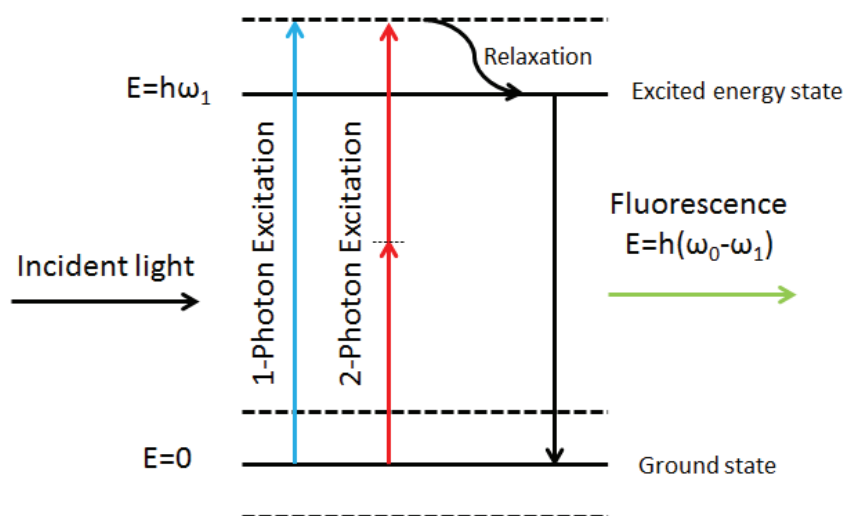


Figure 3.5 Energy scheme of one and two photon excitation and the following relaxation through emission of a fluorescence photon.

As the name indicates, two-photon fluorescence requires that two photons with energy lower than the energy gap between the ground and excited state (higher wavelength) are absorbed at the same time in order to excite the fluorophore. The combined energy of the two photons still has to exceed the energy gap. This can be described in a quantum mechanical manner where the first photon is absorbed exciting the fluorophore to a virtual intermediate state. The second photon is then absorbed to bring the fluorophore energy over the energy gap. This has to happen on a very short timescale of approximately 0.1 fs to 1 fs [98], [99] due to the short lifetime of the virtual intermediate state. Two-photon excitation was first proposed by Göppert-Mayer in 1931 [100], but it was not until 1961 that two-photon excitation was realized experimentally by Kaiser et al. [101]. The implementation of two photon excitation in a LSM setup was performed by Denk et al. in 1990 [102], which was a major development in fluorescence microscopy.

In two-photon fluorescence LSM, the signal is generated from two-photon fluorescence and the image is a representation of the fluorescence intensity of the sample in the imaging region. Relatively high photon densities are required to achieve two-photon excitation due to the low probability of the process. The high laser intensities required for this technique are achieved by a pulsed laser with a short pulse length. This ensures high peak intensity, while keeping the average laser intensity on a reasonable level.

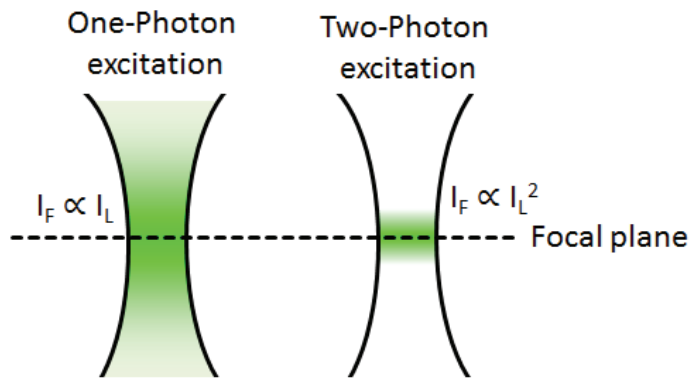


Figure 3.6 Excitation differences of one- and two-photon fluorescence. The fluorescence intensity I_F is proportional to the laser intensity I_L for single photon excitation, whereas it is proportional to the squared laser intensity for two-photon excitation.

Two-photon LSM offers several advantages over the single-photon LSM counterpart. The fluorescence intensity has a quadratic dependence on the incident light intensity [102], [103] as opposed to the linear dependence in single photon fluorescence. This greatly reduces the excitation volume and localizes the region that fluoresces since the incident light intensity peaks in the center of the focal volume and then rapidly declines as depicted in Figure 3.6. Two-photon excitation has a small diffraction-

limited excitation volume down to $0.1 \mu\text{m}^3$ [99], [104]. This provides a high spatial resolution without the need to insert a confocal pinhole that blocks scattered photons, but can cause chromatic aberrations and a reduction in throughput [102]. Another important feature of two-photon LSM is the longer wavelength of the excitation light source. Two-photon LSM is typically operated with an excitation wavelength of 700 nm to 1100 nm. This allows for a deeper penetration into biological tissue and lower background noise due to less Rayleigh scattering [103], [104]. As fluorescence is generated only in the focal volume, any scattered photons at the fluorescent wavelength originate from the focal volume and are thus a useful signal. The small excitation volume combined with the higher penetration depth allow for three-dimensional imaging of samples. The small excitation volume furthermore leads to a significant decrease in bleaching and phototoxicity effects [102]–[104]. Dyes do not necessarily have the same excitation spectrum for single- and two-photon excitation. The two-photon excitation spectrum tends to be broader and blue-shifted compared to single-photon excitation. This often allows for simultaneous excitation of multiple different fluorophores using a single excitation wavelength and thus for a simultaneous imaging of multiple cellular parts or dyes [104]. Not all dyes are excited in a two-photon excitation scheme at the same energy as in a single-photon excitation. One example of this is symmetrical molecules such as Rhodamine B [99], [105]. Finally, the two-photon fluorescence excitation scheme provides the possibility of functional imaging [106]. Two-photon laser scanning microscopy thus provides many and significant advantages over conventional transmission imaging.

The experimental setup used in this work consists of a pulsed laser source coupled to an advanced LSM. The setup is depicted in Figure 3.7. The inverted microscope is a Zeiss laser scanning microscope LSM 510 Meta-NLO which consists of a scanning and a filter unit. The scanning unit contains two galvanometric scanning mirrors that allow for a fast and precise scanning of the laser over the sample. A piezo-electric element allows for precise scanning of the objective in the axial direction with step sizes down to 25 nm. The filter unit consists of a broad range of beam splitters, filter sets and pinholes. This allows for a broad range of applications and can be adapted according to the excitation scheme and the detection range. The microscope is equipped with two highly sensitive photomultiplier tubes for fluorescence LSM as well as another photomultiplier tube for transmission imaging. Finally, the microscope is equipped with a 32 channel polychromatic detector. The setup contains several light sources that can be used depending on the application:

Table 3.1 List of available light sources for the fluorescence LSM setup.

Light source	Properties
Mercury lamp	White light source
Argon laser	458 nm, 488 nm & 514 nm
2 Helium-Neon lasers	543 nm & 633 nm
Ti:Sapphire laser	680 nm-1080 nm Pulsed

The mercury lamp can be used for transmission imaging and the Argon and HeNe laser can be used for single photon LSM. In this work, the Ti:Sapphire laser (Chameleon, Coherent) was the primary light source. The laser wavelength can be tuned in a broad range but in this work the operating wavelength was always 800 nm. The laser produces very short laser pulses of approximately 100 fs using a mode-locked pulse generation scheme. This ensures the very high peak powers required for two-photon excitation. The pulse repetition rate is 80 MHz which corresponds to 12.5 ns between pulses. This is significantly longer than the typical fluorescence lifetime of approximately 1 ns and thus ensures that the excited states have decayed and saturation can be avoided [102]. Either a Zeiss EC Plan-Neofluar 40x 1.4 NA oil objective or a Zeiss Objective EC Plan-Neofluar 10x 0.3 NA air objective was used to focus the laser onto the sample.

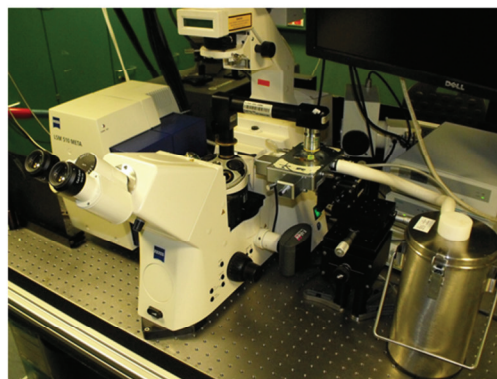
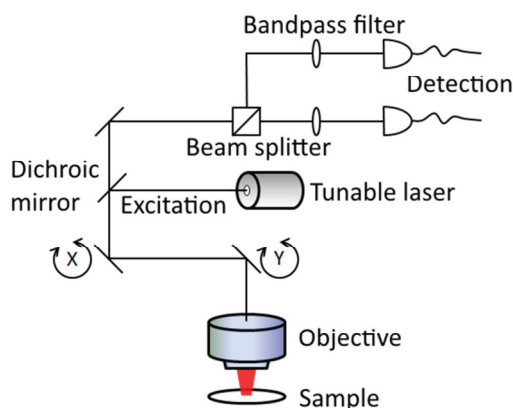


Figure 3.7 Schematic setup and image of the two-photon LSM setup. A pulsed laser is coupled into the microscope over a dichroic mirror and scanned over the sample by a set of galvanometric scanning mirrors. The collected light is filtered to remove excitation light and other background signals before being detected by photomultiplier tubes. The white inverted microscope and its controlling electronics can be at the center and on the left side of the photo. The Ti:Sapphire laser is in the background. The respective cryostage used for low-temperature experiments (see section 3.2) is on the right side of the photo.

3.3.2 Raman laser scanning microscopy

Confocal Raman Microscopy (CRM) allows for visualization of both chemical and physical information, here in particular in and around cells in slowly frozen samples, and is therefore a powerful tool to investigate frozen cells. The chemical imaging is a major advantage over conventional microscopy techniques since this brings another layer of information in addition to morphological information. The fate of a given sample can be determined, in some cases, by correlating certain compounds with physical and chemical events. This can be used to detect ice crystallization in vitrified samples which is a sign of an unsuccessful cryopreservation process [58], [76]. By using

Raman spectroscopy, ice crystallization can be identified with higher precision and lower threshold than with conventional techniques. Ice is, in other words, a marker for devitrification, which in principle can be detected retrospectively during storage. Another major advantage of Raman microscopy is that it is a label-free microscopy technique unlike many fluorescence microscopy techniques. This means that this technology can be employed on samples already in storage and without the introduction of specific fluorescence markers.

Raman microscopy has long since been an established tool in life sciences for a wide variety of applications [107]. It has for example been employed in identification of cancer cells [108]–[110], stem cell differentiation [87] and intracellular hydrodynamics [111]. It was recently introduced into cryobiology by Dong et al [33] in order to study ice crystal distribution in human foreskin fibroblasts during cryopreservation. This is a significant advance since a more detailed study on intracellular ice could be performed whereas TM can only detect whether intracellular ice is present or not. Raman microscopy has since then been used to study devitrification [112], hydrohalite formation with and without DMSO [113]–[115], the redox activity in frozen yeast cells [116] and the characteristics of different CPAs as well as their influence on the cryopreservation process [117]–[120]. Raman spectroscopy has also been employed in a post-thaw analysis of the influence of vitrification of ovine oocytes [85], [121].

3.3.2.1 Raman scattering

CRM is based on Raman scattering first described in 1928 by Raman et al. [122], for which the Nobel prize was awarded in 1930. When a photon interacts with a molecule, there is a chance for it to be scattered either elastically (Rayleigh scattering) or inelastically (Raman scattering). Raman scattering is a rare occurrence with only one in 10^8 photons being Raman scattered [107], [123]. An inelastic scattering event is a process where a part of the photon energy is absorbed by (Stokes scattering) or released from (Anti-stokes scattering) a molecular vibrational mode. Let us consider a Stokes scattering event. An incident photon with the energy $E = \hbar\omega_0$ can excite a virtual energy state in a molecule and upon relaxation it can end up in one of the vibrational modes with the energy $E = \hbar\omega_1$. When the latter happens, part of the photon's energy is absorbed and it will have a frequency corresponding to the energy of: $E = \hbar(\omega_0 - \omega_1)$. This process is depicted in Figure 3.8. The photon energy is similarly changed in an Anti-stokes scattering event to $E = \hbar(\omega_0 + \omega_1)$, where vibrational energy has been absorbed by the photon. The intensity of the Raman signal I_{Raman} can be described as [124]:

$$I_{Raman} = I_{laser}\sigma N, \quad (3.1)$$

where I_{laser} is the laser intensity, σ is the scattering cross section of the investigated compound and N is the number density of scattering molecules. This means that the

magnitude of the Raman signal can be used as a measure for the quantity of a given compound or molecules in the focal volume of a given setup.

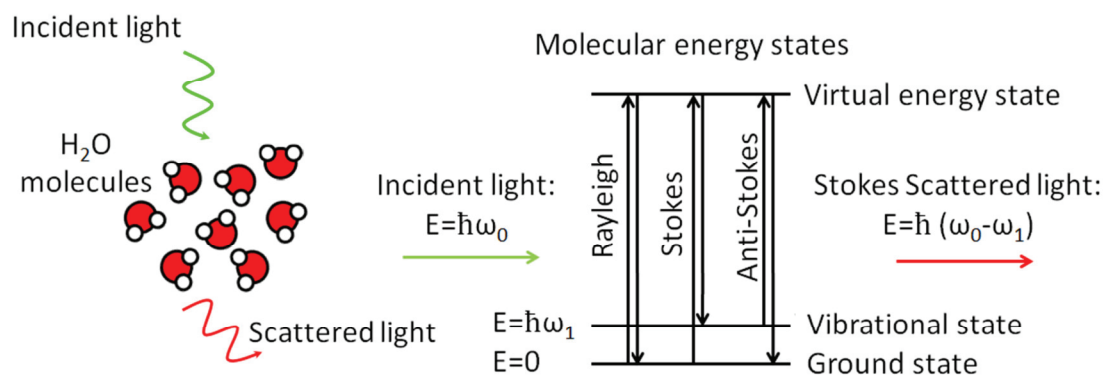


Figure 3.8 Light incident on H₂O molecules is scattered and changes frequency according to the vibrational modes of the molecule. In the case of Rayleigh scattering, the energy of incident and scattered photons are identical. In the case of Raman scattering, the energy of the scattered photons is lower (Stokes) or higher (Anti-Stokes) than the energy of the incident photons according to the vibrational modes of the molecule.

Raman scattering is similar to fluorescence but there is a very important distinction. In Raman scattering, the photon is never completely absorbed as in fluorescence which means that the fluorescence effect only takes place when the photon energy corresponds to the energy difference between energy levels in the molecule. The Raman effect is in contrast a scattering event, meaning that it in principle can occur at any photon energy. The Raman process gives, however, a very weak signal compared to both Rayleigh scattering and fluorescence. In practical applications, mainly fluorescence is a problem since Raman scattered photons can drown in a high fluorescence background whereas Rayleigh scattered photons can be filtered along with the excitation laser. Fluorescence is 10^6 to 10^8 times stronger than Raman scattering [125], mainly due to a huge difference in interaction cross sections. The interaction cross section σ for Raman scattering is typically approximately 10^{-31} cm^2 [126] whereas it is approximately 10^{-19} cm^2 for biological fluorophores [127]. This means that Raman spectroscopy is in general only applicable to samples showing very low autofluorescence and works best on samples with no fluorescence at all. There are approaches to circumvent this problem such as probing in the near-infrared (NIR) region where fluorescence absorption is absent or by separating the fluorescence signal from the Raman signal in the time-domain using a pulsed laser and a signal gate [125]. Both of these methods do, however, require more advanced equipment in form of either a spectrometer for the NIR-region or a time-resolved setup. Two related measurement techniques have been developed exhibiting a significant increase in Raman intensity, but they also have major disadvantages over conventional CRM.

Surface Enhanced Raman Spectroscopy (SERS) exploits the fact that Raman scattering is enhanced in molecules close to a surface (of for example a nano-particle) exhibiting a resonant plasmon surface mode [128]. The main disadvantage of this method is that either nanostructured surface films or metal nanoparticles have to be introduced into the sample. In Coherent Anti-Stokes Raman Scattering (CARS), a second laser source with a frequency corresponding to a single vibrational mode is introduced. This vibrational mode is then populated allowing for a very efficient probing of the anti-stokes Raman mode [129]. This method is, however, limited to only probing this single mode and not the entire Raman spectrum.

3.3.2.2 Confocal Raman Cryomicroscopy

In order to study the local chemical and physical environment in and around frozen cells, a home-built confocal Raman microscope has been employed. A Raman microscopy image consists of a full Raman spectrum at each pixel which is recorded by scanning a laser over the sample and recording the spectrum at each point. A sketch of the confocal Raman microscope is shown in Figure 3.9. The Raman microscope is in principle set up in the same manner as a conventional confocal laser scanning microscope but differs in the choice of filters and detectors. A 532 nm solid-state laser (Compass 315M-150, Coherent) has been used as light source. Before being led into the microscope (Eclipse LV100, Nikon) the beam is expanded using two lenses in order to make full use of the aperture of the microscope objective. The microscope contains a dichroic mirror that reflects the laser beam towards the sample and transmits light at longer wavelengths, i.e. Raman scattered light from the sample. Unless otherwise specified, a 40x oil-immersion objective (EC Plan-Neofluar, Zeiss) with numerical aperture (NA) of 1.4 has been employed for all Raman studies to focus the light onto the sample. A cryo-chamber (MDS600, Linkam), described in section 3.2, containing the sample is placed on a XYZ-piezo stage (P-563.3CD, Physik Instrumente) with a resolution down to 0.5 nm allowing for scanning of the laser over the sample. The Raman scattered light is collected using the same microscope objective and transmitted through the dichroic mirror and coupled into a multimode optical fiber (AFS50/125Y, Thorlabs) with a core diameter of 50 μm . This fiber both acts as a pinhole making the setup a confocal microscope and transmits the light into a spectrometer (Shamrock 303, Andor) mounted with a CCD-camera (iDus DU401A-BR-DD, Andor). A 300 lines/mm grating in the spectrometer was chosen since this allows collection of Raman spectra from the laser wavelength to well beyond the highest frequencies found in Raman spectra, as the focus of this study is to retrieve information on both the fingerprint region and the stretching mode region simultaneously. The disadvantage of such a fine grating, the limited spectral resolution has to be accepted. The piezo-stage and spectrometer were controlled through a LabVIEW interface in order to record CRM images. Single Raman spectra were recorded using the Andor

SOLIS spectrometer software. Samples for CRM were prepared on the cryostage between two coverslips as described in section 3.2.

There is a major drawback to CRM in comparison to other conventional techniques - it is a very slow technique. Since Raman scattering is a rather rare event, relatively long integration times for each pixel are required and in combination with movement times of the XYZ-stage this results in a long acquisition time. In this study, the minimum integration time was 100 ms per pixel and combined with the movement of the XYZ-stage an image takes approximately 13 to 14 minutes for a 64 x 64-pixel image. This should be compared to transmission microscopy or two-photon microscopy where an image takes at most one minute to acquire. In the field of cryobiology, time is not a major issue since the samples are frozen and stable within the timeframe of Raman microscopy image acquisition.

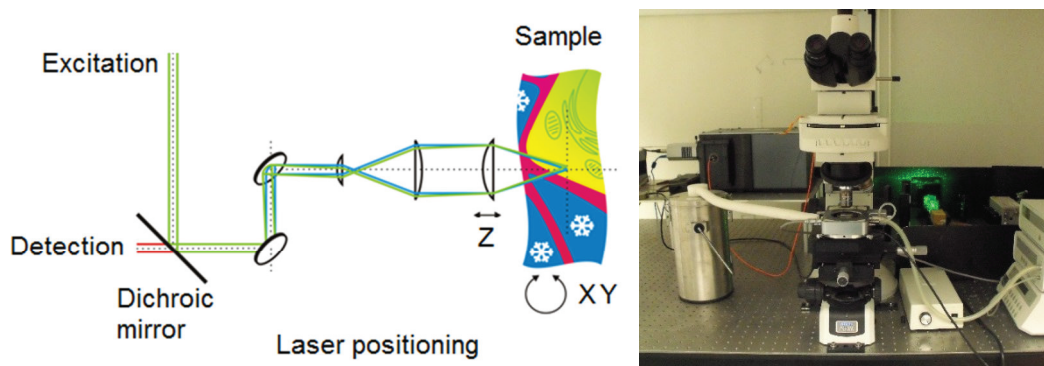


Figure 3.9 Schematic drawing and image of the confocal Raman microscope. The excitation laser is guided over a dichroic mirror to the sample over which it is scanned in a raster fashion. The same optics then collects the Raman scattered light and is transmitted through the dichroic mirror towards a spectrometer using an optical fiber. The confocal Raman microscope is fitted with a Linkam cryostage. Courtesy Dr. Frank Stracke.

The setup is mainly characterized by its spatial and spectral resolution since these are the limiting factors of the setup's capabilities. The point spread function of a given parameter is measured by recording a signal from a source that is much narrower than the actual resolution. The width of this point spread function is correlated to the resolution and can in principle be determined through deconvolution. When the input signal is much smaller than the resolution, the width of the point spread function corresponds to the resolution. The spectral resolution can thus be determined using light only from the laser under the assumption that the laser's wavelength band is much narrower than the spectral resolution of the spectrometer. This is shown in Figure 3.10a, and from this a spectral resolution of 34 cm^{-1} is found by taking the full width at half maximum (FWHM). The spectral resolution is primarily dependent on the grating used, but also the slit width at the entrance of the spectrometer; the narrower a slit the better resolution but this comes at a price of signal strength [130]. In our

setup, it is not possible to change the slit width that is determined by the connecting optical fiber which is 50 μm .

In a similar fashion measure the spatial resolution is found by scanning the laser over particles much smaller than the spatial resolution and their measured size is then the resolution. Such a measurement has been performed using titanium dioxide particles of a size of approximately 500 nm and a Raman microscopy image of such particle is shown in Figure 3.10b. This reveals a lateral FWHM of approximately 810 nm and an axial FWHM of approximately 2500 nm for the point spread function. This does not correspond to the spatial resolution of the setup due to the particle size. The exact shape of the particle is unknown and a deconvolution cannot be made. The resolution is by definition better than the point spread function measured and a lateral spatial resolution of 810 nm is sufficient for the studies performed with the CRM setup.

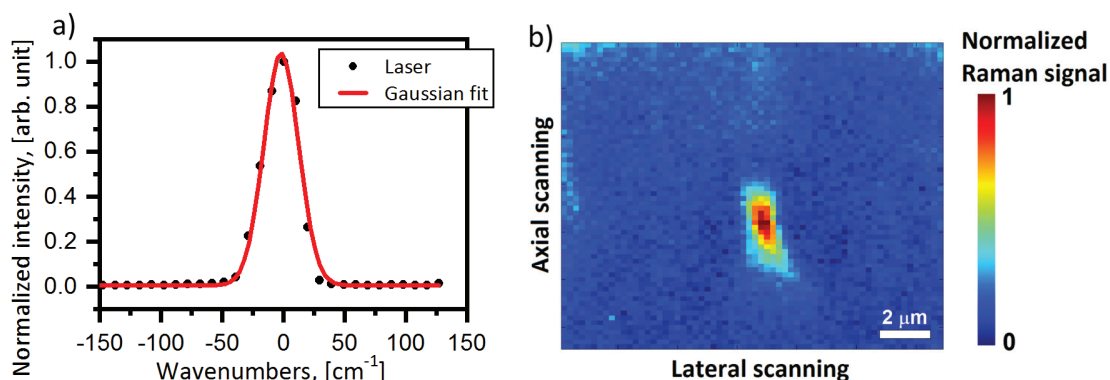


Figure 3.10 a) Instrument response function of the spectrometer. The laser has a narrow linewidth that can be used to record the point spread function. A Gaussian fit gives a spectral FWHM of 34 cm^{-1} . b) Raman image of a titanium dioxide particle smaller than the spatial resolution of the setup. The spatial resolution can be determined by fitting a Gauss function to the intensity. This reveals a lateral FWHM of 810 nm and an axial FWHM of 2500 nm.

3.3.2.3 Analysis of Raman spectra

Raman images are essentially 3D-images where each pixel of a 2D scan consists of a complete Raman spectrum. A 2D-image can be generated by integrating a band in each Raman spectrum corresponding to a specific chemical compound for each pixel (i, j) position:

$$I_{\text{Raman}}(i, j) = \int_{\omega_{\text{start}}}^{\omega_{\text{end}}} I(\omega, i, j) d\omega - I_{\text{Background}}(i, j), \quad (3.2)$$

where $I(\omega, i, j)$ is the measured Raman signal and the integration limits are ω_{start} and ω_{end} . The background correction, $I_{\text{Background}}(i, j)$, are defined as a linear interpolation between the Raman band edges as

$$I_{Background}(i,j) = 0.5 \cdot (\omega_{end} - \omega_{start}) \cdot (I(\omega_{end}, i, j) + I(\omega_{start}, i, j)) \quad (3.3)$$

This particular formula was chosen to allow for a distinction Raman bands that are in very close proximity or even overlapping bands, such as the OH-stretching band and the hydrohalite bands. This method has been described in [115], [131] and is visualized in Figure 3.11.

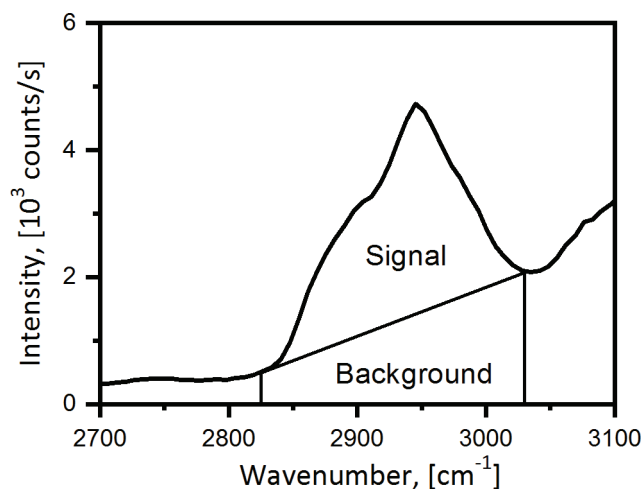


Figure 3.11 A Raman spectrum of a typical CH-stretching mode. This illustrates how the background signal was chosen when integrating a Raman band. First published in [114].

This integration acts as a virtual filter that can be applied in post-processing and a Raman image can be generated for each relevant chemical compound. The results of this data processing are images containing both structural and chemical information. An example of a Raman image of a murine fibroblast cell frozen in PBS to -50 °C at 1 °C/min is shown in Figure 3.12 along with a conventional transmission image for comparison. In the transmission image, the cell and a dendritic channel leading to the left is seen. This is all information that can be extracted from the transmission image. Using Raman imaging, the cellular matter is imaged using the CH₂-stretching mode as well as hydrohalite bands. Here, it is immediately seen that the dendritic channel is filled with hydrohalite and that the cellular matter is displaced towards the edges of the cell indicating that intracellular ice has formed. There is furthermore hydrohalite that has formed in close proximity to the cell. None of this information can be extracted using conventional transmission imaging.

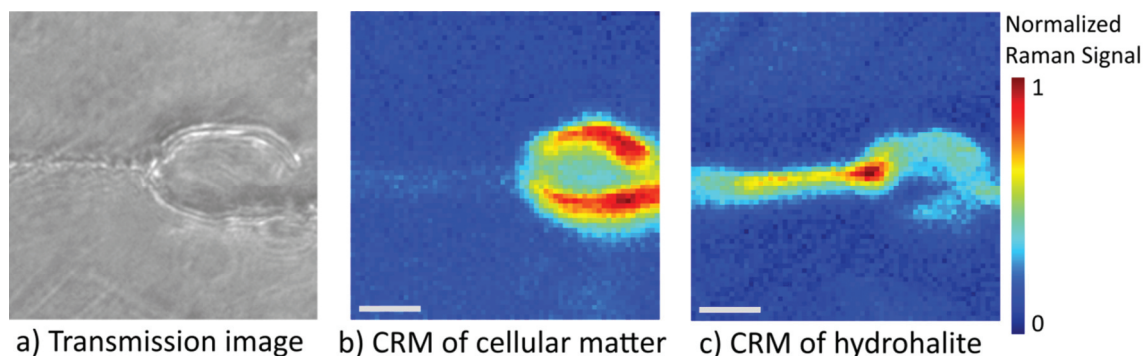


Figure 3.12 Images of a murine fibroblast cell using a) Transmission imaging, b) CRM of cellular matter and c) CRM of hydrohalite. The CRM images give a much more detailed picture on the local environment of the cell. The cellular matter is, for instance, displaced towards the edges of the cell indicating that intracellular ice has formed. This is not visible using transmission imaging. Further information is retrieved on the distribution of hydrohalite in the vicinity of to the cell. Scale bar is 10 μm . First published in [115].

New software was developed using the Matlab environment in order to analyze the data generated by the LabVIEW interface for data acquisition. This was necessary for a further image analysis than what the LabVIEW interface could provide. The main functionality of the software is to calculate Raman images based on equation (3.2). This allows for post processing of the data and makes it easy to perform further analysis of existing data if new correlations between compounds are discovered. The main image statistical analysis method that was implemented was the ability to generate colocalization plots between two compounds. Colocalization plots will be explained and used to a great extent in section 5.3 for the analysis of CRM images. Further methods that were implemented are image correlation, image ratios and the ability to overlay images.

Figure 3.13 shows a screenshot of the graphical user interface of the newly developed image analysis software. The bottom three images are the CRM images generated when integrating the red, green, and blue band shown in the example Raman spectrum. The Raman spectrum corresponds to the pixel marked with the white arrows and can be chosen by the user. Instead of a third image different statistical analysis method based on the two first images can be chosen.

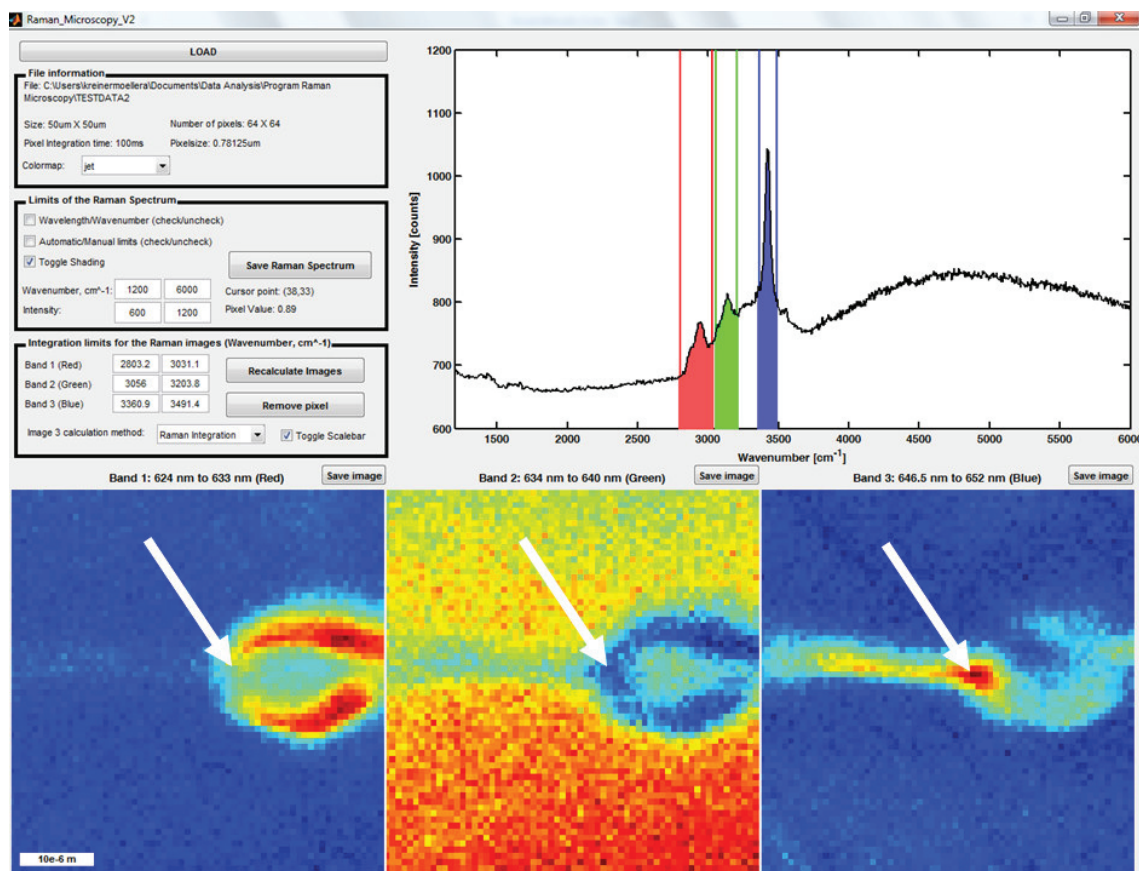


Figure 3.13 Screenshot of the software that was developed in order to analyze the measured Raman data. The three images correspond to CRM images generated from integrating the red, green, and blue band, respectively. The Raman spectrum is displayed when selecting a pixel by clicking one of the images. The shown spectrum corresponds to the pixel marked with arrows. The three bands chosen in this image correspond to cellular matter, ice, and hydrohalite, respectively.

3.4 Differential scanning calorimetry

The phase change from liquid water to crystalline ice plays a major role in cryobiology and cryopreservation. This phase change is heavily influenced by the various chemical additives in the sample medium as well as the temperature profile used. All phase changes either require heat (endothermic) or release heat (exothermic). Ice crystallization can thus be studied on a macroscopic level by measuring the heat released during freezing and the most common method to measure this is by differential scanning calorimetry (DSC). This method can furthermore detect eutectic crystallization as this is an exothermic process and measure the glass transition temperature since the heat capacity of the sample changes at this temperature. This makes this method ideal for characterizing and studying phase changes in media during cryopreservation. Samples undergoing DSC measurements are limited to a relatively small volume and sealed in such a manner that a post-DSC investigation of the microbiological characteristics such as cell viability and functionality is impossible and always requires a separate experiment using other more suitable sample containers.

The DSC used in these experiments (DSC 8500 fitted with an autosampler, Perkin Elmer) is a double-furnace DSC. Here, the relative heat-flow of two sample containers is measured when exposed to a given temperature protocol. One contains the investigated liquid whereas the other is an empty reference container. The relative heat-flow measured thus corresponds directly to the heat-capacity and phase changes of the sample. When ice crystallizes, heat is released and less heat is required to maintain the given temperature. A negative heat-flow thus indicates that an

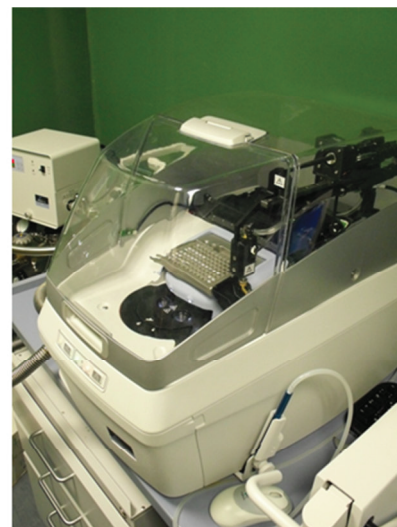
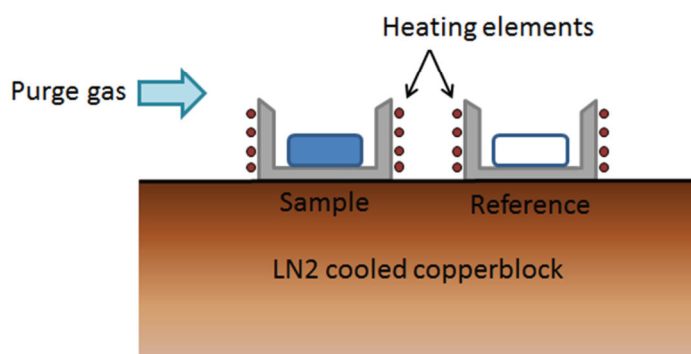


Figure 3.14 Schematic setup and image of a two-furnace DSC. The two furnaces are placed on a copper block that can be cooled with liquid nitrogen and are equipped with electrical heating elements. The combination of the cooled copper block and heating coils allows for temperature control over a broad range. By measuring the difference in electrical power needed to keep both samples at a specific temperature, the relative heat flow can be measured.

exothermic process such as ice crystallization is taking place. Figure 3.14 shows a schematic setup and image of the DSC used. The two sample holders are placed on a copper block that is cooled with liquid nitrogen to $-160\text{ }^{\circ}\text{C}$. The samples can either be cooled slowly or rapidly to below the glass transition temperature using ballistic cooling (as fast as possible but uncontrolled cooling) and thereby vitrifying the samples. Each sample holder is furthermore equipped with an electrical heating element and a thermocouple. This allows for programming of a temperature protocol that the sample experiences, from vitrification to thawing.

A sample container used in the DSC along with the sample press is depicted in Figure 3.15. The sample medium is pipetted into the sample pan and sealed with a lid using the sample press. The pipetted medium is often weighed so that a correlation can be made between the signal size and absolute amount of sample medium undergoing a phase change.

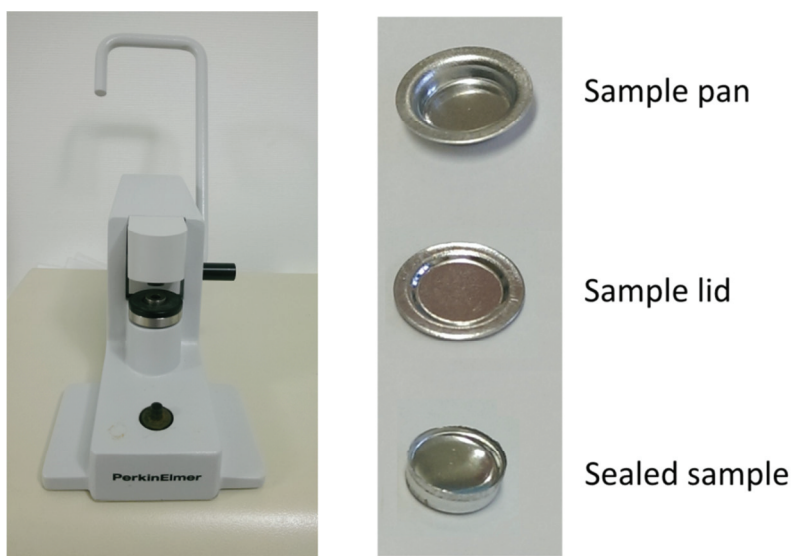


Figure 3.15 Images of the DSC sample press along with the aluminum sample containers.

A typical DSC temperature protocol and measurement is shown in Figure 3.16. Here, the sample is vitrified and subsequently heated at a constant rate until room temperature is reached. This allows for a measurement of the glass transition temperature, crystallization temperature and melting temperature. In the following, such measurements will be called temperature sweep measurements (T-sweep). A crystallization point is commonly determined as the onset temperature which is defined as the point where the tangents of the crystallization dip and base heat flow intersect. The tangents are shown as red lines in Figure 3.16b. The glass transition temperature is determined utilizing that the heat capacity above and below the glass transition temperature is different. This results in a kink in the heat flow over this temperature range and the glass transition temperature is taken at the middle of this inclination. The kink can be seen at the marked glass transition temperature in Figure

3.16b. Using these methods the glass transition and crystallization temperature are determined to $-128.8\text{ }^{\circ}\text{C}$ and $-112.2\text{ }^{\circ}\text{C}$ for 20 wt% DMSO, 20 wt% EG and 30 mMol trehalose mixture from the T-sweep measurement depicted in Figure 3.16b. The determination of a melting temperature is more complicated since these multicomponent samples melt over a broad range of temperatures which causes a broad melting peak that slowly rises before abruptly decreasing when the sample has fully melted. Comparing the maximum of the melting peak with the melting of a single-component sample (water) under the same conditions allows for a determination of the temperature under which water can start to crystallize, i.e. when the sample first reaches the liquidus line in the phase diagram, see Figure 2.1. This makes DSC measurements ideal to study phase changes in cryopreserved samples and can be employed to study devitrification where ice crystallizes releasing heat.

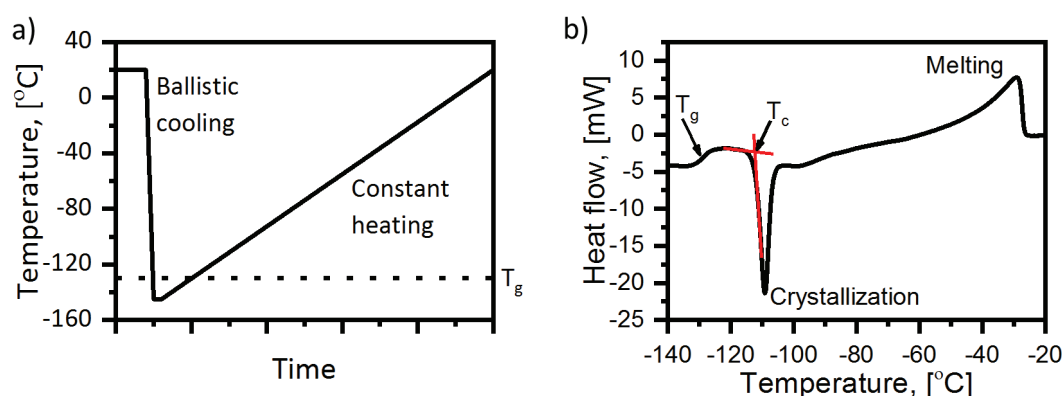


Figure 3.16 a) Temperature protocol used for T-sweep DSC measurements. The sample is first cooled below the glass transition temperature and subsequently heated at a constant rate to room temperature. b) The relative heat flow between the sample and reference is measured during the constant heating. Here, a typical measurement is shown for a sample consisting of 20 wt% DMSO, 20 wt% EG and 300 mMol trehalose. From this measurement, the glass transition T_g , crystallization T_c and melting temperature can be determined.

For some applications a different temperature protocol is used in which the sample is held at a constant temperature in order to study a given process isothermally. In this study devitrification, i.e. ice crystallization in vitrified samples, are investigated isothermally using DSC. The temperature protocol used for the devitrification experiments are presented in Figure 3.17. Compared to the standard protocols used to investigate phase transitions such as the one shown in Figure 3.16, a long isothermal period is added where the sample can devitrify. Using ballistic cooling the sample is first cooled rapidly to $-140\text{ }^{\circ}\text{C}$, clearly below the glass transition temperature T_g at around $-130\text{ }^{\circ}\text{C}$. The sample is kept at this temperature for five minutes in order for the system to equilibrate. Afterwards the sample is heated at $25\text{ }^{\circ}\text{C}/\text{min}$ to the temperature T_{iso} where the devitrification process is investigated isothermally. The ice crystallization rate is proportional to the endothermic heat flow measured at this temperature. The heating rate of $25\text{ }^{\circ}\text{C}/\text{min}$ is sufficiently fast compared to the

duration of the devitrification process that typically occurs on the timescale of over 10 minutes to several hours. The sample is finally heated to room temperature.

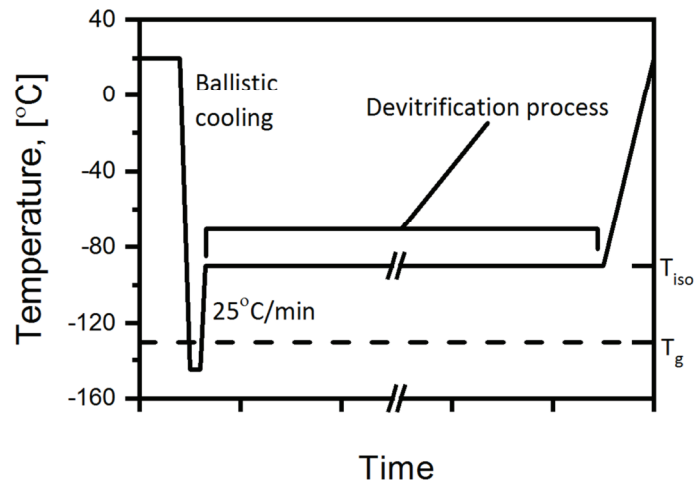


Figure 3.17 Temperature protocol used for the isothermal measurements of devitrification kinetics. Following vitrification, the sample is heated to T_{iso} where the sample is kept for the duration of the devitrification. By repeating this measurement at different T_{iso} , the crystallization constant can be determined.

4 MACROSCOPIC DISTRIBUTION OF SAMPLE COMPOUNDS

Ice crystallization plays a major role in cryobiology. It is therefore worthwhile describing the major influences on crystallization, growth and structures of ice crystals. The following description and discussion primarily apply to the slow freezing approach since ice crystallization is avoided when vitrifying samples in a fast freezing process. Pure water is almost never encountered in the field of cryobiology but instead complex cell media are used with CPAs added. This change the crystallization of ice significantly compared to pure water. In most cases it can be assumed that the system can be described as an aqueous binary mixture. This is possible when one component, besides water, is predominantly present in the mixture. Cell media can often be described as saline water in terms of freezing properties but when CPAs are added to the mixture they becomes the dominant part of the mixture since they are commonly added in higher concentrations compared to NaCl. When multiple CPAs are added to the preservation medium then the system can no longer be approximated as a binary mixture. Ice crystallization in binary mixtures does, however, exhibit many similarities compared to more complex mixtures and these observations can be transferred.

When ice crystallizes a dendritic channel network is formed with high CPA concentrations. The preserving feature utilized in cryopreservation is that the cells are encapsulated in an amorphous glassy substance formed in the dendritic channels. The health of each individual cell is therefore highly dependent on the local environment that is to a large degree governed by the overall macroscopic ice crystal structure and thus the dendritic channel structure. This chapter takes a more macroscopic perspective on ice crystal crystallization and thus the structures commonly found in slowly frozen cryopreserved samples.

4.1 Structure formation process

A macroscopic perspective of a slowly frozen sample is depicted in Figure 4.1. When the temperature decreases, ice crystals will start to form increasing both CPA and NaCl concentration in the remaining liquid. As the ice crystals grow, they will form long dendrites as opposed to spheres. This results in a complex network of dendritic channels. If ice crystals rather grew in spheres then instead small 'islands' of concentrated media would be observed. A vast majority of the cells in the sample will in the storage state be located in the dendritic channel since ice crystals are more

likely to nucleate extracellularly simply due to the higher volume of extracellular medium compared to the relatively low intracellular cytoplasm volume. The overall average concentration of CPA and NaCl does not change in the sample when ice crystallizes but it changes locally in the dendritic channels. If it is assumed that the sample is in a thermodynamical equilibrium then it follows that the CPA and NaCl concentrations are the same in all dendritic channels. Very different dendritic channel structures and ice crystal sizes can be encountered in cryopreserved samples. This affects dendritic channel width and thus whether ice is in direct contact with cell membranes.

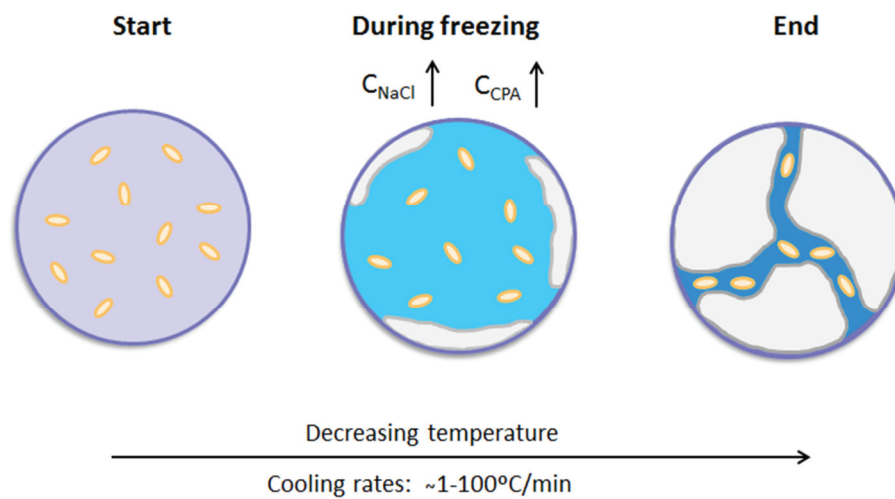


Figure 4.1 Macroscopic perspective on ice crystal crystallization in slowly frozen cell culture samples and how dendritic channel structures are formed.

The overall dendritic channel structure and ice crystal size are from a macroscopic perspective governed by four factors that are listed in Table 4.1. The chemical composition of the cell medium plays the biggest role since this determines both the freezing point according to its phase diagram and viscosity of the sample. The freezing rate, sample chamber and recrystallization can, under certain circumstances, still play a major role in the overall dendritic channel structure. In the following all influence factors and their effect on the cryopreserved sample are described separately.

Table 4.1 The four influences factors on overall dendritic channel structure and their effect on the cryopreserved sample

Influence factor	Effect on cryopreserved sample
Chemical composition	Change in phase diagram & viscosity
Freezing rate	Supercooling & crystallization speed
Sample chamber	Impact on supercooling and ice nucleation
Sample temperature	Recrystallization

Chemical Composition

The chemical composition of the cell medium plays the major role in the formation of a dendritic channel network. The phase diagram of the sample is mainly determined by the chemical composition of the sample. Figure 4.2 contains a phase diagram for a binary system and shows the different states a sample undergoes during freezing (red arrows). From the phase diagram the ice to liquid ration can be calculated at any given temperature as well as for the storage state assuming that an eutectic crystallization is avoided. By using a different CPA or changing the concentration of the current CPA, the overall amount of ice formed in the sample changes. The amount of ice formed in a sample has a strong influence on the dendritic channel structure. The chemical composition furthermore has an effect on the viscosity. A high viscosity will slow down the water flux towards the ice crystal boundaries and thus reduce the ice crystal growth rate. This will potentially lead to a more fine-grained ice crystal structure since new ice nuclei will have time to form in the remaining liquid depending on the freezing rate.

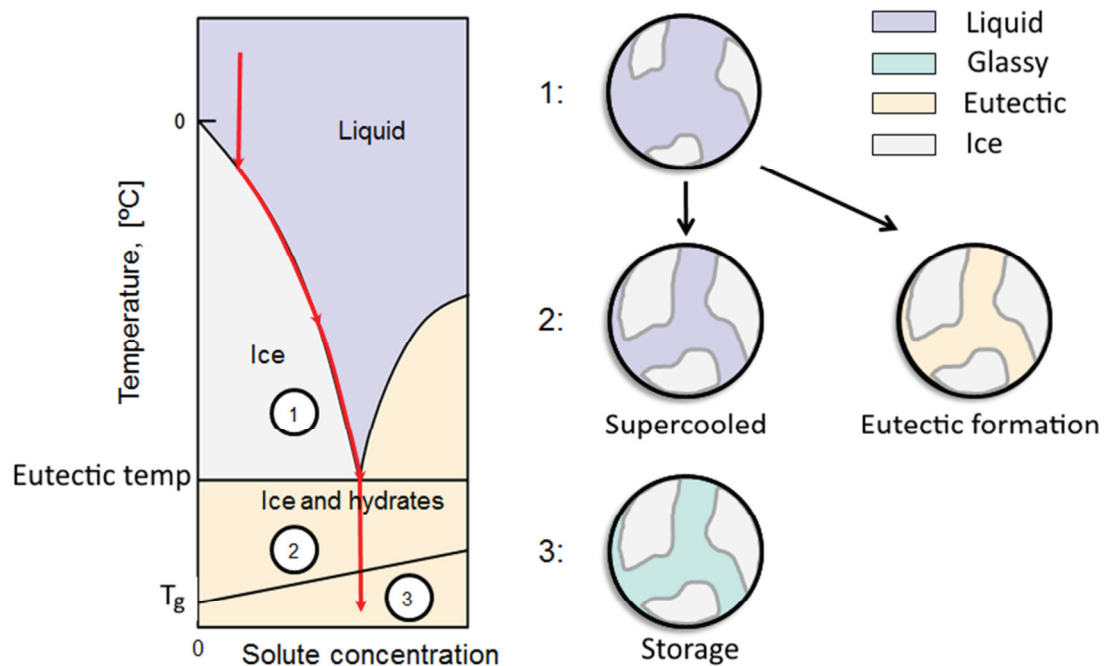


Figure 4.2 Binary phase diagram with the various states that a sample undergoes during freezing. The chemical composition follows the red arrows as temperature decreases. When ice forms, the remaining liquid is concentrated (State 1). The liquid will typically be supercooled (State 2) between the eutectic and glass transition temperature before entering the storage state (State 3) where the remaining liquid becomes glassy. Alternatively, a eutectic crystallization of the liquid occurs at or below the eutectic temperature.

Freezing rate

The ice crystal nucleation rate and the ice crystal growth rate are highly dependent on the temperature of the sample. The interplay between formation of new ice crystal

nuclei and the growth of existing nuclei determines to a great extent the ice crystal structure and granularity. This means that the governing factor over the temperature in the cryopreservation process, i.e. the freezing rate can potentially have a high impact on the resulting ice crystal structure.

If the freezing rate is very low then the ice crystal growth is limited by the phase diagram. As the freezing rate increases, the chance of forming new ice nuclei also increases. This means that a high freezing rate will result in many small ice crystals and therefore a much more fine masked network of dendritic channels whereas a low freezing rate results in fewer but larger ice crystals. Having a fine masked dendritic network mean that the overall length of the dendritic channels will be longer. Since the ice to liquid ratio will remain constant the dendritic channels will be narrower to accommodate for this. The average distance from a cell to the nearest ice boundary is smaller in this case, which might have an impact on cell membrane stability. A high freezing rate also increases the risk of ice crystals to nucleate within cells as previously discussed.

The sample can in some cases also supercool, i.e. when temperatures below the freezing point is reached without nucleation of ice crystals. This is depicted in Figure 4.3. A sample without supercooling will follow the red line through the phase diagram.

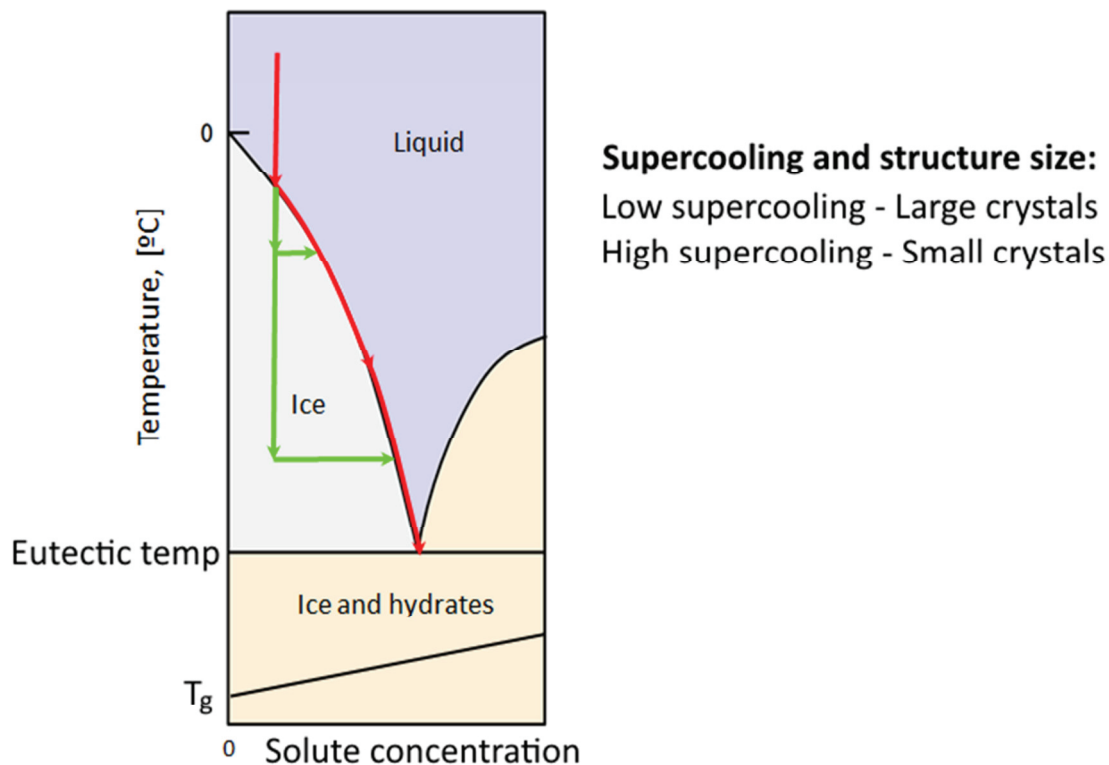


Figure 4.3 Depiction of a binary phase diagram and potential supercooling. The remaining liquid will follow the red arrows when no supercooling occurs. When a sample experiences supercooling it leaves equilibrium along the vertical green arrows. When ice nucleates, the remaining liquid will be brought back to equilibrium at the liquidus line.

When a sample supercool, no ice will nucleate upon reaching the freezing point and further cooling, which is depicted as the green arrows. At some point ice will, however, nucleate and the ice crystals will quickly grow to bring the sample back to thermodynamical equilibrium. At this point both the ice crystal growth rate and nucleation rate are higher compared to the case of a low cooling rate resulting in more, but smaller, ice crystals. The risk of supercooling increases with the freezing rate. If the freezing rate is very low, ice will nucleate very close to the freezing point eliminating supercooling. It should be mentioned that viscosity of the sample also plays a major role in supercooling. The freezing rate should therefore be seen in relation to the viscosity and thus chemical composition with regard to supercooling. Please note that in the case of extremely fast freezing there is a special approach to cryopreservation exploiting extreme supercooling without any ice crystallization at all and is discussed in section 2.1.2.

Sample chamber

The topology of the sample chamber sets the boundary of the sample and thus the dendritic channel structure. The chosen sample container can thus influence the overall structures encountered in a sample especially when the container is small. The most obvious example is the difference between a sample in a common cryotube and a sample sandwiched between two coverslips. In a cryotube, ice crystals can grow in any direction whereas the ice crystal growth is practically limited to two-dimensional growth between the coverslips due to the low height of the sample.

The chosen sample chamber for the cryopreservation process can also have an effect on the nucleation of ice crystals in the sample and thus potentially on supercooling. The origin of nucleation can be considered to be either heterogeneous or homogeneous. Heterogeneous nucleation describes instances where an external effect causes the nucleation such as an impurity [132]. Homogeneous nucleation describes the process where the molecules randomly form a stable crystal structure [133], [134]. The sample chamber can influence both heterogeneous and homogeneous nucleation. An impurity or mechanical deformity in the sample chamber wall can act as a heterogeneous seed and thus increase the nucleation rate. The homogenous nucleation can be influenced by the volume of the sample. Ice nuclei have a higher chance to spontaneously form when more water is present in the sample. A sample with a higher volume thus has a lower risk of supercooling. Supercooling is generally not beneficial to samples cryopreserved with the slow freezing approach. This increases the risk of intracellular ice crystallization and the ice crystal growth then varies between samples due to different amounts of supercooling. This in principle makes the cryopreservation process more inconsistent and a broader range of results from the cryopreservation process should be expected.

Supercooling can be eliminated by employing a scheme where heterogeneous nucleation of ice crystals is initiated at a given temperature through various means such as seeding of ice crystals, chemically or mechanically [132]. Chemically induced

nucleation can be induced through the introduction of a component that is known as a good ice nucleator such as silver iodide [135]. Initial studies of silver iodide encapsulated in an alginate bead have been performed and proved to reduce supercooling in PBS/DMSO samples. The encapsulation served as a method to avoid contamination of the rest of the sample with silver iodide. These experiments are, however, outside the scope of this study. Mechanically induced nucleation by touching the medium with a pre-cooled needle is the widespread method to induce nucleation [132]. Other mechanical methods such as light shaking or ultrasound pulses among others are also employed.

Sample temperature

Relatively high temperatures can lead to recrystallization. Recrystallization describes the effect when two crystals fuse in order to minimize the total surface energy of the crystals. This process also happens in frozen aqueous samples. Recrystallization of ice crystals is typically a slow process compared to ice crystal growth and only occurs well above the glass transition temperature. This means that very specific circumstances have to occur in order for recrystallization to have a significant impact on the dendritic channel structure. Recrystallization is more pronounced when the ice crystals in the sample are small resulting from either high cooling rates or high degree of supercooling. A sample kept on storage at -80°C for an extended period (hours) will probably experience recrystallization. Recrystallization will also occur at temperatures above the eutectic temperature but is then difficult to distinguish from ordinary ice crystal growth. Recrystallization can only be studied under isothermal conditions. This topic will be investigated in more in section 6.2, where recrystallization kinetics is studied at various temperatures.

4.2 Ice crystal morphology in cryopreserved samples

In this section, examples will be shown of typical structures found in cryopreserved samples and how the different parameters discussed in the previous section can affect these. In particular the effect of increasing the CPA concentration or the freezing rate and an example of supercooling will be shown. Here, both two-photon LSM and Raman microscopy will be used to image these different examples.

4.2.1 Typical structures found in cryopreserved samples

Typical examples of structures found can be seen in Figure 4.4. Here, multiple samples of 5 % DMSO in PBS were frozen to -80°C at a rate of $1^{\circ}\text{C}/\text{min}$ using the large volume sample chamber described in section 3.2.1. Fluorescein was added to the sample. This means that the dendritic channels fluoresce green due to the low solubility of the dye in ice and can be imaged using two-photon LSM. In addition to single images multiple overlapping images were recorded from the samples. The overlapping images can be stitched together to form a longer and larger image as the one shown in Figure 4.4.

From the images it can be seen that the ice crystals form a complex network of long narrow channels. The network is comprised of multiple long parallel channels onto which a set of shorter channels are connected that are also parallel to each other. The ice crystals in these samples are thus comprised of long dendrites from which smaller dendrites originate in an almost equidistant manner. From sample 1, the ends of the ice crystal dendrites are seen to have a hexagonal structure. This hexagonal structure will not appear if the ice crystal growth was impeded by other ice crystals or the sample container wall. In addition it can only be visualized if the image perspective is adapted to the ice crystal orientation. The lengths of the channels are seen to vary between the orders of $100\text{ }\mu\text{m}$ to 1 mm . The ice crystals in these samples are thus significantly larger than typical single cell sizes of $1\text{ }\mu\text{m}$ to $10\text{ }\mu\text{m}$. The widths of the channels are here estimated to be in the same order of magnitude as typical cell sizes.

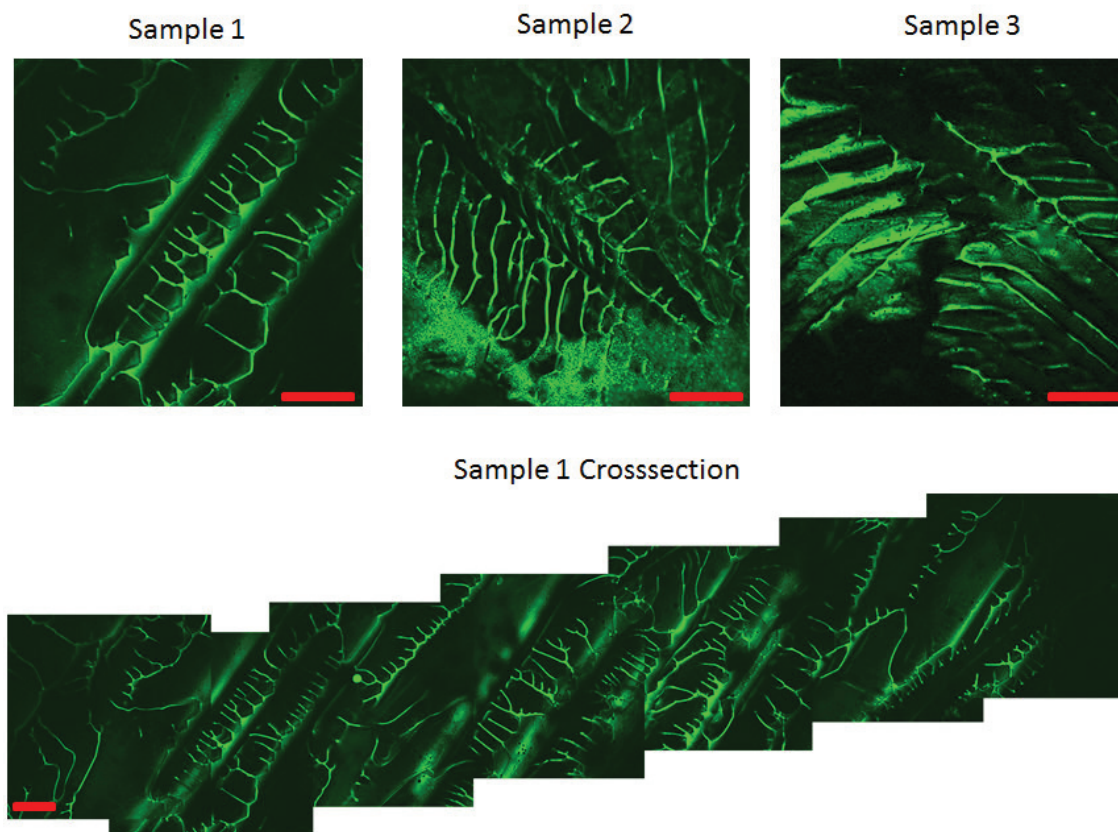


Figure 4.4 Two photon LSM images of cryotube cross section samples comprised of 5 % DMSO in PBS. The samples are cooled to $-80\text{ }^{\circ}\text{C}$ at $1\text{ }^{\circ}\text{C}/\text{min}$. The dendritic channels are dyed with fluorescein. Here, typical structures found in cryopreserved samples can be observed. The sample 1 cross section is comprised of multiple overlapping images that are stitched together. The scale bar is $250\text{ }\mu\text{m}$ for all images.

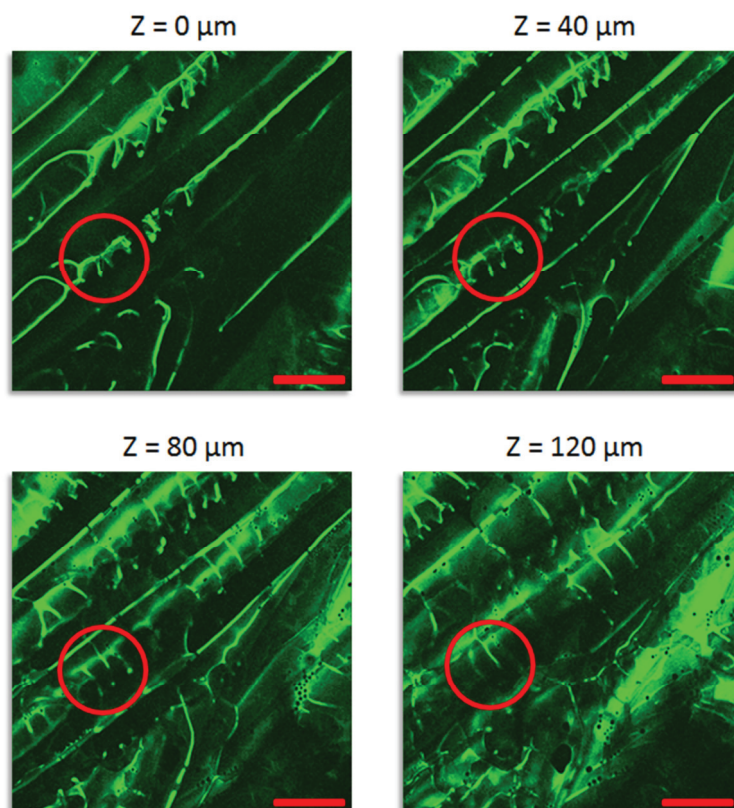


Figure 4.5 Two-photon LSM images of 5 % DMSO in PBS frozen to $-80\text{ }^{\circ}\text{C}$ at $1\text{ }^{\circ}\text{C}/\text{min}$ recorded at different layers of the cryopreserved sample. The images are recorded each with an axial distance of $40\text{ }\mu\text{m}$. The area marked with the red circle shows how two dendritic channels in two different planes are connected by a vertical dendritic channel. Scalebar is $250\text{ }\mu\text{m}$ for all images.

In order to get a sense of the three dimensional network of the dendritic channels, a stack of LSM images can be recorded. One example hereof is shown in Figure 4.5 where four images have been recorded at different layers with a z-distance of $40\text{ }\mu\text{m}$. It should be noted that the axial resolution of the setup is not as good as the lateral resolution. This results in channels from the image at $z = 0\text{ }\mu\text{m}$ (defined as the sample top) still being visible at $z = 120\text{ }\mu\text{m}$ (distance into the sample), but these are out of focus resulting in a higher background fluorescence in these areas. These images also show long dendritic channels with lengths longer than the size of the LSM image ($>1250\text{ }\mu\text{m}$). These channels are not only present in the top image but parallel channels also exist further into the sample. This indicates that the dendrites are not only parallel in an individual plane but are also parallel in a thicker sheet of dendrites. The thickness of this sheet is likely to be dependent on the amount of ice crystal nuclei formed during ice crystallization and growth in the samples. The images in Figure 4.5 underline that the dendritic channel network formed in slowly frozen samples truly is a three-dimensional network. Let us focus on the area marked with a red circle. This area contains a dendritic channel in the focal plane at $z = 0\text{ }\mu\text{m}$ that extends several $100\text{ }\mu\text{m}$ beyond the bottom left edge of the image. Going further into the sample

structures are seen that appears to be isolated islands of the liquid. Finally, at $z = 120\text{ }\mu\text{m}$ a dendritic channel perpendicular to the channel at $z = 0\text{ }\mu\text{m}$ is seen in this area. From this it can be concluded that these two dendritic channels are connected by a vertical channel that appears as isolated islands in images between $z = 0\text{ }\mu\text{m}$ and $z = 120\text{ }\mu\text{m}$. The reason that most of the dendritic channels are in the focal plane is that the images are recorded relatively close to the top surface of the sample. Here, ice dendrite growth is limited by the topology of the sample container, and the images are not a complete replication of a cross section of a cryotube. It is rather a close approximation due to the freezing conditions of the large volume sample chamber used.

When the amount of CPA changes, the chemical properties also change fundamentally and thus also the freezing characteristics. Both a 1 % DMSO and a 10 % DMSO in H_2O sample (20 μL) have been frozen under identical conditions as an example hereof. Raman images of DMSO in these samples are shown in Figure 4.6. The dendritic channels show as the light blue to red regions, whereas the dark blue areas correspond to ice crystals. The Raman images have been recorded using a pixel integration time of 100 ms and an image size of $250\text{ }\mu\text{m} \times 250\text{ }\mu\text{m}$. From these two images, the dendritic channel network qualitatively shows the same type of structure with long channels and a few isolated island of concentrated DMSO. The main difference between these images appears to be the perpendicular distance between the individual channels. The distance was measured to be between $15\text{ }\mu\text{m}$ and $25\text{ }\mu\text{m}$ for the 1 % DMSO sample whereas it is between $25\text{ }\mu\text{m}$ and $40\text{ }\mu\text{m}$ for the 10 % DMSO sample. The ice crystals are thus smaller for lower amounts of DMSO. This can directly be attributed to the nucleation rate of ice crystals. In order for ice crystals to be smaller, there have to be more ice nuclei. The nucleation rate is higher in the 1 % DMSO sample since the initial

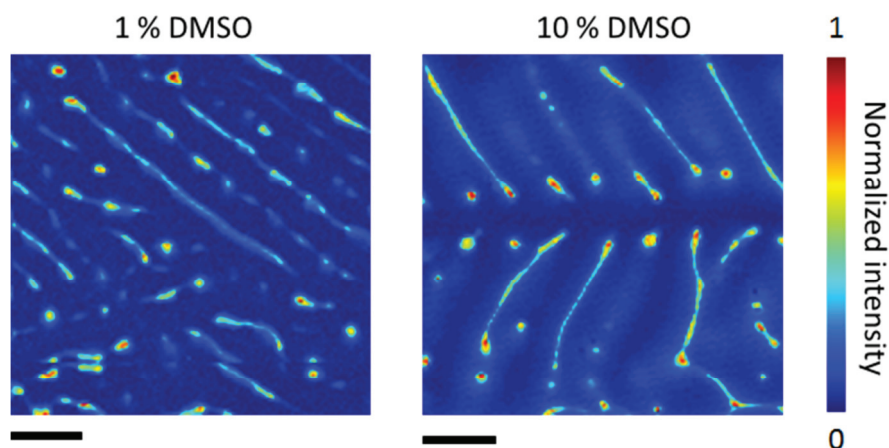


Figure 4.6 Comparison of dendritic channel network formed in a 1 % DMSO in PBS and a 10 % DMSO in PBS sample. The samples were small volume samples ($\sim 20\text{ }\mu\text{L}$) and frozen to $-80\text{ }^{\circ}\text{C}$ at $1\text{ }^{\circ}\text{C}/\text{min}$. The images were recorded using Raman microscopy and are normalized to the maximum DMSO signal within each individual image. Scalebar is $50\text{ }\mu\text{m}$ for both images.

viscosity is lower. At some temperature, the DMSO concentration in the channels is identical in both samples due to the samples consists of the same components, i.e. have the same phase diagram. The difference in DMSO concentration thus only changes the amount of initial ice nuclei formed in the sample. As the end concentration of DMSO in the dendritic channels is identical in both samples it follows that the dendritic channels in the 10 % DMSO sample are significantly wider since the DMSO to ice ratio is higher. The coarser dendritic channel network of the 10 % DMSO sample also result in fewer but broader dendritic channels. Alternatively, more and larger islands of DMSO could form. This is not visible in the Raman images as the images are normalized to the highest Raman signal within each individual image. An absolute measurement of dendritic channel width is highly dependent on the focal plane chosen for the particular image and is subject to variation within the same sample, making a direct comparison of dendritic channel width between different samples impractical. An initial estimate of dendritic channel width in the two Raman images found channel widths of approximately 4 μm to 5 μm for the 1 % DMSO sample and 5 μm to 6 μm for the 10 % DMSO sample.

4.2.2 Influence of supercooling on the dendritic channel structure

Supercooling can have a profound effect on ice crystallization and dendritic channel network. With a high level of supercooling, ice nucleation is delayed but results in a higher nucleation rate and ice crystal growth at the onset of the first ice formation. The effect of supercooling can be seen in Figure 4.7 where a sample consisting of 5 % DMSO in PBS has been frozen following the overall temperature scheme depicted. The sample was a small volume sample between two coverslips and frozen at a rate of 5 $^{\circ}\text{C}/\text{min}$ to ensure a high degree of supercooling. The ice crystallization is delayed due to the supercooling, which results in a slight increase in temperature at the onset of ice nucleation as indicated in the temperature scheme. Ice crystallization releases energy in the form of heat and due to the high crystallization rate, this result in a slight increase in sample temperature. The increase in temperature depends on sample volume, thermal contact to the cooling agent (here the silver block) as well as the heat capacity of the cooling agent. This does not play a role in samples without supercooling since the heat released is readily removed from the sample. The supercooling in this sample results in a very fine-masked dendritic channel network as seen from the LSM image at Time A. The sample was then heated to just below the freezing temperature before being re-cooled to -80 $^{\circ}\text{C}$. This melted most of the ice crystals in the sample but not all. This ensures that ice crystals exists in the sample during the second cooling period and these ice crystals act as controlled nucleation centers of the samples. This means that the sample does not experience supercooling at the second cooling period. The result hereof can be seen in the LSM image taken at Time B. Here, the ice crystals appear significantly larger and the dendritic channel network is coarser. The reheating and subsequent cooling was repeated a second time. The resulting dendritic network

at Time C is also shown. The resulting dendritic channel network shares similarities with that at time B but has regions with slightly bigger ice crystals. This indicates that the sample only partially melted since it is very unlikely that the same dendritic channel network forms at two separate freezing processes that only share small amounts of small ice crystals.

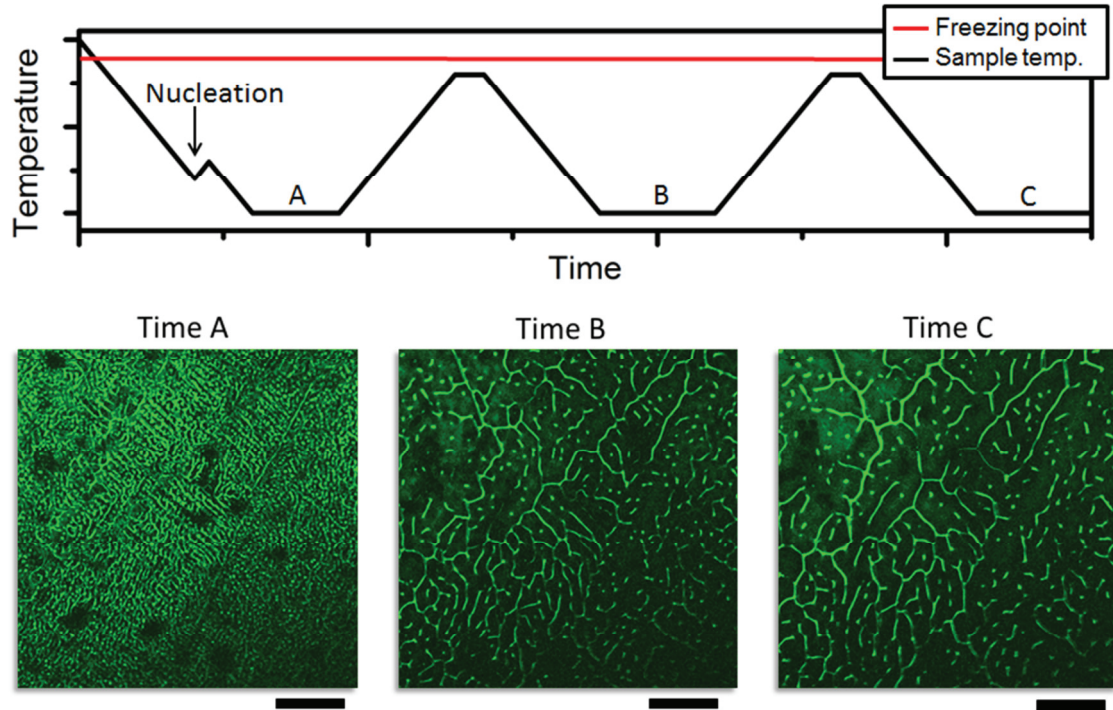


Figure 4.7 Here, a 20 μL 5 % DMSO sample is frozen according the depicted scheme with cooling and heating rates of 5 $^{\circ}\text{C}/\text{min}$. Two-photon LSM images were recorded at three points in time. Supercooling is present resulting in very small ice crystals as seen at time A. Heating the sample to just below the freezing temperature with subsequent freezing simulates controlled nucleation resulting in much larger ice crystals as seen at time B and C. Scale bar is 250 μm for all images.

This experiment shows what profound effect supercooling can have on ice crystallization. Since ice nucleation is random in nature, it follows that also the degree of supercooling is random. To ensure a high consistency and quality of a cryopreservation procedure it is thus required that supercooling is avoided. The success of a cryopreservation procedure using the slowly frozen approach is dependent on controlling cell dehydration effects and thus the ice crystal growth rate. If various supercooling occurs in the cryopreserved samples then it follows that the ice crystallization rate varies and thus also the success of the cryopreservation procedure. Supercooling is an unwanted effect in slowly frozen samples since it increases the risk that intracellular ice form due to a reduction of cell dehydration and a high ice nucleation rate. Depending on the sample and cryopreservation procedure, it might therefore be worthwhile to consider inducing controlled ice crystal nucleation to

improve the rate of success as well as consistency of the preservation procedure since it eliminates supercooling as in the images at time B and C. This can for example be achieved by introducing a precooled needle to the sample.

The cooling rate plays a significant role in the degree of supercooling that appears in a given sample. To visualize this, two samples of 10 % DMSO have been frozen to -80°C at $1^{\circ}\text{C}/\text{min}$ and $50^{\circ}\text{C}/\text{min}$ respectively. Raman images of the samples can be seen in Figure 4.8. The sample frozen at $1^{\circ}\text{C}/\text{min}$ is unlikely to supercool due the significantly longer cooling period compared to the sample frozen at $50^{\circ}\text{C}/\text{min}$. The small ice crystals found for the sample frozen at $50^{\circ}\text{C}/\text{min}$ can thus be attributed to a high degree of supercooling.

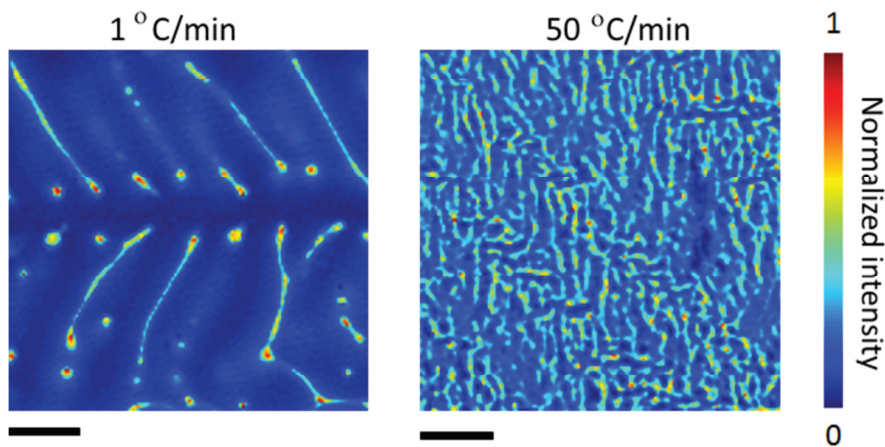


Figure 4.8 Here, two samples of 10 % DMSO in PBS are frozen to -80°C at $1^{\circ}\text{C}/\text{min}$ and $50^{\circ}\text{C}/\text{min}$. The Raman images show significantly different structures what can be attributed to different levels of supercooling. Scale bar is $50\text{ }\mu\text{m}$ for both images.

4.3 Cross sections of cryopreserved cell cultures

Cell cultures have also been frozen using the large volume sample container in order to get a macroscopic perspective on ice crystal structures and cell distribution over the entire sample. Here, murine fibroblasts have been frozen in a 5 % DMSO – 95 % PBS medium down to -80°C at $1^{\circ}\text{C}/\text{min}$. First, the cell medium was added to the sample chamber. The cells were subsequently pipetted to the sample. The cell nuclei were stained with Hoechst 33342 whereas the dendritic channels are dyed using fluorescein. It is possible to excite both dyes by a laser pulse with a wavelength of 800 nm in a two-photon excitation. The dyes emit light at different wavelengths and can through a clever choice of beam splitters and band pass filters be imaged at the same time. Figure 4.9 and Figure 4.10 show two examples of entire cross sections over the samples (see pages 73 and 74). The samples will be denoted sample A and sample B, respectively for future reference. Recording of the cross section is started at one side of the cryochamber marked with red in the figures. The sample was then shifted after

each image was recorded. The laser is then refocused to optimally record the next image. This is required since the focal plane of the microscope does not coincide with the top layer of the sample. The XY-axis of the microscope does furthermore not coincide with the XY-axis of the manual translation stage. This resulted in a horizontal shift in the images over the entire cross section.

Now the ice crystal structures in these two samples will be considered. The ice crystal structure appears to be of different nature in these samples. The ice crystals in sample A consist of ice crystal rods with various orientations. The dendritic channels furthermore appear broader and more irregular as a result of the rod-like ice crystals. The ice crystal structure of sample B coincides more with the other crystal structures observed previously in this chapter. Here, the ice crystals have merged and no distinct ice crystal rods can be observed. Instead a dendritic channel network is formed with channels extending over several images, i.e. several millimeters. The difference of the ice crystal structures might be caused by a significant difference in the primary nucleation origin, i.e. close to or far from the focal plane, or due to the particular topology limitations set by the sample chamber. The ice crystal structures appear consistent over the entire sample for both cases. This could lead to the conclusion that a single image would be representative for the whole sample. This is, however, not necessarily the case which will be evident when the distribution of cells over the cross section is analyzed in more detail.

The distribution of dendritic channels and cells can be studied in a quantitative manner by summing the value of green and blue channels over each horizontal line based on spectral data. This gives an indication of the amount of dendritic channel (green) and cells (blue) in a given horizontal line. The result of the normalized summation is shown for both samples as the graph on the left side of the images. This gives a more quantitative perspective on the respective distributions, but no absolute statistics since the image intensity is dependent on the focal plane chosen as well as other effects such as laser intensity, bleaching, water condensation etc. It can be used an additional tool to evaluate the crystal structures and cell distribution apart from a simple visual inspection of the images. If the distribution of dendritic channels is considered, then a rather uniform distribution is seen over the entire cross section. This is consistent with the observation of the same type of ice crystal structures observed over a cross section. For sample A, two peaks appear in the dendritic channel distribution. Both these spikes can be attributed to a high background signal either originating from underlying dendritic channels or a sheet of dendritic channels located between the top coverslip and the underlying ice crystals. Similar background signals can be observed in the images for sample B, but they do not seem to have an impact on the calculated dendritic channel distribution, possibly due to them being present in a majority of the images.

Now the distribution of cells in the samples will be considered. A visual inspection of the two cross sections reveals that the cells are primarily localized in a smaller area toward the center of the sample. This is confirmed by the calculated distribution based

on spectral analysis of the samples. The calculation of the distribution is here particular useful since cells located in the dendritic channel can be difficult to see. This is to our knowledge the first direct measurement of the macroscopic cell distribution in a large volume cell culture sample. The localization of cells in the sample center is an interesting observation since cell density is a parameter used to optimize a given cryopreservation protocol. This measurement shows that the cell density is not uniform over the sample, and the sample volume and cell count cannot directly be converted to a cell density during a cryopreservation process.

The reason for the cell localization predominately in the center of the sample can be found in one of two effects. The cells are pipetted into a medium with a viscosity higher than water due to the DMSO. The cells might therefore not have had the time to completely disperse in the sample before the onset of ice nucleation. The cells could instead migrate toward the center of the sample during freezing. It is safe to assume that ice starts to nucleate at the side of the sample and during ice growth water will freeze at the ice front increasing the CPA concentration. This creates a flux of CPA toward the center of the sample and this would also push the cells toward the center.

Whether the localization of cells in the sample center has a positive or detrimental effect on the cryopreservation is not known. Cells in the center will on one hand experience a delay and slowdown in the osmolyte increase, reducing the risk of an osmotic shock that can happen when ice is growing rapid. This is a purely positive effect on the quality of the cryopreserved sample. The cell concentration is on the other hand higher in the dendritic channels at the sample center, which increases the risk of contact between a cell membrane and an ice crystal. It has been proposed that such a contact can induce intracellular ice and thus endanger the cell [136]. This could be imagined to have a detrimental destabilizing effect on the cellular membrane and a closer study of the cell distribution can help to understand the predominant mechanism. A close visual inspection of the two cross sections reveals that the cells are primarily located in the broad dendritic channels for sample A, which was to be expected. In sample B, the cells appear to be located in inclusions of CPA, particularly in the center of the sample with the highest cell concentration. For sample A this only happened rarely. It can be detrimental to a cell to be located in such an inclusion since this will increase the risk of contact between the cellular membrane and the surrounding ice which can have a negative effect on the membrane stability. It should, however, be noted that the dendritic channels form a 3D network as previously discussed in section 4.2.1 and it is not possible to exclude that the cells are located in vertical dendritic channels instead of inclusions.

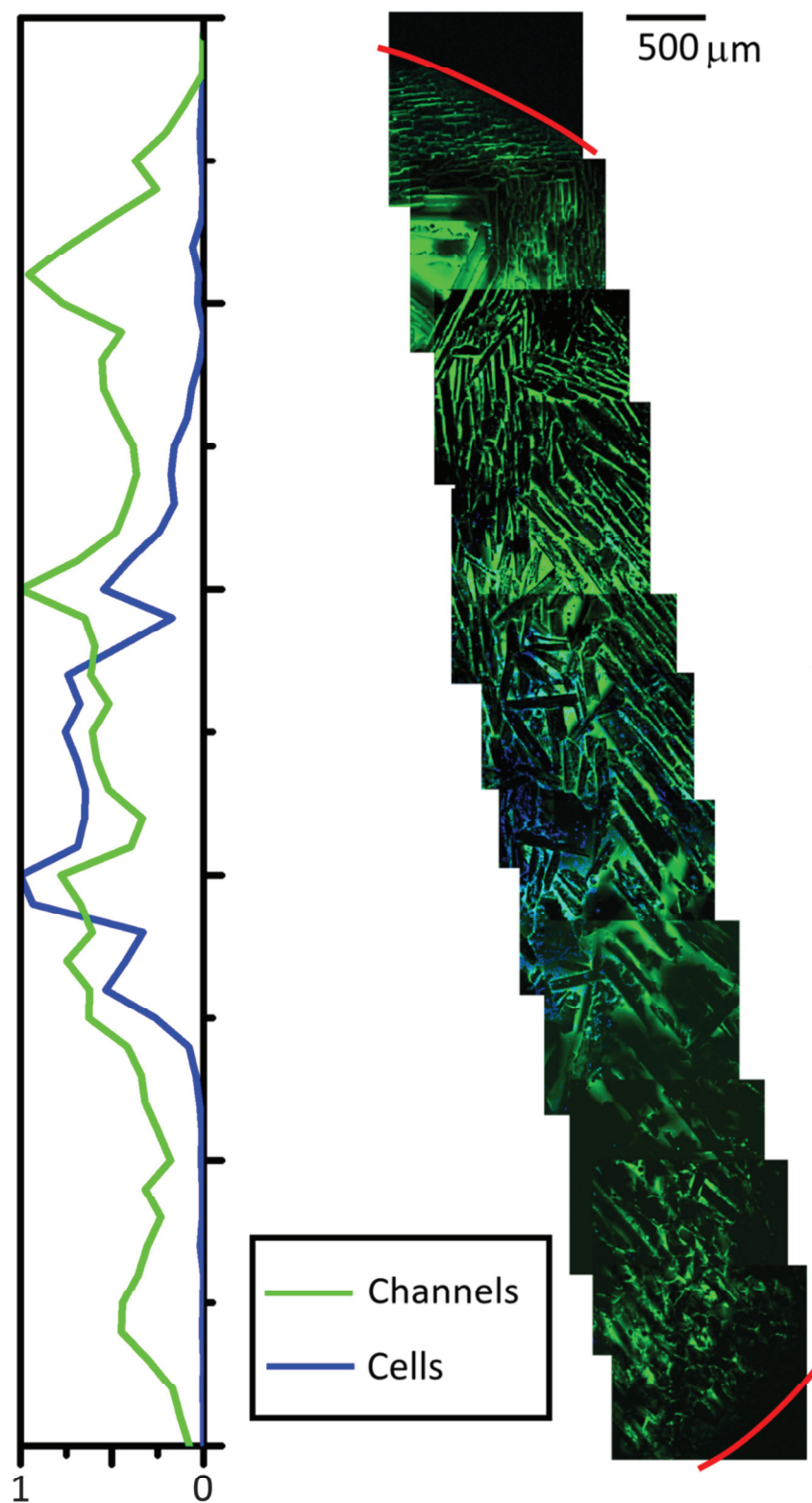


Figure 4.9 Cross section of sample A. Big volume sample of murine fibroblast cells frozen in 5 % DMSO to $-80\text{ }^{\circ}\text{C}$ at $1\text{ }^{\circ}\text{C}/\text{min}$. The dendritic channels and cell nuclei are dyed green and blue, respectively. The red lines describe the sample container wall. The graph on the left describes the overall distribution of dendritic channels and cell nuclei.

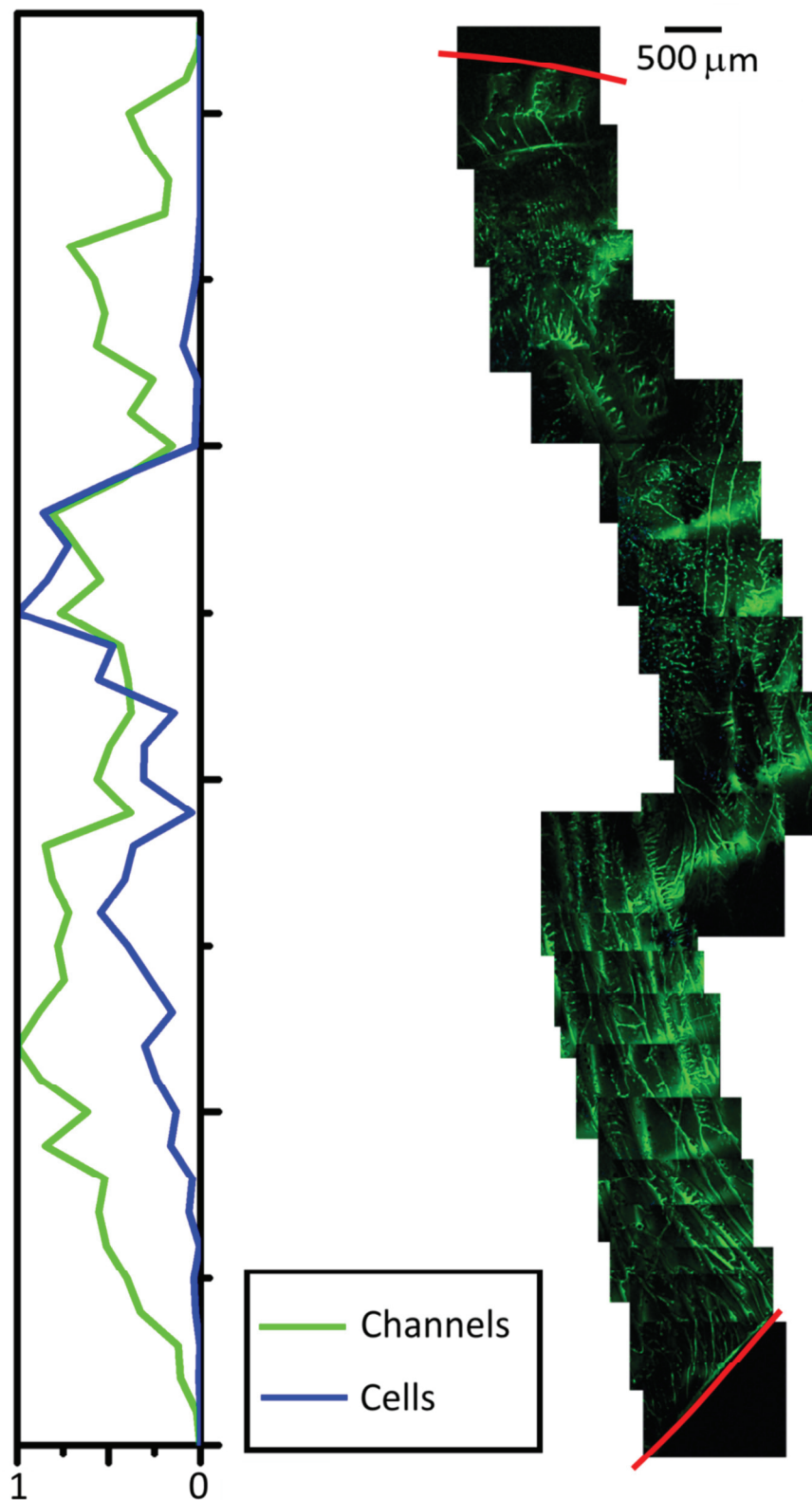


Figure 4.10 Cross section of sample B. Big volume sample of murine fibroblast cells frozen in 5 % DMSO to -80°C at $1^{\circ}\text{C}/\text{min}$. The dendritic channels and cell nuclei are dyed green and blue, respectively. The red lines describe the sample container wall. The graph on the left describes the overall distribution of dendritic channels and cell nuclei.

5 MICROSCOPIC DISTRIBUTION OF SAMPLE COMPOUNDS

Cells and cell media undergo significant changes during the freezing process of cryopreservation mainly due to the phase transition of water from a liquid to a solid state. This changes both the physical structure and chemistry in and around cells and plays a major role in the viability of a given cell. Most of these changes and in particular the local chemistry cannot be observed using conventional microscopy techniques such as transmission microscopy, which only gives morphological information. Cryobiological studies are therefore often performed as analysis of viability and functionality pre and post cryopreservation. Any damaging effects during freezing, storage and thawing will accumulate and are in such a study impossible to distinguish or pinpoint. When a cell culture sample is frozen, ice crystallizes and the remaining liquid forms a complex network of dendritic channels. The cells are primarily located in these channels. The size of the ice crystals, width of dendritic channels, distribution of cells and viability of cells is dependent on the cryopreservation protocol. The ice crystallization rate has a major impact on the sizes of ice crystals and dendritic channels and when supercooling occurs, variations of the phase structures are to be expected even for identically prepared samples. Being able to image these physico-chemical properties can thus shed a new light on cryopreservation since the fate of cells is so dependent on the local environment during freezing.

This chapter will take a microscopic perspective on the cryopreservation process and show how Raman scattering can be utilized to investigate the local environment in and around cells. This can furthermore give insights to events that happened in the sample during freezing retrospectively. In particular, it will be investigated how the chemical compound hydrohalite can be correlated to eutectic formation and thus used to pinpoint where this process occurred in a given sample. This method is an analytical approach to retrospective analysis of cryopreserved samples and the influence of DMSO on hydrohalite formation will also be investigated as it is a common CPA.

5.1 Confocal Raman microscopy

CRM allows for imaging with both chemical and physical information, here in particular in and around cells in slowly frozen samples, and is therefore a powerful tool to investigate frozen cells. It is possible to distinguish between different molecules with Raman spectroscopy since they have different vibrational modes. A chemical

compound or its form can be identified from certain peaks and bands in the Raman spectrum of the scattered light. Raman scattering and the CRM setup was explained in detail in section 3.3.2. In Figure 5.1 several Raman spectra are shown for some relevant compounds, namely water, ice, cellular material, DMSO and hydrohalite. These reference spectra are very important to record before proceeding with the Raman study of a complex mixture of multiple compounds, since these enables an analysis and distinction between the individual compounds. The reference spectra are recorded using samples only containing one compound if possible. The Raman spectrum of cellular material has been recorded using a sample of adherent murine fibroblasts in PBS. The spectrum of hydrohalite has been recorded by first cooling a brine solution with 25 wt% NaCl to $-50\text{ }^{\circ}\text{C}$ and subsequently heating it to just below the eutectic point. This seeds tiny hydrohalite crystals throughout the sample. The Linkam cryostage has a small aperture in the center allowing for transmission microscopy. The temperature is slightly elevated at this location compared to the silver block resulting in large pure hydrohalite crystals along the edge of the cryostage grown from the tiny hydrohalite seeds. This allowed us to record a Raman spectrum of pure hydrohalite.

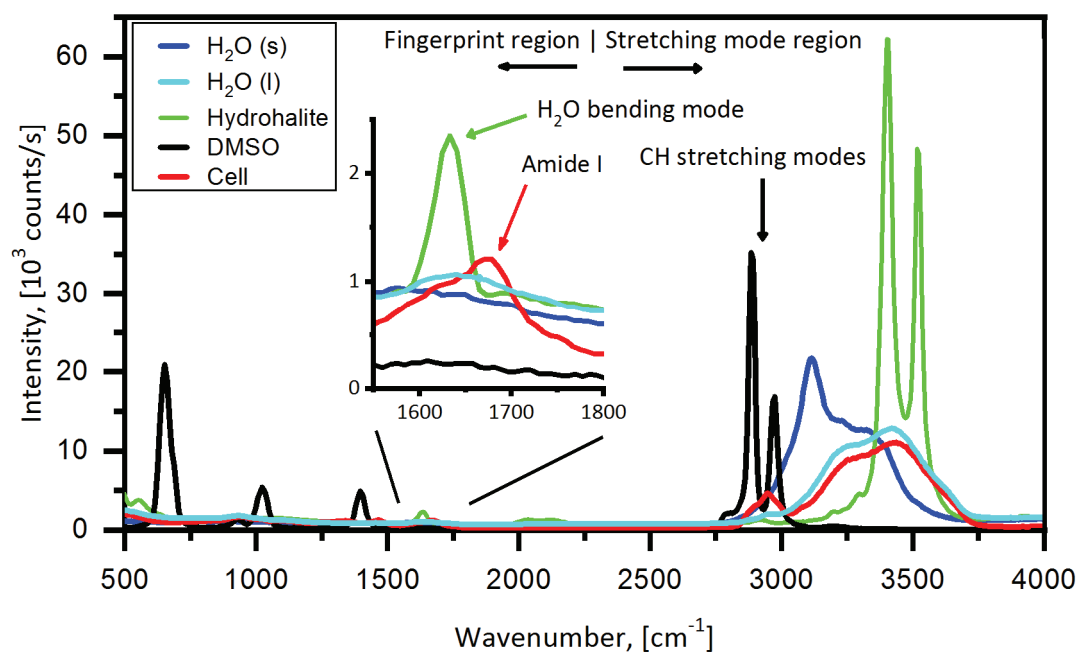


Figure 5.1 Raman spectra of several relevant compounds: Water (solid and liquid), hydrohalite, DMSO and cellular matter. These spectra of single compounds can be used as a reference when studying complex samples. The amide I Raman band seen in the inset can be used to identify cellular matter in samples containing DMSO.

A Raman spectrum is often divided into two regions: the fingerprint region below 2300 cm^{-1} and the stretching mode region above 2300 cm^{-1} . This distinction is made

based on the types of vibrational modes found in the region, i.e. bending and stretching modes. The fingerprint region is the most commonly used region in Raman spectroscopy as it allows to distinguish between chemical compounds. For cryobiological studies the stretching mode region contains some very useful information as will be shown in the following.

Water

Water has a major Raman band in the stretching region between 2800 cm^{-1} and 3600 cm^{-1} , the OH-stretching mode, whose shape depends on whether the water is liquid or solid. Water molecules have three distinct stretching modes that comprise the Raman spectrum: A symmetric stretching mode (3520 cm^{-1} - 3545 cm^{-1}), an anti-symmetric (3625 cm^{-1} - 3650 cm^{-1}) stretching mode as well as a bending overtone mode (3230 cm^{-1} - 3260 cm^{-1}) [137]–[139]. The wavenumber of each mode is dependent on the temperature. Water molecules ordered in an ice crystal enhance the bending overtone mode in the lower frequency side of the OH-stretching band. This makes it possible to distinguish between liquid and solid water in a frozen cell culture.

Hydrohalite

The hydrated NaCl-crystal, hydrohalite, has several stretching modes in the high-frequency end of the OH-stretching band [140]–[142]. These modes are, however, very close in frequency and it is therefore only possible to distinguish two Raman peaks with our current setup, due to a limited spectral resolution, as seen in Figure 5.1. The first is located at 3400 cm^{-1} and the second at 3520 cm^{-1} . They will be denoted hydrohalite I and hydrohalite II, respectively, for future reference. These two peaks

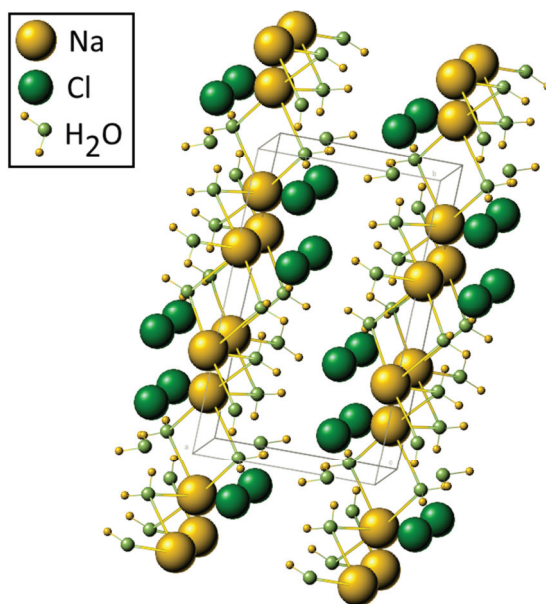


Figure 5.2 Sketch of the hydrohalite crystal lattice. Image taken and modified from [215]. The Na- and Cl-molecules are located pairwise in the crystal lattice. The water molecules have specific positions in the crystal lattice giving rise to a distinct Raman spectrum.

originate from water molecules located at specific positions in the hydrohalite crystal, but exhibit relatively narrow Raman bands in comparison to water molecules in a liquid or ice due to the limited number of positions they can occupy in the hydrohalite crystal [143] as shown in Figure 5.2. This signature enables us to distinguish water molecules in hydrohalite from liquid or solid water. The relative strength between these two peaks depends on the crystal rotation with respect to the laser polarization [142] and this can be used to distinguish between crystals of different orientation. It can furthermore be seen from the Raman spectra that the bending mode of H_2O around 1600 cm^{-1} is enhanced considerably when compared to pure H_2O . This can in principle be used to differentiate hydrohalite in solutions where the high frequency bands overlap with other modes. This is, however, not the case in these studies since very few compounds have vibrational modes with frequencies of magnitudes comparable to hydrohalite.

CH-stretching band

The CH-stretching modes also contain a symmetric and an anti-symmetric mode similar to the OH-stretching [144], which is why the CH-stretching is sometimes seen as one or two peaks depending on the composition of the compound. The CH-stretching band is very favorable to image cellular matter, since this gives the highest signal-to-noise ratio.

Amide I protein band

If a sample however multiple compounds with CH-bonds, such as DMSO, then another band would have to be used to image cellular matter. In this case the CO-stretching mode around 1655 cm^{-1} correlated to the Amide I protein structure [145] can be used instead. This allows for imaging of both cellular matter and hydrohalite in samples containing DMSO although with a worse signal to noise ratio putting an even higher

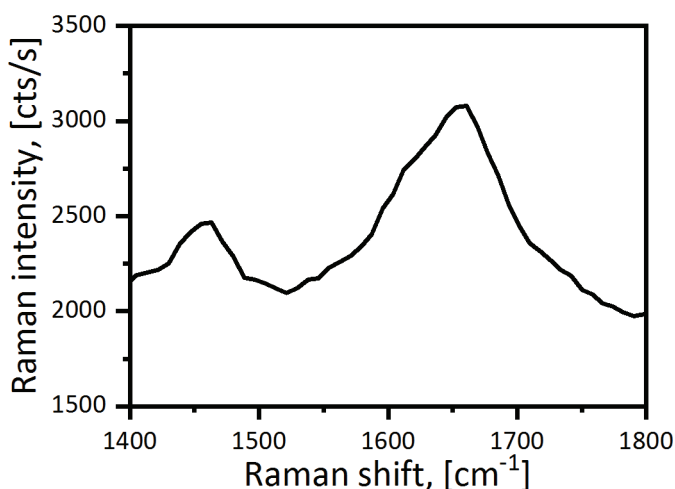


Figure 5.3 Raman spectrum of the Amide I protein structure of Bovine Serum Albumin. Here, the Raman band around 1655 cm^{-1} correspond to the CO-stretching mode of the protein structure.

demand on limiting background noise. Figure 5.3 shows the Raman spectrum of bovine serum albumin with the amide I protein peak clearly visible around 1655 cm^{-1} . The band around 1450 cm^{-1} can be attributed to CH_2 scissoring modes and CH_3 bending modes in side chains [146]. A Pearson's correlation coefficient [147] of 0.91 between $I_{\text{Cell,CH}}$ and $I_{\text{Cell,AmideI}}$ has been found from the CRM image of a frozen murine fibroblast in PBS in Figure 3.12. This sample does not contain any DMSO and can thus be used as a control for this correlation. This correlation was made with the part of the CRM image only containing the cell. This confirms that $I_{\text{Cell,AmideI}}$ can indeed be used to image cellular matter, which is very useful in samples containing CPAs such as DMSO.

Table 5.1 Table of integration limits used to generate the CRM images.

COMPOUND	ω_{start}	ω_{end}
$I_{\text{HH},1}$	3380 cm^{-1}	3460 cm^{-1}
$I_{\text{HH},2}$	3500 cm^{-1}	3580 cm^{-1}
$I_{\text{Cell,CH}}$	2820 cm^{-1}	3030 cm^{-1}
$I_{\text{Cell,AmideI}}$	1530 cm^{-1}	1700 cm^{-1}
I_{DMSO}	2900 cm^{-1}	3580 cm^{-1}

CRM images are created by integrating a Raman peak as described in section 3.3.2.3. Table 5.1 gives the integration limits used to generate the CRM images in this work. For the samples containing DMSO, the Amide I Raman band $I_{\text{Cell,AmideI}}$ will be used to identify cellular matter instead of the CH_2 Raman band $I_{\text{Cell,CH}}$.

5.2 Chemical markers for retrospective analysis

Raman spectroscopy is a non-contact method to identify chemical compounds in frozen biological samples. Depending on the sample composition and cryopreservation protocol, this identification can be used in a retrospective analytical manner to draw conclusions on processes that have occurred in the sample. One example hereof is the identification of ice crystals in vitrified samples that indicate that devitrification has occurred and that the sample most likely has experienced a suboptimal cooling or that the sample has been heated to above the glass transition temperature. The use of Raman spectroscopy to investigate this has been discussed in [112]. The devitrification of vitrified samples will be investigated in section 6.3.

Another example that will be investigated in detail in this chapter is the chemical compound hydrohalite. When isotonic saline water is cooled, ice will at some point start to crystallize, and since NaCl is not dissolvable in ice, the NaCl-concentration will rise in the remaining liquid lowering the freezing point. Upon further cooling, the ice crystals will grow until a temperature minimum is reached, at which the remaining liquid will crystallize in a so-called eutectic crystallization through which hydrohalite will form. This happens at a temperature of $-21.1\text{ }^{\circ}\text{C}$ and a NaCl concentration of 23.3 wt%. The cooling process can be described by a phase diagram, as the one shown

in Figure 5.4, under the assumption that the system is in a thermodynamic equilibrium. Cells are sensitive to eutectic crystallization and Han et al. [52] report a drop in viability from 63.9 ± 2.3 % to 17.8 ± 2.5 % in rat prostate tumor cells due to eutectic crystallization and speculate on the damaging mechanism. It is however not possible to draw a conclusion on the damaging mechanism since it was not possible to establish the location of the eutectic crystallization. This information is critical to increase the understanding of the underlying mechanism. This is now possible by employing CRM, where hydrohalite is used as a marker for eutectic formation under the assumption that the sample can be described as a two-component system of H_2O and NaCl . It is evident from the phase diagram of brine in Figure 5.4 that hydrohalite can only form through an eutectic crystallization in samples with an initial isotonic NaCl -concentration, and will in such a case act as a marker for eutectic crystallization. It is therefore possible to use CRM to pinpoint where eutectic crystallization has occurred. This can for example be seen in Figure 5.5 where a cell has been frozen in a PBS solution. Here eutectic crystallization has occurred in the dendritic channel. A part of the hydrohalite signal overlaps with the signal from the cellular material and eutectic crystallization has therefore occurred either inside the cell or directly outside the cell. A fine spatial resolution is not possible as the cell is flat compared to the focal volume of the incident light. This will be discussed in detail in section 5.3 where image statistics will be employed to determine the location of the hydrohalite.

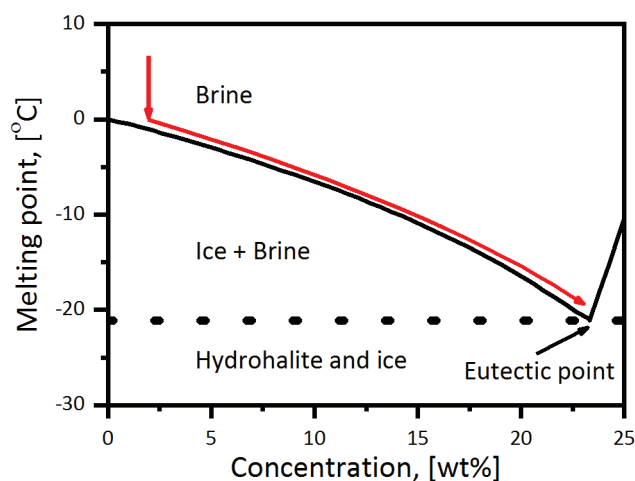


Figure 5.4 Binary phase diagram of NaCl and water. This phase diagram is based on the data in [148]. The red arrows describe the path through the phase diagram that a saline water solution takes with decreasing temperature. For a PBS solution, ice crystals will start to grow below -0.55 °C and thereby increase the NaCl -concentration and decrease the freezing temperature in the remaining liquid. The line between the brine and ice + brine phase is the so-called liquidus line.

Hydrohalite will be a product of eutectic formation in any mixture containing NaCl to a higher or lesser extent. Hydrohalite can also form through other means in solutions more complex than the two-component $\text{H}_2\text{O}/\text{NaCl}$ solution. DMSO is a commonly used

CPA in cryopreservation protocols and it has a profound impact on the physical and chemical characteristics of the solution. Here, hydrohalite is no longer an absolute marker for eutectic formation but rather an indicator that a part of the cryopreservation process has failed. This is investigated and discussed in section 5.4. Besides checking for hydrohalite formation as a marker for a non-ideal cryopreservation procedure Raman spectroscopy can also be applied for phenomenological retrospective analysis in that representative Raman spectra taken over an extended time period are compared. Changes in the Raman spectra indicate that a chemical reaction or a physical transformation (such as ice crystallization) has occurred. Changes in the Raman spectra should in general be considered as bad for the cryopreserved samples since the aim of cryopreservation is to stop all chemical and biological processes. The exact chemical reaction can be difficult to identify due the complexity of Raman spectra in the fingerprint region. With detailed information on the sample composition and the preserved cells it will be possible to detail describe the chemical and biological processes based on the Raman spectra. It will for example be possible to detect stem cell differentiation retrospectively using Raman spectroscopy [87].

5.3 Spatial distribution of hydrohalite frozen cell cultures

It is well established that intracellular ice crystallization is lethal to cells but the precise mechanism still remains unclear. Ice crystals draw and bind water from the entire cell making it inaccessible for the cell. This can have two consequences. Large ice crystals can de-mix the cellular interior and thereby damage the structure of the cell, in particular the cytoskeleton, in such a degree that the cell cannot recover after thawing but ice crystals can also draw water away from for instance proteins and thereby dehydrating them. This induces significant conformational changes [149] and that destabilize the protein, which can be detrimental to the cell. Intracellular hydrohalite can be assumed to have similar effects on a cell as ice since it also is a crystalline structure containing H₂O molecules. Hydrohalite formation can thus be assumed to just as lethal to cryopreserved samples as intracellular ice crystallization.

CRM was performed on samples containing either murine fibroblasts or human IPS cell colonies in PBS in order to study whether hydrohalite forms only outside cells or if it also forms inside cells.

5.3.1 Methods for spatial distribution measurements

Samples containing either murine fibroblasts or IPS colonies have been studied. The murine fibroblasts were cooled to -50 °C at a rate of 1 °C /min. Here, 24 CRM images were recorded distributed over four different samples. The samples with IPS colonies were likewise cooled to -50 °C at a rate of 1 °C/min. 58 CRM images of IPS colonies

were recorded of 11 different samples. All measurements here were performed using PBS and a sample volume of approximately $10\ \mu\text{L}$ – $20\ \mu\text{L}$. This corresponds to a sample height of $40\ \mu\text{m}$ – $80\ \mu\text{m}$. Only adherent cells were used. A pixel integration time of 100 ms was chosen and an image size of 64 pixels x 64 pixels. The scan area was $50\ \mu\text{m}$ x $50\ \mu\text{m}$ for the murine fibroblast samples and $100\ \mu\text{m}$ x $100\ \mu\text{m}$ for the IPS colony samples. The larger imaging area for the IPS colony samples were chosen due to the spatial size of the colonies. It was often not possible to scan the entire IPS cell colony. The imaging parameters were chosen in order to be able to record several images of the same sample which would otherwise have been difficult due to lengthy measurement times. This did however prove to have a sufficient signal-to-noise ratio for a detailed analysis.

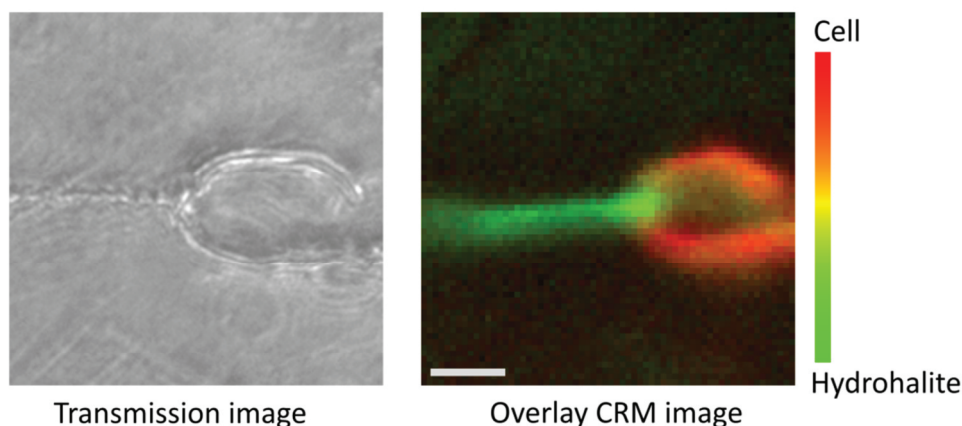


Figure 5.5 Transmission image and a CRM overlay image of a murine fibroblast cell in PBS cooled to $-50\ ^\circ\text{C}$ at $1\ ^\circ\text{C}/\text{min}$. The overlay image is a common RGB-image with the Raman signal from cellular matter and hydrohalite in the red and green channel, respectively. Here, black corresponds to ice. Scale bar is $10\ \mu\text{m}$. First published in [115].

Let us first study the example shown in Figure 5.5 where murine fibroblasts in PBS have been cooled to $-50\ ^\circ\text{C}$ at $1\ ^\circ\text{C}/\text{min}$. Here, the Raman responses from cellular matter, $I_{CH,cell}$, and hydrohalite, I_{HH1} , are shown in red and green respectively. In this example, there is a clear overlap between the Raman responses of cellular matter and hydrohalite in the upper part of the cell. This does lead to a conclusion that the hydrohalite must be located within the cell but great care should be taken when interpreting these images. The cells in the sample are adherent on a glass coverslip and will as such spread out over the glass with the result that the cell are relatively flat compared to the length of the focus. With this in mind a definite conclusion on the location of the hydrohalite cannot be made since hydrohalite located in very close proximity outside the cell or intracellular hydrohalite are indistinguishable. This is also underlined by the fact that this image contains hydrohalite that is located in a dendritic channel, i.e. outside the cell, and that this channel starts at the edge of the cell. At the

channel-cell intersection, the hydrohalite signal is very high, but does the signal come from intracellular or extracellular hydrohalite or even both? Image statistics can be applied in order to answer this question. Due to the fact, that quantity of a compound and its Raman signal are proportional, a spatial correlation between hydrohalite and cellular matter means that the hydrohalite are indeed located within the cell.

Analyzing a large number of samples with CRM, images revealed that the hydrohalite crystals formed are very fine-grained compared to the spatial resolution of the setup. This results in a fixed ratio between the two hydrohalite bands and it is therefore sufficient to only image one of them, i.e. the brighter hydrohalite I band. The distribution of compounds in the eutectic phase also appears to be uniform.

5.3.2 CRM image analysis

A scatter plot can be generated from a CRM image where each data point corresponds to the signal strength of two chemical compounds in a single image pixel. Such a scatter plot is presented in Figure 5.6a and has been generated from Figure 5.5 using the normalized Raman signal from cellular matter and hydrohalite. A pixel, (i, j) , containing only either cellular matter or hydrohalite will thus be located along the x- and y-axis, respectively. Pixels containing neither, i.e. only ice, will be located in the lower left corner. It is evident from the colocalization scatter plot that a large quantity of pixels only contains ice, which was expected by a visual inspection of the CRM image in Figure 5.5. Pixels located in the remainder of the colocalization scatter plot contain hydrohalite and cellular matter in different ratios. The scatter plot can be difficult to interpret as a large quantity of data points located in the lower left corner, corresponding to ice. The only conclusion that can be drawn based on this scatterplot is that the dendritic channel is filled with hydrohalite, which was already concluded based on the CRM overlay image in Figure 5.5. This is seen as a significant amount of data points located along the y-axis above the value 0.2. The low number of data points containing any cell at all can also lead to erroneous correlation calculations. Further processing of the data is therefore required before any conclusions can be drawn.

Instead of a scatter plot a colocalization density map is used, which plots the density, ρ , of the data points $(I_{Cell}(i, j), I_{HH}(i, j))$ on a logarithmic scale. This emphasizes regions with a lower quantity of data points and therefore eases the interpretation of trends found in the image. Using $\log(\rho)$ will lead to a numerical problem in regions of the plot with no data points, i.e. $\rho = 0$, and $\log(\rho + 1)$ has been chosen instead. The colocalization density map of the image in Figure 5.5 is shown in Figure 5.6b. From this density map, three parts can be identified. Firstly, the densely packed data points in the lower left corner that can be attributed to ice. Secondly, data points located along a line close to the hydrohalite axis. Finally, data points located along a line containing both hydrohalite and cellular matter.

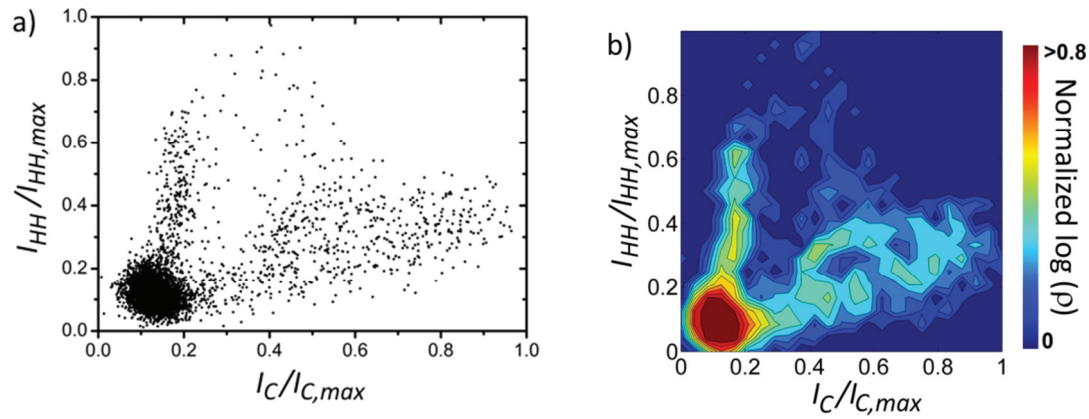


Figure 5.6 a) Colocalization scatter plot of the CRM found in Figure 5.5. Each data point $(I_{Cell}(i,j)/I_{Cell,max}, I_{HH}(i,j)/I_{HH,max})$ in the scatterplot corresponds to a pixel in the CRM image. b) Colocalization density plot of the CRM image found in Figure 5.5. The colocalization density plot show the normalized $\log(\rho + 1)$ where ρ is the density of data points found in the colocalization scatter plot. First published in [115].

Parts of a CRM image with no signal of cellular matter are straightforward to interpret, both based on the CRM image itself and using the colocalization density map. Here, the hydrohalite is strictly located outside the cells. The corresponding data points are located close to the x- and y-axes in the colocalization density map. Part of the hydrohalite in the CRM image shown in Figure 5.5 can therefore be identified as extracellular.

Most of the CRM images do however contain an overlap and it is here that the colocalization maps prove the most useful, since a distinction between intra- and extracellular hydrohalite is here almost impossible to make just by a visual inspection. The recorded CRM images will be categorized into three cases using these colocalization density maps: Extracellular hydrohalite, Intracellular hydrohalite, and Extracellular shell of hydrohalite. Some of the images do however fit into more than one case. An image can for instance both contain a hydrohalite filled dendritic channel as well as a cell with intracellular hydrohalite. The example in Figure 5.5 is a good example of this. This will be elaborated during the analysis of the different cases.

5.3.3 Types of hydrohalite formation

In this section, the spatial distribution of hydrohalite will be analyzed for different samples containing murine fibroblasts. Three different cases of hydrohalite can be identified (based on this model system):

- A. Extracellular hydrohalite
- B. Intracellular hydrohalite
- C. Extracellular shell of hydrohalite

Case A: Extracellular hydrohalite

A typical example of extracellular hydrohalite is shown in Figure 5.7. Here it can be clearly seen from the CRM that the hydrohalite is primarily located in dendritic channels surrounding the cell. This is also confirmed by the colocalization density map where the data points are primarily located at the axes. This is the most distinct feature of extracellular hydrohalite indicating a clear spatial separation of cells and hydrohalite. At the edge of the cell some pixels contain both hydrohalite and cellular matter and this results in the data points located closer to the center of the colocalization density map when taking into account the limited resolution in the axial direction. It should however be safe to assume that all hydrohalite in this image is extracellular. This type of extracellular hydrohalite was found in 11 of 24 images.

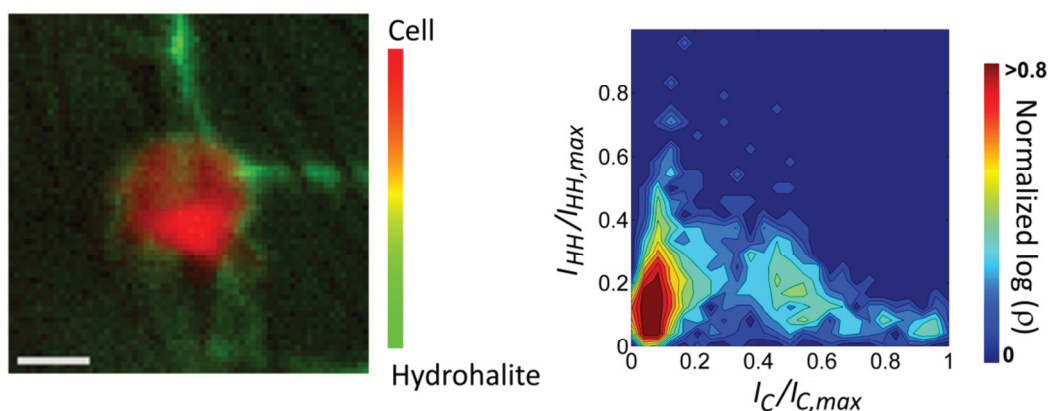


Figure 5.7 CRM image and corresponding colocalization density map typical for extracellular hydrohalite. The image contains a single murine fibroblast cell in PBS that is frozen to -50 °C at 1 °C/min. Scale bar is 10 μ m. First published in [115].

Case B: Intracellular hydrohalite

Figure 5.8 shows a typical example of a cell containing intracellular hydrohalite. It can be seen from the colocalization density map that a significant part of the data points are located along a truncated line towards the top right corner, indicating that the hydrohalite is indeed intracellular. This is a direct proof that eutectic crystallization can indeed take place inside a cell. There are however also parts of the cell containing no hydrohalite. This could be areas where some of the cellular component have concentrated, such as organelles, nucleus etc. This results in data points located under the line and the data points form a triangular pattern in the colocalization density map. It is thus the particular shape of the density plot that reveals the true intracellular nature of hydrohalite.

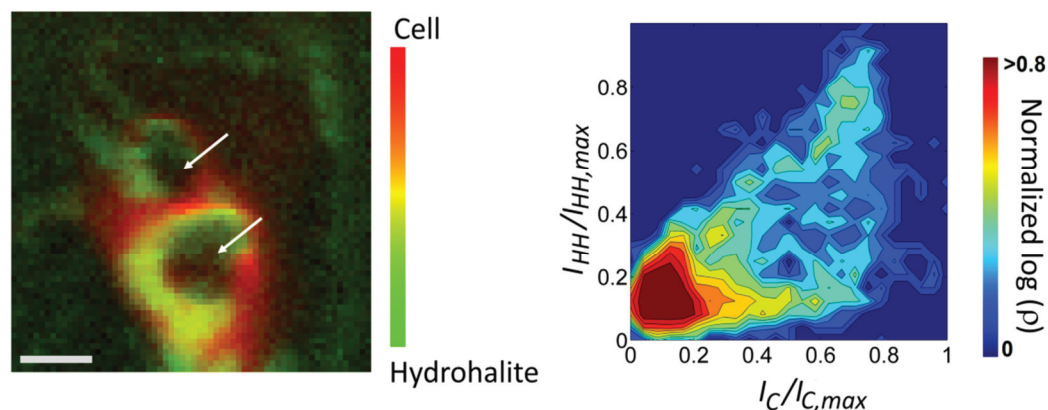


Figure 5.8 CRM image and corresponding colocalization density map typical for intracellular hydrohalite. The image contains two murine fibroblast cells in PBS that is frozen to -50 °C at 1 °C/min. The cells both contain relatively large ice crystals marked by arrows. Scale bar is 10 μm. First published in [115].

Extracellular hydrohalite will not spatially correlate with cellular matter. The hydrohalite found in these samples are finely grained as previously mentioned and will consequently have a uniform distribution within a cell. This results in a linear correlation between the Raman signal from cellular matter and hydrohalite. This has been illustrated in Figure 5.9. Imagine a laser scanning over a cell filled with fine-grained hydrohalite from left to right. No signal from the hydrohalite or cellular matter is recorded outside the cell. As soon as the laser hits the cell, a signal from hydrohalite and cellular matter is recorded which increases further into the cell. The relative increase of the signal from hydrohalite and cellular matter are identical since the fine-grained hydrohalite results in a fixed volume ratio of the two components. Regions in the image containing either extracellular hydrohalite or only cellular matter can have a stronger signal compared to the intracellular eutectic phase, but a combination of the two are not possible. A linear correlation in the colocalization density map is therefore a clear sign that the hydrohalite in the image has formed in the cytoplasm of the cell.

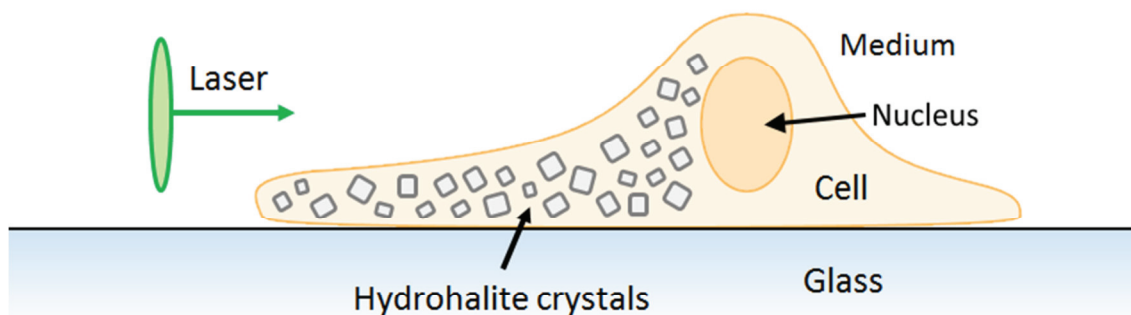


Figure 5.9 Sketch of a laser scanning through a cell filled with fine-grained hydrohalite crystals. If the hydrohalite is evenly distributed then there will be a linear correlation between the Raman signal from the hydrohalite and cellular matter.

Of the 24 recorded CRM images, 12 contained cells with intracellular hydrohalite. The cells shown in Figure 5.8 also contain a large intracellular ice crystal. The ice crystals can be seen as dark spots marked with arrows and that are surrounded by hydrohalite and cellular matter. In fact 11, of the 12 CRM images showing intracellular hydrohalite contained intracellular ice and all 12 images were taken of two of the four samples. This could indicate that there is a close correlation between intracellular ice formation and hydrohalite crystallization.

The single image containing intracellular hydrohalite but no ice is shown in Figure 5.10. The image contains two cells and the colocalization map shows that hydrohalite must indeed be located within the cell due to a spatial correlation of the two components. Based on these observations of intracellular ice, one of the following two conclusions can be made. Either the chemical and physical conditions favoring intracellular ice crystal crystallization are also favoring hydrohalite crystallization or ice acts as nucleator or promoter for hydrohalite crystallization. Both of these conclusions seem plausible since the hydrohalite crystal does contain water molecules.

A cell will dehydrate during cooling and if no intracellular ice crystals are formed then the osmotic inactive water might be bound to biomolecules, which in turn could be thought to inhibit hydrohalite crystal formation and growth. On the other hand, if intracellular ice is forming then the cell will have a larger volume, but here the water is bound to the ice crystals. Both cases do however have the same amount of free water in the cell that is necessary for hydrohalite crystallization, but different morphologies that influence hydrohalite crystallization.

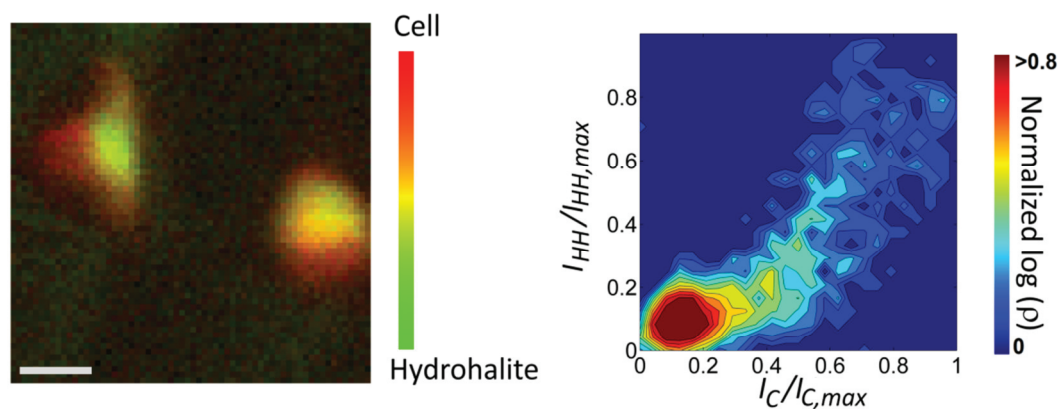


Figure 5.10 CRM image and corresponding colocalization density map showing intracellular hydrohalite but no intracellular ice crystals. The image contains two murine fibroblast cells in PBS that were frozen to $-50\text{ }^{\circ}\text{C}$ at $1\text{ }^{\circ}\text{C}/\text{min}$. Scale bar is $10\text{ }\mu\text{m}$. First published in [115].

It would be reasonable to assume that the intracellular ice crystals are formed first, since ice can start crystallizing under the freezing point of $-0.52\text{ }^{\circ}\text{C}$ whereas hydrohalite can only form below the eutectic temperature of $-21.2\text{ }^{\circ}\text{C}$. For the ice and hydrohalite

to form simultaneously, the sample would have to be supercooled to a least 20 °C below the freezing point. This is not impossible and is very dependent on the experimental conditions. Since the samples were cooled at 1 °C/min it does, however, seem unlikely that the samples reach a supercooling of 20 °C. This does seem to favor the assumption that ice is formed first, since the chemical and physical conditions are different at the time of ice nucleation and hydrohalite nucleation.

It has been shown that hydrohalite particles in the atmosphere can act as a heterogeneous ice crystal nucleator [150], [151]. The opposite mechanism therefore seems likely, which further strengthens the argument that ice can act as a nucleator for hydrohalite. Upon further inspection of Figure 5.8, it is also seen that all of the hydrohalite seems to be located close to the intracellular ice crystals which would be the case if the ice crystals act as nucleators. It should however be noted that ice is not necessary for hydrohalite crystallization and it can form spontaneously, which was observed in one CRM image.

Case C: Extracellular shell of hydrohalite

Figure 5.11 shows a typical example for an extracellular shell of hydrohalite. As in the case of intracellular hydrohalite the Raman signals of cells and hydrohalite overlap in the CRM image but the colocalization density maps typically show an inverted “U” pattern that can be explained using Figure 5.12. Imagine a laser scanning from left to right over a cell where fine-grained hydrohalite crystals have formed a shell just outside the membrane. The laser starts outside the cell where only an ice signal is recorded. When the laser moves over the cell both the signal from the hydrohalite and cellular matter will increase until a maximum of hydrohalite is reached. Further scanning into the cell will then have an increased signal from cellular matter whereas the signal from hydrohalite decreases. This leads to the inverted “U” pattern. Since there is no obvious spatial correlation, it would be expected that this hydrohalite is extracellular and have formed a shell just outside the cellular membrane. This has also been proposed by Okotrub et al. [113] in a spectroscopic study of yeast cells but has never been shown using CRM. Out of the 24 images, nine showed an extracellular shell of hydrohalite. In these nine images, no intracellular ice crystal formation was observed. The shell hydrohalite was only found in the two samples where no intracellular hydrohalite was found.

Cells are located among large extracellular ice crystals, not necessarily in direct contact, and an unfrozen liquid. When a eutectic crystallization occurs, the unfrozen liquid between the cell and ice crystals turns into hydrohalite forming a shell around the cell. It is safe to assume that the hydrohalite will have an effect on the membrane due to direct contact of the compounds. Hydrohalite has a density of 1.61 g/cm³ that is significantly different from a density of a 23.3 wt% brine solution, which are 1.18 g/cm³. A larger quantity of hydrohalite formed in very close proximity to a cell could therefore induce a sudden pressure differential over the membrane and thereby mechanically damage or even rupture the membrane. Hydrohalite furthermore binds

electrolytes from the immediate surroundings of the cell changing the local chemical

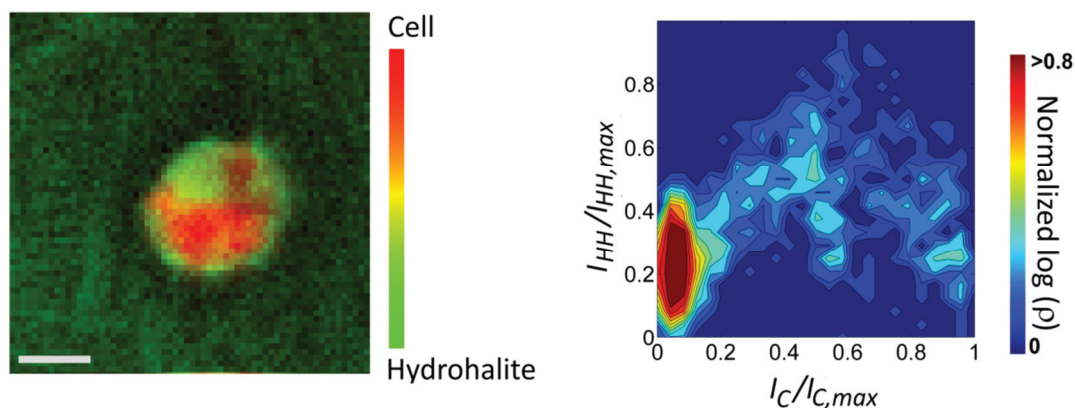


Figure 5.11 CRM image and corresponding colocalization density map typical for extracellular shell hydrohalite. The image contains a single murine fibroblast cell in PBS that is frozen to $-50\text{ }^{\circ}\text{C}$ at $1\text{ }^{\circ}\text{C}/\text{min}$. Scale bar is $10\text{ }\mu\text{m}$. First published in [115].

environment significantly. A sudden drop in unbound electrolytes will cause an osmotic shock and an influx of water into the cell. This could also be detrimental to the viability of the cell. Hydrohalite does however also draw Na^+ and Cl^- ions from the surrounding medium, which in turn changes the osmotic properties of the cell. This can induce an osmotic shock to the cell with even more water flowing out of the cell. Big changes of cell volume will not occur since cells at this point are surrounded by ice. Hydrohalite crystallization does however only happen below the eutectic temperature, where all liquid phases in principle should have turned solid and might thus not play a role in cell viability.

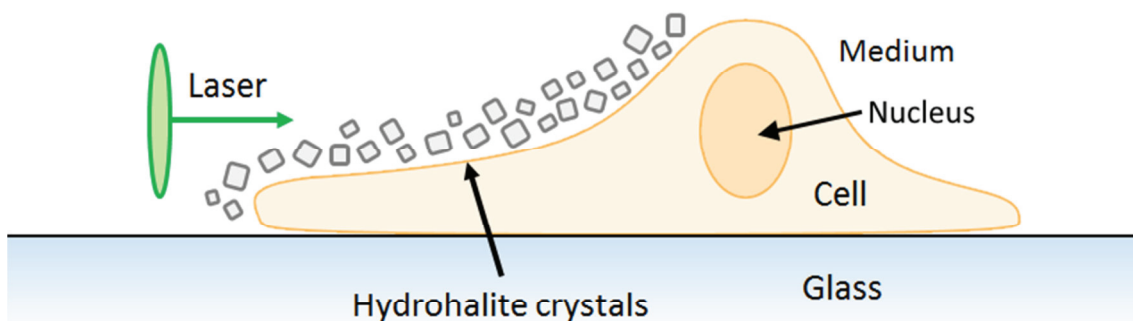


Figure 5.12 Sketch of a laser scanning through a cell where hydrohalite crystals have formed an extracellular shell just outside the lipid membrane. When the laser scans over the cell, the Raman signal from cellular matter and hydrohalite will rise evenly at the start. As the laser focus moves further into the cell the Raman signal from hydrohalite will decline compared to that of cellular matter.

5.3.4 Statistics of hydrohalite distribution in murine fibroblasts

Table 5.2 summarizes the findings of our study on spatial distribution of hydrohalite in murine fibroblast cells. This study supports the findings of Okotrub et al. in that hydrohalite can form a shell around cells, but this conclusion should be extended. It has been shown here that hydrohalite can indeed form within cells by eutectic crystallization. The lethality of eutectic crystallization should therefore be seen as a two-fold damaging mechanism.

It was also found that intracellular hydrohalite formation is much more probable in samples where intracellular ice formation occurs. This indicates that ice acts as an important nucleator for eutectic crystallization but based on one image with intracellular hydrohalite where no intracellular ice was present it could be shown that ice is not required as a promoter for hydrohalite formation.

Table 5.2 Summary of the CRM studies of spatial hydrohalite distribution in murine fibroblast cells. Some of the CRM images could be assigned to multiple classes. 24 CRM images were recorded.

MURINE FIBROBLAST CELLS	
CASE	Quantity
A: EXTRACELLULAR HYDROHALITE	11
B: INTRACELLULAR HYDROHALITE	12
C: SHELL HYDROHALITE	9
NO HYDROHALITE IN IMAGE	2

5.3.5 Spatial distribution of hydrohalite in IPS cell colonies

The experiment was repeated using IPS cell colonies. Here 58 CRM images on 11 different samples which were frozen to -50 °C at 1 °C/min similar to the murine fibroblast samples were recorded in collaboration with Manon Schmidt (student internship at Fraunhofer IBMT). IPS cell colonies are usually preserved using vitrification [152] and slow freezing protocols are still under development for these sample types. The IPS cell colony samples will also give another perspective on hydrohalite formation due to the colony forming aspect of the IPS cells. The recorded CRM images can be subdivided in three categories depending on the colony size and the location of the image acquisition. Roughly a quarter of the CRM images were recorded of small IPS cell colonies, i.e. colonies smaller than the 100 µm x 100 µm scan area. The remaining images contain large colonies, i.e. colonies larger than the scan area, and are taken either at the edge or the center of the colony. This can have an influence on the analysis of the individual image since a different amount of the surrounding environment is contained within the image.

The study of cell colonies larger than the scan area can lead to two problems in the analysis:

1. Hydrohalite and ice crystals located in between cells could erroneously be categorized as intracellular.
2. A larger quantity of cells in the image affects how the colocalization density maps look in a few cases.

It turns out that the second problem poses the biggest challenge in the analysis of the CRM images.

Case A: Extracellular hydrohalite

Extracellular hydrohalite is often easily recognizable due to the decoupling of the Raman signals from cellular matter and hydrohalite. Figure 5.13 shows the CRM and corresponding colocalization density map of the center of an IPS cell colony where extracellular hydrohalite has formed. This can be deduced even with the significant spatial overlap between the two signals and a colocalization density map that slightly resembles that of case B for murine fibroblasts shown in Figure 5.8. Here long channels filled with hydrohalite with small channels branching off are seen. These channels are considerably longer than the dimension of a single cell in the colony and must therefore be located outside the cells. If the hydrohalite were located within the cell then the hydrohalite crystal growth would be limited by the cellular dimensions. For the CRM images recorded at the edge of a large colony or of a small colony, extracellular hydrohalite was also found in the surrounding environment. Extracellular hydrohalite was found in 21 of the 58 CRM images. This is a slightly lower frequency compared to the murine fibroblast samples (11 of 24 CRM images). Considering that 21 of the CRM images were recorded at the center of large IPS cell colonies where this type of extracellular hydrohalite is a rare occurrence. The probability of finding

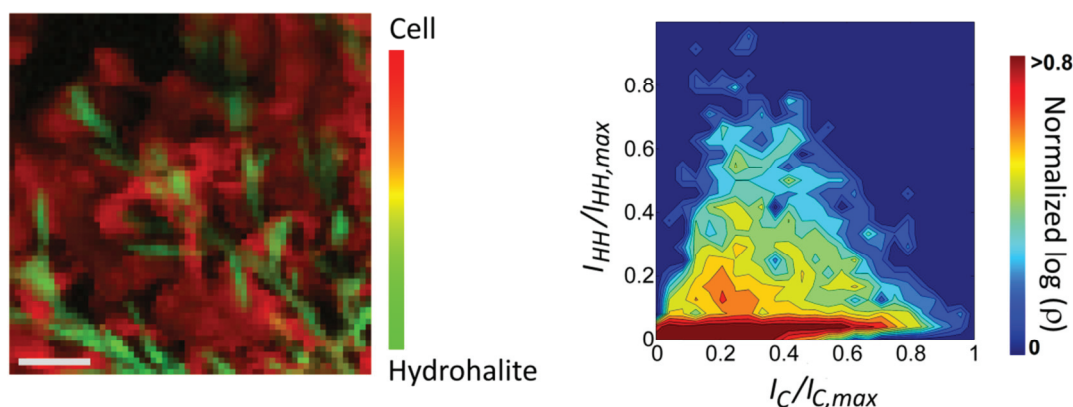


Figure 5.13 CRM image and corresponding colocalization map showing extracellular hydrohalite. The image contains a frozen IPS cell colony in PBS that were frozen to $-50\text{ }^{\circ}\text{C}$ at $1\text{ }^{\circ}\text{C}/\text{min}$. The CRM image was recorded at the center of a large colony. Scale bar is $20\text{ }\mu\text{m}$.

extracellular hydrohalite is even slightly higher in IPS cell colony samples compared to murine fibroblast samples.

Case B: Intracellular hydrohalite

Figure 5.14 shows the CRM and corresponding colocalization density map of the edge of an IPS cell colony where intracellular hydrohalite has formed. The hydrohalite in this image is found to be spatially overlapping with the IPS cell colony in such a manner that it has to be located within the cells. The hydrohalite structures are limited by the extent of the cells and no hydrohalite is found in the surrounding environment. This can also be seen in the colocalization density map where no data points are located along the hydrohalite axis and a pattern is formed resembling that found for intracellular hydrohalite for the murine fibroblast cells as seen in Figure 5.8. It could be speculated that the hydrohalite is not located within the cell, but rather outside and between the cells. If the hydrohalite were located outside the cells then there would be an equal probability that hydrohalite would form just on the edge of the colony or in channels in the ice phase. This is here not the case and it thus seems very likely that the hydrohalite is located intracellular. For the IPS cell colony samples 18 CRM images is considered to contain intracellular hydrohalite crystals, i.e. belonging to Case B.

It would be interesting to investigate whether intracellular ice crystals are similarly frequent in samples with IPS cell colonies as with the murine fibroblast samples. It is, however, not possible to determine whether the IPS cells contain intracellular ice crystals due to the colony formation. In the murine fibroblast cells, ice crystals were identified as dark areas surrounded by cellular material. This is only possible for single cells and not for colonies. In colonies, dark areas could just as well correspond to ice crystals situated between two cells and it is thus not possible to identify intracellular ice crystals based on CRM images. The example in Figure 5.14 does not seem to contain any dark areas in cells that might be attributed to ice crystals. A closer visual

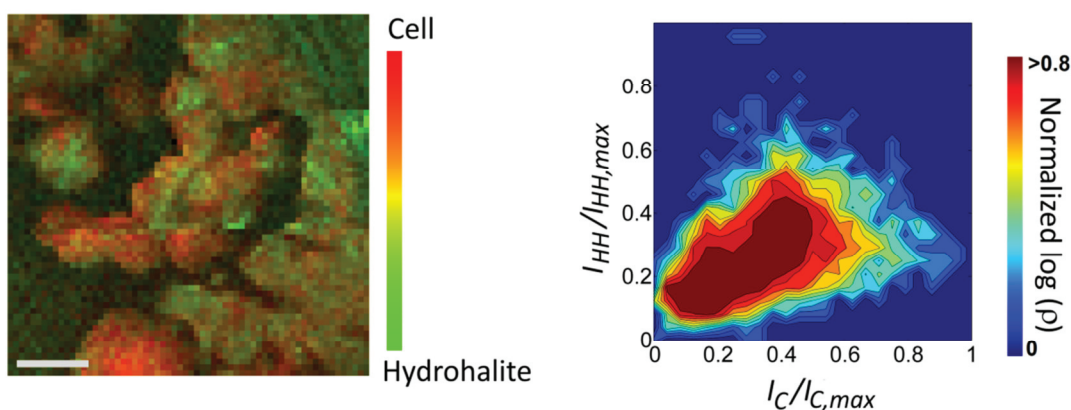


Figure 5.14 CRM image and corresponding colocalization map showing intracellular hydrohalite. The image contains a frozen IPS cell colony in PBS that were frozen to $-50\text{ }^{\circ}\text{C}$ at $1\text{ }^{\circ}\text{C/min}$. The CRM image was recorded at the edge of a large colony. Scale bar is $20\text{ }\mu\text{m}$.

inspection of the remaining CRM images containing IPS cells with intracellular hydrohalite only reveals four out of the 18 images with structures that might arise due to intracellular ice. Compared to the murine fibroblast samples were almost all cells that contained hydrohalite also contained ice. It seems unlikely that intracellular hydrohalite would form without any ice crystals either being present already or form as the hydrohalite forms. If the ice crystals are very fine-grained then they would be rather difficult to contrast and spot in a CRM image, and this could be the reason why ice crystals are not visually seen. This could indicate that the supercooling has been high in these cases, which will increase the ice crystallization speed and form very small ice crystals.

Case C: Extracellular shell of hydrohalite

The identification of shell hydrohalite over IPS cell colonies is significantly more difficult than with the single cell analysis of murine fibroblasts. The cells often fill the entire image with a large amount of hydrohalite spatially overlapping the cells and if care is not taken then this can erroneously be categorized as intracellular. Two examples of shell hydrohalite are shown in Figure 5.15. It was first observed that a part of the hydrohalite is located away from the cells and forming a sheet along the sample. This result in almost all of the images categorized as class C are also categorized as class A – 14 of 18 CRM images. This can also be seen in the colocalization density map, in particular for the first example, as data points located along the hydrohalite axis. This means that a sheet of the remaining liquid has formed along the glass coverslip instead of dendritic channels.

A significant amount of the hydrohalite does also overlap the cellular matter. The colocalization density map does, however, not exhibit the characteristic 'U' pattern as found in the case of single murine fibroblast cells. This can in part be attributed to the amount of extracellular hydrohalite and in part the spatial extent of the colonies. The surface of an IPS cell colony is rather rough and it seems like hydrohalite has only gathered in crevasses in the surface. The colocalization map is thus instead an expression of the roughness of the colony surface and does not always result in the inverted 'U' pattern. Both shown examples do, however, show a tendency towards this pattern. The hydrohalite structures found in the CRM images are significantly different from those found with intracellular hydrohalite, see Figure 5.14, and have sizes larger than single IPS cells. The hydrohalite must therefore have formed an extracellular shell around the IPS cell colony. This type of shell hydrohalite is found in 22 of 58 CRM images.

The long extracellular hydrohalite stripes in the CRM images indicate that the hydrohalite has nucleated far from the colony and has grown in the remaining liquid phase close to the coverslip. The crystal growth direction is then slightly changed upon reaching a colony and thereby overgrowing the colony. The hydrohalite structures seen in Figure 5.15 have the same appearance as lamellar eutectic growth, which is a common occurrence in metal alloys [153], [154].

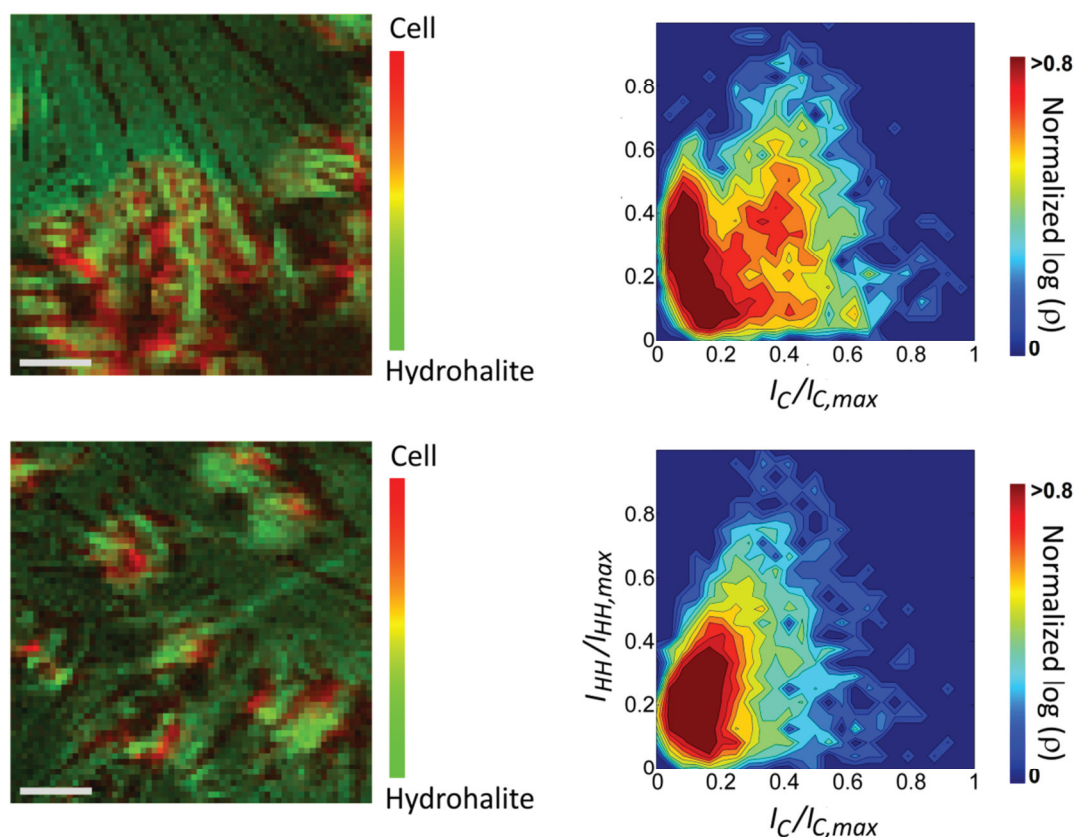


Figure 5.15 CRM images and corresponding colocalization maps showing extracellular shells of hydrohalite. The images contain frozen IPS cell colonies in PBS that were frozen to -50 °C at 1 °C/min. The CRM images were recorded at the edge and the center of large colonies, respectively. Scale bar is 20 μ m.

Summary: Hydrohalite formation in IPS cell colonies

The measurements of hydrohalite in IPS cell colony samples are summarized in Table 5.3. As with the murine fibroblasts, three distinct cases of hydrohalite were identified, albeit with slightly different frequency. Eutectic crystallization can occur in colony forming cells or in very close proximity to the colonies. Formation of colonies does thus not offer any protection against eutectic crystallization. This was expected since the eutectic crystallization is dependent on physical and chemical conditions of the sample. Only the chemical composition is changed inside the cells, but not sufficiently strong to inhibit the eutectic crystallization of the brine. It appears from Table 5.3 that intracellular hydrohalite is more frequent in large colonies compared to small colonies. Large colonies thus promote a physio-chemical state where eutectic crystallization can more likely occur. One explanation for this correlation could be that cells in the center of the colony could dehydrate less than cells at the edge. When more water is available then a eutectic crystallization is more likely. Another scenario could be that the larger intracellular volume of the large colonies can reach a higher supercooling

than that of smaller colonies, thereby promoting intracellular hydrohalite formation when compared to smaller colonies.

From Table 5.3 it is evident that the most cases of shell hydrohalite happen at the edge of a colony (including small colonies). This could be explained by hydrohalite nucleating far from the colony and grow toward it before being stopped at some point near the edge of the colony. One important aspect of an extracellular shell of hydrohalite in the context of cell colonies is that this shell has the possibility to disrupt cell-cell contacts. The cell-cell contact in IPS cell colonies plays a major role both in their generation but also for further survival and differentiation. If the cell-cell contacts are disrupted in such a manner that the colony will start to dissociate post-thawing then that can lead to apoptosis or unwanted differentiation of the stem cells [152], [155]–[157]. It is therefore highly relevant not only to check for intracellular hydrohalite formation but also closely monitor the formation of hydrohalite shells in order to establish a sufficient quality control for stem cell colonies.

Table 5.3 Summary of the CRM studies of spatial hydrohalite distribution in IPS cell colonies. Images were recorded of small colonies as well as of the edge and center of large colonies. The number in parenthesis indicates how many images were recorded of each colony type. Some of the CRM images could be assigned to multiple classes. 58 CRM images were recorded.

IPS CELL COLONIES				
CASE	Small (16)	Edge (21)	Center (21)	Total (58)
A: EXTRACELLULAR HYDROHALITE	8	10	3	21
B: INTRACELLULAR HYDROHALITE	2	7	9	18
C: SHELL HYDROHALITE	8	10	4	22
NO HYDROHALITE IN IMAGE	4	1	6	11

5.4 Influence of DMSO on hydrohalite crystallization

Through the addition of just a tiny amount of DMSO as a CPA to a saline solution, the freezing properties are changed dramatically. The mixture is no longer binary and can only be described by the more complex ternary phase diagram as shown in Figure 5.16. Here, a 2D projection of the liquidus surface onto the composition plane is shown for the water-rich part of the phase diagram. The liquidus surface describes the surface between the liquid phase and the ice/liquid phase. The isothermal black lines thus indicate the freezing point of ice for a given mixture. The concentration of each of the three components can thus be read by following a line parallel to the dotted line to the corresponding scale. The concentration at a given point of water is for example found by reading the scale horizontal adjacent of the given point. The red line denotes the

so-called eutectic trough and is a temperature minimum, i.e. the freezing temperature increases again at the other side of the red line and the freezing component changes.

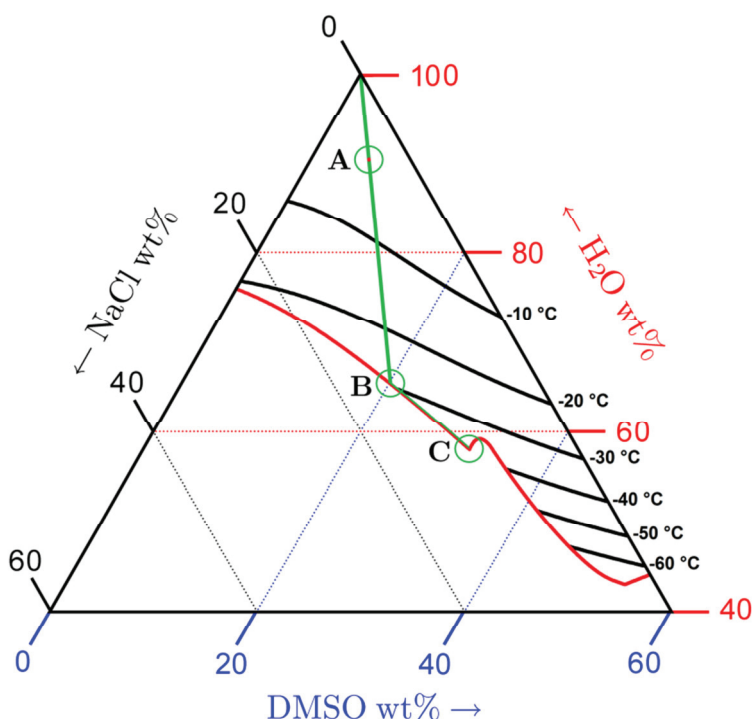


Figure 5.16 Ternary phase diagram of NaCl/H₂O/DMSO describing the liquidus surface between the liquid phase and ice/liquid phase. This phase diagram is generated using the equations found in [158]. This phase diagram shows a 2D-projection of the liquidus surface. The red line describes the eutectic trough at which two phases will crystallize instead of one. The green line describes how a sample moves through the phase diagram upon cooling until the eutectic point at point C is reached. First published in [114].

The Water/NaCl/DMSO phase diagram does not only contain one eutectic point. Three eutectic points has been proposed for this system: One at 13 wt% NaCl, 28 wt% DMSO and -35 °C, one at 11 wt% NaCl, 31 wt% DMSO and -38 °C and one at 3 wt% NaCl, 54 wt% DMSO and -70 °C [158], [159]. The exact positions of these eutectic points have not been established precisely due to the tendency of watery solutions with a high content of DMSO to form a glass before any crystallization takes place. At these eutectic points, both hydrohalite will form as well as DMSO hydrates on the form DMSO·3H₂O.

In order to describe the freezing process in such a phase diagram, the ratio R of a solution is defined as the ratio of mass percentages of DMSO and NaCl:

$$R = \frac{C_{DMSO}}{C_{NaCl}} \quad (5.1)$$

Depending on R and the initial concentration of DMSO, the freezing process can fully be described. It can also be determined how and when hydrohalite will form as well as which of the three eutectic points will be reached.

Consider as an example a solution with an initial composition of $R = 1.2$ at position A in the phase diagram that is cooled beyond the initial freezing point. Since both NaCl and DMSO are not dissolvable in ice, these will be concentrated in the remaining liquid, keeping their ratio R constant during the freezing process. The composition of the remaining liquid will thus follow the line toward position B under growth of the ice crystals upon further cooling as shown by the green line in Figure 5.16.

At point B, the remaining liquid will reach a so-called eutectic trough at which two phases will start to crystallize as opposed to only ice. Depending on R , this can be either hydrohalite or a DMSO-hydrate. In our example and for all solutions with $R < 2.5$, hydrohalite will start to form. Since now both water and hydrohalite are crystallizing, DMSO will concentrate with the result that R is no longer constant but rises as more and more hydrohalite crystallizes. Upon further cooling point C will be reached which is a eutectic point at which the solution can undergo a eutectic crystallization. This is, however, a rare occurrence since the remaining liquid is so viscous at this point that it will rather form a glass. It is exactly this formation of glass in and around a cell that protects during cryopreservation and explains the beneficial effect of DMSO on cryopreserved samples and why it can act as a CPA. This type of protection is similar to many other types of CPAs.

5.4.1 CRM of hydrohalite in a DMSO solution

Figure 5.17 contains a transmission image and a Raman microscopy image of a sample with 4.85 wt% DMSO in concentrated PBS with corresponding to $R = 1.2$ frozen to $-60\text{ }^{\circ}\text{C}$ at a rate of $5\text{ }^{\circ}\text{C}/\text{min}$. By employing a hypertonic solution, broader dendritic channels will be formed along with larger hydrohalite crystals making them easier to image. The initial hypertonic concentration will not affect the path through the phase

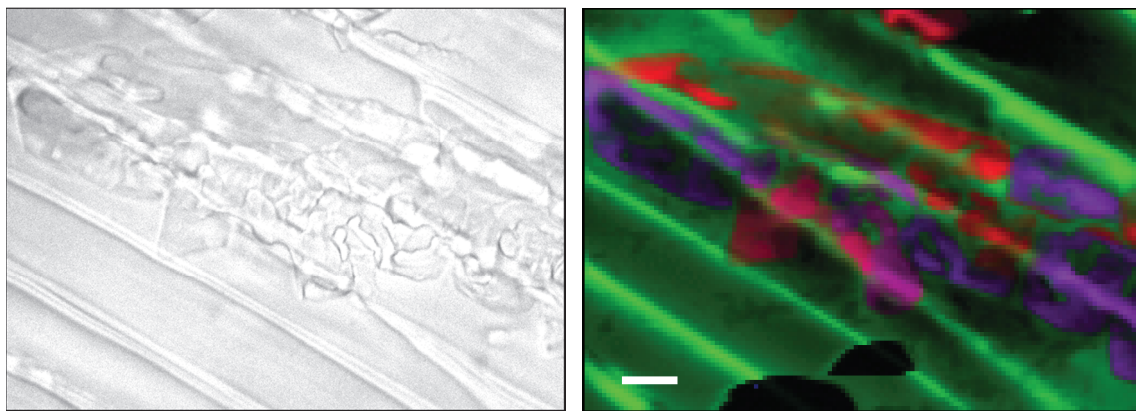


Figure 5.17 Transmission image and CRM of hydrohalite crystal cluster in a solution of 4.85 wt% DMSO in concentrated PBS corresponding to an $R = 1.2$. The sample was cooled to $-60\text{ }^{\circ}\text{C}$ at $5\text{ }^{\circ}\text{C}/\text{min}$. Scale bar is $10\text{ }\mu\text{m}$. First published in [114].

diagram or the end concentration since these are solely governed by R . Dendritic channels are clearly visible in the lower left corner of the transmission image. Structures in the remainder of the image cannot readily be identified, revealing some of the limitations of conventional transmission imaging and the need for additional imaging technology like CRM. By analyzing the spectral band from 2870 cm^{-1} to 2925 cm^{-1} corresponding to the CH-vibration mode and using equation (3.2) a Raman image of DMSO is generated. This is shown as green in Figure 5.17. The two visible hydrohalite bands are likewise imaged by integrating from 3340 cm^{-1} to 3440 cm^{-1} and from 3490 cm^{-1} to 3550 cm^{-1} and overlaying them in Figure 5.17 as blue and red, respectively. The tone of red/purple/blue indicates the orientation of the hydrohalite crystal with respect to the polarization of the incident light. The dark areas in Figure 5.17 can be attributed to ice crystals where neither DMSO nor hydrohalite are present. It should be noted that the black area in the lower left corner of the image arises from an air bubble in the immersion oil at the coverslip surface changing the focus of the objective dramatically and decreasing the collection efficiency.

The resulting multi-channel Raman image shown in Fig 515 can now be analyzed in order to reveal much more detailed information on the sample than the transmission image could provide. The DMSO is seen to be concentrated into long narrow channels. Closer inspection of the Raman spectra of these channels, do not exhibit signs of ice. This would have been expected if a eutectic crystallization has taken place and the sample temperature of $-60\text{ }^{\circ}\text{C}$ is indeed below the first eutectic point. There is furthermore not seen any Raman signal that could originate from a DMSO-hydrate or hydrohalite. It can thus be concluded that the remaining liquid is supercooled due to a very high viscosity and that it is unlikely that any further phase transitions will happen in the remaining liquid.

The Raman image reveals that the structures found in the center of the image are formed from hydrohalite crystals. Here a cluster of hydrohalite crystals has formed and since the color tone of the hydrohalite crystals varies over the image it can be concluded that it is indeed a cluster of separate crystals and not a single contiguous crystal. Clusters like this were found throughout the sample. It is curious that the hydrohalite crystals clump together in this manner, since the probability of the nucleation of a hydrohalite crystal should in principle be equal throughout the remaining liquid. This could either be attributed to regions of the sample with favorable nucleation conditions or one hydrohalite crystal can promote the nucleation of further hydrohalite crystals in close vicinity. As no smaller clusters of hydrohalite crystals corresponding to small regions with favorable nucleation conditions could be imaged, the nucleation promotion through other hydrohalite crystals seems more likely. It can also be seen that the hydrohalite seems to extend between the dendritic channels. This indicates that a thin layer of the remaining liquid exists just below the glass surface of the coverslip, where the hydrohalite can form and propagate. It can be concluded from the CRM image that the hydrohalite has not formed as a result of a eutectic crystallization supporting what was expected based on the phase diagram of

the mixture. A eutectic crystallization would in principle occur simultaneously in all the dendritic channels leading to an evenly distribution of hydrohalite over the entire sample, which clearly is not the case.

This shows that CRM can be used to image samples for cryopreservation also containing DMSO and spatially resolve the relevant structures found.

5.4.2 Temperature-dependence of hydrohalite crystallization

Hydrohalite can also form in a continuous crystallization process in aqueous samples containing DMSO. This process is possible can be visualized by exploiting the fact that freezing and heating are exactly reverse processes in the absence of supercooling. As the heating process is easier to monitor, it will be used to gain a better understanding of hydrohalite crystallization from an aqueous solution also containing DMSO. 4.85 wt% DMSO in concentrated PBS corresponding to $R = 1.2$ is first cooled to $-60\text{ }^{\circ}\text{C}$ at $5\text{ }^{\circ}\text{C}/\text{min}$ and then heated while taking CRM images at regular intervals during the heating process. The sample will follow the same path as described in Figure 5.16 and

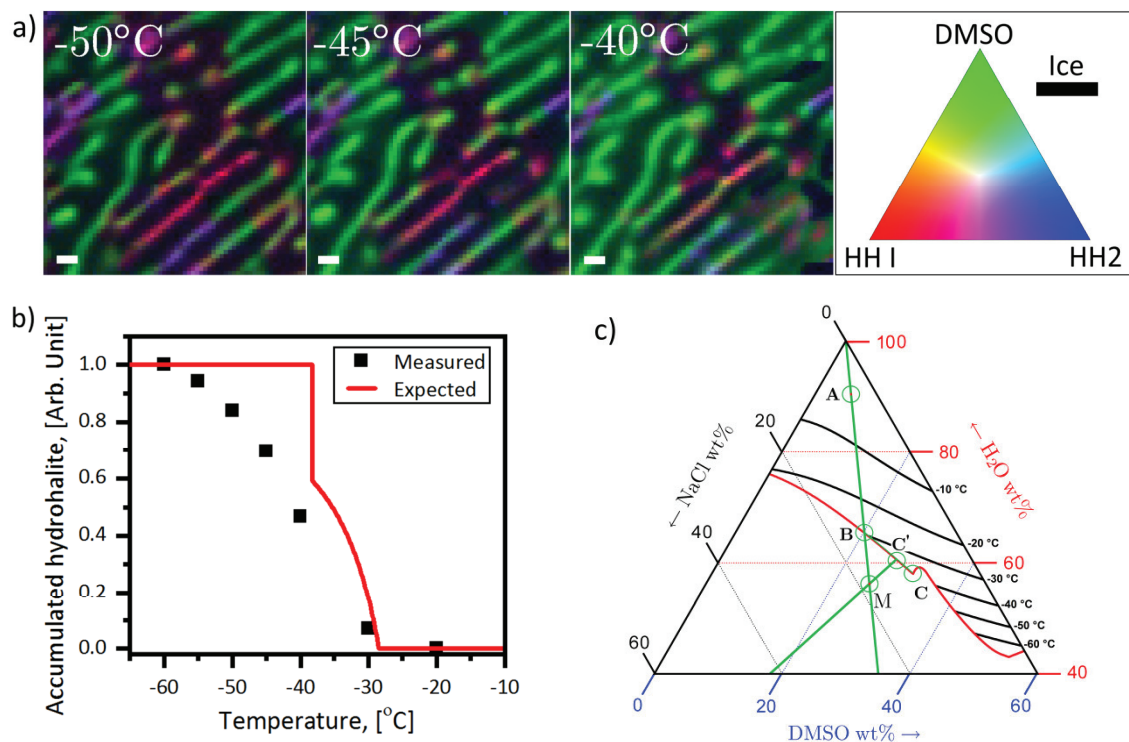


Figure 5.18 a) CRM images of hydrohalite crystals in a solution of 4.85 wt% DMSO in concentrated PBS corresponding to an $R = 1.2$ at $-50\text{ }^{\circ}\text{C}$, $-45\text{ }^{\circ}\text{C}$ and $-40\text{ }^{\circ}\text{C}$. The sample was cooled to $-60\text{ }^{\circ}\text{C}$ at $5\text{ }^{\circ}\text{C}/\text{min}$ and subsequently heated and held at given temperatures where a CRM image was recorded. Scalebar is $10\text{ }\mu\text{m}$. First published in [114]. b) Measured amount of hydrohalite at various temperatures. The predicted shape of the amount of hydrohalite is based on the ternary phase diagram and the lever rule. c) Ternary phase diagram of the NaCl/H₂O/DMSO system containing the points noted used for calculating the quantity of hydrohalite formed during freezing. The line through point C' and M also goes through the point 100 % NaCl which is outside the shown phase diagram.

will thus contain hydrohalite formed continuously as well as eutectically. At regular intervals, the temperature was kept constant in order to record a CRM image. Three of the images are shown in Figure 5.18a taken at -50 °C, -45 °C and -40 °C. Due to the quantity of images, a resolution of 64 x 64 pixels and an integration time of 100 ms per pixel were chosen to keep the recording time manageable. In these images, it can again be seen that the DMSO concentrates in dendritic channels. Also the hydrohalite is located in dendritic channels, but these domains do not contain any DMSO. The hydrohalite gradually melts as the temperature is increased releasing brine into the dendritic channels where it mixes with the highly concentrated DMSO. This remaining liquid then flows into the domains previously occupied by hydrohalite. The hydrohalite does furthermore seem to keep its orientation during the melting process. The melting process has also been visualized in Figure 5.18b, where the hydrohalite signal from entire images has been summarized and plotted against temperature. Here it is seen that the hydrohalite signal decreases significantly until -30 °C is reached and stays stagnant at higher temperatures, indicating that the hydrohalite crystals are completely melted. This corresponds nicely with the phase diagram shown in Figure 5.16, from which a melting point at approximately -30 °C at point B is expected. Since the decrease of hydrohalite happens over a temperature range of approximately 20 °C and thus over hours it can be concluded that the hydrohalite has formed in a continuous process and not through eutectic crystallization since this process can only occur at a specific temperature. Hydrohalite is furthermore only found in specific areas and not distributed throughout the dendritic channel network, which would be the case when a eutectic crystallization has occurred. Any continuous formation of hydrohalite will have a significant impact on the chemical environment surrounding cells in the sample and thus an influence on the success of the cryopreservation process.

Figure 5.18b shows an approximation of the expected amount of hydrohalite as a function of temperature for a sample with R of 1.2 that has been calculated by applying the lever rule twice for the corresponding ternary phase diagram and the initial conditions of the given sample. This method has been outlined for general ternary phase diagrams in [46], [160] and will here be applied to the NaCl/H₂O/DMSO ternary system. To this end the ratio K is defined. Similarly to the definition of R the ratio K can be defined as

$$K = \frac{C_{DMSO}}{C_{H_2O}} \quad (5.2)$$

K remains constant along the line from the point 100 % NaCl, 0 % DMSO & 0 % H₂O through the point M to point C' in the ternary phase diagram shown in Figure 5.18c.

At a given point C' along the eutectic trough, i.e. between point B and C in the phase diagram shown in Figure 5.18c, the fraction of ice f_{ice} and the fraction comprised of

the remaining liquid and hydrohalite $f_{liq\&HH}$ in the sample can be found by applying the lever rule, as described in section 2.1.1, once to get

$$f_{ice} = \frac{C_{NaCl+DMSO,M} - C_{NaCl+DMSO,A}}{C_{NaCl+DMSO,M}} \quad (5.3)$$

$$f_{liq\&HH} = \frac{C_{NaCl+DMSO,A}}{C_{NaCl+DMSO,M}} \quad (5.4)$$

Here $C_{NaCl+DMSO}$ denotes the total amount of NaCl and DMSO, i.e. $C_{NaCl+DMSO} = C_{NaCl} + C_{DMSO}$, with the following subscript (A, M) denoting the position in the ternary phase diagram as defined in Figure 5.18c. The points A and M correspond to the initial sample composition and the intersection of the line defined by R and K , in the ternary phase diagram respectively.

To solve this equation the composition at point M needs to be known. Along with the definition of R and utilizing that the sample only consist of NaCl, H₂O and DMSO

$$R = \frac{C_{DMSO}}{C_{NaCl}} \quad (5.5)$$

$$1 = C_{H_2O} + C_{DMSO} + C_{NaCl} \quad (5.6)$$

Exploiting all of the established equations the sample composition at point M is found to:

$$C_{NaCl,M} = \frac{K}{K \cdot R + K + R} \quad (5.7)$$

$$C_{DMSO,M} = \frac{K \cdot R}{K \cdot R + K + R} \quad (5.8)$$

$$C_{H_2O,M} = \frac{R}{K \cdot R + K + R} \quad (5.9)$$

By applying the lever rule a second time $f_{liq\&HH}$ can be split into a liquid and a hydrohalite part and thereby calculate the fraction of the remaining liquid that has been turned into hydrohalite, f_{HH} :

$$f_{HH} = \frac{C_{DSMO+H_2O,C'} - C_{DSMO+H_2O,M}}{C_{DSMO+H_2O,C'} - \alpha_{H_2O}} \quad (5.10)$$

Here C_{DSMO+H_2O} denotes the total amount of DMSO and H₂O at the positions M and C' in the phase diagram as denoted by the subscripts. The amount of H₂O bound in hydrohalite is denoted α_{H_2O} and calculated from molecular weight to comprise

≈38.1 wt% of hydrohalite. A prediction of the quantity of hydrohalite as a function of temperature can be calculated by determining f_{HH} for all points between *B* and *C* in the phase diagram. A further estimate can be made of the amount of hydrohalite formed through eutectic crystallization by converting the remaining amount of NaCl at point *C* to hydrohalite. The approximation shown in Figure 5.18b has been normalized to coincide with the measured values.

The approximation of the expected hydrohalite does to some extent correspond to the actual findings. Below -30 °C, the amount of hydrohalite increases until the eutectic point is reached at -38.3 °C, where the liquid crystallizes creating hydrohalite crystals instantly. Below the eutectic point, the expected amount of hydrohalite deviates from the expected, since the hydrohalite amount should remain constant, but it instead increases steadily. This deviation can be attributed to the fact that phase diagrams always describe the system in thermodynamic equilibrium. This is most likely not the case in this experiment especially at lower temperatures where the viscosity of the liquid rises significantly inside very narrow dendritic channels. This results in a non-equilibrium supercooled state with respect to the eutectic point and a slow increase in hydrohalite instead of the sudden increase of hydrohalite as expected from the calculation based on the phase diagram. The deviation from the thermodynamic equilibrium seen here can be attributed to the higher supercooling found in small volume samples as previously discussed in section 4.2.2. This result underlines that phase diagrams should only be used with care in cryobiology respecting the limited applicability of equilibrium equations to highly dynamic systems prone to supercooling. Samples containing the common CPA DMSO tend to deviate from a thermodynamic equilibrium at temperatures below the eutectic temperature. Both ice crystallization and eutectic crystallization are random processes and will therefore only occur with a given probability. In order to illustrate this, differential scanning calorimetric measurements were performed on four different samples each repeated three times. This measurement technique can determine phase transitions and was described in section 3.4. Eutectic crystallization was detected in six of the twelve repetitions. Two example DSC curves are shown in Figure 5.19, one with and one without eutectic crystallization. The endothermic peaks upon heating are smaller than the exothermic dips on cooling due to a lower heating rate of 2 °C/min compared to a cooling rate of -10 °C. This will make the endothermic peak appear smaller when plotted against temperature as opposed to time. When plotting against time the peak have the same area. This underlines that eutectic crystallization is a random event that only happen with a given probability according to the experimental parameters.

It would be ideal if hydrohalite could be used as an absolute marker for eutectic crystallization in a retrospective analysis of samples during storage, since this information can be extracted using Raman spectroscopy and will give an indication of the sample quality with respect to cell viability. It has, however, been seen that when DMSO is added to a brine solution, hydrohalite does not only form through eutectic crystallization but also continuously. This relation also holds true for most other CPAs.

Hydrohalite is thus not a universal direct marker for eutectic crystallization, but it should not be disregarded on this basis. During any eutectic process of solutions containing NaCl, hydrohalite will be a product. When no hydrohalite is seen in a sample then it can be concluded that eutectic crystallization has not occurred under the assumption that the performed measurement is representative for the whole sample.

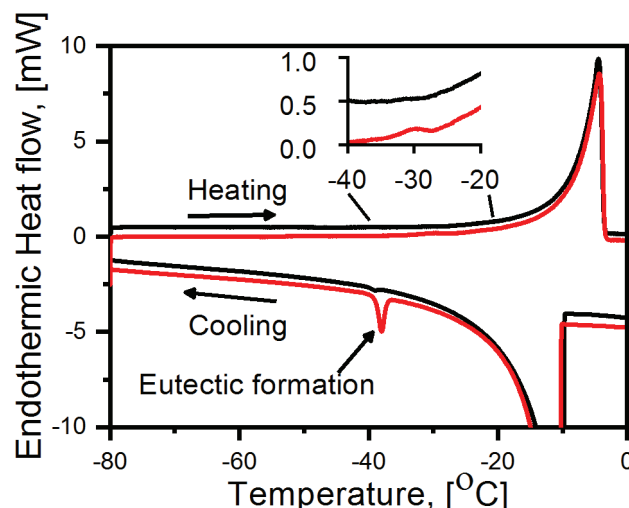


Figure 5.19 DSC-measurement of a sample containing 4.85 wt% DMSO in concentrated PBS corresponding to $R = 1.2$ with a total volume of 5 μL . The cooling rate was $-10\text{ }^{\circ}\text{C}/\text{min}$ and the heating rate was $2\text{ }^{\circ}\text{C}/\text{min}$. Broad peaks between $0\text{ }^{\circ}\text{C}$ and $-30\text{ }^{\circ}\text{C}$ that can be attributed to crystallization (on cooling) and melting (on heating) of ice. A pronounced dip can furthermore be seen for the red trace at $-38\text{ }^{\circ}\text{C}$ during cooling, which can be attributed to eutectic crystallization. First published in [114].

5.4.3 Murine fibroblast cells frozen in PBS with DMSO as CPA

CRM studies have been performed on samples containing murine fibroblasts similar to the ones in section 5.3 but in a medium with the addition of DMSO. A clear difference in results compared to samples without DMSO as presented in section 5.3 where hydrohalite was found in every sample would be expected. Six samples with adherent murine fibroblast cells were cryopreserved in a medium consisting of PBS and 0.5 wt% DMSO corresponding to $R = 0.6$ instead of $R = 1.2$ as in the previous studies. This does however not significantly change the overall path through the ternary phase diagram during the freezing process and a large part of hydrohalite will form over a continuum of temperatures.

The samples were frozen to $-50\text{ }^{\circ}\text{C}$ at $1\text{ }^{\circ}\text{C}/\text{min}$. Hydrohalite is only observed in two of the six samples and one of them only contained a very small limited quantity of hydrohalite. The previous results showed that hydrohalite always form in hypertonic solutions with $R = 1.2$. The main difference between these measurements and the

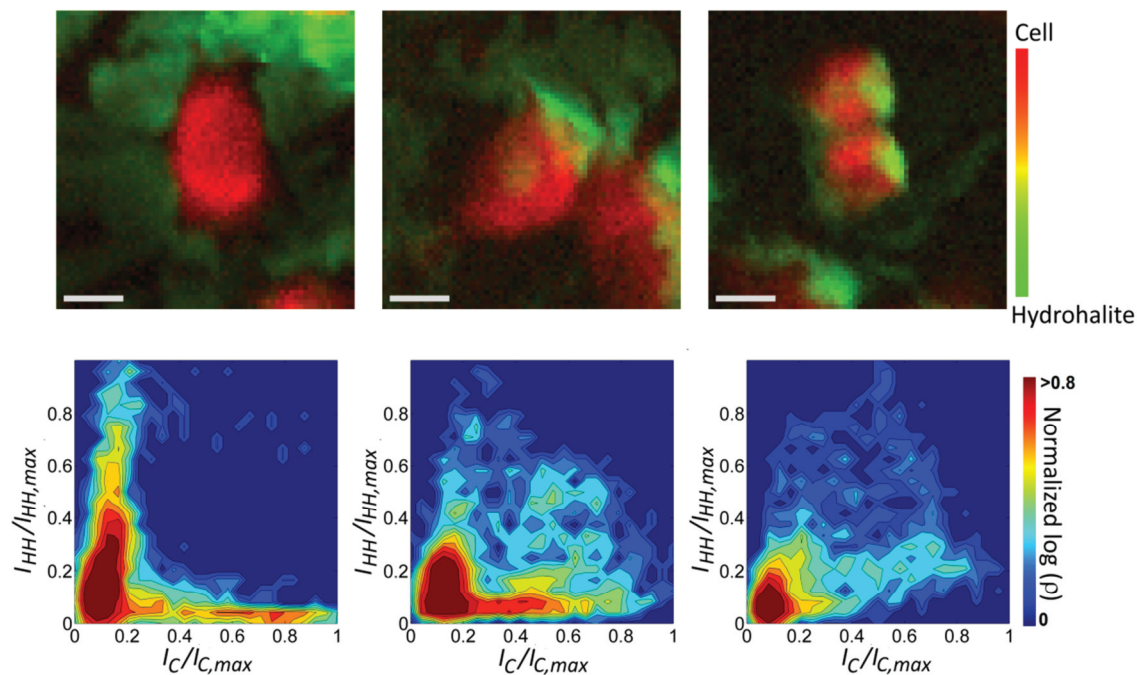


Figure 5.20 CRM images and corresponding colocalization density maps of murine fibroblast cells in a PBS solution with 0.5 wt% DMSO. The images originate from the same sample that was frozen to -50 °C at 1 °C/min. Scale bar is 10 μ m.

ones done on hypertonic solutions is that the dendritic channels are in this case narrower when the eutectic trough is reached and hydrohalite crystallization can commence. Assuming a ratio $R = 0.6$ and employing equation (5.4) the liquid fraction can be found to be composed 4.8 wt% and 23.9 wt% for the isotonic and hypertonic solution, respectively upon reaching the eutectic trough. This cannot directly be translated to dendritic channel width, but it underlines that the amount of liquid phase is much smaller upon reaching the eutectic trough for lower DMSO concentrations. The dendrite arm width is directly correlated with the solidification time and it can thus be speculated that the main factors inhibiting hydrohalite formation in this case are of kinetic nature. In the very narrow dendritic channels, higher viscosity or impeded diffusion could play a major role in preventing hydrohalite formation. The viscosity of the liquid is very dependent on temperature and DMSO content. The temperature and chemical composition of the liquid are, however, comparable for the initial isotonic and hypertonic solutions along the eutectic trough and it is therefore unlikely that the viscosity is the main factor impeding hydrohalite growth. When the dendritic channels are very narrow then the diffusion flux is very limited towards any hydrohalite crystal nuclei. This effect is furthermore enhanced by the high viscosity found in the channels. These kinetic effects slow hydrohalite formation down considerably. If the samples were held at a constant temperature of -50 °C for a long period hydrohalite would be expected to form. It is however not possible to tell how much time would be needed for this to happen. This could be days or even longer and has therefore not been experimentally tested.

Figure 5.20 shows three CRM images and their corresponding colocalization density maps recorded for the sample containing a significant amount of hydrohalite crystals. In these images, $I_{Cell,AmideI}$ has been used to image the cells instead of $I_{Cell,CH}$, as this signal could not be distinguished from the Raman signal of the CH-bonds in. The first image clearly shows extracellular hydrohalite with no spatial overlap between cellular matter and hydrohalite. The two other images show an extracellular hydrohalite shell. None of the images in Figure 5.20 or the additional ones taken but not depicted here showed any intracellular hydrohalite or ice. This could in general be due to the physical and chemical conditions found in the cells are inhibiting hydrohalite formation. Through the addition of DMSO to the sample, hydrohalite will only form at lower temperatures as compared to pure brine. This means that the cell will dehydrate more up until the point where hydrohalite can form. Supercooling is not expected to have any different influence on intracellular hydrohalite formation as ice can start to form at $-0.7\text{ }^{\circ}\text{C}$ and $-0.5\text{ }^{\circ}\text{C}$ with and without 0.5 wt% DMSO, respectively and similar levels of supercooling are expected. It is not possible to conclude that hydrohalite formation is an exclusively extracellular phenomenon in samples containing DMSO based on these results. This will require a larger data set and in particular CRM images where hydrohalite are present. The data set however clearly show how the presence of DMSO decreases the probability of hydrohalite formation and thereby providing protection to the cryopreserved cells.

5.4.4 IPS cell colonies

A common concentration of DMSO in cryopreservation protocols is around 10 % [22]. CRM studies have therefore been performed on IPS cell colonies in PBS with 10 % DMSO (11 wt%), in order to investigate the storage state of such a system. The lower DMSO concentration for the murine fibroblasts was chosen in order increase the probability of hydrohalite crystallization. The eutectic temperature of the current solution is approximately $-70\text{ }^{\circ}\text{C}$. The CRM images are recorded at $-80\text{ }^{\circ}\text{C}$ clearly below the eutectic temperature and to ensure that no further chemical processes occur within the timeframe of the experiment.

Here, seven samples were frozen to $-80\text{ }^{\circ}\text{C}$ at $1\text{ }^{\circ}\text{C}/\text{min}$ and 26 CRM images were recorded. Two examples are shown in Figure 5.21 including a transmission image and CRM images of DMSO and cellular material. The DMSO signal shows a strong spatial overlap with both cellular material and dendritic channels. The IPS cells are thus filled with DMSO, which is expected since DMSO is a membrane-penetrating chemical compound. The magnitude of the DMSO signal appears to be comparably strong inside cells and in the dendritic channels.

A clear indicator that a glassy storage state has been reached and that the sample is not in a thermodynamic equilibrium is that hydrohalite was not detected in any of the measurements. It is well-known that aqueous solutions with a high concentration of DMSO tend to form a glass upon cooling due to a drastic increase in viscosity. This means the liquid phase becomes so viscous that no further ice crystallization can take

place both inside as well as outside the cells and a phase diagram can no longer describe the state of the sample. The storage state of a cell is therefore a glassy state where no chemical, physical or metabolic processes can occur and it can be reached by two very different cryopreservation approaches: slow freezing and vitrification of samples. The main difference between the two approaches is the way in which the glassy state is achieved. In slowly frozen samples, ice concentrates CPA up to a point where it is so viscous that it can be described as a glass. In vitrification, the solution is frozen fast enough so that ice cannot crystallize before a glassy phase is reached.

With the initial composition of 11 wt% DMSO and 0.9 wt% NaCl it is estimated that around 60 % of all hydrohalite found would have formed due to eutectic crystallization. This is based on similar calculations as in section 5.4.2. The onset of hydrohalite formation is calculated to be -69.1°C just above the eutectic crystallization temperature. This means that the sample has left the thermodynamic equilibrium before this temperature has been reached. This means that that no eutectic crystallization has occurred in the samples.

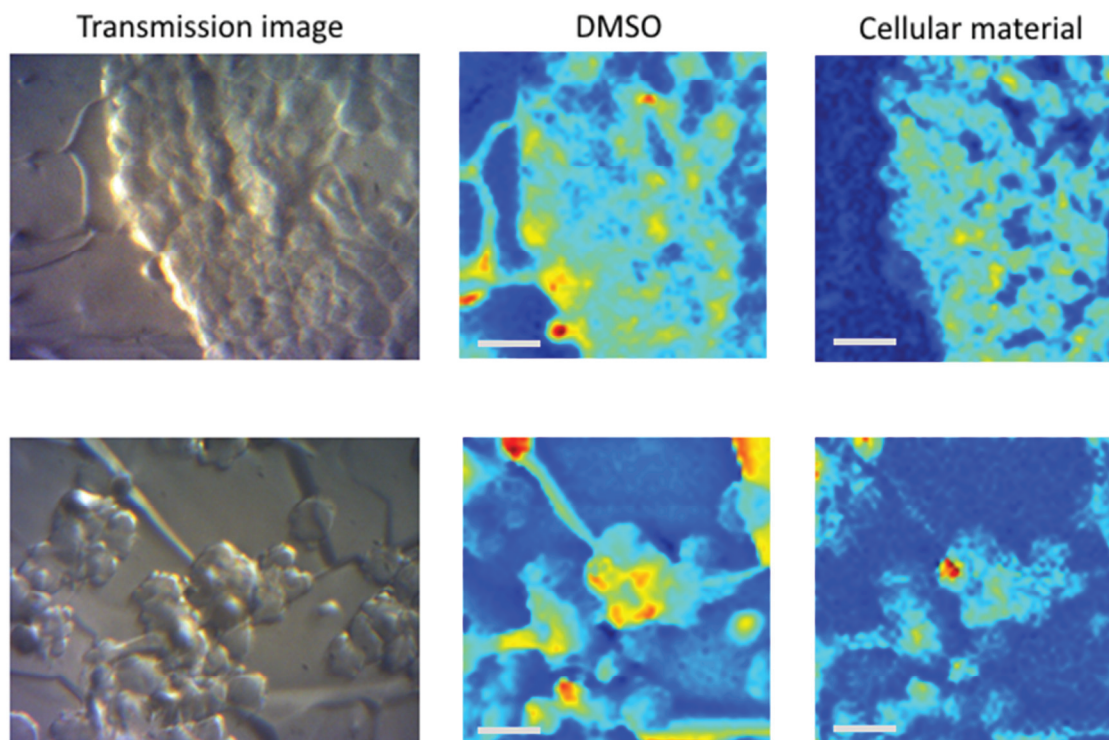


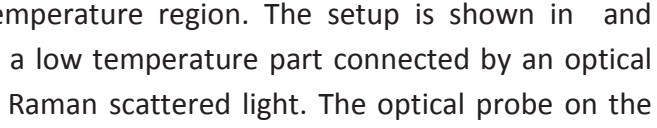
Figure 5.21 Transmission image and CRM images of DMSO and cellular material of two samples containing IPS cell colonies in a PBS solution with 11 wt% DMSO (10 % DMSO). The samples were frozen to -80°C at $1^{\circ}\text{C}/\text{min}$. DMSO was found both in dendritic channels and cells. No hydrohalite was observed. Scale bar is $20\text{ }\mu\text{m}$.

5.5 Fiber based Raman spectroscopy of cryopreserved samples

It is not possible to deploy the previously described Raman laser scanning microscope, see section 3.3.2, in an environment that allow for measurements on samples during storage due to both the delicate nature of the microscope but also due to the topology of samples in storage, since the CRM setup is optimized for flat surfaces with a good optical access. This led to the development of a fiber based Raman spectroscopy probe in collaboration with Askion GmbH. The aim of this collaboration was to develop an optical sensor technology that can extract Raman spectra of stored samples in a cryo-workbench such as the Askion C-line workbenches. A cryo-workbench is a workbench that allows for manipulation and freezing of cryopreserved samples in a dry cryogenic environment so that the cold-chain is maintained. These Raman spectra can be used in a retrospective analysis of cryopreserved samples to retrieve chemical information already during storage instead of a post thaw analysis. The spectra extracted can then be used in a retrospective analysis based on the knowledge established in the preceding sections. First a detailed description of the setup will be given and followed by a presentation several Raman spectra as a proof of concept while underlining the advantages and challenges in designing such a setup.

5.5.1 Experimental Raman probe setup

One of the requirements for this setup was that the Raman spectra generated represent an average of the whole sample and the focal volume of the setup should therefore be relatively large. The setup should furthermore reduce the amount of delicate instrumentation that is required to be present in the same cold environment as the sample in order to minimize technical issues arising from thermally induced mechanical stress. This led to the choice of a single-fiber design where the laser excitation and signal collection pass through the same fiber between the low temperature and room temperature region. Finally, the setup should be designed for the analysis of samples in commonly used cryotubes with a diameter of 10 mm and a container wall thickness of 1 mm.

The setup is similar to the fluorescence and Raman microscopes described in this chapter but has some significant particularities due to the inclusion of optical components and fibers in a low temperature region. The setup is shown in  and consists of a room temperature and a low temperature part connected by an optical fiber transferring the excitation and Raman scattered light. The optical probe on the low temperature part was kept relatively simple in order to minimize technical issues due to thermal induced mechanical stress and designed in such a manner that it can be deployed in several different environments such as a liquid nitrogen dewar or a cryo-workbench. A solid state 561 nm laser (Oxxius Slim) with a power of 140 mW was used as the excitation light source. The excitation light was led over a beam expander and laser clean-up filter (Semrock LL02-561-25). A dichroic mirror (Semrock Di02-R561-

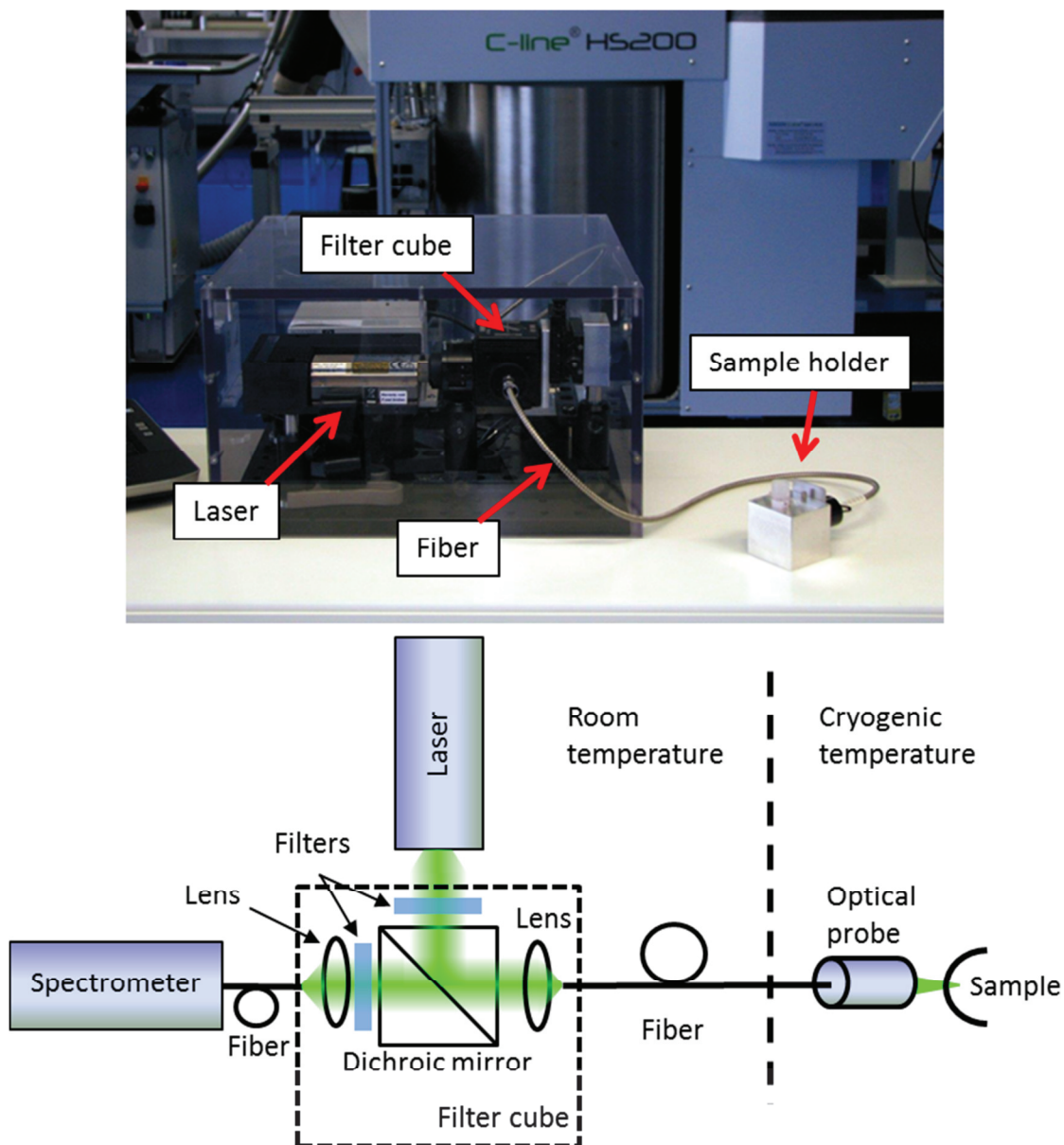


Figure 5.22 Image and sketch of the fiber based Raman spectroscopy setup.

25x36) directs the excitation light to a lens that couples the light into a multimode optical fiber (Leoni AFS600) with a core diameter of 600 μm . The optical fiber acts as the optical connection between the room temperature part of the setup and the low temperature part. The optical fiber was connected to a probe that was developed for this study. The probe consists of a small metal cylinder containing three lenses where the optical fiber can be attached. The three lenses are designed to collimate and focus the light exiting the fiber and correct for aberrations, respectively. The aberration correction using a toric lens is required since the sample surface is curved and therefore acts as a lens in itself. This specific design of the probe ensures the highest possible focal volume quality. The probe also acts as a detection path and collects the Raman scattered light and couples it into the optical fiber. Since the Raman scattered light has a longer wavelength than the excitation light, it can pass through the dichroic

mirror and a detection filter (Razoredge F76-561 – Semrock LP561RS) that further filters out any light from the laser as well as stray light. The light is then coupled into another multimode optical fiber (Thorlabs) with a core diameter of 1000 μm . This optical fiber leads the collected light to a spectrometer (Ocean Optics – USB 2000) that records the Raman signal. Two sample holders were developed for the use in the fiber based Raman setup, one with a fixed position for the use in a cryo-workbench and one where the focus can be scanned over the sample positioned in a dewar using manual translation stages. The sample holder designed for cryo-workbench use is shown in Figure 5.22.

5.5.2 Fiber-based Raman cryospectroscopy

The fiber-based Raman spectroscopy is now applied to samples contained in cryotubes that are typically used for storage in biobanks. As a reference the signal from an empty tube is also measured. The samples were frozen in the vapor phase of liquid nitrogen in a dewar close to the liquid nitrogen surface. This mimics a slow freezing protocol, albeit not with a perfectly controlled cooling rate. This is sufficient as the first measurements should serve as a proof of concept. Figure 5.23 shows the Raman spectra of a cryotube containing 10 % DMSO in H₂O and an empty cryotube for comparison. When subtracting the signal of the empty cryotube from the sample spectrum as shown on the right in the features in the spectrum can be identified as this removes the other features found the recorded spectra.

In the 10 % DMSO sample, the OH-stretching band between 3000 cm^{-1} and 3400 cm^{-1} and the pronounced peak signifying ice around 3100 cm^{-1} can be seen. This method thus can be used to detect ice in frozen samples which is an important marker for vitrified samples since this indicates that the sample has undergone devitrification. The formation of ice is detrimental for vitrified samples and will be investigated in detail in section 6.3. This is an example of how chemical information can be extracted and used to investigate the history of a sample retrospectively.

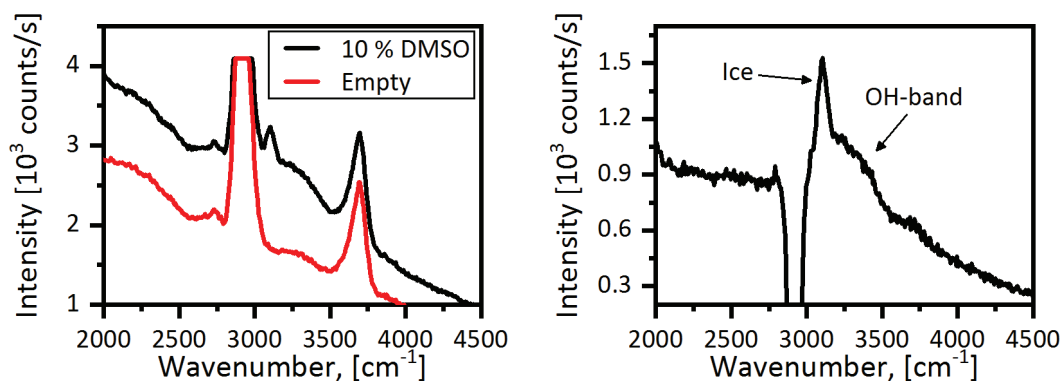


Figure 5.23 Raman spectra of an empty cryotube and a cryotube containing 10 % DMSO in H₂O. When subtracting the two spectra from each other the Raman spectrum of ice is clearly visible.

The two presented spectra however also show some of the issues when designing this type of sensor technology for the use in biobanks. First of all there are two pronounced Raman peaks around 2900 cm^{-1} and 3700 cm^{-1} in the spectra not related to the sample. The two peaks have rather different origins. The peak at 2900 cm^{-1} originates from the CH molecule bonds in Polyethylene of the sample container wall. When the excitation light crosses the container wall, Raman scattered light from the CH bonds will be collected by the optical probe and get mixed with the signal from the sample. This signal is so strong that the spectrometer was saturated in this region for the chosen integration time. A longer integration time was chosen in order to maximize the signal from the sample. This Raman peak completely overlaps the signal from DMSO and biological material in the sample used in the previous studies. If these components are to be investigated with this technology it is required to take other vibration modes into consideration. This is, however, not a trivial matter since these are significantly weaker and can easily drown in the background signal. This issue can in principle be resolved by changing the cryotube material to glass that has a very low Raman response. On a large scale this is very impractical due to the higher cost and lower mechanical stability of glass containers. An alternative could be to use cryotubes with a thinner container wall in order to minimize the Raman signal. Further investigations could also be made into the Raman response of various types of cryotubes to find the most ideal sample container with respect to a retrospective analysis using Raman spectroscopy. The second Raman peak at 3700 cm^{-1} originates from OH in the optical fiber [161]–[163] connecting the warm and cold part of the setup. Since a single fiber is used for both excitation and detection signal the Raman response of the fiber gets mixed with the Raman signal from the sample. A residue of OH molecules remains in the optical fibers during production. Special fibers have a lower amount of OH residue but even though these were used for all fiber-based measurements in this work the Raman peak is still visible. Due to sufficient spectral separation it does not overlap any relevant Raman information from the sample. There is furthermore Raman peaks around 800 cm^{-1} and 500 cm^{-1} , not visible in the spectra shown in Figure 5.23 originating from fused silica in the optical fiber [164]. The Raman peak at 500 cm^{-1} is the most intense and problematic. When analyzing the fingerprint region below 2300 cm^{-1} of the Raman spectra is of importance. This response from the optical fiber might overlap with some of the features limiting the application range of the technology. The fingerprint region below 2300 cm^{-1} is especially important when conducting a phenomenological retrospective analysis of cryopreserved samples as shown in section 5.1. This region contains the most complex vibrational modes and changes over time signify chemical or biological changes of the sample whereas changes in the stretching mode region rather indicate changes in the chemico-physical state of the sample. All of these cannot be observed when Raman scattering of the optical fiber is present in the recoded spectra.

The first and most practical solution is to shorten the optical fiber as much as possible, since this will reduce the absolute amount of Raman scattered light generated. This

will not completely remove Raman scattered light from the optical fiber but can reduce it to a bearable amount. The fiber should still be long enough so that measurements are practically viable in the various environments. This can easily be implemented and has also been used in all of the fiber-based measurements in this work. Another solution would be to use separate fibers for the excitation light and detected signal. The Raman scatter arises as the relatively high power of the excitation laser without significant contributions from the relatively weak detection signal. Using a two-fiber design requires much more complex optics on the cold side of the experiment including optical filters that are not designed to be cooled to the temperatures required. This means that equipment could be destroyed or suffers changes in their otherwise well-defined optical characteristics to such a degree that repeatable measurements are not possible.

The Raman spectra are also influenced by autofluorescence in the optical fiber. This fluorescence was highest close to the laser excitation wavelength. Fluorescence is a much stronger process compared to Raman scattering as discussed in section 3.3.2.1. Autofluorescence of the fiber superimposes the fingerprint region of a recorded Raman spectrum and is an important challenge to solve in order to expand the usable range of this sensor technology. To mitigate this problem investigations of various fibers were conducted to identify the fibers with the lowest fluorescence but a truly fluorescence-free fiber does not exist. A fiber with low OH content and a large core diameter was chosen and it was furthermore ensured that the coupling of the excitation light into the fiber was as good as possible so that fluorescence from the fiber cladding was eliminated.

Fluorescence could be reduced by to using an excitation light source with a longer wavelength. Fluorescence is dependent on the excitation wavelength and a longer wavelength will reduce or even remove fluorescence from the optical fiber. Using excitation light with a higher wavelength will shift the Raman scattered light to even longer wavelengths. The frequency difference dependence of Raman scattering mean that a wavelength shift of the excitation light causes an even larger shift of Raman scattering in the wavelength space. This is both an advantage and a disadvantage. This shifts the Raman scattered light further away from the fluorescence light and should therefore be easier to detect. The detection efficiency of silicon-based spectrometers does however drop with increasing wavelength and is not possible above 1100 nm [165]. This could be resolved by employing GaAs based spectrometers, but their significantly higher costs are a clear disadvantage for widespread use in biobanks. A tradeoff between fluorescence and detection efficiency should therefore be made when choosing the excitation light source.

Despite its limited applicability to the fingerprint region this sensor technology is very promising in that it provides information that has been inaccessible up until now from stored samples. Figure 5.24 show two Raman spectra obtained with this technology. Samples with 50 % DMSO and 20 % NaCl are frozen in the vapor phase of liquid nitrogen right above the liquid surface. In the DMSO sample, the Raman response from

the DMSO at around 3000 cm^{-1} can be identified as the characteristic double peak even though a high CH-band signal from the container wall superimposes the spectrum. It can furthermore be concluded that the sample has vitrified and not undergone devitrification since the characteristic ice peak at 3100 cm^{-1} is absent in the OH-stretching part of the Raman spectrum. For the 20 % NaCl solution the ice peak is present as expected. A hydrohalite peak is furthermore clearly visible in the Raman spectrum at 3400 cm^{-1} and it can thus be concluded that eutectic crystallization has occurred in this sample.

These are two examples of how Raman spectroscopy can be used to retrospectively analyze the history of given cryopreserved samples. Here, specific markers have first been identified in model experiments using the CRM technique for the analysis of samples under storage conditions using the fiber based Raman spectroscopy sensor technology. This serves as a proof of concept for retrospective analysis. It also demonstrates that more information can be extracted from stored samples in order to ensure an ongoing high quality of the cryopreservation storage performed by biobanks. This technology can also be applied in a phenomenological manner where Raman spectra are recorded in regular intervals. Any changes detected when comparing spectra taken at different times of the storage period indicate that relaxation processes are still present and could impair the quality of the sample.

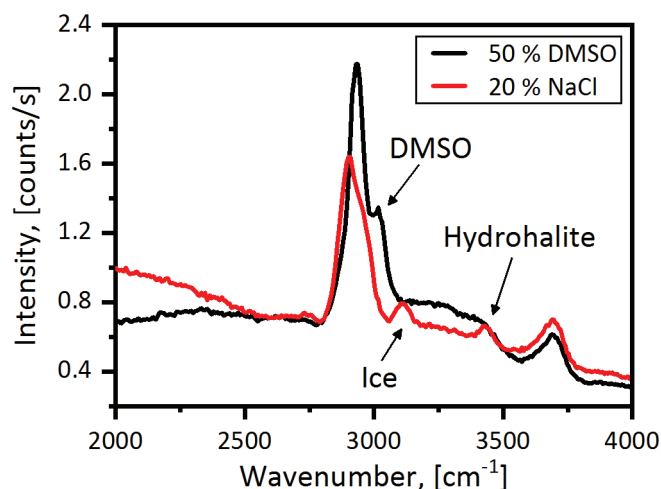


Figure 5.24 Raman spectra of two samples containing 50 % DMSO or 20 % NaCl dissolved in H₂O. The DMSO sample is seen to be vitrified due to the absence of ice. An eutectic crystallization has occurred in the 20 % NaCl sample signified by the hydrohalite peak.

5.6 Raman spectroscopy in retrospective analysis

The application of confocal Raman microscopy (CRM) in cryobiology has been demonstrated in this chapter. It has been shown how CRM can be used to image

frozen cell culture samples. These microscopy images reveal detailed information on the distribution and concentration of various chemical constituents of the sample on a microscopic scale. Also crystal size and distribution can be studied with CRM with the help of related chemical compounds. CRM has been used to investigate the formation and distribution of hydrohalite crystals in cryopreserved samples. It has been shown that hydrohalite can act as a marker for eutectic crystallization, which has been shown to reduce to significantly reduce the cryopreservation success in vital cell biobanking [52]. Intracellular hydrohalite formation was directly proven and on the basis of this study it can be concluded that also intracellular eutectic crystallization appeared. This direct proof contributed to the understanding of the lethal mechanisms of eutectic crystallization.

This work focused on the stretching mode region in the high frequency end of the Raman spectrum. This region primarily represents the structural information of the sample where different compounds directly related to the phase composition of the sample can be distinguished. This includes glassy water, ice, CPA or hydrohalite. Detrimental effects derived from a retrospective analysis based on the stretching mode region are therefore related to unwanted crystalline structures in the sample. Relevant chemical markers identified here are hydrohalite for eutectic crystallization in slowly frozen samples and ice for devitrification of vitrified samples.

Further studies should also consider the low frequency region of the Raman spectrum also called the fingerprint region. This region contains information on more complex molecules that can directly be related to specific biological compounds and the biofunctionality of the stored cells. In this manner, the biological state of the sample could be extracted and analyzed already during storage. Such analysis could for example reveal information on CPA cytotoxicity [85], [86] or stem cell differentiation [87].

Raman scattering is a very promising physical effect for the use in retrospective analysis as it allows the identification of various chemical compounds in a non-contact mode with diffraction limited spatial resolution. It is also particularly suited for an analytical approach to retrospective analysis since specific chemical compounds often give direct information on specific events that have taken place in the sample. However, it is not possible to employ CRM on cryopreserved samples due to restrictions imposed by typical sample containers. For practical use in biobanking, simpler Raman spectroscopy methods such as the fiber-based method presented in section 5.5 are better suited than CRM. This method allow for as a meaningful application of retrospective analysis in biobanking since analyzing Raman spectra from samples in storage is possible with this technology. The fiber-based Raman spectroscopy setup shown in section 5.5 acts as a proof of concept in this regard. It is optimized for a specific common container type, but could just as well be optimized for other sample container geometries.

In order to exploit Raman scattering for retrospective analysis purposes in biobanking, model systems should first be studied using CRM and this knowledge can then be exploited to measure cryopreserved samples in storage with one-shot spectroscopy measurements.

For the use in retrospective analysis, a Raman spectrum should represent the entire sample in order to acquire comprehensive data. This, however, has the disadvantage that intracellular ice crystals cannot be distinguished from extracellular ice crystals meaning that one of the most prevalent mechanisms for cryoinjuries related to sample structure cannot be identified. Such a distinction would only be possible with a microscopic investigation of the ice crystal distribution. This shows one of the limits related to simple one-shot measurements where only average values can be extracted and detailed spatially resolved information is not available.

Although the strength of Raman spectroscopy lies in the analytical approach to retrospective analysis, it can also be employed in a phenomenological manner. Phenomenological retrospective analysis allows confirming whether the freezing procedure was successful according to the markers identified in a preceding analytical study of this sample type. Alternatively, a Raman spectrum is recorded upon reaching the storage temperature and in regular intervals thereafter. Changes in Raman spectra from a sample over time indicate that chemical or biological processes are taking place. If this is the case, then the sample is not stable and the integrity of the sample is at risk. The exact changes in the Raman spectra could possibly reveal what processes are occurring in the sample. Further analysis might reveal the exact type of processes and changes that are taking place in the sample. This would, however, require a detailed understanding not only of the sample constituents and how they are represented in a Raman spectrum but also how processes influence the constituents and their manifestation in the spectrum.

The present study focused on cell culture samples but can in principle be extended to other sample types such as blood plasma or urine. This would require the identification of another set of markers for retrospective analysis that can describe typical degradation processes in these sample types. The application of Raman spectroscopy on cryopreserved samples containing complex pieces of biological material such as tissue samples or seeds can, however, be more challenging. Such samples are significantly larger than focal volumes practically possible for a Raman spectroscopy setup. It would thus be required to record many spectra in order to obtain representative data. It should however still be kept in mind that such samples are very heterogeneous and Raman spectroscopy is therefore not necessarily a viable option.

6 STRUCTURAL KINETICS AT ELEVATED TEMPERATURES

6.1 Introduction

The core idea of a cryopreservation process is to halt relaxation processes both physico-chemical, such as ice crystallization, recrystallization and chemical changes, as well as biological, such as metabolism and stem cell differentiation. This is achieved by cooling samples below their glass transition temperature, T_g . The glass transition depends on the composition and history of the sample, especially the cooling and heating rate employed in its preservation and measurement [83] and is typically measured to be approximately -130 °C for aqueous samples. Below this temperature the sample is considered stable. Above this temperature the sample is instead only metastable or even unstable depending on the time spent at the given temperature and the chemical composition of the sample [58]. These regions in the stability diagram are depicted in Figure 6.1a. This plays an important role for the understanding of the vitrification process of cryopreserved samples, since the samples must pass through the metastable region fast enough to avoid any ice crystallization.

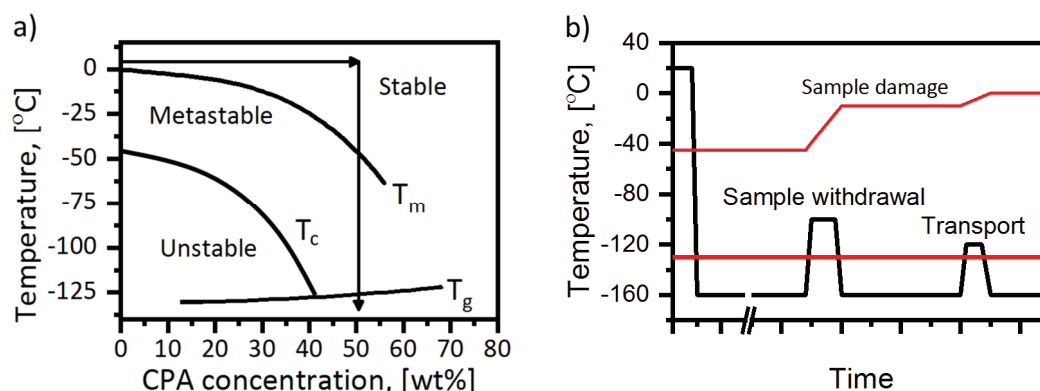


Figure 6.1 a) Path through a stability diagram for a typical vitrification process. The sample is passing through a metastable region where ice can possibly start to crystallize, which will reduce the viability of cells in the sample. Inspired by [58]. b) If a sample is heated above the glass transition temperature devitrification can start to occur. Here, sample transport and withdrawal of a neighboring sample are possible causes. The damage to the sample is irreversible and will accumulate throughout its lifetime.

Samples are typically stored in the vapor phase above a liquid nitrogen reservoir. The temperature in this gas phase is not as well defined as in liquid nitrogen, making it difficult to monitor and control the sample temperature at all times during storage. In a biobank, the temperature of a sample may experience unwanted fluctuations during storage. This can happen accidentally through power or LN2 shortages, but also through handling of the samples, for instance when a neighboring sample is being extracted, when the sample is being transported or when the sample is being handled in a cryo-workbench where the temperature often is in the range of -100 °C to -130 °C. Figure 6.1b illustrates an example of a cryopreserved sample that is accidentally heated due to the retrieval of a neighboring sample and sample transport. As the sample temperature is not monitored at all time it is currently not possible to determine if a sample has experienced temperature elevations during storage or the magnitude and period of such incidents.

Such temperature elevation can have a detrimental impact on the sample quality. Germann et. al. [166] have for instance shown that repeated temperature elevation causes reduced cell viability, recovery and immune response in slowly frozen stored T-cells, compared to samples without temperature elevations. It is furthermore well established that ice crystallization in vitrified samples, called devitrification, has a significant impact on sample quality [76]. This will only happen if the sample is exposed to temperatures above the glass transition temperature and maintaining a cold-chain below -130 °C is therefore paramount to a high sample quality in biobanking. Despite being a focus area of biobanks it is not always possible to keep such a cold chain. In addition, some samples are stored at -80 °C only, which will slow down relaxation processes in the sample drastically, but never stop them completely.

How a sample responds to a temperature elevation depends on the cryopreservation approach chosen; slowly frozen or vitrified and can start to arise above the glass transition temperature in both cases. In slowly frozen samples, ice recrystallization is prominent whereas devitrification is the dominant mechanism impairing the quality of vitrified samples. The rate of a given effect is very dependent on temperature and might therefore be too slow to be observed directly, but has to be investigated over months or even years. It is further unknown what has happened to samples stored for decades. All kinetic effects are, however, accumulative and irreversible, meaning that it is not possible to recover a ruined sample and multiple short exposures to high temperatures can have a similarly detrimental effect on sample quality as a longer exposure or higher temperature.

In this chapter first the kinetics of recrystallization of ice crystals in slowly frozen samples consisting of 10 % DMSO in H₂O will be investigated using fluorescence microscopy. Thereafter the devitrification of vitrified samples will be studied on four different CPA solutions in varying concentration using isothermal differential scanning calorimetry (DSC).

6.2 Structural dynamics in slowly frozen media

When a sample is slowly frozen, ice will form during the freezing process. Usually many smaller ice crystals will form depending on supercooling and crystal growth rate compared to the cooling rate. Higher cooling rates will produce smaller ice crystals. When the sample is subsequently elevated to higher temperatures, large ice crystal will grow at the expense of smaller crystals, as depicted in Figure 6.2.

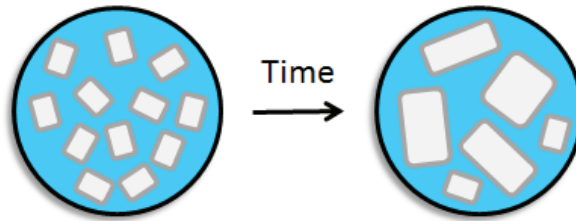


Figure 6.2 During recrystallization, large ice crystals grow due to a mass transfer from small ice crystals. This process occurs to minimize the overall total surface energy in the system.

Recrystallization happens in order to minimize the surface energy of the ice crystals bringing the system closer to an equilibrium state without changing the macroscopic phase composition, i.e. the overall amount of ice in a sample remains constant but only the ice crystal morphology changes due to recrystallization. The Kelvin effect also plays a role in recrystallization as mentioned in section 2.2.3 and describes the effect that the size of an ice crystal has on the ice freezing point [84]. Small crystals have a higher surface to volume ratio causing a depression of the freezing point compared to large crystals. This means that smaller ice crystals, sharp edges or narrow parts of ice crystals melt faster than larger rounded crystals at a given temperature. Multiple temperature elevation for extended periods of time will eventually result in a mass transfer towards the larger crystals. Recrystallization has been shown to be the cause of cell blackening during thawing of cryopreserved oocytes [31], [167]. Blackening of cells is commonly used as an indicator for intracellular ice crystallization and has a negative effect on cell viability. Recrystallization is thus seen as a major threat to cells during the thawing of the cryopreservation process [34], [168].

There are three types of recrystallization: Isomass, migratory and accretive recrystallization [84]. Isomass recrystallization only changes the geometry of a single crystal toward a more spherical geometry through mass transfer from one part of the crystal to another and thereby minimizing the surface energy. Migratory recrystallization describes the mass transfer from one ice crystal to another one minimizing the overall free energy of the system. Finally, accretive recrystallization describes the process where two crystals merge and form a larger crystal with corresponding lower surface energy.

In the following the recrystallization of slowly frozen samples consisting of 10 % DMSO in H₂O will be studied at different temperatures. A fluorescence microscope is used in order to image the dendritic channels and ice crystals in the samples. Fluorescence images are recorded at regular and relevant intervals in order to record changes in the ice crystal morphology. The mean diameter of the ice crystals present in the sample is a parameter that describes the recrystallization process well, since large ice crystals grow at the expense of smaller ones, thereby increasing the overall average ice crystal diameter. The mean ice crystal diameter takes into account both migratory and accretive recrystallization into account. It does, however, not consider isomass recrystallization that would require a study of isolated ice crystals. Since the ice crystals are very closely packed in the sample it can be safely assumed that the other two types of recrystallization will dominate.

A recrystallization model has been proposed for fructose solutions [84], [169] and aqueous solutions with anti-freeze glycoproteins [170]. This model only considers recrystallization of distant ice crystals not in direct contact with each other. The typical structure of cryopreserved samples with narrow dendritic channels cannot fully be described with the help of this model that ignores limitations of crystal growth. It is well known from metallurgy that the driving force behind recrystallization declines as the grain sizes increases approaching a limit size [171]. For the samples studied in this work, this is due to an inhibitory effect of the remaining liquid in the dendritic channels. A more suitable model, denoted recrystallization curvature model in the following, relates ice crystal growth to the ice crystal curvature [172]:

$$\frac{dD_{mean}(t)}{dt} = k \left(\frac{1}{D_{mean}(t)} - \frac{1}{D_1} \right) \quad (6.1)$$

Here, $D_{mean}(t)$ is the average diameter of ice crystals in the sample undergoing recrystallization, k is the kinetic recrystallization constant and D_1 is the maximum diameter achievable through recrystallization. This equation cannot be solved analytically for $D_{mean}(t)$. A regular regression can thus not be used to find the characteristic parameters for the given system. The differential equation is instead solved numerically in Matlab. This is done by inserting a set of parameters (k, D_1) and initial condition $D_{mean}(0)$ into the differential equation (6.1) and calculating $D_{mean}(t + \delta t)$ from $D_{mean}(t)$ and $D'_{mean}(t)$ for the entire measurement duration. The parameters k and D_1 are then varied in order to minimize the summed square of residuals SSE:

$$SSE = \sum (D_{model} - D_{data})^2 \quad (6.2)$$

From this a coefficient of determination, R^2 , can be calculated that describes how well the model fit the data.

$$R^2 = 1 - \frac{SSE}{SStot} = 1 - \frac{\sum (D_{model} - D_{data})^2}{\sum (D_{model} - D_{mean}(t))^2} \quad (6.3)$$

This provides the kinetic recrystallization constant and the maximum diameter for the investigated sample at the given temperature. The initial condition is given from the average ice crystal diameter in the first measurement of a measurement series.

The ice crystals in the slowly frozen samples are, however, not spherical but rather irregular elongated shaped. The resulting deviation from the model can be estimated based on the circularity C of a given area [173]:

$$C = \frac{4\pi A}{P^2} \quad (6.4)$$

Here, A and P are the area and perimeter of a given area. The circularity is a parameter between zero and one where a circle has a circularity of one. Since the recorded images are two-dimensional, this will give the best estimation of whether the imaged ice crystals are indeed spherical.

Recrystallization is a highly temperature dependent relaxation process. This is expressed in the recrystallization curvature model through an Arrhenius temperature dependence of the kinetic recrystallization constant [172]. The initial ice crystal structure, and thus the initial parameters of the recrystallization process, is highly dependent on various parameters such as chemical composition, cooling rate and supercooling as discussed in chapter 4. The measurements performed here give insights to temperatures and time scales on which the recrystallization process occurs in samples containing CPAs. The results are not directly transferrable to other media due to the variation in the experimental parameters and initial state of the sample. Each medium composition thus has to be characterized separately. These investigations do however provide insights to the durations at given temperatures for a DMSO at a commonly used concentration.

6.2.1 Experimental setup

In order to investigate the recrystallization process, the simple fluorescence microscope described in section 3.2.2 was used as this very simple and compact setup allows long duration studies, i.e. several days or even weeks. In principle, the more advanced two-photon fluorescence microscope described in section 3.3.1 could have been used to achieve a better image quality but long-term studies are impractical when the Linkam cryostage is employed, due to a constant requirement of liquid nitrogen and a limited storage capacity at the experimental setup of maximum 2 l. This amount of liquid nitrogen is sufficient for approximately four hours of cryostage operation depending on the temperatures and cooling rates employed in a given

experiment. The whole microscope would therefore be required to be cooled in a freezer or cryo-workbench what is feasible with the smaller and simpler microscope but not with the large and delicate two-photon laser scanning microscopy setup. The measurements in this study were performed in time periods of maximum 7 hours. Experiment durations above four hours were achieved by manually refilling the storage dewar during operation of the cryostage.

Samples consisting of 10 % DMSO in H₂O with fluorescein added were investigated in this study. The dye will concentrate in the dendritic channels since it is not dissolvable in ice. This allows for a direct imaging of the dendritic channels with the dark areas being the surrounding ice crystals. Samples of 10 μ L were prepared on the cryostage as described in section 3.2 and continuously cooled to a temperature of -30 °C, -40 °C, -50 °C or -70 °C at a cooling rate of 3 °C/min. The samples were then kept at their temperature and fluorescence images were recorded regularly in order to study the recrystallization dynamics. The initial recrystallization speed is higher than the subsequent part of the recrystallization process. Therefore more images were recorded at the first part of each experiment. This gives an insight both to the temporal recrystallization phenomenon as well as the influence of temperature on this process.

6.2.2 Fluorescence image analysis

The recorded fluorescence images were analyzed using the Nikon NIS-Elements software in order to detect ice crystals and their size automatically. Each image was treated with the following analysis protocol in order to obtain consistent data:

- 1: Locate regional minima
- 2: Convert image to binary based on threshold
- 3: Detect edges of crystals
- 4: Segment oblong structures
- 5: Detect and list crystal size and circularity

First, local minima were detected in an image to establish an approximate position of all ice crystals, since dark areas in the image correspond to ice crystals. The image was then converted to a binary image based on a fixed threshold for all measurements. In other words, all pixels with values below a certain threshold were given the value 1, i.e. an ice crystal, whereas pixels with values above the threshold were assigned the value 0. This is not an ideal method of ice crystal detection since the decision of whether or not an ice crystal exists in the given location can be more complex than just the pixel value. This simple method could lead to small errors in detection of ice crystal sizes but still allows for comparison between images if the threshold is kept constant. This method can in any case be used to detect ice crystal size trends and relaxation processes.

The edges of ice crystals were then identified as pixels with the binary value of one that have least one neighboring pixel with the binary value of zero. The Nikon NIS Elements software was then used to segment oblong ice crystals at narrow parts of the ice crystals. This was necessary in order to differentiate between closely packed ice crystals. If this step was excluded, all of the ice crystals in an image would be identified as very few large ice crystals instead of the hundreds or thousands of ice crystals actually in the sample. The parameters for this segmentation were kept constant for the analysis of all images. Finally, each separate ice crystal is identified and listed along with its corresponding area, i.e. the amount of pixels surrounded by perimeter pixels, as well as the perimeter pixels from which the circularity can be calculated.

Figure 6.3 shows an example of the image analysis performed with the Nikon NIS elements software. Here, a sample frozen to -40°C and kept at this temperature for five minutes is shown both as raw data and as the image resulting from the analysis algorithm. The first image shows the complex network of dendritic channels as the light areas, whereas the ice crystals are the dark areas in the image. The second image shows the pixels identified as ice crystals in red and all ice crystal perimeter pixels are shown in green. An ice crystal is thus identified as a red area surrounded by a green line. This image also shows how the software segments larger oblong ice crystals at points where the ice crystals get narrower. In this image, 1087 ice crystals were detected with diameters ranging between $4.1\text{ }\mu\text{m}$ and $18.3\text{ }\mu\text{m}$ and with a mean diameter of $7.8\text{ }\mu\text{m}$.

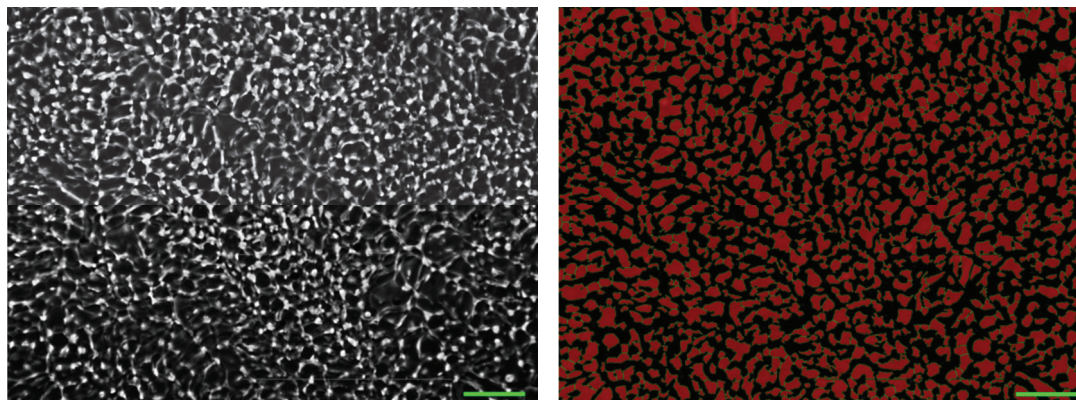


Figure 6.3 Here, the raw data and the result of the image analysis using the Nikon NIS elements software is shown for a sample frozen to -40°C at 3°C/min and kept for five minutes. The image on the left shows the dendritic channel network and ice crystals (dark areas) as recorded with the fluorescence microscope. The image on the right shows the result of the image analysis with red pixels identifying ice crystals and green pixels their perimeter. Scale bar is $50\text{ }\mu\text{m}$.

6.2.3 Recrystallization in slowly frozen media

The ice crystal size and circularity distribution are the key indicators for recrystallization and a typical example will be shown for a better understanding of the remaining analysis. The dynamics of recrystallization will then be investigated based on the recrystallization curvature model. The influence of different sample temperatures on the recrystallization dynamics is studied by comparing samples kept at different temperatures between -30 °C and -50 °C. Finally the detrimental effect of water condensation on the measurements is briefly discussed.

Ice crystal size and circularity distribution

Each recorded fluorescence image contain between several hundred and a few thousand ice crystals. As can be seen from Figure 6.3 these crystals appear in various shapes and sizes. It appears from the fluorescence image in Figure 6.3 that the ice crystal sizes are not homogenously distributed over the entire image. There are regions with either smaller (top and center part of image) or bigger crystals (bottom left and right part of image). The image is, however, large enough to show a representative distribution of ice crystals in the sample since over 1000 ice crystals are contained within this single image. Two parameters that characterize the ice crystals are the approximated ice crystal diameter as well as the circularity of the ice crystal as defined by equation (6.4). The distribution of the ice crystal diameters as well as the circularity for a sample upon freezing to -30 °C is shown in Figure 6.4.

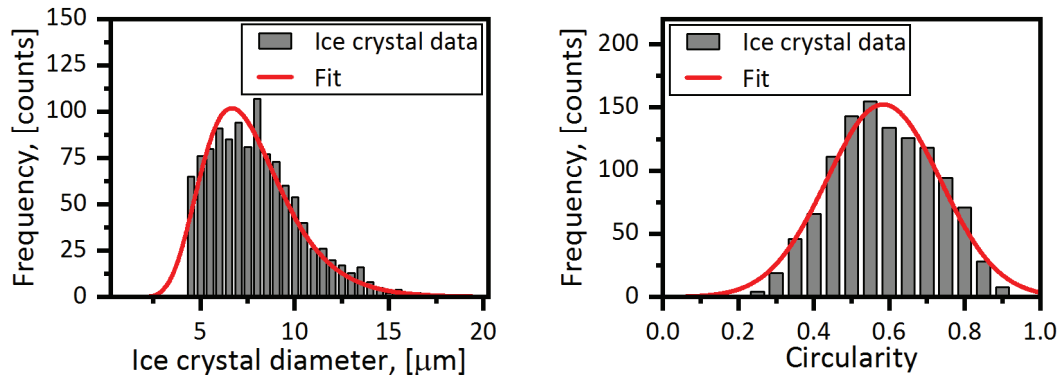


Figure 6.4 Histograms of the initial ice crystal diameter and circularity distributions for a sample cooled to -30 °C at a cooling rate of 3 °C/min. A lognormal and normal distribution function has been fitted to the two datasets, respectively.

The distribution of ice crystal diameters at a given time t , $D(t)$, seems to follow a lognormal distribution of the form:

$$f(D(t)) = \frac{A}{\sqrt{2\pi}\sigma D(t)} \exp\left(-\frac{\left(\ln D(t) - \ln D_{mean}(t) - \frac{\sigma^2}{2}\right)^2}{2\sigma^2}\right) \quad (6.5)$$

Here, σ is a scaling parameter that defines the width of the distribution. The mean diameter at time t is denoted $D_{mean}(t)$. The distribution of crystal sizes does thus not follow a normal distribution but is skewed towards smaller ice crystals. From the histogram it can furthermore be observed that the analysis algorithm cannot identify very small ice crystals with a diameter below 4 μm . No ice crystals were detected below this size in any of the measurements and it is very unlikely that these small ice crystals do not appear in any of the samples. This effect occurs due to the threshold settings chosen for the analysis algorithm. The choice of threshold is a balancing act between removing noise, only identifying ice crystals in the focal plane and segmenting the oblong ice crystal structures in a meaningful consistent manner for all images where the ice crystal sizes vary greatly. By choosing consistent threshold settings trends and developments of the ice crystal size can still be observed in a quantitative manner even though the image analysis algorithm only provides an approximation to the real structure of the sample. The lognormal distribution was fitted to the ice crystal size distribution for each fluorescence image in order to extract the scaling parameter σ . This give information on how the size distribution changes with time during recrystallization.

The distribution of ice crystal circularity is also shown in Figure 6.4. Here it is seen that the distribution approximately follow a normal distribution with a center value of 0.58. The recrystallization curvature model generally assumes spherical ice crystals. The description of a sample based on this model is thus more accurate for samples with higher values of the circularity. The ice crystals found in slowly frozen samples are never spherical, but rather oblong and irregular crystals and the circularity is a measure of this irregularity. Ice crystals with a lower circularity have regions with a higher melting point due to the Kelvin effect as previously stated. A given sample with a lower average circularity will thus exhibit average recrystallization rates higher than in samples with few completely spherical ice crystals.

Dynamics of recrystallization

Let us now consider a single sample kept at $-40\text{ }^{\circ}\text{C}$. The Fluorescence images shown in Figure 6.5 were recorded at 5 min, 30 min, 60 min and 120 min after the isothermal holding temperature of $-40\text{ }^{\circ}\text{C}$ has been reached. The overall duration of this experiment was 300 min. A majority of the recrystallization did however occur within the first hour of the experiment and it is therefore difficult to see any changes visually beyond the 120 min measurement. The fluorescence images clearly show that ice crystals grow bigger over time and that the dendritic channel network gets coarser through a recrystallization process. Since the overall composition of the sample and the relative amount of ice do not change during this experiment, the average ice crystal size increases while the number of ice crystals decreases. It can furthermore be concluded that the dendritic channels get wider since the ice in the sample is contained in fewer but larger ice crystals.

Figure 6.6 shows the temporal development of the mean ice crystal diameter, $D_{mean}(t)$, of the sample shown in Figure 6.5. Here it is seen that the mean ice crystal diameter initially grows rapidly to around 9 μm and then the growth slowly tapers off approaching a limit diameter of 9.3 μm . The recrystallization curvature model given in equation (6.1) has been applied to this dataset with the initial condition $D_{mean}(0) = 7.8 \mu\text{m}$ given as the ice crystal mean diameter retrieved from the first data point in this measurement series. The resulting fitting curve plotted in Figure 6.6 follows the data very well which is also confirmed by the calculated parameter R^2 of 0.97. From this analysis, values for the kinetic recrystallization constant $k = 1.80 \mu\text{m}^2/\text{min}$ and the diameter limit value $D_1 = 9.32 \mu\text{m}$ could be retrieved. Figure 6.6 also shows the scaling parameter σ characterizing the width of the ice crystal size distribution as a function of measurement time. The distribution width increases in a similar manner as the mean ice crystal diameter.

This indicates that the large ice crystals grow relatively more than smaller ice crystals. This will result in a bigger spread of ice crystal sizes and thus a wider size distribution. This form of ice crystal growth where some crystals grow significantly faster than others can be denoted as abnormal crystal grain growth as defined in [174]. Normal grain growth in contrast describes processes where the individual crystal growth rate is relatively uniform within a sample resulting in a decreasing number of crystals. Several

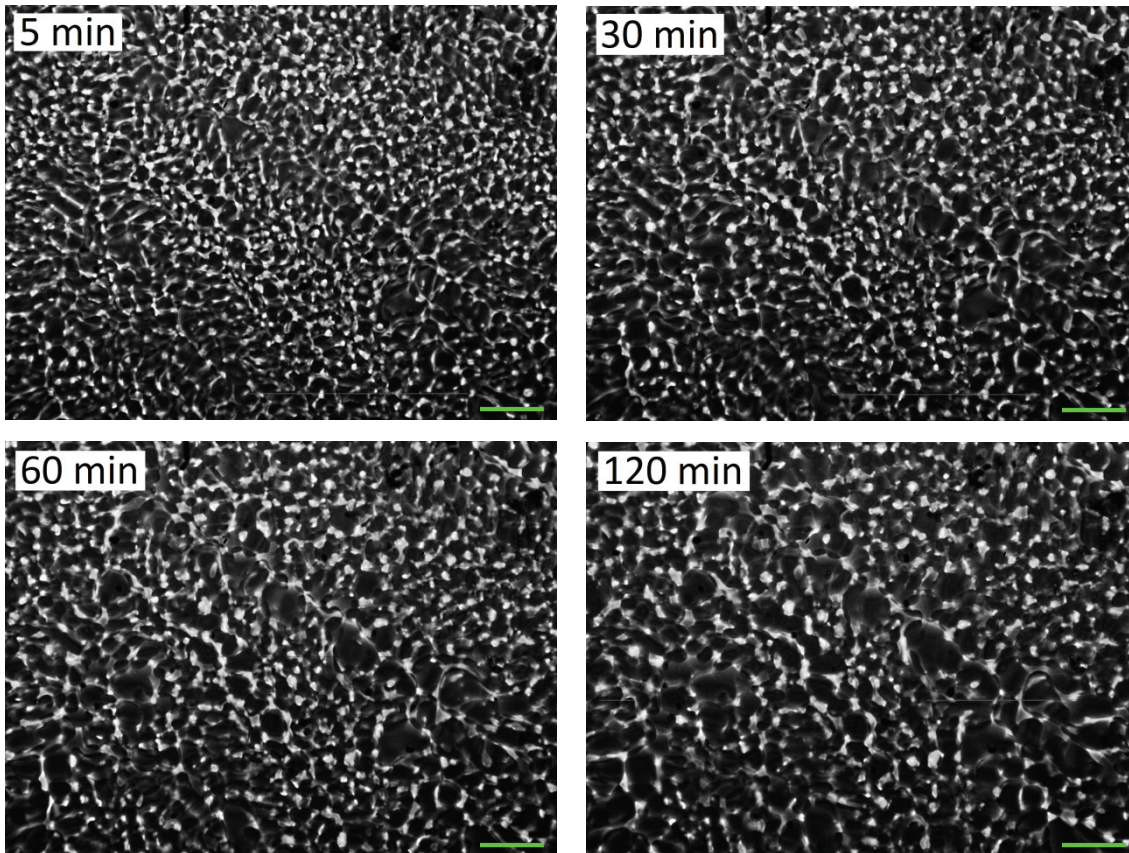


Figure 6.5 Fluorescence images of the same sample recorded 5 min, 30 min, 60 min and 120 min after the isothermal holding temperature of $-40 \text{ }^{\circ}\text{C}$ has been reached. Scalebar is 50 μm .

conditions can contribute to abnormal crystal growth as the dominant process [174]. Normal crystal growth is generally limited due to the high DMSO concentration of the dendritic channels acting as second phase particles, i.e. particles not participating in the recrystallization process. An ice crystal can thus only grow on the expense of other ice crystals at the stage where the samples are investigated, i.e. after at the nucleation and initial ice crystal growth stage. This holds true for most recrystallization processes in cryopreserved samples. Ice crystals being the limit diameter of the ice crystal recrystallization process are another condition required for abnormal growth. Comparing the limit value of $9.32\ \mu\text{m}$ to the initial mean crystal diameter shows that abnormal growth is indeed possible during the experiments performed.

The samples furthermore initially contain a few ice crystals that are significantly bigger than the remainder of the sample. The first fluorescence image for this investigated sample has an ice crystal with an approximated diameter of $17.09\ \mu\text{m}$ whereas the mean diameter is $7.83\ \mu\text{m}$. The large ice crystal is thus over twice as big as the mean crystal which is another indicator for abnormal grain growth [172].

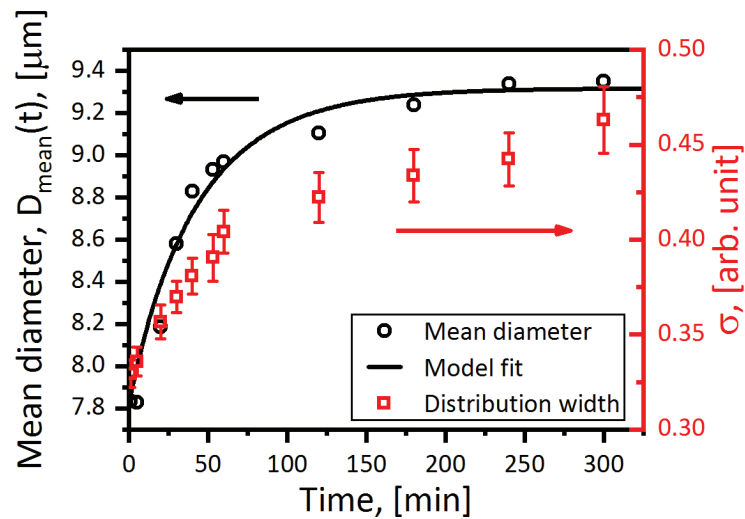


Figure 6.6 Mean crystal diameter $D_{mean}(t)$ (black) and width of the ice crystal size distribution σ (red) of a sample cooled to $-40\ ^\circ\text{C}$ at $3\ ^\circ\text{C}/\text{min}$ and kept isothermally for 300 min. The recrystallization curvature model of equation (6.1) has been fitted to the ice crystal diameter.

By repeating the experiment at different temperatures, the recrystallization curvature model can be tested for various conditions and the influence of temperature on the recrystallization process can be investigated. Figure 6.7 shows fluorescence images of three different samples kept isothermally at $-30\ ^\circ\text{C}$, $-40\ ^\circ\text{C}$ and $-50\ ^\circ\text{C}$, respectively. The images were recorded at 5 or 60 minutes after the hold temperature has been reached. It is clearly evident from these images that the recrystallization process is significantly faster at higher temperatures. Major structural changes of the ice crystals can be observed within the first hour of measurement for the sample kept isothermally at $-30\ ^\circ\text{C}$ whereas only minor or no changes can be visually detected for

the sample at $-50\text{ }^{\circ}\text{C}$. It is even possible to observe clear differences after only five minutes for the sample kept at $-30\text{ }^{\circ}\text{C}$. These fluorescence images are thus a good example of how recrystallization is dependent on temperature through the kinetic recrystallization constant and how temperature-sensitive a sample can be when a given threshold temperature is exceeded.

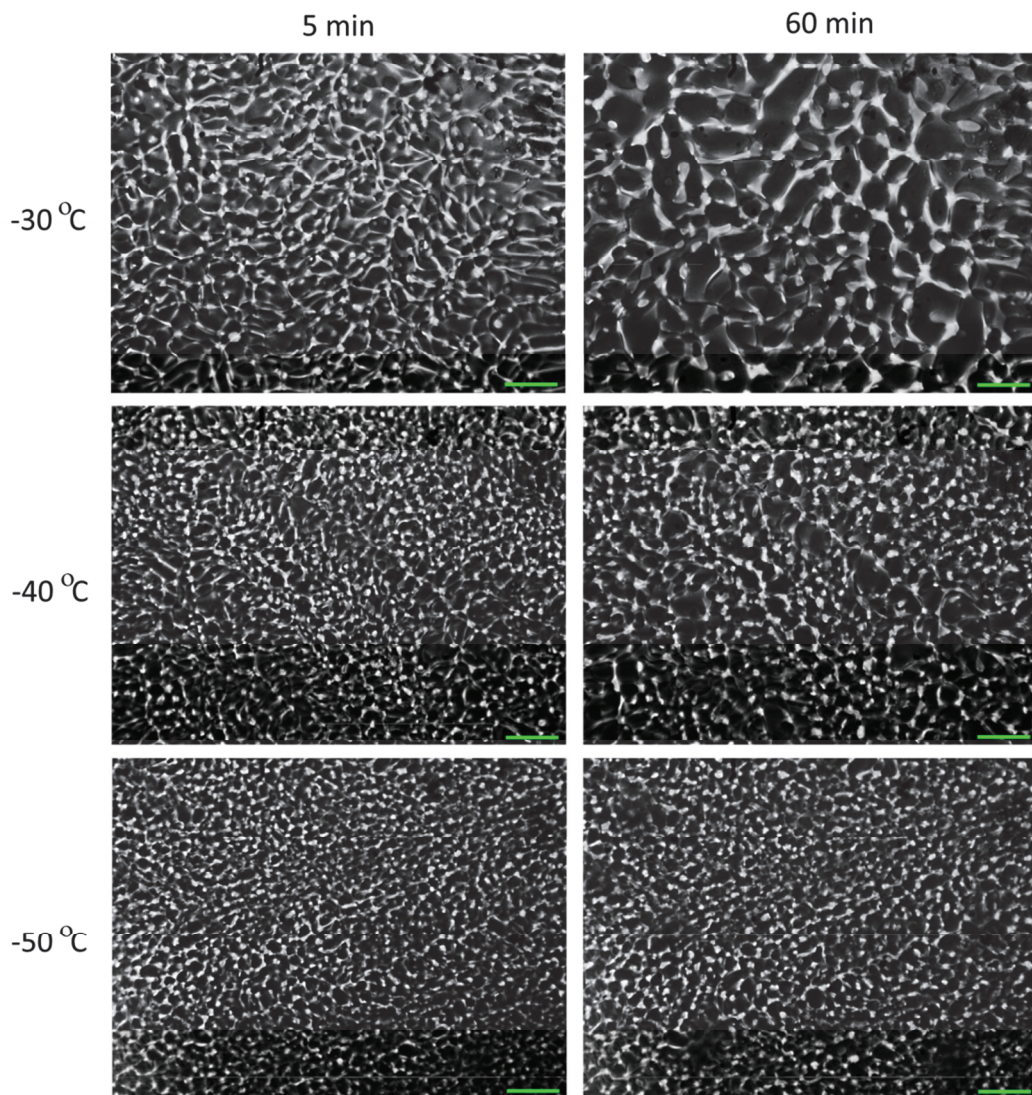


Figure 6.7 Fluorescence images of three different samples kept at $-30\text{ }^{\circ}\text{C}$, $-40\text{ }^{\circ}\text{C}$ and $-50\text{ }^{\circ}\text{C}$, respectively. The images are recorded 5 min and 60 min after reaching the isothermal temperature. Scale bar is $50\text{ }\mu\text{m}$.

The collected data for all measurements are shown in Figure 6.8. Three samples were kept at $-30\text{ }^{\circ}\text{C}$ and are denoted sample #1, #2 and #3. The two samples kept at $-40\text{ }^{\circ}\text{C}$ and the single sample kept at $-50\text{ }^{\circ}\text{C}$, are denoted sample #4, #5 and #6, respectively. The recrystallization process appears to have run its course within approximately one hour for the samples kept at $-30\text{ }^{\circ}\text{C}$, what can be seen as the mean crystal diameter being constant from one hour and onward. For the samples kept at $-40\text{ }^{\circ}\text{C}$ the limit mean crystal diameter is first reached after several hours. The recrystallization process was still ongoing for sample #6 kept at $-50\text{ }^{\circ}\text{C}$ when the measurement series was terminated due to time constraints after 4.5 hours. It is furthermore seen that the ice

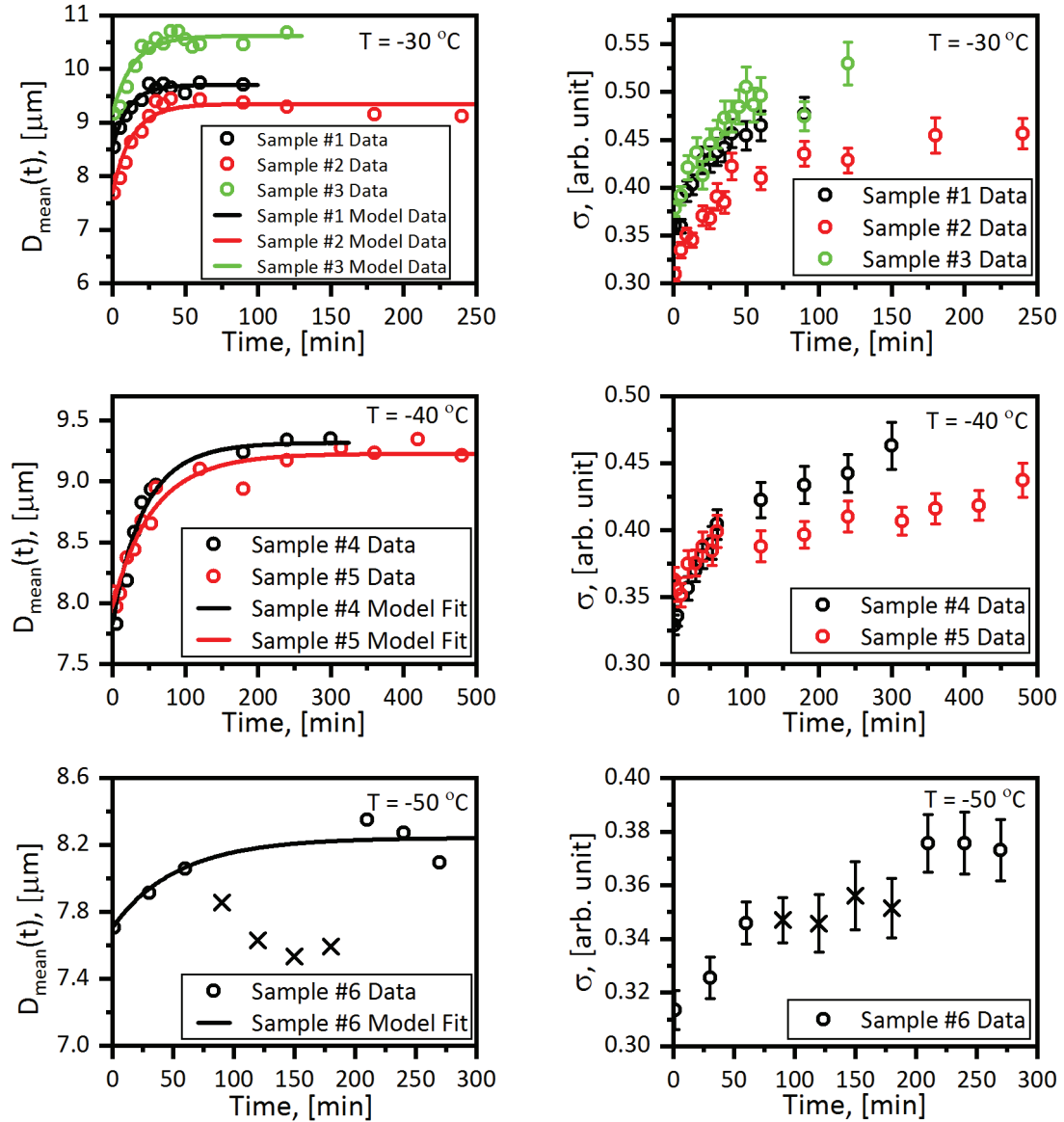


Figure 6.8 Mean crystal diameter $D_{mean}(t)$ and ice crystal size distribution width for all measurements carried out at $-30\text{ }^{\circ}\text{C}$, $-40\text{ }^{\circ}\text{C}$ and $-50\text{ }^{\circ}\text{C}$. The recrystallization curvature model of equation (6.1) has been fitted to the mean ice crystal diameter. Data points marked as a 'x' for sample #6 has been excluded from the model fit due to problems with ice condensation on top of the sample manifested by a significant decrease in mean ice crystal diameter.

crystal mean diameter for sample #6 appears to decrease in the middle of the measurement series. The ice crystals in the sample do not decrease in size in reality. This artifact can be attributed to condensation of water on top of the sample introducing errors in the automated image analysis. This will be discussed in more detail at the end of this section. The data points marked as an 'x' are therefore excluded from further analysis of this dataset. For all samples, an increase in the ice crystal size distribution width σ can be observed. The width initially increases rather rapidly before becoming approximately constant as the recrystallization rate decreases. This is expected since then the ice crystal size distribution and thus the width should remain unchanged when no recrystallization occurs. The increase in σ indicates that abnormal ice crystal growth occurs in all samples as expected on the reasoning presented before.

The recrystallization curvature model has been applied to each measurement series and the resulting kinetic recrystallization constant k , limit diameter D_1 as well as coefficient of determination R^2 is collected in Table 6.1 along with the initial mean diameter $D_{mean}(0)$. The recrystallization curvature model describes the data well for sample #1 through #5 as seen from $R^2 > 0.9$. The model does not describe sample #6 as well which is reflected in a reduced R^2 and would be expected due to the issues with water condensation. The kinetic recrystallization constant is an expression of the speed of the process. The mean $D_{mean}(0)$ for the samples at $-30\text{ }^\circ\text{C}$ and $-40\text{ }^\circ\text{C}$ was found to $8.47\text{ }\mu\text{m} \pm 0.74\text{ }\mu\text{m}$ and $8.00\text{ }\mu\text{m} \pm 0.04\text{ }\mu\text{m}$. The mean kinetic recrystallization constant was found to $7.01 \pm 1.09\text{ }\mu\text{m}^2/\text{min}$ and $1.60 \pm 0.29\text{ }\mu\text{m}^2/\text{min}$ for the samples kept at $-30\text{ }^\circ\text{C}$ and $-40\text{ }^\circ\text{C}$ respectively. This means that the recrystallization rate is a factor of 4.4 higher for a population of ice crystals with the same initial ice crystal size distribution when the temperature is increased with $10\text{ }^\circ\text{C}$. If this trend holds true then a much lower k than the $1.21\text{ }\mu\text{m}^2/\text{min}$ found for sample #6 would be expected what seems possible when considering the limited reliability of the data caused by water condensation. Also the much lower limit diameter found compared the other

Table 6.1 Table contains the initial condition and values extracted by applying the recrystallization curvature model to the measured data. $D_{mean}(0)$ is the initial condition for the differential equation. k and D_1 are the kinetic recrystallization constant and ice crystal limit diameter respectively. The goodness of fit parameter R^2 is also given. Four data points has been excluded from the analysis of sample #6 which is why it is marked by a *.

Sample	Temperature	$D_{mean}(0)$ [μm]	k [$\mu\text{m}^2/\text{min}$]	D_1 [μm]	R^2
Sample #1	$-30\text{ }^\circ\text{C}$	8.54	7.92	9.71	0.96
Sample #2	$-30\text{ }^\circ\text{C}$	7.69	5.81	9.35	0.93
Sample #3	$-30\text{ }^\circ\text{C}$	9.17	7.31	10.62	0.92
Sample #4	$-40\text{ }^\circ\text{C}$	8.03	1.80	9.32	0.97
Sample #5	$-40\text{ }^\circ\text{C}$	7.97	1.39	9.23	0.96
Sample #6*	$-50\text{ }^\circ\text{C}$	7.71	1.21	8.24	0.87

measurements is questionable. Even though the recrystallization process is not completed it would still be expected that the recrystallization curvature model to take this into account and successfully model the process from the initial rise in ice crystal diameters. Variations in image contrast, however, can lead to changes in the measured ice crystal size since they are detected automatically based on threshold values. When the image contrast is not consistent over a measurement series, what could also have been the issue for sample #6 as a result of the water condensation, the retrieved values for the ice crystal sizes might be skewed.

Since measurements were only conducted successfully for two holding temperatures, a definitive value for the activation energy of the kinetic recrystallization constant cannot be given but a tentative estimation of the activation energy of 69.9 kJ/mol based on an Arrhenius relation. This value should only be used with care but gives a rough estimation of the activation energy for the type of samples investigated in this study. The activation energy for ice recrystallization has been studied under various conditions. One study has utilized the recrystallization curvature model in a same manner as this study to investigate recrystallization in frozen muscle tissue and found an activation energy of 116.4 kJ/mol [172]. Further studies found an activation energy of 121.3 kJ/mol for two ice crystals brought into contact in air [175] and 114.9 kJ/mol for the recrystallization of intracellular ice in oocytes upon warming [31]. Two other studies found activation energies of 112-126 kJ/mol [176] and 46-48 kJ/mol [177] for aqueous glucose and sucrose solutions intended for ice cream production. Most of the reported activation energies are much higher than what was found here. A comparison of these activation energies should only be compared with caution due to the low number of data points available. For the glucose and sucrose solutions it was argued that a variation of sample constituents and experimental parameters caused the high difference in activation energies. The investigated samples in this study contained fewer second phase particles compared to the other reports where often other types of material were present such as muscle, fat and oocytes. The activation energy thus seems sensitive to the sample in question as well as the experimental parameters.

The limit diameter appears to be correlated to the initial mean diameter in some manner. This is illustrated in Figure 6.9 where the limit diameter D_1 is plotted against the initial mean diameter $D_{mean}(0)$ for sample #1 through #5 showing a direct proportionality except for sample #2. The absolute increase in mean ice crystal diameter is thus higher in samples that initially contain larger ice crystals but the relative size increase is approximately consistent for the investigated samples. This means that large ice crystals can more easily incorporate small ice crystals and thereby absolutely grow more than medium-sized ice crystals. This is another indicator for the abnormal ice crystal growth.

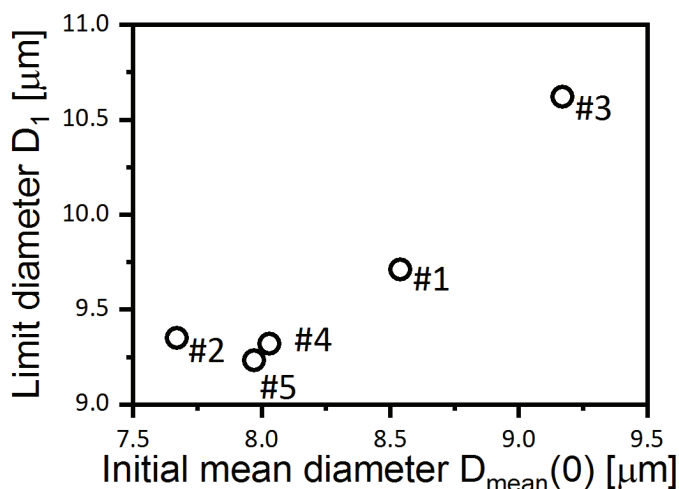


Figure 6.9 Ice crystal limit diameter D_1 as function of initial mean ice crystal diameter $D_{mean}(0)$ for samples #1 through #5.

Water condensation

An experimental problem was encountered when the sample was cooled to $-50\text{ }^{\circ}\text{C}$ or below. At these temperatures, water vapor condensation appeared on top of the samples and ice crystals started to form on top of the sample due to a leak in the cryostage. An example of the formed ice crystals can be seen in Figure 6.10 where the investigated sample has been cooled to $-70\text{ }^{\circ}\text{C}$. Already at the onset of the isothermal part of the experiment, small ice crystals can be observed. The size of these ice crystals should not pose any significant issues with the experiment. These ice crystals, however, grew to diameters of approximately $30\text{ }\mu\text{m}$ to $40\text{ }\mu\text{m}$ during the course of the experiment. In macroscopic terms, these are still small ice crystals but they were large enough to disturb the recording of the fluorescence images. They cast significant shadows in the fluorescence images and lead to a decreased image contrast in these parts of the image. Since the image quality was too poor and inconsistent over a single measurement series a meaningful image analysis was not possible in this case. Already for an isothermal temperature of $-50\text{ }^{\circ}\text{C}$ this problem posed a challenge to record high quality fluorescence images. Multiple attempts were conducted but only sample #6 could successfully be measured without significant water condensation on top of the sample but the subsequent data analysis showed that this problem also persisted for this data set.

The cryostage should in principle provide a dry atmosphere by forming a closed chamber around the sample and pumping the dry nitrogen exhaust gas into the chamber. The cryostage is designed in this manner to allow for microscope investigations using air objectives. Due to the growth of ice crystals on the sample it can however be deduced that moist air must be leaking into the cryostage chamber continuously throughout the experiments. With the duration of the measurement series performed here, this only manifested as ice crystals at temperatures

below -50°C . It should be expected that ice crystals can also form on top of samples at higher temperatures if the experiment duration is extended significantly.

The fluorescence microscope was designed to work in a cooled environment or freezer so that the disadvantages of a constant needed supply of liquid nitrogen for the cryostage can be circumvented allowing for significantly extended measurement series duration. If the microscope is employed in such an environment it is paramount that the atmosphere is kept very dry or that a method is developed that can gently remove ice from the sample before each fluorescence image recording.

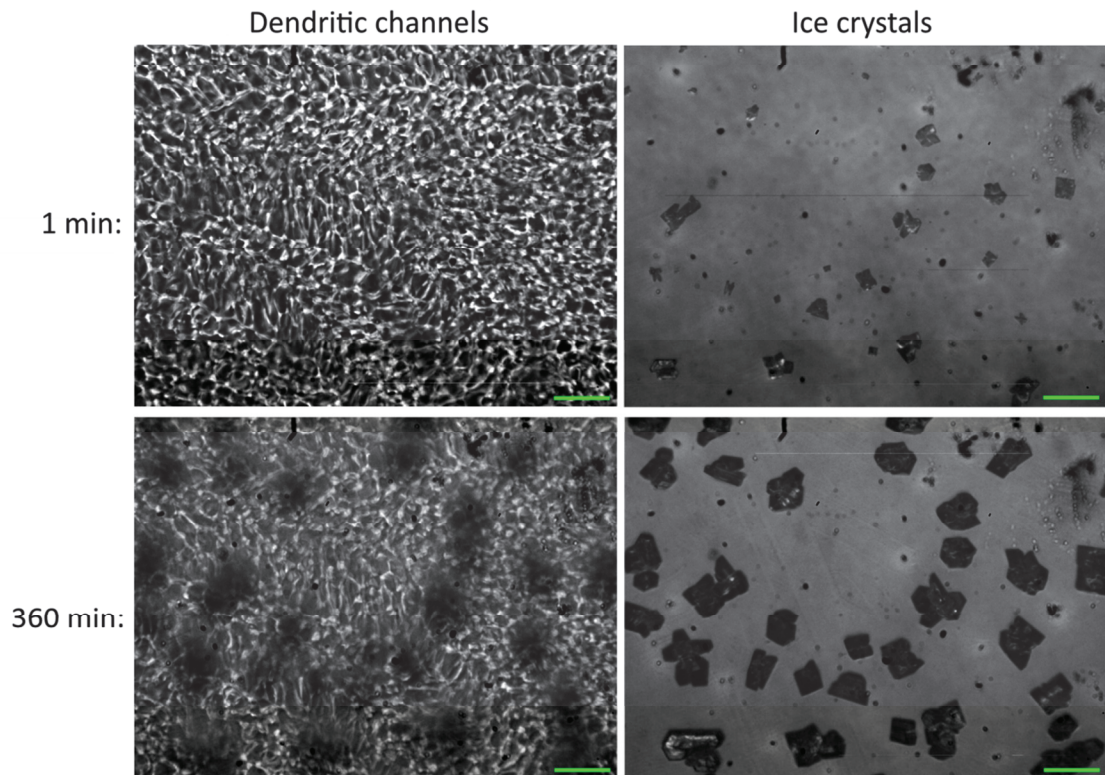


Figure 6.10 Fluorescence images of a sample and transmission images from the top of the sample. The sample has been cooled to -70°C at $3^{\circ}\text{C}/\text{min}$. Ice crystals are seen to grow on top of the sample casting dark shadows in the fluorescence image. Scalebar is $50\ \mu\text{m}$.

6.2.4 Retrospective analysis based on recrystallization

Recrystallization can be seen as an aging marker for slowly frozen cryopreserved samples. It is a thermally activated process that can occur in a cryopreserved sample if it experiences elevated temperatures. This process is faster at higher temperatures and the study shown in this work can serve as an example of how a relaxation process can be accelerated through temperature elevations and thus studied within a reasonable timeframe. Samples are stored below the glass transition temperature in order to avoid changes the ice crystal morphology and local cell environment..

Recrystallization is dependent on the initial ice crystal size distribution. An analysis of the ice crystal size distribution is an example for the phenomenological approach to retrospective analysis. An initial measurement is required, to which further measurements can be related to and changes in the ice crystal size distribution can then be attributed to recrystallization. A single measurement of the ice crystal size distribution cannot in itself reveal to what extent recrystallization has occurred in a slowly frozen sample. Measurements of the mean ice crystal sizes over time will indicate retrospectively if a cryopreserved sample has been heated significantly above the glass transition temperature.

The method that has been introduced here to measure recrystallization cannot directly be applied to cryopreserved samples stored in biobanks. The method presented here requires both a fluorescence dye and a good optical access to the sample. As phenol red is often contained in cryopreserved samples, the fluorescence should be sufficient for this type of analysis. The optical access to stores is, however, very limited. Biological samples are typically preserved in cryotubes where optical measurements are only possible through the strongly bent and slightly opaque surface of the sidewalls. While transparent material in principle allows for optical measurements, the high resolution imaging required for the analysis of recrystallization is not possible with these standard sample containers.

In order to use recrystallization as marker in retrospective analysis another method needs to be developed. An obvious choice for such a technology would be light scattering measurements. Here a light beam is sent through the sample and scattering of light can be detected by decreased transmission intensity. Such methods are well established to for example measure ice crystal sizes in clouds [178] or measuring particle and colloid sizes by dynamic or static light scattering [179], [180]. For an application of this scattering method to cryopreserved samples, several challenges need to be addressed. On the one hand, there are some technical obstacles related to high-precision optical measurements at cryogenic temperatures like water condensation or the mechanical stability of individual components at very low temperatures. On the other hand, the samples themselves possess some characteristics that limit the applicability of scattering techniques to cryopreserved samples [181]. The large amount of ice in the sample results in a high density and overall quantity of scattering surfaces that makes a quantitative description of small variations very difficult. Also the non-uniform ice crystal size distribution typically found in the samples limits the reliability of the scattering measurements since the effect of large crystallites is dominating over other contributions. In addition, the application of light scattering methods in biobanks is generally limited to static measurements since the scattering particles are not mobile in cryopreserved samples.

In order to still exploit the fluorescence imaging method presented in this work to cryopreserved samples in biobanks, a monitoring seal can be added to each sample container or sample rack. This could for example be a planar seal in which the ice crystals can form and allows for a good optical access. Monitoring the ice crystal size

distribution within this seal can then reveal recrystallization and thus indicate that the cold chain has been broken. This technology will be discussed in the following section.

6.2.5 Application of recrystallization kinetics as a TTI

It is not always possible to track temperature fluctuation of a single sample throughout its lifetime. The temperature is typically measured in the controlled environment surrounding the samples. Therefore it is often unknown if a sample has been exposed to high temperatures during its storage time and if so for how long. The understanding of the recrystallization dynamics in cryopreserved samples allows for a retrospective analysis using the simple fluorescence microscopy method. Based on the studies shown in this work, a new method was developed that allows determining locally for each slowly frozen sample whether it has been exposed to too high temperatures for extended periods. As Time-Temperature-Indicator (TTI), a quality seal is attached to each cryopreserved sample. A TTI is an indicator that shows the accumulated temperature history of a sample as it shows when the sample has been exposed to a given temperature for a given duration. Such a seal activates as it is heated above a given threshold and is thus ideal to prove if the cold-chain of a sample has been maintained.

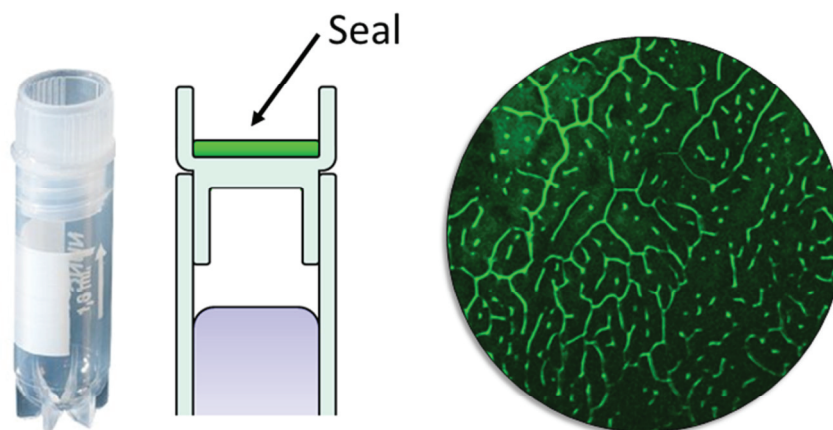


Figure 6.11 A Time-Temperature indicator could be positioned in the lid of a cryotube as indicated in the sketch. The TTI would consist of a thin layer of liquid consisting of water, a CPA and a fluorescent dye. When frozen with the sample, a unique pattern will form that can be imaged with fluorescent microscopy. Changes in the pattern during storage indicate recrystallization and thus exposure to high temperatures.

The seal could contain a binary mixture, for example DMSO in H₂O, and a fluorescent dye. Upon freezing of the sample, the seal would also freeze generating a unique pattern or fingerprint of dendritic channels and ice crystals. By designing the TTI using an aqueous mixture of DMSO, it is ensured that the freezing process of the seal closely

follows the processes also occurring in the cryopreserved sample it is attached to. The TTI would thus be sensitive to temperature in the way as the sample itself. By placing the TTI in direct contact with the cryotube it is ensured that the quality seal will experience the same temperature variations as the sample. Such a seal could be located in the lid of each cryotube as sketched in Figure 6.11 or in a sample rack.

When the sample is exposed to elevated temperatures, this pattern will irreversibly change depending on the temperature and duration of the incident due to recrystallization. A qualitative comparison (either visually or by an automated image comparison) of the pattern right after freezing, at regular intervals and before thawing will reveal if the sample has been exposed to elevated temperatures during its storage. In other words, if recrystallization is detected it can be concluded that the cold chain for the sample has been broken.

The readout of the seal cannot be falsified since the pattern generated will always be unique and can be regarded as a fingerprint of the cryopreserved sample. It cannot be replaced and proves the genuineness of a sample. The idea of using patterns that can be readout optically to prevent counterfeiting has already been proposed. One such study employs luminescence in polyvinyl alcohol thin films from the doped lanthanides europium, terbium and dysprosium to create patterns that are virtually impossible to replicate [182]. The study reports a staggering encoding capacity of 7^{3600} for a 60 x 60 pixel RGB image. The fluorescence images produced in this current study have an even higher resolution and therefore an even higher potential encoding capacity. The unique pattern can also help in sample tracking. An error rate for sample tracking and relabeling of up to 0.1 % [183] has been reported. This can cause a loss of valuable specimens or errors in research in particular for studies where the investigated specimens are of limited quantity.

Instead of tracking the specific pattern of each specific sample, a generic measure would make this technology easier to implement as it does not require a full record of the sample history. As shown in the present study, the ice crystal size can be used as an indicator for the storage conditions a cryopreserved sample has been exposed to in the past. The use of this metric number also circumvents the problematic requirement of image analysis of fluorescence images recorded at the same spot on the TTI for a meaningful comparison. In addition, it also provides quantitative information on the recrystallization process that can be used to estimate the damage that the temperature fluctuations have caused in the sample. The size of the ice crystals is related both to the magnitude and duration of temperature variations, i.e. a small $\Delta T \cdot \Delta t$ (change in temperature and time) results in a small change and a big $\Delta T \cdot \Delta t$ result in a big change of the average ice crystal size. It is therefore possible to estimate the severity of temperature elevations in the storage history.

The concept of TTIs is not new and different technologies have been developed for the food industry in order to track if the cold-chain has been broken [184]. These TTIs are often based on chemical reactions or mechanical processes [185] but the proposed method does possess several advantages over conventional TTIs. To our knowledge

the first method that is applicable very low temperatures encountered in biobanking. It also provides a quantitative measure and allows a determination of the extent to which the cold chain has been broken. In addition, the quality seal is directly activated upon freezing as it has a chemical composition comparable to the sample. The readout of a fluorescence image is a convenient method that only requires basic training or that can be automated and can be performed in a cryo workbench. The main advantage of such a seal is that the quality of the sample can be monitored in a non-contact manner without thawing the sample. This is a decisive advantage over conventional methods for quality control that would typically require that the sample is being thawed [186]. The application of such a seal would furthermore allow for a simple control of the freezing protocol by comparing the actual ice crystal size distribution in the seal with an expected distribution based on the wanted temperature profile.

Such a seal could find its application for samples where a very high quality is needed, and an unbroken kept cold-chain is crucial. This is for example important in personalized medicine where samples are sensitive and limited in quantity [183]. Samples that have suffered temperature related damage during storage could be discarded whereas undamaged samples could come with a certification proving proper storage. Another area where a high quality cryopreservation process is required is in systems biology [186]. Biobanks could use the quality seal as guarantee for personal samples in storage and ensure that the samples are of high enough quality to allow for systematic comparisons required in systems biology and identify disease-related alterations. Another field of application could be samples in long-term storage. Here, multiple violations of the cold chain could occur during the storage period which can lead to accumulated and irreversible effects within the sample. Through regular controls of the seal it can be determined if the quality is degrading over time and if it is worth keeping the sample in storage.

6.3 Kinetics of devitrification

The preserving feature of the vitrification cryopreservation method is that no kinetic chemical or biological processes can proceed both extracellular and intracellular. In contrast to the slow freezing approach studied before, the entire sample is a glass without any ice formation. The vitrification of samples can be achieved with high cooling rates above 100 °C/min depending on CPA and its concentration [61]. It is paramount for the sample quality that ice does not start to crystallize during the entirety of the preservation process from freezing to thawing of the sample. When the sample is elevated above the glass transition temperature, the kinetics in the sample is activated through a decreased viscosity, which means that ice crystals can nucleate and start to grow. This relaxation process is called devitrification and should be avoided in order to preserve the integrity and quality of the cryopreserved sample. Devitrification is an irreversible effect and it is impossible to recover a devitrified

sample. As in the case of slowly frozen samples, temperature elevations above the glass transition temperature during the storage period can have fatal consequences for the sample quality and the risk of devitrification rises with the period and magnitude of the temperature elevation. It is also well-established that devitrification during warming has a detrimental effect on the quality of vitrified samples [75], [76]. It has recently been shown that high warming rates are very important for the survival and recovery of vitrified mouse oocytes [21], [34], [45], [77], [78]. In these studies, the role of the warming rate was shown to have an even higher impact on the success of the preservation than the cooling rate. This underlines that even short temperature elevations pose a significant risk of devitrification. This threat can be mitigated through an increased stability of the vitrified state, achieved for example by advanced cryopreservation media or temperature protocol. This will improve the resistance of a vitrified sample against unforeseen temperature elevations and ultimately leading to more consistent recovery rates of samples in long term storage.

The cooling rate required to reach the vitrified state is effectively another way to state a maximum duration and temperature a sample can withstand before ice is crystallizing. It is also highly dependent on the chemical composition of the sample [58], [61] and it can therefore be assumed that also the devitrification process is also dependent on the chemical composition of the sample. Devitrification is a relaxation process and does not occur instantaneously when the temperature exceeds the glass transition temperature. It is rather a time dependent process that depends both on the temperature and the chemical composition of the vitrification medium, i.e. the choice of CPA and its concentration.

Several studies have been performed to determine the ice crystallization kinetics for vitrified aqueous solutions with different CPA compositions [61], [75], [82], [187]–[189]. Most of these studies focus on determining the minimum cooling and heating rate required to successfully achieve a vitrified state and subsequently thaw under optimal conditions. In practice the highest possible cooling and heating rates are usually employed to ensure a successful preservation process.

The study in this work aims at shedding more light on the practical consequences of devitrification on biobank procedures and the handling of vitrified samples. To this end, commercially available PBS and CPAs will be used without any further purification steps in order to mimic conditions found in practical applications. The focus of the investigation addresses the question how long it takes for a sample to devitrify and thus indirectly how long a vitrified sample can safely be kept at this temperature.

In this section the devitrification and thus stability of glasses in samples with different CPA compositions will be investigated. In this manner, a protocol can be established and evaluated in order to estimate maximum exposure time a vitrified sample can withstand without appreciable devitrification. Furthermore, the influence of CPA concentration on the devitrification kinetics is investigated of common CPAs. The experimental procedure is tested on an established vitrification medium to preserve human embryonic stem cells (hESC) so that the stability of the vitrified state can be

directly compared for common CPAs. Based on these findings, improvements to current vitrification protocols are proposed.

In the following, the Johnson-Mehl-Avrami-Kolmogorov (JMAK) model is introduced to describe the devitrification process. Then, the methods used for sample preparation and experimental setup are described. The following common CPAs will be studied with respect to their influence on the devitrification dynamics: DMSO, ethylene glycol (EG) as well as EG/DMSO mixed at a 50:50 volume ratio. The three CPAs will be mixed in different concentrations expressed in wt%. In addition an established vitrification medium for hESC cultures in the following denoted the VS medium [26], [190], [191]. DSC measurements are performed at different temperature for each sample type to study the devitrification process. The results presented in this section have been published in [192].

6.3.1 Johnson-Mehl-Avrami-Kolmogorov model for devitrification

The devitrification process is usually described by the JMAK model [75], [188], [193]–[195]. This model will therefore be employed to analyze the ice crystallization kinetics during the devitrification process. The JMAK model describes crystallization in glasses or supercooled liquids. The model was developed and presented in a series of papers between 1937 and 1941 [196]–[200]. Here, the will be applied to model ice crystallization in vitrified samples. The JMAK model is developed for isothermal conditions only. Other studies used the JMAK model as a basis for further models where the temperature is increased constantly over time [193], [195], [201]–[204]. As pointed out in [194], [195] some theoretical problems arise with these models and only isothermal will therefore be used in this study.

Consider now a vitrified medium that has been heated to a constant temperature T_{iso} above the glass transition temperature T_g . It can be described as a supercooled liquid. At some point, ice crystals will nucleate and start to grow as show in Figure 6.12.

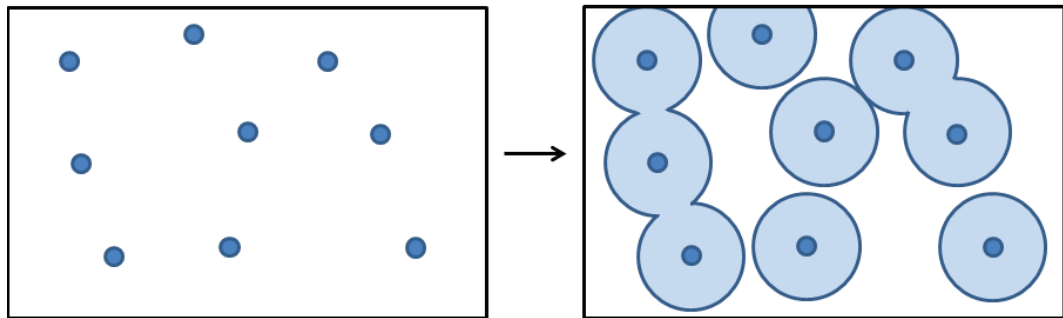


Figure 6.12 Schematic of the devitrification process. Above the glass transition temperature a series of ice nuclei can form and start to grow. Initially the crystal growth is not impeded, but as time goes on the ice crystals will come into contact. This slows down crystal growth since the crystal surface area is decreasing. Eventually, the crystal growth will come to a standstill.

During this initial part of the devitrification process the overall ice crystallization rate will increase as more ice grains form and grow. At some point ice crystals will come in contact and merge, reducing the surface area and thus the overall ice crystallization rate. In addition, the volume where new ice grains can nucleate is reduced slowing the nucleation of new ice crystals. Eventually the ice crystallization saturates and will come to a practical standstill. The devitrification process is thus dependent on both the nucleation rate and the growth rate of ice crystals. Both of these processes are dependent on temperature. Devitrification kinetics should thus be described as a time- and temperature-dependent process.

Under the assumption of isothermal conditions, the JMAK model gives an expression for the fraction of ice crystallized X at a time t [195]:

$$X(t) = 1 - \exp\left(-A \int_0^t I_v \left(\int_{t'}^t u dt'\right)^m dt'\right) \quad (6.6)$$

Here, I_v and u denotes the ice nucleation and growth rate, respectively. t' is the onset of nucleation. The dimensionality of ice crystallization growth is contained in m , a parameter that coincides with the dimensionality of the sample in the case of interface limited ice formation. A is a combined expression for all parameters that are constant over time. If the ice nucleation and crystal growth rate are assumed to be independent from each other and constant over time at the sample temperature T_{iso} , then equation (6.6) can be rewritten to the so-called Avrami equation [194]:

$$X(t) = 1 - \exp(-(K(T_{iso})t)^n) \quad (6.7)$$

Here, $K(T_{iso})$ denotes the crystallization constant at the sample temperature T_{iso} and contains both the ice nucleation and growth terms. n is related to the dimensionality of the crystallization in a similar manner as m . In this analysis a three-dimensional crystallization will be assumed. Dependent on the nucleation rate and whether the controlling mechanism of the ice crystallization is interface or diffusion limitation, the dimensionality parameter n can take different values as listed in Table 6.2 [194].

Table 6.2 Table with possible values for n under various conditions.

Nucleation rate	Interface limited	Diffusion limited
Constant	$n = 4$	$n = 5/2$
Zero	$n = 3$	$n = 3/2$

The crystallization constant exhibits an Arrhenius dependence on temperature:

$$K(T_{iso}) = K_0 \exp\left(-\frac{E_A}{RT_{iso}}\right) \quad (6.8)$$

The activation energy of devitrification and gas constant are denoted E_A and R respectively. K_0 is a constant that hypothetically describes the asymptotic crystallization constant at infinitely high temperature $T = \infty$, $K_0 = K(\infty)$. In order to ensure robust fitting of the crystallization constant equation (6.8) is transformed to a linear relation between $\ln(K)$ and T^{-1} :

$$\ln(K) = \ln(K_0) - \frac{E_A}{R} \cdot T^{-1} \quad (6.9)$$

To compare the devitrification kinetics between different chemical compositions a devitrification time t_x can be defined as the time it takes for x % of the devitrification to occur. Based on equation (6.7), the relative devitrification of the sample can be expressed as:

$$x = X(t_x) = 1 - \exp(-(K(T)t_x)^n) \quad (6.10)$$

This equation can then be solved to find the devitrification time t_x

$$t_x(T) = -\frac{\ln(1-x)^{1/n}}{K(T)} \quad (6.11)$$

This expression can then be used to extrapolate the devitrification time also for temperatures that exceed the measurement range once the temperature dependent crystallization constant has been determined. The devitrification time is an expression for the stability of a sample and high t_x indicates that the cryopreserved sample is robust against temperature fluctuations. Due to the asymptotic nature of the devitrification process, a full crystallization cannot be observed. Therefore t_{95} will be used in the following analysis as a timescale for quasi-complete devitrification. Devitrification times t_x for alternate crystallization fractions would effectively only shift $t_x(T)$ curves vertically and maintaining their shape. Any $t_x(T)$ -curve can thus be used as a parameter for the stability of the vitrified state.

6.3.2 Methods for devitrification measurements

By employing DSC, the devitrification process can be measured as it allows for measurement of the heat released during ice crystallization. By employing this technique isothermally, the devitrification process can be studied, since the heat flow is directly proportional to the ice crystallization rate. This section will describe the experimental procedures used and the application of the JMAK model to the measured data for these investigations before summarizing the parameters that will be extracted.

Sample preparation

To investigate the influence of the chemical composition on the devitrification, different CPAs in PBS and an established medium for vitrification, were used to prepare the samples. The following CPA compounds have been investigated: DMSO (WAK-Chemie Medical), EG (Sigma-Aldrich Chemie) and a 50 vol%/50 vol% EG/DMSO mixture. These compounds were added to PBS (Gibco, Thermo-Fischer Scientific) in varying concentrations in the range 43 wt% to 54 wt% and a total of 14 samples were prepared in this way. In addition, an established medium (VS) for vitrification of hESC cultures was investigated. The medium is prepared as described in the following [26]. A hESC medium comprised of Dulbecco's modified eagle medium (Gibco, Thermo Fisher Scientific DMEM F12) is supplemented with 0.1 mMol/l β -mercaptoethanol (Sigma-Aldrich Chemie GmbH), 20 % syntactical serum replacer, 2 mMol/l L-glutamine, 1 % non-essential amino acids, 4 ng/ml human recombinant bFGF, 100 U/ml penicillin and 100 μ g/ml streptomycin (all from Invitrogen). Then, 20 vol% DMSO and 20 vol% EG were added to the hESC culture medium as CPAs. Finally, 300 mMol sucrose (Sigma-Aldrich Chemie) was added.

To prepare samples for DSC measurements, 45 μ L of each solution were pipetted into a sample pan (B016-9321, 50 μ L, Perkin Elmer) as described in section 3.4. Each sample was weighed so that the magnitude of the DSC signal can be related to a specific amount of water. Then, the sample was sealed with an aluminum lid using a sample press (Perkin Elmer Universal Crimper Press). These steps are depicted in Figure 3.15. The sample was then loaded into the DSC along with an empty reference sample.

Temperature protocol

The JMAK model is only valid for isothermal conditions and a corresponding temperature DSC protocol will have to be employed. The devitrification is studied at different temperatures for each sample type so that the activation energy of the devitrification process E_A and the asymptotic crystallization constant K_0 can be determined for the different chemical compositions. After the sample is vitrified, the sample is heated to the isothermal temperature T_{iso} at which it is held so that the devitrification process can be investigated. Details on the isothermal DSC protocol can be found in section 3.4. Typically, isothermal temperatures range of 10-15 °C was investigated for each sample type.

To determine an upper limit for the isothermal temperature T_{iso} , a temperature-sweep (T-sweep) measurement was performed for each sample type before proceeding with isothermal measurements. Samples were heated from -145 °C to 20 °C at a heating rate of 10 °C/min and both a crystallization temperature T_C and the glass transition temperature T_g are retrieved from this experiment. As the heating rate of 10 °C is rather fast compared to the duration of the isothermal measurements, crystallization indicates that the devitrification is a very fast process at this crystallization temperature. This temperature can thus be used as a practical

temperature limit when studying devitrification at isothermal conditions. The theoretical upper limit for this type of measurements is the eutectic crystallization temperature, which will be discussed in section 6.3.4. Details on typical T-sweep protocols and the determination of crystallization and glass transition temperatures have been outlined in section 3.4.

Calorimetric measurements

In DSC the heat-flow, $Q(t)$ is measured over the course of a given temperature profile. In the case of devitrification, it can be assumed to be proportional to the crystallization rate of. This can be expressed in the following equation:

$$Q(t) \propto \frac{dX(t)}{dt} \quad (6.12)$$

The fraction of crystallized ice $X(t)$ can be retrieved from the heat flow $Q(t)$ determined in the DSC measurements based on the following equation:

$$X(t) = \frac{\int_0^t Q(t') dt'}{\int_0^{t_{end}} Q(t') dt'} \quad (6.13)$$

Here t_{end} is defined as the time when the crystallization process is complete, i.e. when $Q(t) = 0$ mW. In practice t_{end} is chosen as the time where $Q(t)$ is negligible and smaller than the background noise. This allows for an application of the JMAK model to data retrieved from the DSC measurements and thereby investigate the devitrification kinetics.

Dimensionality exponent n in the JMAK-model

Before taking a look on the complete DSC results the dimensionality exponent n has to be determined so that the DSC measurements can be properly interpreted. The value of n depends on the nucleation rate during the devitrification and the limiting factor of the crystallization process. The crystallization will be assumed to be a three-dimensional process what is justified considering that ice crystals have no preferred growth direction and that the sample containers do not limit growth in specific directions. To double check this, the JMAK model was applied to all data sets while keeping n as a variable. An average value of $n = 3.07 \pm 0.57$ has been found across all samples and temperatures investigated and $n = 3$ will therefore be used for all further analysis of the measurement data. This corresponds to an interface-limited crystallization process, see Table 6.2. Ice crystal growth is in this case limited from water molecules crossing the ice crystal surface.

Evaluation of measured data using the JMAK model

Here, an outline for the extraction of the devitrification kinetic parameters will be presented through an example of a typical measurement. Figure 6.13 shows an isothermal DSC measurement of the heat flow. Here, a 49 wt% EG/DMSO sample was kept at an isothermal temperature $T_{iso} = -100$ °C. From this measurement a maximum ice crystallization rate is seen at approximately 12 minutes and the devitrification process has run its course at around 30 minutes. Using equation (6.13), the crystallized fraction $X(t)$ can be calculated. From this the time t_{95} after which 95 % of the crystallization is completed can be determined to $t_{95} = 20.9$ minutes, as shown in Figure 6.13. The JMAK model described by equation (6.7) using $n = 3$ has been fitted to $X(t)$ and the crystallization constant $K(-100$ °C) of 0.067 min^{-1} for the isothermal temperature $T_{iso} = -100$ °C could be retrieved. The same experiment has been repeated at six different temperatures for this particular sample. The determined crystallization constants are shown in Figure 6.13 with an Arrhenius fit on the form of equation (6.9). The parameters for the devitrification constant could then be determined based on these data. For the 49 wt% EG/DMSO sample an activation energy for devitrification E_A of $57.8 \pm 0.7 \text{ kJ/mol}$ is found and the asymptotic crystallization constant $\ln(K_0)$ of $37.5 \pm 0.5 \ln(\text{min}^{-1})$. This data analysis has been applied to all measurements of the devitrification kinetics.

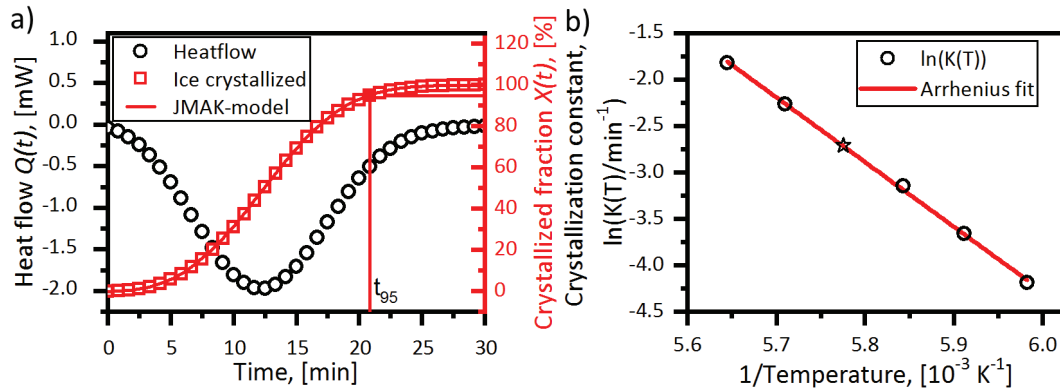


Figure 6.13 Here the heat flow of a typical isothermal measurement is shown. The sample consisted of 49 wt% EG/DMSO and was kept at -100 °C. From the heat flow the crystallized fraction $X(t)$ has been calculated. The JMAK model has been fitted to $X(t)$ to yield a crystallization constant of 0.067 min^{-1} using $n = 3$. A measured value for t_{95} has also been marked as a square. b) Here an Arrhenian fit is shown for the crystallization constant of the 49 wt% EG/DMSO sample. The fit yielded E_A of $57.8 \pm 0.7 \text{ kJ/mol}$ and a $\ln(K_0)$ of $37.5 \pm 0.5 \ln(\text{min}^{-1})$. The data point marked as a star corresponds to the measurement performed at -100 °C as shown in a).

The symmetrical shape of the devitrification curve remains unchanged as long as $I_v u^3$ describing the product of nucleation and growth rate is kept constant [196]. Since our data can be modelled by the JMAK model it can be concluded that either changes in $I_v u^3$ are negligible or that changes in the ice crystal nucleation and growth rates

compensate each other for the conditions used in the experiments. The latter scenario seems very improbable as the devitrification process is expected to be far more sensitive to changes in growth rate than nucleation rate due to the growth rate being cubed. For both DMSO and EG it is safe to assume that the nucleation rate during devitrification is zero above $-104\text{ }^{\circ}\text{C}$ according to literature [81], [205]. The devitrification experiments are however conducted at temperatures as low as $-120\text{ }^{\circ}\text{C}$ and nucleation cannot be neglected. The nucleation rate of DMSO has been shown to have a maximum at approximately $-130\text{ }^{\circ}\text{C}$ that rapidly decreases with increasing temperature [81]. Here the JMAK model with an exponent of $n = 3$ was furthermore found to model the data well indicating a negligible nucleation rate according to Table 6.2. The temperature-dependence of the devitrification process must therefore be dominated by changes in ice crystal growth rates in the experiments shown in this work.

CPA concentration increase through ice crystallization

When ice crystallizes in a vitrified sample then the CPA will concentrate between the ice crystals as they are poorly dissolved in ice. By integrating the crystallization dip of the T-Sweep measurement the amount of water crystallizing in the sample as a percentage of the total sample weight can be estimated. Correlating this to the total amount of water in the sample the overall increase of CPA concentration in the non-crystallized part of the sample can be estimated assuming that the CPA will be evenly distributed in the remaining liquid. CPA could be strongly enriched at the ice crystal grain boundaries during crystallization. It still allows for an estimation of the average increase of DMSO in the liquid. It is safe to assume that only ice is crystallizing during the course of the experiments. Since the formation of hydrates, the only other compounds that possibly could be present, is extremely unlikely compared to ice crystallization. This is corroborated by the absence of eutectic melting in the T-sweep measurement, which would have shown as an endothermic peak at the eutectic temperature depending on the hydrate formed [206].

A T-sweep measurement for the 43 wt% DMSO sample provides an example for the calculation of the CPA concentration increase. Here, energy of 1.13 J was found to be released during crystallization. Assuming a heat of fusion of pure water of 334 J/g ice must have formed from 3.38 mg H_2O corresponding to 7.0 wt% of the sample. In the following, this ratio of water crystallized will be denoted r_{ice} . The actual heat of fusion of ice crystals is slightly lower in binary mixtures [207] which leads to a slight underestimation of the water crystallized. The sample contained a total of 27.55 mg of water and the final DMSO concentration in the non-crystallized part of the sample can be calculated as:

$$\begin{aligned}
 C_{\text{CPA,end}} &= \frac{m_{\text{DMSO},0}}{m_{\text{DMSO},0} + m_{\text{H}_2\text{O},0} - m_{\text{H}_2\text{O},\text{crystallized}}} \\
 &= \frac{20.79\text{ mg}}{20.79\text{ mg} + 27.55\text{ mg} - 3.38\text{ mg}} = 0.462
 \end{aligned}
 \tag{6.14}$$

The absolute increase in CPA concentration, ΔC_{CPA} in the non-crystallized part is thus given as

$$\Delta C_{CPA} = C_{CPA,end} - C_{CPA,0} \quad (6.15)$$

$$\Delta C_{DMSO} = C_{DMSO,end} - C_{DMSO,0} = 46.2 \text{ wt\%} - 0.430 \text{ wt\%} = 3.2 \text{ wt\%} \quad (6.16)$$

It should be noted that these values are only estimates and not exact as the slope of the heat flow curve changes before and after the crystallization due to changes in heat capacity and a precise calculation of the heat flow integral is thus not possible. Precise integrals are not possible to perform due to a change in heat capacity and therefore slope of the DSC curve before and after the crystallization event. The heat of fusion is also unknown for these particular samples which leads to an underestimation of the CPA concentration increase as previously argued.

Summary of devitrification parameters extracted using DSC

For all the samples data is retrieved from both the T-sweep as well as the isothermal DSC measurements. Here a brief summary of the parameters describing the devitrification kinetics that is determined in work will be given.

From the T-Sweep the glass transition temperature T_g and a crystallization temperature T_C can be determined. From the magnitude of the crystallization dip the amount of water crystallizing in the sample r_{ice} can be calculated when related to the weight of the sample. This furthermore leads to an estimation of the resulting absolute increase in CPA concentration ΔC_{CPA} in the non-crystallized part of the samples for the relevant samples.

From the isothermal measurements and the application of the JMAK model the devitrification parameters of activation energy E_A and the asymptotic crystallization constant K_0 can be determined. In a second step $t_{95}(-100 \text{ }^\circ\text{C})$, the devitrification at $-100 \text{ }^\circ\text{C}$, and $T(t_{95} = 1 \text{ h})$, the temperature required for quasi-complete devitrification within one hour, can be calculated. Both $t_{95}(-100 \text{ }^\circ\text{C})$ and $T(t_{95} = 1 \text{ h})$ serve as a method to investigate the effect of changing the initial CPA concentration on the devitrification kinetics. This gives a measure that allow for a direct comparison of CPAs and concentration. This measures how stable a given sample is at specific temperatures and can be used as a parameter to evaluate handling procedures for a sample with a given CPA composition. Other temperatures or devitrification times could similarly be used to mimic the conditions of the handling procedure.

After the data has been presented for the various CPAs these parameters will be presented in Table 6.3.

6.3.3 Measurements of devitrification kinetics

Using this DSC technique DMSO, EG and EG/DMSO mixtures were investigated at varying concentrations. Each compound was investigated at four or five concentrations. Furthermore the VS medium was investigated. Here both the T-sweep measurements and the isothermal measurements will be presented for each CPA type along with the application of the JMAK model. The results are collected in Table 6.3.

DMSO:

The DSC measurements for the DMSO mixtures are summarized in Figure 6.14. Five concentrations of DMSO were investigated: 43 wt%, 44 wt%, 45 wt%, 46 wt% and 47 wt%. For each concentration, a 10 °C/min T-sweep DSC measurement was performed. These are shown in Figure 6.14a where the glass transition (triangle) and crystallization (circle) temperatures are marked. The crystallization temperature poses a practical upper limit to the isothermal DSC measurements and retrieved from the T-sweep measurements. It is seen to increase significantly with concentration which was expected as higher concentrations of DMSO typically result in a stronger tendency to form a glass [61]. By increasing the concentration of DMSO from 43 wt% to 46 wt%, the crystallization temperature increases from -110 °C to -77 °C. The crystallization temperature for the 47wt% sample is seen to be higher than that of 46 wt% which was unexpected and can be attributed to the crystallization dip partly overlapping the melting peak. This effectively skews and stretches the crystallization dip and a precise determination of the crystallization temperature becomes very difficult. The aim of these measurements was to establish an upper temperature limit for the isothermal measurements and a rough estimate of the crystallization temperature is sufficient. Isothermal measurements should generally not be performed close to or above the

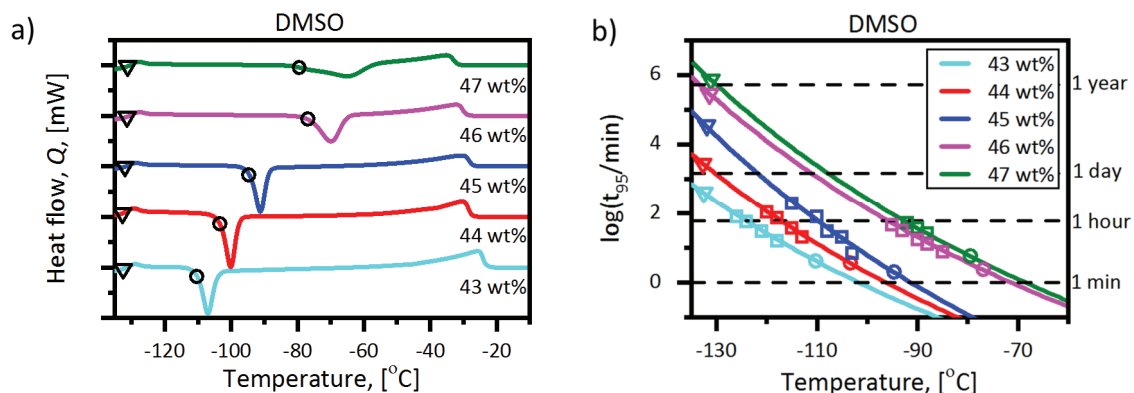


Figure 6.14 a) T-sweep DSC measurement using a heating rate of 10 °C/min for the DMSO-mixtures and the retrieved glass transition (triangles) and crystallization (circles) temperatures have been determined. b) Measured devitrification times t_{95} (squares) and fits according to the JMAK model. The glass transition temperature T_g (triangles) and crystallization temperature T_c (circles) retrieved from the 10 °C/min T-sweep measurement are also included.

eutectic temperature, which is approximately $-70\text{ }^{\circ}\text{C}$ for aqueous mixtures of DMSO [206]. It is furthermore observed that the glass transition temperature only varied slightly from $-132.5\text{ }^{\circ}\text{C}$ to $-131.1\text{ }^{\circ}\text{C}$ for different concentrations of DMSO. The melting temperature decreased with increasing the DMSO concentration. Both of these observations are accordance with other studies of DMSO mixtures [206], [208].

From the T-sweep measurements the amount of water crystallized in the sample has been estimated. This crystallization resulted in the DMSO concentration in the non-crystallized part increased by 3.2 wt% for the 43 wt% DMSO sample. Similarly a DMSO concentration increase of 3.5 wt% was found for both the 44 wt% and 45 wt% samples. It was not possible to estimate the amount of crystallized water in the 46 wt% and 47wt% samples since the crystallization dip were close to or overlapping the melting peak.

For each concentration, a series of isothermal DSC measurements were carried out at different temperatures. From these measurements, the devitrification time t_{95} was determined for all different concentrations of DMSO and isothermal holding temperatures. From these measurements, the temperature dependence of the crystallization constant is determined. Figure 6.14b shows these values (squares) along with a fit (lines) based on equations (6.9) and (6.11) that allows to retrieve the values of t_{95} based on the crystallization constant $K(T)$. The glass transition (triangles) and crystallization (circles) temperature retrieved from the $10\text{ }^{\circ}\text{C}/\text{min}$ T-sweep DSC measurement are shown along with at the devitrification times t_{95} for every particular mixture and temperature.

The devitrification times in Fig. 6.16b shows that the devitrification kinetics exhibits a strong dependence on the initial DMSO concentration. The higher the DMSO concentration, the more stable the amorphous state is. It can thus be concluded that the devitrification process slows down at higher concentrations. If samples are given devitrification times of, for example, one hour, the 43 wt% DMSO sample experiences a full crystallization already at very low temperatures around $-125\text{ }^{\circ}\text{C}$ whereas the 47 wt% DMSO is only fully devitrified at $-92\text{ }^{\circ}\text{C}$. This difference in sample stability is considerable and the 47 wt% DMSO sample is significantly less sensitive to short-term temperature elevations slightly above the glass transition temperature. These results show that even small changes in CPA concentration can lead to significant changes in the stability of the amorphous state.

EG

The results of the DSC measurement of the EG samples are shown in Figure 6.15. EG was investigated in concentrations of 50 wt%, 51 wt%, 52 wt%, 53 wt% and 54 wt%. The $10\text{ }^{\circ}\text{C}/\text{min}$ T-sweep measurements are shown in Figure 6.15a. Here the same overall trend as with the DMSO samples are seen, where higher concentrations lead to a higher crystallization temperature and a lower melting temperature whereas the glass transition temperature remains unaffected. By increasing the EG concentration from 50 wt% to 53 wt%, the crystallization temperature increases from $-94\text{ }^{\circ}\text{C}$

to -65°C . Even though EG has a higher eutectic temperature than DMSO [209] an overlap of the crystallization dip and the melting peak is still seen for the highest concentrations used in this study. Therefore, only the results from lower EG concentrations were used for the ice crystallization analysis. From the 50 wt% and 51 wt% samples, an increase of EG concentration during the crystallization by 5.5 wt% and 6.9 wt% in the non-crystallized part of the sample is estimated. This increase in the EG concentrations resulting from ice crystallization is significantly stronger than the concentration increase found for DMSO samples indicating that a higher percentage of the water crystallizes and that DMSO to a larger extent inhibits ice crystallization. The 52 wt% sample showed a lower melting temperature than expected compared to the other data sets. This is likely due to an error in the experimental procedure for this particular sample that caused a shift or mismatch of the temperature scale. The data for this sample have been kept to allow for a discussion of the consequences of such errors in the experimental procedure in section 6.3.4.

Figure 6.15b contains the measured devitrification times t_{95} (squares) and corresponding fit (lines) based on the JMAK model in equation (6.11). Again the same trend is seen as with the DMSO samples, namely a strong dependence of the devitrification time on the initial EG concentration. For the EG samples the one hour devitrification time spans the temperature range of approximately -110°C to -81°C for the investigated concentrations. This is a slightly shorter more narrow temperature range as that of DMSO. This indicates that the devitrification of EG samples is less dependent on the initial CPA concentration compared to DMSO. The measured values for the devitrification times of the 52 wt% sample does not lie in the expected ranges when comparing to the 51 wt% and 53 wt% samples what could be expected based on the errors in the experimental procedure mentioned before. An indication hereof was already found in the T-sweep measurements.

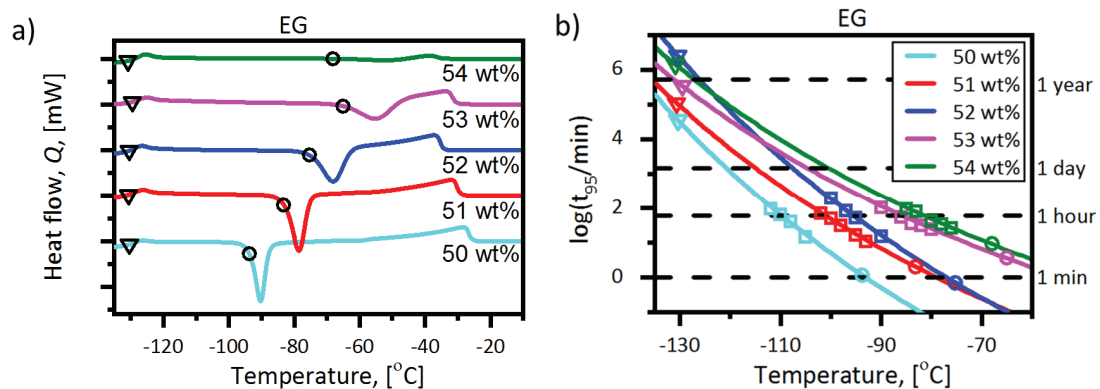


Figure 6.15 a) T-sweep DSC measurement using a heating rate of $10^{\circ}\text{C}/\text{min}$ for the EG-mixtures and the retrieved glass transition (triangles) and crystallization (circles) temperatures have been determined. b) Measured devitrification times t_{95} (squares) and fits according to the JMAK model. The glass transition temperature T_g (triangles) and crystallization temperature T_c (circles) retrieved from the $10^{\circ}\text{C}/\text{min}$ T-sweep measurement are also included.

EG/DMSO

The 50 vol% / 50 vol% EG/DMSO mixture was investigated in four different concentrations: 47 wt%, 48 wt%, 49 wt% and 50 wt%. The results of the DSC measurements are shown in Figure 6.16. The 10 °C/min T-sweep measurements in Figure 6.16a show that the crystallization temperature increases from -100 °C to -80 °C when increasing the CPA concentration from 47 wt% to 50 wt%. This increase of the crystallization temperature is, however, smaller compared to the samples with only either DMSO or EG where the crystallization temperature increased by the same variation of the concentration of 25 to 30 °C. This already gives a first hint that the EG/DMSO mixture is less sensitive to concentration changes. For the highest investigated concentration of 50 wt%, an overlap between the crystallization and melting peak can be observed. The crystallization temperature determined for this sample seems to align with the other measured crystallization temperatures retrieved from the EG/DMSO measurement series. This was slightly unexpected since an overlap between the crystallization dip and melting peak in the pure EG or DMSO samples led to an underestimation of the crystallization temperature. From the T-sweep measurements only small variations in the glass transition temperature between -130.5 °C and -131.5 °C are found. The increase in concentration ΔC_{CPA} after complete devitrification is 5.3 wt% for the 47 wt% sample and 5.1 wt% for the 48 wt% sample. These values are in between the data retrieved for the DMSO and EG samples as expected. For the 49 wt% sample there is a potential overlap between the crystallization dip and melting peak and the amount of crystallized water cannot be determined accurately. The measured and fitted devitrification times t_{95} are shown in Figure 6.16b. Here, an increase in devitrification times with increasing CPA concentration is seen as expected. The temperature required for complete

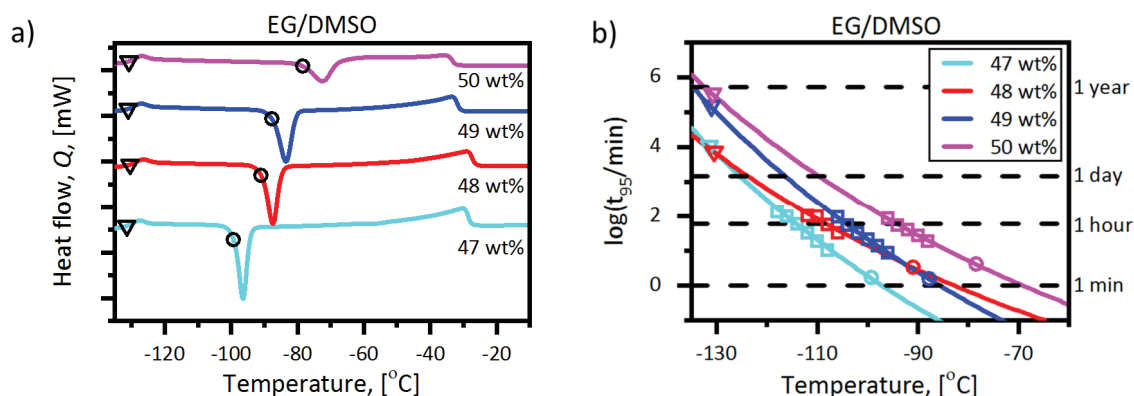


Figure 6.16 a) T-sweep DSC measurement using a heating rate of 10 °C/min for the EG/DMSO-mixtures and the retrieved glass transition (triangles) and crystallization (circles) temperatures have been determined. b) Measured devitrification times t_{95} (squares) and fits according to the JMAK model. The glass transition temperature T_g (triangles) and crystallization temperature T_c (circles) retrieved from the 10 °C/min T-sweep measurement are also included.

devitrification within one hour increases from -115 °C to -95 °C when increasing the concentration of EG/DMSO from 47 wt% to 50 wt%. This is a slightly shorter temperature interval as compared to either the DMSO or EG samples. This still holds true when compensating for the higher concentration range of 4 wt% that was investigated in the case of the EG and DMSO samples. The devitrification kinetics are thus less dependent on the concentration for the EG/DMSO mixture. As with the EG samples, there is one sample where the devitrification kinetics does not seem to align with the other samples. The devitrification times for the 48 wt% EG/DMSO sample has a lower slope compared to the other samples. This deviation could in part be attributed to the measurement performed at -112 °C where the measured t_{95} is lower than the corresponding extrapolation based on the measurements at other isothermal temperatures. The retrieved isothermal crystallization constant $K(-112\text{ °C})$ is then also lower which in effect reduces the activation energy E_A as yielded from the Arrhenius fit and thus the slope of the fitted t_{95} . From Figure 6.16a a melting temperature higher than expected for this particular sample was observed. This could indicate an error in the experimental procedure as with the 52 wt% EG sample and will also be discussed in section 6.3.4.

VS medium

Due to its application in the vitrification of hESC cultures, only a single sample with the VS medium was measured and the CPA concentration was thus not varied. Figure 6.17 shows the results of the DSC measurements. As it contains 38.5 wt% of the 50/50 EG/DMSO mixture, it can best be compared to the EG/DMSO samples and the data for the 47 wt% EG/DMSO sample are included in Figure 6.17 for comparison. The 10 °C/min T-sweep measurement of the VS medium is shown in Figure 6.17a. Here it is seen that the crystallization temperature is -104.4 °C which is lower than the lowest concentration of the EG/DMSO samples. This was to be expected since it only contain 38.5 wt% EG/DMSO as opposed to 47 wt%. The difference is, however, unexpectedly small when the significant difference in EG/DMSO concentration is taken into consideration. This effect can be attributed to the sucrose in the sample since the VS medium contains 300 mMol sucrose or 9.0 wt% sucrose in addition to the EG/DMSO. Sucrose is also used frequently as a CPA [22] and the 9.0 wt% thus contribute significantly to the overall preservation properties of the VS medium. Another noteworthy feature of the VS medium is that it shows the highest glass transition temperature $T_g = -128.9\text{ °C}$ of all the investigated samples. The low crystallization temperature is a clear indication that the sample should be less stable than the 47 wt% EG/DMSO sample but only the isothermal DSC measurements can reveal whether this can also be translated to decreased sample stability. From the crystallization dip an estimation of the ratio of crystallized water $r_{ice} = 7.8\text{ wt\%}$ is made. In the non-crystallized part of the sample initially containing 52.5 wt% water this causes an absolute increase of 3.3 wt% and 0.7 wt% of EG/DMSO and sucrose, respectively. This increase in the EG/DMSO concentration is very low compared to the values retrieved

for the EG/DMSO samples. Especially when considering the much lower initial CPA concentration in the VS medium, a much higher increase in CPA concentration would be expected.

The results of the isothermal DSC measurements are shown in Figure 6.17b. Here it is observed that the devitrification times t_{95} for the VS medium are lower than those of the 47 wt% EG/DMSO sample. It can thus be concluded that the VS medium has the least stable glass phase of all samples where both EG and DMSO are present. This was expected due to the low crystallization temperature found in the 10 °C/min T-Sweep measurement and the higher glass transition temperature does not seem to have a significant influence on the devitrification kinetics. As the concentration of 38.5 wt% EG/DMSO in the VS medium is significantly lower even shorter devitrification times would have been expected when comparing the 47 wt% EG/DMSO sample. The sucrose in the VS medium seems thus to have a significant stabilizing effect on the sample stability. The stability effect of sucrose on the VS medium is also confirmed by the temperature of -118.1 °C required for complete devitrification within one hour, very close to the value of -114.2 °C found for 47 wt% EG/DMSO.

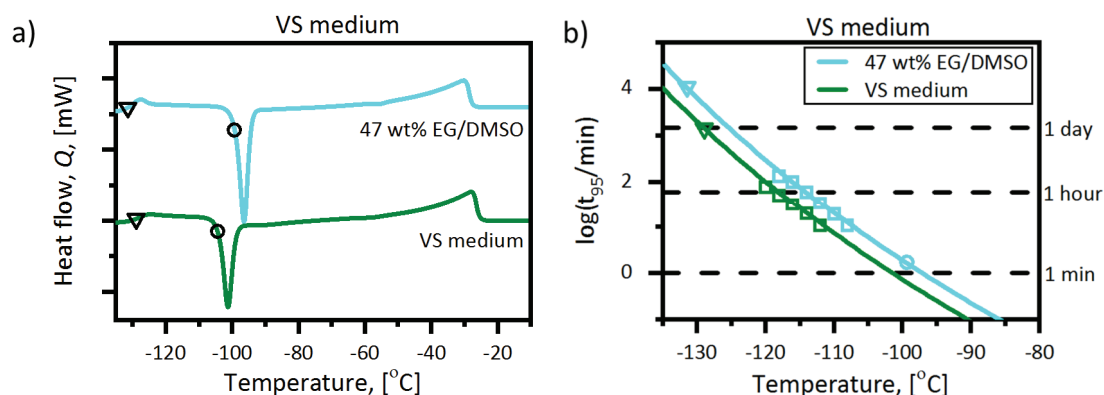


Figure 6.17 a) T-sweep DSC measurement using a heating rate of 10 °C/min for the VS medium and the retrieved glass transition (triangles) and crystallization (circles) temperatures have been determined. The DSC measurements for the 47 wt% EG/DMSO sample has also been shown for comparison. b) Measured devitrification times t_{95} (squares) and fits according to the JMAK model. The glass transition temperature T_g (triangles) and crystallization temperature T_c (circles) retrieved from the 10 °C/min T-sweep measurement are also included.

Summary of DSC measurements.

The parameters characterizing the devitrification are collected in Table 6.3 for all sample compositions. The values for the crystallization temperature marked with a star indicate an overlap between the crystallization dip and melting peak. The samples marked with two stars contain potential experimental errors as previously mentioned. From these isothermal measurements it should be clear that some chemical compositions are significantly more sensitive to temperature elevation in that the devitrification time is very short at -100 °C.

Table 6.3 Parameters extracted the T-sweep and isothermal DSC measurements. T_g , T_c , r_{ice} and ΔC_{CPA} were retrieved from the T-sweep measurements. E_A , K_0 , $t_{95}(-100^\circ\text{C})$ and $T(t_{95} = 1\text{ h})$ were retrieved from the isothermal measurements and based on fits to the JMAK model. T_c data points marked with a * indicate overlap between the crystallization dip and melting peak in the T-sweep measurements. ** indicates samples with potential experimental errors.

CPA	$C_{CPA,0}$	T_g	T_c	r_{ice}	ΔC_{CPA}	E_A	$\ln(K_0)$	$t_{95}(-100^\circ\text{C})$	$T(t_{95} = 1\text{ h})$
	[wt%]	[°C]	[°C]	[wt%]	[wt%]	[kJ/mol]	$\ln(\text{min}^{-1})$	[min]	[°C]
DMSO	43	-131.5	-110.2	7.0	3.2	38.8±1.4	27.6±1.1	0.77	-124.1
	44	-132.7	-103.3	7.4	3.5	41.8±4.6	28.7±3.5	1.92	-117.2
	45	-132.0	-94.6	6.6	3.5	54.6±7.1	36.5±5.2	6.13	-109.8
	46	-131.4	-76.8	NA	NA	49.9±0.9	30.1±0.6	136.0	-95.8
	47	-131.1	-79.4*	NA	NA	52.1±9.2	31.0±6.0	263.4	-92.6
EG	50	-130.4	-93.7	10.0	5.5	59.9±6.9	40.4±5.0	5.00	--109.8
	51	-130.7	-83.2	12.0	6.9	51.6±2.4	32.3±0.7	48.80	-101.0
	52**	-130.4	-75.2	NA	NA	64.2±1.1	39.7±0.7	188.4	-95.5
	53	-129.5	-65.0*	NA	NA	44.1±1.5	24.6±1.0	620.6	-85.8
	54	-130.9	-68.0*	NA	NA	46.1±5.9	25.2±3.7	1352.7	-81.4
EG/DMSO	47	-131.5	-99.3	10.2	5.3	55.9±1.4	38.5±3.0	1.88	-114.2
	48**	-130.5	-90.9	9.7	5.1	42.0±7.9	26.9±5.7	13.99	-108.3
	49	-131.0	-87.7	NA	NA	57.9±0.7	37.5±0.5	21.78	-104.3
	50	-130.8	-78.4*	NA	NA	49.7±1.9	29.6±1.3	186.1	-94.2
VS medium	38.5/9.0	-128.9	-104.4	7.8	3.3/0.7	54.3±2.4	38.4±1.8	0.73	-118.1

6.3.4 Discussion of the DSC measurements and the JMAK model

The devitrification can be studied using isothermal DSC measurements. As shown in Figure 6.13, the JMAK model can be used to describe the devitrification kinetics of the investigated chemical compositions. The Arrhenius dependence of the crystallization constant is a further indicator that the JMAK model provides a correct description of devitrification. It also allows us to make further observations regarding the crystal growth rate, ice crystal nucleation and the influence of CPA concentration. Based on the JMAK model, different media can directly be compared with respect to the amorphous state stability for temperatures above the glass transition temperature. It is, however, worth taking a closer look on the JMAK model before proceeding with a comparison of the media.

General discussion of the JMAK model

Multiple methods have been developed using non-isothermal DSC to investigate the devitrification kinetics [194]. Typically T-sweep measurements are used to investigate the dependence of the crystallization temperature on the heating rate. A T-sweep measurement usually takes less than a quarter of the time of an isothermal measurement depending on the experimental parameters. While this makes the isothermal technique used for the present study a very time-consuming technique this method is easy to perform and the data analysis does not require further assumptions or approximations to the JMAK model [193]–[195]. This makes the data processing straight forward and the obtained results in data that are easy to understand and employ in further practical applications.

Devitrification describes the process of ice crystallization in a sample that initially was vitrified, i.e. in a glassy state. Devitrification has several implications for the cryopreserved sample. As more and more water is crystallizing to ice, the water content of the remaining sample decreases what leads to an effective increase of the CPA concentration. This means that less water is available for further ice crystal growth and the higher CPA concentration results in a higher viscosity of the non-crystallized fraction of the sample [210], [211]. Both of these effects will cause a slowdown in the crystal growth rate. The JMAK model, however, assumes a constant crystal growth rate [196]. This discrepancy might lead to a deviation of the measured data from the model. Taking a look at the measurements again, for example the one depicted in Figure 6.13, a noticeable slowdown in the crystallization is not seen. It can thus be concluded that changes in the crystal growth rate due to an increase in CPA concentration are negligible. This becomes even more obvious when considering the variations of the crystal growth rate induced by temperature changes which is clearly seen from the devitrification charts shown in Figure 6.14b through Figure 6.17b. This is in accordance with another study using video-microscopy where ice crystal growth rates in 45 wt% DMSO samples were found to be constant albeit in a short timeframe below one minute [82].

From Table 6.3 it can furthermore be seen that the concentration increase in the non-crystallized fraction is in the range of the initial concentration differences between the individual samples. While it was observed that the initial concentration has a significant impact on the overall devitrification kinetics, the changes in CPA concentration due to crystallization of ice have only a negligible influence on the devitrification process and thus crystal growth rate. It can thus be concluded that the initial CPA concentration is mainly influencing the nucleation part of the devitrification process. This could in principle be checked by studying the granularity of the samples during vitrification similar to the experiments in section 6.2.3, but the non-transparent aluminum sealed sample containers required for ballistic cooling do not allow for optical measurements of the vitrified sample.

Nucleation in a vitrified sample can either be homogeneous when ice nuclei spontaneous self-assemble or heterogeneous when related to impurities, defects in the sample container or at cells in the samples. If this heterogeneous nucleation is constant it will not change the shape of the devitrification curve [196] but speed up the overall devitrification. Here, it is believed that this effect is minimal since sample to sample variations are not seen but rather consistent trends when changing the CPA concentration. For the EG/DMSO and VS medium samples, studies of the nucleation during the devitrification process have not been reported in the literature and there exists a possibility that ice crystals can nucleate during the devitrification process. A distinction between the temperature dependence on ice nucleation and the crystal growth rate can thus not be made. In order to make this distinction, other types of experiments would have to be performed for example in a similar way as the video-microscopy studies in [82]. For the EG/DMSO medium it can, however, still be concluded that the initial CPA concentration is primarily influencing the nucleation part of the devitrification process.

Finally, it can be extracted that the crystallization reaction must be an interface-controlled reaction from the JMAK model. This means that the ice crystal growth is limited by the rearrangement of water molecules directly on the ice grain surface and not by long-range transport of water molecules through the surrounding medium towards the ice crystal surface. This conclusion is first of all based on the average dimensionality exponent n that could be determined to 3.07 ± 0.57 . Under the assumption that the nucleation rate is negligible, this is an indication that the reaction is interface controlled. Another argument for this conclusion is that any appreciative effects of a decreasing water concentration are not seen and thereby increasing viscosity in the non-crystallized part of the sample. This would significantly influence the diffusion of water in the sample and thus have a non-negligible effect on the crystal growth kinetics. With a high-viscosity phase, such as the vitrified glassy aqueous phase in these samples, a gradient of water concentration would then arise leading to a lower water concentration at the ice-grain surface. Low water content in the direct vicinity of the ice grain surface would then slow down the ice crystal growth due to the limited availability of water molecules required for further ice crystal growth. This

effect is analogous to diffusion controlled chemical reactions where the reaction rate is limited by the transport rate of the reactants to the location of the chemical reaction. From this it follows that the ice crystal growth is interface limited.

The theoretical upper limit of the JMAK model is the eutectic temperature. Care should be taken when extrapolating t_{95} towards the glass transition and melting temperature. A vitrified sample is not in thermodynamic equilibrium and devitrification is a process in order to bring the sample back into equilibrium. A sample above the eutectic temperature has a different equilibrium sample composition compared to below this temperature. Ice crystal growth is then limited at a different absolute amount of ice in the sample which change the devitrification dynamics. This makes the eutectic temperature the theoretical upper limit for the JMAK model. The lower limit of the JMAK model is the glass transition temperature since this mark a change in the physical properties of the vitrified state such as the viscosity and heat capacity. Below the glass transition temperature the molecules in the sample are packed in a configuration with a low enough energy to be in a stable configuration compared to the amount of thermal energy present in the system and no crystallization will occur at all.

It turns out that both nucleation and ice crystal growth are not exhibiting Arrhenius dependence over a broad temperature range. It has been shown that nucleation of crystals in a solution of containing DMSO is not exhibiting an Arrhenius dependence [58], [81]. The ice crystal growth rate can be assumed to be an Arrhenian in a broader temperature range [195]. It does, however, deviate from an Arrhenius dependence since the viscosity shows that behavior close to the glass transition temperature according to the Vogel-Tammann-Fulcher- model [58] as discussed in section 2.2. In all cases an Arrhenius dependence of the crystallization constant was seen, as shown in Figure 6.13b. The crystal growth rate thus follows an Arrhenius dependence in the temperature ranges investigated. To approximate the devitrification kinetics in the ranges of time and temperatures used in practical applications handling procedures in biobanks, extrapolations of the crystal growth rates to higher temperatures can be assumed to be valid for temperatures below the eutectic temperature.

Measurement deviations

Two samples (52 wt% EG and 48 wt% EG/DMSO) showed a significantly different behavior compared to all the other measurements. It is noteworthy that these two samples deviate from the other ones in opposite directions, i.e. the 52 wt% EG sample has the highest activation energy with rather low standard deviation and the 48 wt% EG/DMSO has the lowest activation energy with rather high standard deviation. This indicates that different effects are influencing the measurements for the two samples. These will be discussed individually starting with the EG/DMSO sample at 48 wt%.

The deviation of the 48 wt% EG/DMSO can be attributed to an erroneous single measurement at -112 °C leading to a low activation energy with a high standard deviation. The raw data of the heat flow $Q(t)$, its conversion to crystallized fraction

$X(t)$ and the corresponding fit to the JMAK model of this particular measurement is shown in Figure 6.18a. The heat flow is seen to start at a negative value. From the isothermal measurement at $-112\text{ }^{\circ}\text{C}$ a devitrification time t_{95} of 100 min was found. If this particular measurement is excluded from further analysis, then devitrification times as shown in Figure 6.18b are found. Here the measurement at $-112\text{ }^{\circ}\text{C}$ is included as a red star while not part of the further analysis. Now the devitrification times for 48 wt% EG/DMSO sample align with the other concentrations.

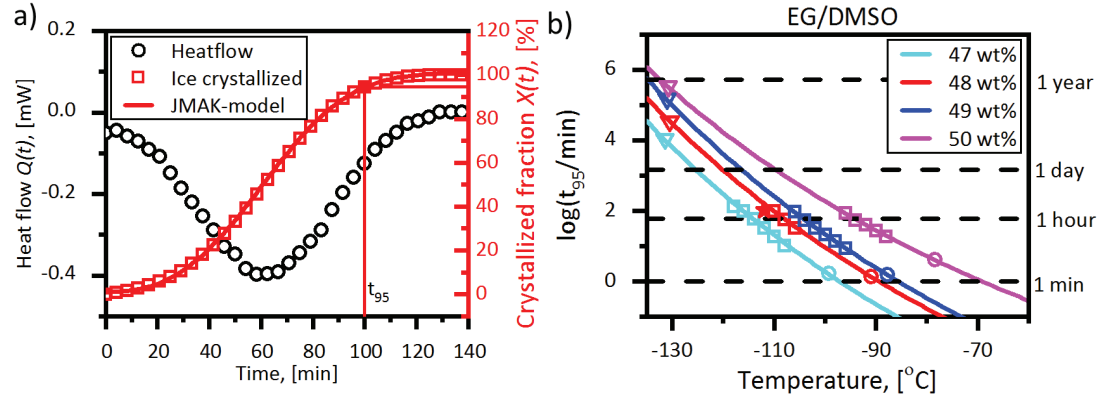


Figure 6.18 a) Heat flow data for the $-112\text{ }^{\circ}\text{C}$ 48 wt% EG/DMSO measurement. The heat flow has additionally been converted to the crystallized fraction $Q(t)$. A fit to the JMAK model gives the devitrification time $t_{95} \approx 100\text{ min}$. b) Devitrification times t_{95} for the EG/DMSO samples. Here the, $-112\text{ }^{\circ}\text{C}$ 48 wt% EG/DMSO measurement (marked as a red star) has been disregarded in the analysis. Based on fitting all other data points to the JMAK model (lines), a devitrification time t_{95} of 160 min was found for 48 wt% EG/DMSO sample.

The values extracted from applying the JMAK model to the 48 wt% EG/DMSO sample with and without the $-112\text{ }^{\circ}\text{C}$ measurement are listed in Table 6.4. Without the $-112\text{ }^{\circ}\text{C}$ measurement, both E_A and K_0 are seen to increase. Their standard deviations decrease which would be expected when excluding a deviating measurement from the analysis. The data shown in Table 6.4 give a better description of the devitrification kinetics in a sample containing 48 wt% EG/DMSO in PBS than the values listed in Table 6.3 and should be used for further discussion. Care should however be taken when concluding from this dataset since it only contain three data points.

Table 6.4 Comparison of devitrification parameters for the 48 wt% EG/DMSO sample with and without the inclusion of the measurement at $-112\text{ }^{\circ}\text{C}$ in the JMAK model analysis.

	With $-112\text{ }^{\circ}\text{C}$	Without $-112\text{ }^{\circ}\text{C}$
E_A	$42.0 \pm 7.9\text{ kJ/mol}$	$55.5 \pm 4.5\text{ kJ/mol}$
$\ln(K_0/\text{min}^{-1})$	26.9 ± 5.7	36.7 ± 3.3
$t_{95}(-100\text{ }^{\circ}\text{C})$	13.99 min	9.21 min
$T(t_{95} = 1\text{ h})$	$-108.3\text{ }^{\circ}\text{C}$	$-108.0\text{ }^{\circ}\text{C}$

Based on this analysis a devitrification time t_{95} of 160 min at $-112\text{ }^{\circ}\text{C}$ would be expected which is significantly longer than the measured 100 min. The isothermal has thus been subject to an event that resulted in a faster devitrification. If for instance the purge gas flow was incorrectly adjusted then a discrepancy between measured and actual sample temperature could occur which then leads to a faster than expected devitrification time. If not caused by an error in the experimental procedure, this can only be caused by the crystallization process already proceeding at a constant rate for the first ten minutes or a change in heat capacity before and after the devitrification. The baseline for the heat flow is determined as the plateau after the devitrification process. In this case a constant heat flow over 20,000 data points was used to determine the baseline heat flow representing 33 minutes after the devitrification process has ended. It seems unlikely that the crystallization rate starts and remains constant for a while before increasing. It is furthermore interesting that the starting heat flow differs from the heat flow after the devitrification process has ended. The consequence of this is that the JMAK model starts to deviate from the measured data at the tails of the crystallized fraction. As this deviation is minor as seen from Figure 6.18a and it cannot be the major concern for this particular sample and another reason must be found for the deviating values

The measured devitrification times for the 52 wt% EG sample did also not align with the other sample as the slope of the devitrification times seems be steeper than expected when compared to the other samples. All measurements of a single concentration are performed on a single sample and the measurements of the 52 wt% sample are consistent over the entire temperature range. Errors in the mixture preparation can be excluded since a too high or low EG concentration would shift the curve towards the 51 wt% or 53 wt% samples maintaining the slope. Either the nucleation properties of this particular sample have been influenced in some manner, thereby increasing the temperature sensitivity of the sample or an error has occurred in the experimental procedure. The nucleation would be affected by impurities in the mixtures or defects in the sample container. The calibration of the DSC instrument is highly dependent on a constant stable purge gas flow and changes in this can cause errors in the temperature or heat flow readout. This could have caused the deviations observed. The errors persisted for all measurements for this particular sample. It is therefore not possible to compensate as it was for the 48 wt% EG/DMSO measurement.

Both the crystallization temperature retrieved from the T-sweep measurements and the devitrification times determined in the isothermal measurements that were in good agreement with the results found for the other samples. These measurements can thus still be used to estimate the stability of these samples, but the results should not be extrapolated beyond temperatures used for the experiment due to the increase in slope. Even though the overall devitrification times seem to deviate substantially, the devitrification time at $-100\text{ }^{\circ}\text{C}$ $t_{95}(-100\text{ }^{\circ}\text{C})$ and the temperature required for quasi-complete vitrification $T(t_{95} = 1\text{ h})$ values can therefore still provide useful

information on a given medium composition. The isothermal measurement approach is thus rather robust toward minor errors in the experimental procedure.

EG & DMSO

Let us now evaluate the different CPA compositions investigated. The DMSO, EG and EG/DMSO samples will be discussed first before proceeding with the VS medium and relate the properties of this vitrification medium to the common CPA mixtures. It should be noted that in the following, only the initial CPA concentration used to prepare the samples is considered and not the increasing CPA concentration of non-crystallized fraction of the sample. The stability of the glassy state is determined by the initial CPA concentration. In the following, it will be investigated for all different CPA types which concentration is required in order to achieve a given level of stability and how changes in the CPA concentration translate into changes of the sample. To this end, the devitrification time at $-100\text{ }^{\circ}\text{C}$ $t_{95}(-100\text{ }^{\circ}\text{C})$ and the temperature required for quasi-complete devitrification $T(t_{95} = 1\text{ h})$ are studied as a function of concentration. These are shown in Figure 6.19 and convey the same information as the devitrification charts in Figure 6.14b through Figure 6.17b albeit on different scales due to the exponential correlation between time and temperature.

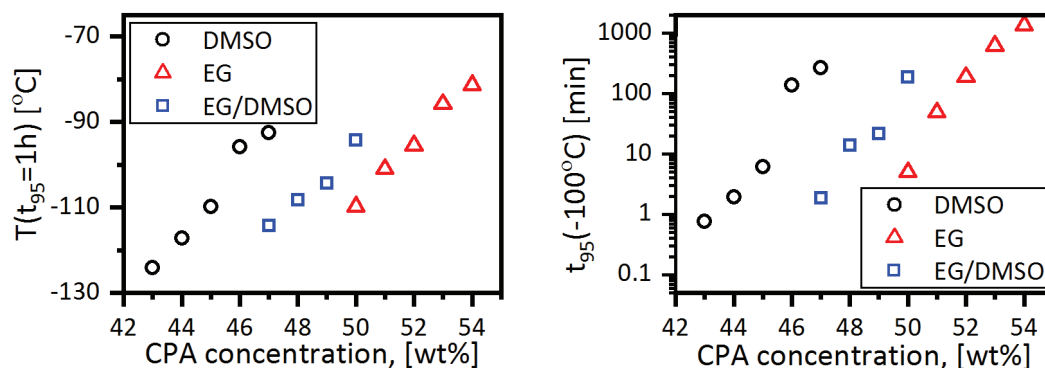


Figure 6.19 Dependence of initial CPA concentration on the devitrification kinetics. a) $T(t_{95} = 1\text{ h})$ and b) $t_{95}(-100\text{ }^{\circ}\text{C})$. $T(t_{95} = 1\text{ h})$.

From Figure 6.19 it can be seen that DMSO forms a glass that is more stable than EG which has also been found in other studies [189], [208]. The EG/DMSO mixture shows an intermediate stability as expected. In addition the CPA concentration required to achieve the same stability of the vitrified state is lower in the case of DMSO compared to EG. Let us now take a close look on the effect of changing the initial CPA concentration. The devitrification time $t_{95}(-100^{\circ}\text{C})$ changes by a factor of 342 when changing the concentration of DMSO by 4 wt%. This shows that even small increases in the CPA concentration can have a significant impact on the stability of the vitrified sample and make the difference between a devitrified and an intact sample, when handling the sample at a given temperature. When increasing the EG concentration by 4 wt%, the devitrification time $t_{95}(-100\text{ }^{\circ}\text{C})$ increases by a factor of 271. This means

that samples with DMSO as a CPA are more sensitive to changes in the initial CPA concentration. For practical applications in the field of cryopreservation, this can be viewed as a positive attribute since the properties of the vitrification medium can be manipulated with smaller concentration changes. This means that DMSO is the better CPA compared to EG when looking from the perspective of stability and its sensitivity to concentration change. There are, however, numerous other aspects affecting the choice of CPA. In order to achieve a successful vitrification procedure, these need to be considered when developing new vitrification media and protocols. One of these aspects is the cytotoxicity of the CPA. It is commonly known that DMSO is cytotoxic and extended exposure of cells to high concentrations of DMSO, should be avoided. This cytotoxicity is higher at elevated temperatures and different methods are employed where for example the CPA concentration is gradually increased along with decreased temperatures such as multistep or liquidus tracking have been developed [26], [58]. A high sensitivity of the amorphous state with respect to initial CPA concentration is advantageous for these approaches as it allows the stability to be improved with only minor concentration variations. In the case of a cytotoxic CPA, the sample stability can then be optimized while minimizing the detrimental effects by keeping the concentration relatively low. This underlines that the choice of CPA is always based on a trade-off between multiple parameters and the stability of the vitrified state is only one of many parameters that has to be taken into account.

The range of concentrations of EG/DMSO required to achieve a stable vitrified state comparable is in between the ones found for DMSO and EG as seen from Figure 6.19. This does not come as a surprise as an intermediate behavior would be expected for a mixture. It is therefore and unexpected finding that EG/DMSO is less sensitive to concentration changes than both DMSO and EG individually. By changing the concentration by 3 wt%, the devitrification time $t_{95}(-100\text{ }^{\circ}\text{C})$ only changes by a factor of 99 as compared to 177 and 124 for DMSO and EG, respectively. This means that the formation of new nuclei during freezing is less dependent on the overall CPA concentration in the vitrification medium. This can be attributed to the fact that the individual CPAs DMSO and EG are present in these samples in much lower concentrations. The concentrations required in order for water to react with DMSO or EG and form hydrates are much harder to reach in the EG/DMSO mixture. The properties of water are strongly changing when at least one compound in the solution allows for the formation of a hydrate. This effect is directly described in the binary phase diagrams for DMSO and EG. Far from the eutectic crystallization temperature the freezing point varies less with the concentration for lower absolute amounts of CPA. When both DMSO and EG are present but in lower concentrations, the properties of water and thus the formation of new ice nuclei is influenced by the presence of CPA to a lower extent.

VS medium

Let us now consider the VS medium. This sample has the shortest devitrification time $t_{95}(-100\text{ °C})$ of 0.73 min of all investigated samples and is thus less stable above the glass transition temperature compared to the other investigated CPA compositions. This is a very short devitrification time and appropriate measures would have to be implemented when cooling, handling and heating samples with this CPA composition. This can furthermore prove detrimental during longer storage times where the risk of unwanted temperature elevations increases. In addition, higher cooling and heating rates would be required for a successful preservation process. This raises the question of why this medium is employed in biobanking instead of more stable CPA compositions. Vitrification procedures are constantly being developed further and optimized [212], [213]. Especially the cooling and heating of cryopreserved samples have been the focus in order to improve the vitrification procedure. This means that the key to improve further and being able to preserve also very sensitive cell types does not lie in cooling or thawing more effectively but in the composition of the vitrification media. When the exterior parameters such as cooling, thawing and a very stable storage temperature have been fully optimized, any further improvements on the vitrification technique can only come from optimizing the interior parameters, i.e. the media composition, and new innovation can afford to not include the most stable and robust media compositions. If best practices are employed in maintaining high standards regarding the temperature protocol it can be beneficial for the overall quality of the sample to accept lower sample stability in order to reduce the negative effects of the CPAs. In the case of the VS medium studied here, the CPAs DMSO and EG have partially been replaced by sucrose. This effectively reduces the cytotoxic effects of DMSO and EG while maintaining the glass forming tendency. A trade-off was thus made where stability of the vitrified state was sacrificed in order to reduce cytotoxic effects. This does, however, require good standards for cooling, thawing and storage where the sample is protected against unwanted temperature elevations.

Activation energy

One of the describing characteristics of devitrification is the activation energy. A previous study found activation energies between 30 and 35 kJ/mol for ice crystal growth in DMSO solutions [194]. This is significantly lower than the activation energies in the range of 38 to 55 kJ/mol determined in this study as seen from Table 6.3. The activation energy for the 45 wt% was found here to 54.6 kJ/mol which is around 70 % higher than the value of 31.5 kJ/mol reported in [194]. This discrepancy can be attributed to the way both experiments are performed. The study in [194] is only investigating growth rates of single ice crystals that are spaced apart. Here, a macroscopic perspective is taken on the entire devitrification process including nucleation, ice crystal growth and recrystallization. These are all thermally activated processes that influence the overall activation energy of the devitrification. The main reason of the deviations is, however, found in the sample composition. The study in

[194] uses pure water as solvent whereas the PBS used for this study contains 155 mMol NaCl and 3 mMol phosphates (with different protonation levels). Electrolytes disturb the order of water on a molecular level which can have a significant impact on the ice crystal growth process. This shows that even small changes to such an experiment can have an effect on the devitrification dynamics and such DSC measurements should be done on samples that mimic real samples for cryopreservation as close as possible.

Critical cooling rate

Due to the direct relation between vitrification and devitrification, the data presented here mirror the critical cooling rate required to achieve a successful vitrification. Higher concentrations of CPA were found to result in a more stable vitrified state above the glass transition temperature. The critical cooling rate is similarly dependent on the CPA concentration and higher CPA concentrations have a lower critical cooling rate. Since the critical cooling rate is directly linked to the time a sample can stay at a given temperature before ice starts to crystallize, the presented devitrification data can directly reveal the cooling rates required to reach the vitrified state for a given sample composition. This means that samples with high concentrations of CPA are not only more robust towards temperature elevations over the glass transition temperature but also pose fewer requirements to the cooling method used.

A definite advantage of using the approach presented in this study is that the result is two parameters specific to a given media (E_A and K_0) and from these the stability of the vitrified sample can be described and the effect of exposure to elevated temperatures for a given duration can be determined. This is opposed to extracting the information from a time-temperature-transition (TTT) chart as presented in section 2.2.2 that states the time required for a given fraction to crystallize at a specific temperature [59]. The TTT-chart should similarly be established for each media in question.

6.3.5 DSC as an evaluation tool in biobanking

The use of DSC has already proven to be a valuable tool in biobanking for the characterization of cryopreservation media where phase transitions can be determined and investigated. It has furthermore been used to investigate critical cooling rates for different vitrification media [61]. The application of DSC has, however, not been limited to investigating purely chemical and physical characteristics of media used in cryobiology. Biological processes have also been investigated and one example of this is the use of DSC to measure water transport in cells during freezing [90], [214]. The study presented in this work shows that DSC can be used to study the devitrification kinetics of vitrified media.

In particular it was shown that DSC can be used to determine the stability of the amorphous state in a vitrified sample. This is an important parameter to characterize a

vitrification medium. Depending on the actual application and cell line that is to be preserved the robustness towards slight temperature elevations could prove to be the key to assure high quality of cryopreserved samples even small increases in initial CPA concentration increase the devitrification time significantly. The trade-off between sample stability and risks resulting from high CPA concentrations might be worth considering. It could be imagined that it is worth increasing the CPA slightly for an improved stability of the amorphous state at the cost of the detrimental effects caused by higher CPA concentrations.

The devitrification behavior can be determined in samples with well-defined vitrification media. The robustness towards temperature elevations above the glass transition temperature can be determined based on the characterization of a representative sample with the same chemical composition without extracting the sample from the storage tank and thereby endangering the preserved biological material. If a sample has experienced temperature elevations, for example through LN2 shortage, power shortage or prolonged handling in a cryobench, a worst case scenario can be established to determine the risk of devitrification.

The overall temperature is only rising slowly when the sample is exposed to an environment with elevated temperatures due to the low heat capacity of air. As the data in this work the devitrification kinetics at given isothermal sample temperatures the devitrification time t_{95} determined in this study can be seen as a worst case scenario. However, the sample volumes used for the preparation of vitrified samples are often small or have a container with high heat conductivity as described in section 2.1. Such samples would then experience a fast adaptation to the reservoir temperature and a rather pessimistic estimation of the stability might hold true in that case. When developing handling procedures, the worst case scenario described by isothermal DSC measurements can be used as upper limit for the temperature budget of the cryopreserved sample in such a manner that devitrification would not occur even for the most sensitive samples.

One could speculate that when a sample has been exposed to short temperature elevations multiple times but below temperatures where devitrification occurs that more ice nuclei form in the sample. The formation of these nuclei is irreversible and would be conserved below the glass transition temperature. More ice nuclei in a given sample before thawing commences increases the risk of devitrification. This puts an emphasis on the requirement of a very rapid thawing process in order to avoid devitrification upon warming. This effect can be deduced from the DSC measurements since the CPA concentrations reduce the amount of ice nuclei formed in the sample and thus increase the devitrification time. This can be concluded based on Figure 6.19 which shows the increase in devitrification time with CPA concentration and that $n = 3.07 \pm 0.57$. This is in line with other studies where it was shown that high heating rates are critical for the success of vitrification as a cryopreservation procedure [21], [34], [45], [77].

An evaluation of a new medium for vitrification would include four distinct steps. First the appropriate sample volume for the measurements is established so that the heat released during crystallization does not exceed the measurement capability of the DSC. Then a T-sweep measurement is performed in order to establish a temperature region in which the isothermal measurements can be performed. Here the upper limit is the onset of crystallization in the T-sweep measurement, as this temperature indicates the temperature where crystallization is a relatively fast event. Then isothermal measurements are performed where the sample is heated rapidly from a vitrified state to a holding temperature and held here for the duration of the devitrification process. This is repeated with the same sample for several temperatures at relevant temperature intervals. The final step is the data analysis where the heat flow data is converted to the crystallized fraction and fitted to the JMAK model. From this the devitrification times can be extracted for the relevant temperature intervals and crystallization fractions.

Since the measurements are performed on model samples DSC can as such not be applied in a retrospective analysis, but it gives valuable insight into the pitfalls and structural kinetics of vitrified samples. If a DSC analysis of the vitrification medium shows that there exists a major risk of devitrification in a sample then this particular sample could be investigated closer using a non-contact method such as Raman spectroscopy that method would be able to determine whether ice has crystallized in a sample. This could be done by employing a fiber-based Raman spectroscopy setup as discussed in section 5.5 [112]. This setup is capable to detect devitrification of vitrified samples and can thus be used as an additional tool for quality control in biobanks storing vitrified samples. DSC measurements and Raman spectroscopy complement each other. The DSC data can for instance help in quantifying the chemical compounds found with Raman spectroscopy and Raman spectroscopy can help identifying the processes measured using DSC. While neither of the methods alone can show the complete picture, they provide a powerful tool for quality control in biobanks when used together.

6.4 Recrystallization and devitrification: Parallels and differences

This chapter has been devoted to studying relaxation processes in cryopreserved samples. Here, both recrystallization in slowly frozen samples and devitrification of vitrified samples have been investigated. Recrystallization and devitrification can appear as very different processes but they do share similarities. In this section, various parallels and differences between the two processes will be highlighted.

Both recrystallization and devitrification are temperature-dependent relaxation processes that bring the sample toward a more favorable state with lower free energy in the sample. Both processes are unwanted in cryopreserved samples since they signify an unstable condition. Cryopreservation aims at keeping the sample in a stable

state where chemical and biological processes are arrested. Both processes thus indicate suboptimal storage conditions and can be used as a marker for sample aging. This can be exploited for quality control of cryopreserved samples during storage and sample conditions can be monitored and tracked when detecting markers for recrystallization and devitrification. The study of devitrification can furthermore be used to evaluate preservation media with respect to the stability of the vitrified state. Recrystallization cannot be used to evaluate preservation media in a similar fashion, since the slow freezing approach does not rely on the structural integrity of the sample but rather on the interplay between ice crystallization, medium concentration and cellular response.

Recrystallization mainly occurs in samples preserved using the slow freezing approach whereas devitrification only occurs in samples preserved through vitrification. The samples are thus very different in a structural manner. Slowly frozen samples consist of ice crystals and a complex network of concentrated medium whereas vitrified samples are a uniformly distributed glass. A slowly frozen sample is closer to equilibrium with respect to the phase composition at the given temperature, whereas the vitrified state is far from equilibrium. The resulting relaxation processes are therefore of completely different nature. Recrystallization is the redistribution of a crystalline phase whereas devitrification is a phase transition where ice crystals nucleate and grow.

Recrystallization and devitrification are similar in that both processes are governed by diffusion of water molecules and thus the viscosity in the dendritic channels and amorphous state, respectively. Both relaxation processes can be accelerated through an increase in temperature since this will lower the viscosity and this increase the mobility of the individual constituents of the sample. The viscosity in the dendritic channels of a slowly frozen sample is expected to be comparable to that of a vitrified sample since the CPA is concentrated to similar levels as used for the vitrification approach upon ice formation and growth. The temperature regime required for comparable process rates in the different sample types are, however, very different. Recrystallization requires higher temperatures in order for water molecules to break the crystal lattice bonds before a net diffusion takes place toward the larger ice crystals. This extra energy is not required in the devitrification process. This difference is reflected in the fact that similar relaxation rate were found when studying recrystallization around $-40\text{ }^{\circ}\text{C}$ but devitrification at much lower temperatures around $-100\text{ }^{\circ}\text{C}$.

Also the temperature-dependences of these processes are different in nature. Recrystallization is governed by diffusion and crystal surface effects. Both these processes depend on temperature in a similar manner. The temperature-dependence of recrystallization can thus be expressed as a simple Arrhenius relation. Devitrification is driven by nucleation and growth of ice crystals. These processes have maxima at very different temperatures. Growth of ice crystals is similar in nature to recrystallization but include only surface effects on the growing ice crystal and not on

both growing and shrinking ice crystals as in recrystallization. Devitrification will have a more complex temperature-dependence compared to recrystallization, with a maximum of the relaxation rate at a given temperature and smaller rates at lower and higher temperatures. In section 6.3 it was, however, shown that ice crystal nucleation has only a minor influence on the devitrification dynamics and the devitrification rate can still be approximated by an Arrhenius relation in the temperature range investigated. While devitrification and recrystallization is driven by different processes, they still show similarities in their temperature dependence albeit with different activation energies and process rate in the high temperature limit.

Devitrification and recrystallization lead to different changes in the sample morphology. Therefore, different measurement methods are optimal or even required in order to detect the different relaxation processes. In this work, DSC was used to study devitrification. This method cannot be applied for the detection of recrystallization since the absolute quantity of energy released by this process is too low and standard calorimetry cannot be used. As DSC measurements require special sealed aluminum containers, this technology cannot be used on stored cryopreserved samples. Here, Raman spectroscopy would be more suitable where distinct spectral signatures of ice or other involved compounds like hydrohalite can be detected. Also this method is not applicable for detection of recrystallization in stored samples since all these signatures are expected to be present in the sample but it is only their spatial distribution that reveals the recrystallization dynamics. Therefore, fluorescence imaging was used to study recrystallization in this work. Slowly frozen samples are well-suited for two-dimensional imaging technologies. For stored samples, however, the quality of the optical access is typically too bad in order to allow for a fine resolution of the ice crystal size distribution inside the sample. More quantitative methods like light scattering are better suited for this task as described in section 6.2.4. This technology should in principle also be able to detect devitrification, but even low amounts of ice could be detrimental and this low amount of ice crystals might be below the detection threshold. It is therefore crucial to choose a suitable method adapted to both the underlying aging process of a specific cryopreserved sample and to the specific limitations imposed by maintaining existing samples in their storage state.

7 CONCLUSION AND OUTLOOK

This thesis investigates different methods for retrospective analysis of cryopreserved samples and study slow processes that can occur in frozen media. To this end, a broad range of experimental techniques has been applied. It was possible to address the challenges and identifying specific requirements that need to be fulfilled in order to allow for a meaningful analysis. On this basis, key technologies suitable for retrospective analysis of cryopreserved samples during storage could be developed and tested.

Raman spectroscopy has been identified as a key technology since it can provide chemical and biological information of samples in a non-contact manner. Confocal Raman microscopy (CRM) allows for unprecedented chemical imaging of frozen samples and can be used to identify chemical compounds that act as a marker for specific events during a cryopreservation process. In-situ CRM has been used to probe the phase structure of slowly frozen samples at temperatures below the eutectic temperature. Here, ice and hydrohalite has been identified as two chemical markers that correlate to detrimental events that might occur during cryopreservation. Ice signifies devitrification for vitrified samples whereas hydrohalite signifies eutectic crystallization in slowly frozen samples. By using CRM at cryogenic temperatures along with novel colocalization data analysis, the hydrohalite distribution in murine fibroblasts and IPS cell colonies was investigated. With this method it was for the first time possible to distinguish between intra- and extracellular hydrohalite. The influence of CPA on hydrohalite formation was also investigated and it was found to significantly inhibit hydrohalite formation.

To gain further insights into the dynamics when the sample temperature is elevated during storage structural relaxation processes were investigated for both slowly frozen and vitrified samples. For slowly frozen samples, the rate of recrystallization of ice crystals was investigated using fluorescence microscopy. This study provides sufficient information in order to perform phenomenological retrospective analysis of sample during storage. By measuring the ice crystal size distribution and comparing it to its initial value it can be detected whether a sample has been exposed to elevated temperatures. For vitrified samples the formation of ice crystals, so-called devitrification, was investigated using differential scanning calorimetry (DSC). Here the JMAK model was found to describe the devitrification process well. Measurements showed that the initial CPA composition has a significant influence on the devitrification time of the amorphous vitrified sample and thus on the stability and robustness of the vitrified state toward devitrification.

The findings of these very fundamental studies can then be transferred into technologies and methods that allow improving on current protocols and quality control mechanisms. Throughout this work, several applications for the use in cryopreservation and biobanking have been discovered.

Vitrification media can be evaluated by DSC. Based on the procedure used in this work a vitrification medium can be characterized and its robustness toward devitrification can be predicted. When developing handling procedures, the stability of the vitrified state can be used to determine an upper limit for the temperature budget of a cryopreserved sample in such a manner that devitrification would not occur even for the most sensitive samples.

A method that allows for cross section imaging of whole vials during a cryopreservation process has been developed. Cross-section imaging of whole vials during cryopreservation is possible based on a novel sample container and freezing method. In this work, it has been used to study the distribution of cells in a suspension during slow freezing. This technology could also be used to study supercooling under more realistic conditions or help establishing deliberate freezing protocols where the cell position in the vial is controlled to further optimize the cryopreservation outcome. As method for non-contact measurements of cryopreserved samples, a fiber-optical method has been developed. It allows for retrospective analysis of samples during storage based on the extraction of Raman spectra. Relevant chemical markers that directly relate to the state of both slowly frozen and vitrified samples have been identified and can be used for monitoring samples already in storage. Such a sensor technology allows retrieving detailed information about the quality of a cryopreserved sample without the need for thawing of the sample.

Finally, a novel quality seal technology has been proposed that allows monitoring that the cold-chain has been kept throughout the lifetime of a cryopreserved sample. A protection from elevated temperatures is an important requirement for successful biobanking and a concept for a time-temperature indicator (TTI) based on recrystallization was developed in order to analyze the cold chain retrospectively. The TTI consists of a thin film of an aqueous binary mixture that is frozen along with the sample and provides good optical access for fluorescence imaging. If its ice crystal size distribution changes over time it can be concluded that the cold chain has been broken and a careful characterization of the TTI allows for an estimation of a time-temperature equivalent that the sample has been exposed to.

Despite numerous relevant findings and cryopreservation being in use for decades, there are still many open questions that will require further studies. Besides contributing to a better understanding of the cryopreservation process, this work highlights some of the scientific questions that are still unanswered.

The methods used in this work can be distinguished in imaging and non-imaging technologies. This work shows how novel optical measurement techniques can be employed in the field of cryobiology to gain new insights. While conventional

fluorescence microscopy is widely used to image biological samples, two-photon microscopy provides higher resolution and a longer penetration depth into the sample. It does, however, still require that relevant components of the sample are labeled with fluorescence markers. This restriction can be circumvented with CRM that images chemical compounds present throughout the sample without the need for specific additions or sample treatment. It allows for a study of the changing chemical environment that occurs during freezing of cell suspensions and is especially suitable for a detailed analysis of model systems. Since cryotubes that are commonly used as sample containers do not allow for imaging, other non-contact methods need to be used in order to extract information from samples in storage. The most promising non-imaging technology is Raman spectroscopy. It can extract chemical information of stored samples that was previously inaccessible. Different markers could be identified that are directly related to the quality of the sample and allow for retrospective analysis of the structural integrity. Further studies should be made in order to correlate these markers with the post-thaw quality of different sample types. In addition, direct markers for the biofunctionality should be sought in the fingerprint region of the Raman spectrum in order to directly retrieve information on the biological state of the sample. The corresponding signature of these markers is, however, expected to be very weak since cells are diluted in the extracellular matrix. A highly sensitive Raman measurement would need to be developed in order to resolve meaningful information from the fingerprint region.

Based on Raman spectroscopy, cryopreserved samples can be analyzed in a retrospective manner. Retrospective analysis is a new perspective on quality control in biobanking where the sample quality is monitored already during storage and not only assessed post thaw. This is particularly relevant for applications where a high sample quality is required or for applications where the sample material is very limited and valuable.

This thesis shows retrospective analysis of cryopreserved samples offers a distinctive advantage for quality control in biobanks.

8 REFERENCES

- [1] T. H. Jang *et al.*, “Cryopreservation and its clinical applications”, *Integr. Med. Res.*, vol. 6, no. 1, pp. 12–18, 2017.
- [2] P. J. Schmidt, “Basile J. Luyet and the Beginnings of Transfusion Cryobiology”, *Transfus. Med. Rev.*, vol. 20, no. 3, pp. 242–246, 2006.
- [3] R. Gosden, “Cryopreservation: A cold look at technology for fertility preservation”, *Fertil. Steril.*, vol. 96, no. 2, pp. 264–268, 2011.
- [4] C. Polge, A. U. Smith, and A. S. Parkes, “Revival of spermatozoa after vitrification and dehydration at low temperatures”, *Nature*, vol. 164, no. 4172, p. 666, 1949.
- [5] S. Loft and H. E. Poulsen, “Cancer risk and oxidative DNA damage in man”, *J. Mol. Med.*, vol. 74, pp. 297–312, 1996.
- [6] M. Yuille *et al.*, “Biobanking for Europe”, *Brief. Bioinform.*, vol. 9, no. 1, pp. 14–24, 2007.
- [7] D. Gross *et al.*, “Willingness to Donate Human Samples for Establishing a Dermatology Research Biobank: Results of a Survey”, *Biopreserv. Biobank.*, vol. 9, no. 3, pp. 265–271, 2011.
- [8] B. Kang *et al.*, “Current Status, Challenges, Policies, and Bioethics of Biobanks”, *Genomics Inform.*, vol. 11, no. 4, pp. 211–217, 2013.
- [9] F. Mackenzie, “Biobanking Trends, Challenges, and Opportunities”, *Pathobiology*, vol. 81, pp. 245–251, 2014.
- [10] E. Schmidt-Jortzig, Ed., *Human biobanks for research*. Deutscher Ethikrat, 2010.
- [11] J. Kinkorová, “Biobanks in the era of personalized medicine: objectives, challenges, and innovation”, *EPMA J.*, vol. 7, no. 4, pp. 1–12, 2016.
- [12] R. E. Hewitt, “Biobanking: the foundation of personalized medicine”, *Curr. Opin. Oncol.*, vol. 23, no. 1, pp. 112–119, 2011.
- [13] J. C. Davila, G. G. Cezar, M. Thiede, S. Strom, T. Miki, and J. Trosko, “Use and Application of Stem Cells in Toxicology”, *Toxicol. Sci.*, vol. 79, no. 2, pp. 214–223, 2004.
- [14] V. Ramakrishna, P. B. Janardhan, and L. Sudarsanareddy, “Stem Cells and Regenerative Medicine – A Review”, *Annu. Rev. Res. Biol.*, vol. 1, no. 4, pp. 79–110, 2011.
- [15] J. C. Schulz, A. Germann, B. Kemp-kamke, A. Mazzotta, H. von Briesen, and H. Zimmermann, “Towards a xeno-free and fully chemically defined cryopreservation medium for maintaining viability, recovery, and antigen-specific functionality of PBMC during long-term storage”, *J. Immunol. Methods*, vol. 382, pp. 24–31, 2012.
- [16] Y. Lou and X. Liang, “Embryonic stem cell application in drug discovery”, *Acta Pharmacol. Sin.*, vol. 32, pp. 152–159, 2011.
- [17] M. Rao, “Stem cells and regenerative medicine”, *Stem Cell Res. Ther.*, vol. 3, p. 27, 2012.
- [18] J. E. Olson *et al.*, “Biobanks and personalized medicine”, *Clin. Genet.*, vol. 86, pp. 50–55, 2014.
- [19] P. Mazur, “The Role of Intracellular Freezing in the Death of Cells Cooled at

- Supraoptimal Rates”, *Cryobiology*, vol. 14, no. 3, pp. 251–272, 1977.
- [20] S. Angel, H. von Briesen, Y.-J. Oh, M. K. Baller, H. Zimmermann, and A. Germann, “Toward Optimal Cryopreservation and Storage for Achievement of High Cell Recovery and Maintenance of Cell Viability and T Cell Functionality”, *Biopreserv. Biobank.*, vol. 14, no. 6, pp. 539–547, 2016.
 - [21] S. Seki and P. Mazur, “The dominance of warming rate over cooling rate in the survival of mouse oocytes subjected to a vitrification procedure”, *Cryobiology*, vol. 59, pp. 75–82, 2009.
 - [22] Z. Hubálek, “Protectants used in the cryopreservation of microorganisms”, *Cryobiology*, vol. 46, no. 3, pp. 205–229, 2003.
 - [23] J. E. Lovelock and M. W. H. Bishop, “Prevention of Freezing Damage to Living Cells by Dimethyl Sulphoxide”, *Nature*, vol. 183, no. 4672, pp. 1394–1395, 1959.
 - [24] R. Martin-Ibañez, C. Unger, A. Strömberg, D. Baker, J. M. Canals, and O. Hovatta, “Novel cryopreservation method for dissociated human embryonic stem cells in the presence of a ROCK inhibitor”, *Hum. Reprod.*, vol. 23, no. 12, pp. 2744–2754, 2008.
 - [25] F. Holm *et al.*, “An effective serum- and xeno-free chemically defined freezing procedure for human embryonic and induced pluripotent stem cells”, *Hum. Reprod.*, vol. 25, no. 5, pp. 1271–1279, 2010.
 - [26] A. F. Beier, J. C. Schulz, and H. Zimmermann, “Cryopreservation with a twist - Towards a sterile, serum-free surface-based vitrification of hESCs”, *Cryobiology*, vol. 66, no. 1, pp. 8–16, 2013.
 - [27] J. Saragusty and A. Arav, “Current progress in oocyte and embryo cryopreservation by slow freezing and vitrification”, *Reproduction*, vol. 141, pp. 1–19, 2011.
 - [28] M. Baker, “Building Better Biobanks”, *Nature*, vol. 486, pp. 141–146, 2012.
 - [29] P. Mazur, “Freezing of living cells: mechanisms and implications”, *Am. J. Physiol.*, vol. 247, no. 3, pp. C125–C142, 1984.
 - [30] R. Spindler, B. Rosenhahn, N. Hofmann, and B. Glasmacher, “Video analysis of osmotic cell response during cryopreservation”, *Cryobiology*, vol. 64, no. 3, pp. 250–260, 2012.
 - [31] S. Seki and P. Mazur, “Kinetics and activation energy of recrystallization of intracellular ice in mouse oocytes subjected to interrupted rapid cooling”, *Cryobiology*, vol. 56, no. 3, pp. 171–180, 2008.
 - [32] D. Dörr, M. Stark, F. Erhart, H. Zimmermann, and F. Stracke, “Multiphoton microscopy for the in-situ investigation of cellular processes and integrity in cryopreservation”, *Biotechnol. J.*, vol. 4, pp. 1215–1221, 2009.
 - [33] J. Dong, J. Malsam, J. C. Bischof, A. Hubel, and A. Aksan, “Spatial distribution of the state of water in frozen mammalian cells”, *Biophys. J.*, vol. 99, no. 8, pp. 2453–2459, 2010.
 - [34] S. Seki and P. Mazur, “Effect of Warming Rate on the Survival of Vitrified Mouse Oocytes and on the Recrystallization of Intracellular Ice”, *Biol. Reprod.*, vol. 79, pp. 727–737, 2008.
 - [35] A. A. Gage and J. Baust, “Mechanisms of tissue injury in cryosurgery”, *Cryobiology*, vol. 37, pp. 171–86, 1998.
 - [36] N. E. Hoffmann and J. C. Bischof, “The cryobiology of cryosurgical injury”, *Urology*, vol. 60, no. 2A, pp. 40–49, 2002.
 - [37] P. Mazur, “Stopping Biological Time: The Freezing of Living Cells”, *Ann. N. Y.*

- Acad. Sci.*, vol. 541, no. 1, pp. 514–531, 1988.
- [38] J. G. Day and G. N. Stacey, “Biobanking”, *Mol. Biotechnol.*, vol. 40, no. 2, pp. 202–213, 2008.
 - [39] T. Remer, G. Montenegro-Bethancourt, and L. Shi, “Long-term urine biobanking: Storage stability of clinical chemical parameters under moderate freezing conditions without use of preservatives”, *Clin. Biochem.*, vol. 47, no. 18, pp. 307–311, 2014.
 - [40] J. E. Lovelock, “The haemolysis of human red blood-cells by freezing and thawing”, *Biochim. Biophys. Acta*, vol. 10, pp. 414–426, 1953.
 - [41] J. E. Lovelock, “The Protective Action of Neutral Solutes against Haemolysis by Freezing and Thawing”, *Biochem. J.*, vol. 56, pp. 265–270, 1954.
 - [42] B. Fuller and S. Paynter, “Fundamentals of cryobiology in reproductive medicine”, *Reprod. Biomed. Online*, vol. 9, no. 6, pp. 680–691, 2004.
 - [43] H. T. Meryman, “Cryopreservation of living cells: principles and practice”, *Transfusion*, vol. 47, pp. 935–945, 2007.
 - [44] A. Sakai and F. Engelmann, “Vitrification, encapsulation-vitrification and droplet-vitrification: A review”, *CryoLetters*, vol. 28, no. 3, pp. 151–172, 2007.
 - [45] S. Seki and P. Mazur, “Ultra-rapid warming yields high survival of mouse oocytes cooled to -196°C in dilutions of a standard vitrification solution”, *PLoS One*, vol. 7, no. 4, pp. 1–9, 2012.
 - [46] M. L. Shepard, C. S. Goldston, and F. H. Cocks, “The H₂O-NaCl-Glycerol Phase Diagram and Its Application in Cryobiology”, *Cryobiology*, vol. 13, pp. 9–23, 1976.
 - [47] N. K. Gilra, “Homogeneous Nucleation Temperature of Supercooled Water”, *Phys. Lett. A*, vol. 28A, no. 1, pp. 51–52, 1968.
 - [48] F. W. Starr, C. A. Angell, and H. E. Stanley, “Prediction of entropy and dynamic properties of water below the homogeneous nucleation temperature”, *Phys. A Stat. Mech. its Appl.*, vol. 323, pp. 51–66, 2003.
 - [49] A. Fowler and M. Toner, “Cryo-Injury and Biopreservation”, *Ann. N. Y. Acad. Sci.*, vol. 1066, pp. 119–135, 2005.
 - [50] J. O. M. Karlsson and M. Toner, “Long-term storage of tissues by cryopreservation: critical issues”, *Biomaterials*, vol. 17, no. 3, pp. 243–256, 1996.
 - [51] H. Ishiguro and B. Rubinsky, “Mechanical Interactions between Ice Crystals and Red Blood Cells during Directional Solidification”, *Cryobiology*, vol. 31, pp. 483–500, 1994.
 - [52] B. Han and J. C. Bischof, “Direct cell injury associated with eutectic crystallization during freezing”, *Cryobiology*, vol. 48, no. 1, pp. 8–21, 2004.
 - [53] G. M. Fahy, D. R. Macfarlane, C. A. Angell, and H. T. Meryman, “Vitrification as an Approach to Cryopreservation”, *Cryobiology*, vol. 21, pp. 407–426, 1984.
 - [54] W. F. Rall and G. M. Fahy, “Ice-free cryopreservation of mouse embryos at -196°C by vitrification”, *Nature*, vol. 313, no. 6003, pp. 573–575, Feb. 1985.
 - [55] P. G. Debenedetti and H. Stillinger Frank, “Supercooled liquids and the glass transition”, *Nature*, vol. 410, pp. 259–267, 2001.
 - [56] C. A. Angell, “Formation of Glasses from Liquids and Biopolymers”, *Science*, vol. 267, no. 5206, pp. 1924–1935, 1995.
 - [57] D. R. Macfarlane, “Physical Aspects of Vitrification in Aqueous Solutions”, *Cryobiology*, vol. 24, pp. 181–195, 1987.
 - [58] B. Wowk, “Thermodynamic aspects of vitrification”, *Cryobiology*, vol. 60, no. 1,

- pp. 11–22, 2010.
- [59] D. R. Uhlmann, “A Kinetic Treatment of Glass Formation”, *J. Non. Cryst. Solids*, vol. 7, pp. 337–348, 1972.
 - [60] J. Dubochet and A. W. McDowell, “Vitrification of Pure Water for Electron Microscopy”, *J. Microsc.*, vol. 124, pp. 3–4, 1981.
 - [61] R. L. Sutton, “Critical cooling rates to avoid ice crystallization in solutions of cryoprotective agents”, *J. Chem. Soc. Faraday Trans.*, vol. 87, no. 1, pp. 101–105, 1991.
 - [62] G. Vajta *et al.*, “Open pulled straw (OPS) vitrification: A new way to reduce cryoinjuries of bovine ova and embryos”, *Mol. Reprod. Dev.*, vol. 51, pp. 53–58, 1998.
 - [63] M. Lane and D. K. Gardner, “Vitrification of mouse oocytes using a nylon loop”, *Mol. Reprod. Dev.*, vol. 58, pp. 342–347, 2001.
 - [64] B. E. Reubinoff, M. F. Pera, G. Vajta, and A. O. Trounson, “Effective cryopreservation of human embryonic stem cells by the open pulled straw vitrification method”, *Hum. Reprod.*, vol. 16, no. 10, pp. 2187–2194, 2001.
 - [65] M. Kuwayama, “Highly efficient vitrification for cryopreservation of human oocytes and embryos: The Cryotop method”, *Theriogenology*, vol. 67, pp. 73–80, 2007.
 - [66] J. K. Choi *et al.*, “Bio-inspired solute enables preservation of human oocytes using minimum volume vitrification”, *J. Tissue Eng. Regen. Med.*, pp. 1–8, 2017.
 - [67] L. Ji, J. J. De Pablo, and S. P. Palecek, “Cryopreservation of adherent human embryonic stem cells,” *Biotechnol. Bioeng.*, vol. 88, no. 3, pp. 299–312, 2004.
 - [68] B. C. Heng *et al.*, “Loss of viability during freeze-thaw of intact and adherent human embryonic stem cells with conventional slow-cooling protocols is predominantly due to apoptosis rather than cellular necrosis”, *J. Biomed. Sci.*, vol. 13, no. 3, pp. 433–445, 2006.
 - [69] K. J. Amps, M. Jones, D. Baker, and H. D. Moore, “In situ cryopreservation of human embryonic stem cells in gas-permeable membrane culture cassettes for high post-thaw yield and good manufacturing practice”, *Cryobiology*, vol. 60, no. 3, pp. 344–350, 2010.
 - [70] J. Farrant, “Mechanism of cell damage during freezing and thawing and its prevention”, *Nature*, vol. 205, no. 4978, pp. 1284–1287, 1965.
 - [71] B. C. Elford, “Diffusion and distribution of dimethyl sulphoxide in the isolated guinea-pig taenia coli”, *J. Physiol.*, vol. 209, pp. 187–208, 1970.
 - [72] B. C. Elford and C. A. Walter, “Preservation of Structure and Function of Smooth Muscle cooled to -79°C in Unfrozen Aqueous Media”, *Nat. New Biol.*, vol. 236, pp. 58–60, 1972.
 - [73] B. C. Elford and C. A. Walter, “Effects of electrolyte composition and pH on the structure and function of smooth muscle cooled to -79°C in unfrozen media”, *Cryobiology*, vol. 9, pp. 82–100, 1972.
 - [74] A. Abazari, N. M. Jomha, J. A. W. Elliott, and L. E. McGann, “Cryopreservation of articular cartilage”, *Cryobiology*, vol. 66, no. 3, pp. 201–209, 2013.
 - [75] D. R. Macfarlane, “Devitrification in glass-forming aqueous solutions”, *Cryobiology*, vol. 23, pp. 230–244, 1986.
 - [76] J. O. M. Karlsson, “A theoretical model of intracellular devitrification”, *Cryobiology*, vol. 42, no. 3, pp. 154–169, 2001.
 - [77] P. Mazur and S. Seki, “Survival of mouse oocytes after being cooled in a

- vitrification solution to -196°C at 95° to $70,000^{\circ}\text{C}/\text{min}$ and warmed at 610° to $118,000^{\circ}\text{C}/\text{min}$: A new paradigm for cryopreservation by vitrification”, *Cryobiology*, vol. 62, pp. 1–7, 2011.
- [78] B. Jin, F. W. Kleinhans, and P. Mazur, “Survivals of mouse oocytes approach 100% after vitrification in 3-fold diluted media and ultra-rapid warming by an IR laser pulse”, *Cryobiology*, vol. 68, no. 3, pp. 419–430, 2014.
 - [79] T. Loerting, M. Bauer, I. Kohl, K. Watschinger, K. Winkel, and E. Mayer, “Cryoflotation: Densities of amorphous and crystalline ices”, *J. Phys. Chem. B*, vol. 115, no. 48, pp. 14167–14175, 2011.
 - [80] C. A. Angell, K. L. Ngai, G. B. McKenna, P. F. McMillan, and S. W. Martin, “Relaxation in glassforming liquids and amorphous solids”, *J. Appl. Phys.*, vol. 88, no. 6, pp. 3113–3157, 2000.
 - [81] J. M. Hey and D. R. MacFarlane, “Crystallization of Ice in Aqueous Solutions of Glycerol and Dimethyl Sulfoxide 1. A Comparison of Mechanisms”, *Cryobiology*, vol. 33, pp. 205–216, 1996.
 - [82] J. M. Hey and D. R. MacFarlane, “Crystallization of Ice in Aqueous Solutions of Glycerol and Dimethyl Sulfoxide 2: Ice Crystal Growth Kinetics”, *Cryobiology*, vol. 37, pp. 119–130, 1998.
 - [83] C. T. Moynihan, A. J. Easteal, J. Wilder, and J. Tucker, “Dependence of the Glass Transition Temperature on Heating and Cooling Rate”, *J. Phys. Chem.*, vol. 78, no. 26, pp. 2673–2677, 1974.
 - [84] K. L. K. Cook and R. W. Hartel, “Mechanisms of Ice Crystallization in Ice Cream Production”, *Compr. Rev. Food Sci. Food Saf.*, vol. 9, pp. 213–222, 2010.
 - [85] L. Bogliolo *et al.*, “Evaluation of the impact of vitrification on the actin cytoskeleton of in vitro matured ovine oocytes by means of Raman microspectroscopy”, *J. Assist. Reprod. Genet.*, vol. 32, pp. 185–193, 2015.
 - [86] M. A. Khalili, A. Shahedi, S. Ashourzadeh, S. A. Nottola, G. Macchiarelli, and M. G. Palmerini, “Vitrification of human immature oocytes before and after in vitro maturation : a review”, *J. Assist. Reprod. Genet.*, vol. 34, pp. 1413–1426, 2017.
 - [87] A. Downes, R. Mouras, P. Bagnanichi, and A. Elfick, “Raman spectroscopy and CARS microscopy of stem cells and their derivatives”, *J. Raman Spectrosc.*, vol. 42, no. 10, pp. 1864–1870, 2011.
 - [88] T. Acharya and R. V. Devireddy, “Cryomicroscopic Investigations of Freezing Processes in Cell Suspensions”, *Open Biotechnol. J.*, vol. 4, pp. 26–35, 2010.
 - [89] D. Peckys and P. Mazur, “Regulatory volume decrease in COS-7 cells at 22°C and its influence on the Boyle van’t Hoff relation and the determination of the osmotically inactive volume”, *Cryobiology*, vol. 65, no. 1, pp. 74–78, 2012.
 - [90] S. Mori, J. Choi, R. V. Devireddy, and J. C. Bischof, “Calorimetric measurement of water transport and intracellular ice formation during freezing in cell suspensions”, *Cryobiology*, vol. 65, no. 3, pp. 242–255, 2012.
 - [91] J. Choi and J. C. Bischof, “Review of biomaterial thermal property measurements in the cryogenic regime and their use for prediction of equilibrium and non-equilibrium freezing applications in cryobiology”, *Cryobiology*, vol. 60, no. 1, pp. 52–70, 2010.
 - [92] S. L. Stott and J. O. M. Karlsson, “Visualization of intracellular ice formation using high-speed video cryomicroscopy”, *Cryobiology*, vol. 58, no. 1, pp. 84–95, 2009.
 - [93] P. Mazur, S. Seki, I. L. Pinn, F. W. Kleinhans, and K. Edashige, “Extra- and intracellular ice formation in mouse oocytes”, *Cryobiology*, vol. 51, no. 1, pp. 29–53, 2005.

- [94] R. C. Prickett, L. A. Marquez-Curtis, J. A. W. Elliott, and L. E. McGann, "Effect of supercooling and cell volume on intracellular ice formation", *Cryobiology*, vol. 70, no. 2, pp. 156–163, 2015.
- [95] A. Sartori, R. Gatz, F. Beck, A. Rigort, W. Baumeister, and J. M. Plitzko, "Correlative microscopy: Bridging the gap between fluorescence light microscopy and cryo-electron tomography", *J. Struct. Biol.*, vol. 160, no. 2, pp. 135–145, 2007.
- [96] A. I. Younis, M. Toner, D. F. Albertini, and J. D. Biggers, "Cryobiology of non-human primate oocytes", *Hum. Reprod.*, vol. 11, no. 1, pp. 156–165, 1996.
- [97] C. L. Schwartz, V. I. Sarbash, F. I. Ataullakhanov, J. R. McIntosh, and D. Nicastro, "Cryo-fluorescence microscopy facilitates correlations between light and cryo-electron microscopy and reduces the rate of photobleaching", *J. Microsc.*, vol. 227, no. 2, pp. 98–109, 2007.
- [98] P. Schwille, U. Haupts, S. Maiti, and W. W. Webb, "Molecular Dynamics in Living Cells Observed by Fluorescence Correlation Spectroscopy with One- and Two-Photon Excitation", *Biophys. J.*, vol. 77, no. 4, pp. 2251–2265, 1999.
- [99] W. R. Zipfel, R. M. Williams, and W. W. Webb, "Nonlinear magic : multiphoton microscopy in the biosciences", *Nat. Biotechnol.*, vol. 21, no. 11, pp. 1369–1377, 2003.
- [100] M. Göppert-Mayer, "Über Elementarakte mit zwei Quantensprüngen", 1931.
- [101] W. Kaiser and C. G. B. Garrett, "Two-photon Excitation in $\text{CaF}_2:\text{Eu}^{2+}$ ", *Phys. Rev. Lett.*, vol. 7, no. 6, pp. 229–232, 1961.
- [102] W. Denk, J. H. Strickler, and W. W. Webb, "Two-Photon Laser Scanning Fluorescence Microscopy", *Science*, vol. 248, pp. 73–76, 1990.
- [103] P. T. C. So, C. Y. Dong, B. R. Masters, and K. M. Berland, "Two-Photon Excitation Fluorescence Microscopy", *Annu. Rev. Biomed. Eng.*, vol. 2, pp. 399–429, 2000.
- [104] K. Svoboda and R. Yasuda, "Principles of Two-Photon Excitation Microscopy and Its Applications to Neuroscience", *Neuron*, vol. 50, pp. 823–839, 2006.
- [105] C. Xu and W. W. Webb, "Measurement of two-photon excitation cross sections of molecular fluorophores with data from 690 to 1050 nm", *J. Opt. Soc. Am. B*, vol. 13, no. 3, pp. 481–491, 1996.
- [106] C. J. Engelbrecht, R. S. Johnston, E. J. Seibel, and F. Helmchen, "Ultra-compact fiber-optic two-photon microscope for functional fluorescence imaging in vivo", *Opt. Express*, vol. 16, no. 8, pp. 5556–5564, 2008.
- [107] R. Petry, M. Schmitt, and J. Popp, "Raman spectroscopy - A prospective tool in the life sciences", *Chemphyschem*, vol. 4, no. 1, pp. 14–30, 2003.
- [108] C. Krafft, B. Dietzek, and J. Popp, "Raman and CARS microspectroscopy of cells and tissues", *Analyst*, vol. 134, no. 6, pp. 1046–1057, 2009.
- [109] M. Diem *et al.*, "Molecular pathology via IR and Raman spectral imaging", *J. Biophotonics*, vol. 6, no. 11–12, pp. 855–886, 2013.
- [110] U. Neugebauer, T. Bocklitz, J. H. Clement, C. Krafft, and J. Popp, "Towards detection and identification of circulating tumour cells using Raman spectroscopy", *Analyst*, vol. 135, pp. 3178–3182, 2010.
- [111] E. Potma, W. P. de Boei, P. J. van Haastert, and D. A. Wiersma, "Real-time visualization of intracellular hydrodynamics in single living cells", *Proc. Natl. Acad. Sci. U. S. A.*, vol. 98, no. 4, pp. 1577–1582, 2001.
- [112] D. Dörr, F. Stracke, and H. Zimmermann, "Noninvasive Quality Control of Cryopreserved Samples", *Biopreserv. Biobank.*, vol. 10, no. 6, pp. 529–531, 2012.

- [113] K. A. Okotrub and N. V. Surovtsev, "Raman scattering evidence of hydrohalite formation on frozen yeast cells", *Cryobiology*, vol. 66, no. 1, pp. 47–51, 2013.
- [114] A. Kreiner-Møller, F. Stracke, and H. Zimmermann, "Confocal Raman microscopy as a non-invasive tool to investigate the phase composition of frozen complex cryopreservation media", *Cryo-Letters*, vol. 34, no. 3, pp. 248–254, 2013.
- [115] A. Kreiner-Møller, F. Stracke, and H. Zimmermann, "Hydrohalite spatial distribution in frozen cell cultures measured using confocal Raman microscopy", *Cryobiology*, vol. 69, no. 1, pp. 41–47, 2014.
- [116] K. A. Okotrub and N. V. Surovtsev, "Redox State of Cytochromes in Frozen Yeast Cells Probed by Resonance Raman Spectroscopy", *Biophys. J.*, vol. 109, no. 11, pp. 2227–2234, 2015.
- [117] Y. A. Karpegina, K. A. Okotrub, E. Y. Brusentsev, S. Y. Amstislavsky, and N. V. Surovtsev, "Cryoprotectant redistribution along the frozen straw probed by Raman spectroscopy", *Cryobiology*, vol. 72, no. 2, pp. 148–153, 2016.
- [118] J. Solocinski, Q. Osgood, M. Wang, A. Connolly, M. A. Menze, and N. Chakraborty, "Effect of trehalose as an additive to dimethyl sulfoxide solutions on ice formation, cellular viability, and metabolism", *Cryobiology*, vol. 75, pp. 134–143, 2017.
- [119] I. Kratochvílová *et al.*, "Theoretical and experimental study of the antifreeze protein AFP752, trehalose and dimethyl sulfoxide cryoprotection mechanism: correlation with cryopreserved cell viability", *RSC Adv.*, vol. 7, no. 1, pp. 352–360, 2017.
- [120] L. Zhang *et al.*, "Cryobiological characteristics of L-proline in mammalian oocyte cryopreservation," *Chin. Med. J.*, vol. 129, no. 16, pp. 1963–1968, 2016.
- [121] L. Bogliolo *et al.*, "Raman microspectroscopy as a non-invasive tool to assess the vitrification-induced changes of ovine oocyte zona pellucida", *Cryobiology*, vol. 64, no. 3, pp. 267–272, 2012.
- [122] C. V. Raman and K. S. Krishnan, "A New Type of Secondary Radiation," *Nature*, vol. 121, no. 3048, pp. 501–502, 1928.
- [123] K. J. I. Ember *et al.*, "Raman spectroscopy and regenerative medicine: a review", *npj Regen. Med.*, vol. 2, no. 1, p. 12, 2017.
- [124] J. Popp and W. Kiefer, "Raman Scattering, Fundamentals", in *Encyclopedia of Analytical Chemistry*, R. A. Meyers, Ed. John Wiley & Sons, Ltd, 2006, pp. 13104–13142.
- [125] P. Matousek, M. Towrie, and A. W. Parker, "Fluorescence background suppression in Raman spectroscopy using combined Kerr gated and shifted excitation Raman difference techniques", *J. Raman Spectrosc.*, vol. 33, no. 4, pp. 238–242, 2002.
- [126] C. M. Penney, L. M. Goldman, and M. Lapp, "Raman Scattering Cross Sections", *Nat. Phys. Sci.*, vol. 235, pp. 110–111, 1972.
- [127] J. W. Lichtman and J. Conchello, "Fluorescence microscopy", *Nat. Methods*, vol. 2, no. 12, pp. 910–919, 2005.
- [128] P. L. Stiles, J. A. Dieringer, N. C. Shah, and R. P. Van Duyne, "Surface-Enhanced Raman Spectroscopy", *Annu. Rev. Anal. Chem.*, vol. 1, no. 1, pp. 601–626, 2008.
- [129] C. L. Evans and X. S. Xie, "Coherent anti-Stokes Raman scattering microscopy: Chemical imaging for biology and medicine", *Annu. Rev. Anal. Chem.*, vol. 1, pp. 883–909, 2008.
- [130] A. Kreiner-Møller, "Quantum dots in photonic crystal nanocavities", Technical University of Denmark, 2011.

- [131] D. Dörr, "Laseroptische Methoden zur Untersuchung von intra- und extrazellulären Eisbildungsprozessen im Hinblick auf Schädigungsmechanismen bei der Kryokonservierung therapeutisch relevanter Zellen", University of Saarland, 2014.
- [132] G. J. Morris and E. Acton, "Controlled Ice nucleation in cryopreservation - a review", *Cryobiology*, vol. 66, no. 2, pp. 85–92, 2013.
- [133] H. R. Pruppacher, "A New Look at Homogeneous Ice Nucleation in Supercooled Water Drops", *J. Atmos. Sci.*, vol. 52, no. 11, pp. 1924–1933, 1994.
- [134] B. T. Koop, "Homogeneous Ice Nucleation in Water and Aqueous Solutions", *Zeitschrift für Phys. Chemie*, vol. 218, pp. 1231–1258, 2004.
- [135] G. R. Edwards and L. F. Evans, "Ice Nucleation by Silver Iodide: I. Freezing vs Sublimation", *J. Meteorol.*, vol. 17, pp. 627–634, 1960.
- [136] M. Toner, E. G. Cravalho, and M. Karel, "Thermodynamics and kinetics of intracellular ice formation during freezing of biological cells", *J. Appl. Phys.*, vol. 67, no. 3, pp. 1582–1593, 1990.
- [137] G. E. Walrafen, "Raman Spectral Studies of Water Structure", *J. Chem. Phys.*, vol. 40, no. 11, pp. 3249–3256, 1964.
- [138] J. R. Scherer, M. K. Go, and S. Kint, "Raman Spectra and Structure of Water in Dimethyl Sulfoxide", *J. Phys. Chem.*, vol. 77, no. 17, pp. 2108–2117, 1973.
- [139] C. I. Ratcliffe and D. E. Irish, "Vibrational Spectral Studies of Solutions at Elevated Temperatures and Pressures. 5. Raman Studies of Liquid Water up to 300 °C", *J. Phys. Chem.*, vol. 86, no. 25, pp. 4897–4905, 1982.
- [140] J. Dubessy, D. Audeoud, R. Wilkins, and C. Kosztolanyi, "The use of the Raman microprobe MOLE in the determination of the electrolytes dissolved in the aqueous phase of fluid inclusions", *Chem. Geol.*, vol. 37, pp. 137–149, 1982.
- [141] R. J. Bakker, "Raman spectra of fluid and crystal mixtures in the systems H₂O, H₂O–NaCl and H₂O–MgCl₂ at low temperatures applications", *Can. Mineral.*, vol. 42, pp. 1283–1314, 2004.
- [142] M. Baumgartner and R. J. Bakker, "Raman spectra of ice and salt hydrates in synthetic fluid inclusions", *Chem. Geol.*, vol. 275, pp. 58–66, 2010.
- [143] B. Klewe and B. Pedersen, "The crystal structure of sodium chloride dihydrate", *Acta Crystallogr.*, vol. B30, pp. 2363–2371, 1974.
- [144] R. G. Snyder, H. L. Strauss, and C. A. Elliger, "C-H Stretching Modes and the Structure of n-Alkyl Chains. 1. Long, disordered chains", *J. Phys. Chem.*, vol. 86, no. 26, pp. 5145–5150, 1982.
- [145] T. G. Spiro and B. P. Gaber, "Laser Raman scattering as a probe of protein structure", *Annu. Rev. Biochem.*, vol. 46, no. 1, pp. 553–572, 1977.
- [146] B. A. Bolton and J. R. Scherer, "Raman spectra and water absorption of bovine serum albumin", *J. Phys. Chem.*, vol. 93, no. 22, pp. 7635–7640, 1989.
- [147] V. Zinchuk, O. Zinchuk, and T. Okada, "Quantitative colocalization analysis of multicolor confocal immunofluorescence microscopy images: Pushing pixels to explore biological phenomena", *Acta Histochem. Cytochem.*, vol. 40, no. 4, pp. 101–111, 2007.
- [148] K. S. J. Hilderbrand, "Preparation of Salt Brines for the Fishing Industry", 1998.
- [149] S. J. Prestrelski, N. Tedeschi, T. Arakawa, and J. F. Carpenter, "Dehydration-induced conformational transitions in proteins and their inhibition by stabilizers", *Biophys. J.*, vol. 65, no. 2, pp. 661–671, 1993.
- [150] M. E. Wise, K. J. Baustian, T. Koop, M. A. Freedman, E. J. Jensen, and M. A.

- Tolbert, "Depositional ice nucleation onto crystalline hydrated NaCl particles: A new mechanism for ice formation in the troposphere", *Atmos. Chem. Phys.*, vol. 12, no. 2, pp. 1121–1134, 2012.
- [151] R. Wagner and O. Möhler, "Heterogeneous ice nucleation ability of crystalline sodium chloride dihydrate particles", *J. Geophys. Res. Atmos.*, vol. 118, no. 10, pp. 4610–4622, 2013.
- [152] C. J. Hunt, "Cryopreservation of human stem cells for clinical application: A review", *Transfus. Med. Hemotherapy*, vol. 38, no. 2, pp. 107–123, 2011.
- [153] J. D. Hunt and K. A. Jackson, "Binary Eutectic Solidification", *Trans. Metall. Soc. AIME*, vol. 236, pp. 843–852, 1966.
- [154] K. A. Jackson and J. D. Hunt, "Lamellar and Rod Eutectic Growth", *Trans. Metall. Soc. AIME*, vol. 236, pp. 1129–1142, 1966.
- [155] G. Chen, Z. Hou, D. R. Gulbranson, and J. A. Thomson, "Actin-myosin contractility is responsible for the reduced viability of dissociated human embryonic stem cells", *Cell Stem Cell*, vol. 7, no. 2, pp. 240–248, 2010.
- [156] M. Ohgushi *et al.*, "Molecular pathway and cell state responsible for dissociation-induced apoptosis in human pluripotent stem cells", *Cell Stem Cell*, vol. 7, no. 2, pp. 225–239, 2010.
- [157] J. W. Han and Y.-S. Yoon, "Induced pluripotent stem cells: emerging techniques for nuclear reprogramming", *Antioxid. Redox Signal.*, vol. 15, no. 7, pp. 1799–1820, 2011.
- [158] P. E. Pegg, "Equations for Obtaining Melting Points and Eutectic Temperatures for the Ternary System Dimethyl Sulphoxide/Sodium Chloride/Water", *Cryo-Letters*, vol. 7, pp. 387–394, 1986.
- [159] W. H. Hildebrandt, F. H. Cocks, and M. L. Shepard, "The primary ice phase field in the H₂O-NaCl-dimethyl sulphoxide ternary system", *J. Mater. Sci.*, vol. 13, no. 5, pp. 1099–1104, 1978.
- [160] F. H. Cocks and W. E. Brower, "Phase diagram relationships in cryobiology", *Cryobiology*, vol. 11, no. 4, pp. 340–358, 1974.
- [161] G. E. Walrafen, "Raman spectra from Si – OH groups in solid optical fibers", *J. Chem. Phys.*, vol. 62, pp. 297–298, 1975.
- [162] G. E. Walrafen and S. R. Samanta, "Infrared absorbance spectra and interactions involving OH groups in fused silica", *J. Chem. Phys.*, vol. 69, pp. 493–495, 1978.
- [163] G. E. Walrafen, P. N. Krishnan, and S. W. Freiman, "Raman investigation of optical fibers under high tensile stress", *J. Appl. Phys.*, vol. 52, pp. 2832–2836, 1981.
- [164] S. Logunov and S. Kuchinsky, "Experimental and theoretical study of bulk light scattering in CaF₂ monocrystals", *J. Appl. Phys.*, vol. 98, p. 053501 1-7, 2005.
- [165] T. C. Larason, S. S. Bruce, and C. L. Cromer, "The NIST High Accuracy Scale for Absolute Spectral Response from 406 nm to 920 nm", *J. Res. Natl. Inst. Stand. Technol.*, vol. 101, no. 2, pp. 133–140, 1996.
- [166] A. Germann, Y. J. Oh, T. Schmidt, U. Schön, H. Zimmermann, and H. von Briesen, "Temperature fluctuations during deep temperature cryopreservation reduce PBMC recovery, viability and T-cell function", *Cryobiology*, vol. 67, no. 2, pp. 193–200, 2013.
- [167] P. Mazur, "A biologist's view of the relevance of thermodynamics and physical chemistry to cryobiology", *Cryobiology*, vol. 60, no. 1, pp. 4–10, 2010.
- [168] D. Gao and J. K. Critser, "Mechanisms of cryoinjury in living cells", *ILAR J.*, vol. 41, no. 4, pp. 187–196, 2000.

- [169] R. L. Sutton, A. Lips, G. Piccirillo, and A. Sztchelo, "Kinetics of ice recrystallization in aqueous fructose solutions", *J. Food Sci.*, vol. 61, no. 4, pp. 741–745, 1996.
- [170] C. Budke, C. Heggemann, M. Koch, N. Sewald, and T. Koop, "Ice recrystallization kinetics in the presence of synthetic antifreeze glycoprotein analogues using the framework of LSW theory", *J. Phys. Chem. B*, vol. 113, no. 9, pp. 2865–2873, 2009.
- [171] P. A. Beck, "Annealing of cold worked metals", *Adv. Phys.*, vol. 3, no. 11, pp. 245–324, 1954.
- [172] M. N. Martino and N. E. Zaritzky, "Ice recrystallization in a model system and in frozen muscle tissue", *Cryobiology*, vol. 26, no. 2, pp. 138–148, 1989.
- [173] Nikon, *NIS-Elements AR User's Guide Ver. 4.50*.
- [174] M. Hillert, "On the Theory of Normal and Abnormal Grain Growth", *Acta Metallurgica*, vol. 13, pp. 227–238, 1965.
- [175] W. D. Kingery, "Regelation, Surface Diffusion, and Ice Sintering", *J. Appl. Phys.*, vol. 31, no. 5, pp. 833–838, 1960.
- [176] D. P. Donhowe and R. W. Hartel, "Recrystallization of Ice During Bulk Storage of Ice Cream", *Int. Dairy J.*, vol. 6, pp. 1209–1221, 1996.
- [177] F. T. Ndoeye and G. Alvarez, "Characterization of ice recrystallization in ice cream during storage using the focused beam reflectance measurement", *J. Food Eng.*, vol. 148, pp. 24–34, 2015.
- [178] K. Wyser and P. Yang, "Average ice crystal size and bulk short-wave single-scattering properties of cirrus clouds", *Atmos. Res.*, vol. 49, pp. 315–335, 1998.
- [179] P. Doty and R. F. Steiner, "Light Scattering and Spectrophotometry of Colloidal Solutions", *J. Chem. Phys.*, vol. 18, pp. 1211–1220, 1950.
- [180] R. Pecora, "Dynamic light scattering measurement of nanometer particles in liquids," *J. Nanoparticle Res.*, vol. 2, pp. 123–131, 2000.
- [181] A. R. Jones, "Light scattering for particle characterization", *Prog. Energy Combust. Sci.*, vol. 25, pp. 1–53, 1999.
- [182] M. R. Carro-Temboury, R. Arppe, T. Vosch, and T. J. Sørensen, "An optical authentication system based on imaging of excitation-selected lanthanide luminescence", *Sci. Adv.*, vol. 4, no. 1, e1701384, 2018.
- [183] M. J. Bledsoe, W. E. Grizzle, B. J. Clark, and N. Zeps, "Practical implementation issues and challenges for biobanks in the return of individual research results", *Genet. Med.*, vol. 14, no. 4, pp. 478–483, 2012.
- [184] B. M. Riva, L. Piergiovanni, and A. Schiraldi, "Performances of Time-Temperature Indicators in the Study of Temperature Exposure of Packaged Fresh Foods", *Packag. Technol. Sci.*, vol. 14, pp. 1–9, 2001.
- [185] J. D. Selman, "Time-temperature indicators", in *Active Food Packaging*, 1st ed., M. L. Rooney, Ed. 1995, pp. 215–237.
- [186] M. Asslaber and K. Zatloukal, "Biobanks: transnational, European and global networks", *Briefings Funct. Genomics Proteomics*, vol. 6, no. 3, pp. 193–201, 2007.
- [187] P. Boutron, "Comparison with the theory of the kinetics and extent of ice crystallization and of the glass-forming tendency in aqueous cryoprotective solutions", *Cryobiology*, vol. 23, pp. 88–102, 1986.
- [188] P. Mehl, "Isothermal and non-isothermal crystallization during warming in aqueous solutions of 1,3-butanediol: Comparison of calorimetry and cryomicroscopy", *Thermochim. Acta*, vol. 155, pp. 187–202, 1989.

- [189] A. Baudot, L. Alger, and P. Boutron, "Glass-Forming Tendency in the System Water-Dimethyl Sulfoxide", *Cryobiology*, vol. 40, pp. 151–158, 2000.
- [190] M. Richards, C.-Y. Fong, S. Tan, W.-K. Chan, and A. Bongso, "An Efficient and Safe Xeno-Free Cryopreservation Method for the Storage of Human Embryonic Stem Cells", *Stem Cells*, vol. 22, pp. 779–789, 2004.
- [191] J. C. Neubauer, A. F. Beier, N. Geijssen, and H. Zimmermann, "Cryopreservation and Freeze-Drying Protocols", in *Cryopreservation and Freeze-Drying Protocols*, W. F. Wolters and H. Oldenhof, Eds. Springer Science, 2015, pp. 321–328.
- [192] A. Kreiner, F. Stracke, and H. Zimmermann, "On the assessment of the stability of vitrified cryo-media by differential scanning calorimetry: A new tool for biobanks to derive standard operating procedures for storage, access and transport", *Cryobiology*, vol. 89, pp. 26–34, 2019.
- [193] J. Farjas and P. Roura, "Modification of the Kolmogorov-Johnson-Mehl-Avrami rate equation for non-isothermal experiments and its analytical solution", *Acta Mater.*, vol. 54, pp. 5573–5579, 2006.
- [194] J. M. Hey and D. R. MacFarlane, "Kinetic analyses of crystallization and devitrification: Comparison of activation energies in aqueous solutions of glycerol and dimethyl sulphoxide", *J. Non. Cryst. Solids*, vol. 211, pp. 262–270, 1997.
- [195] H. Yinnon and D. R. Uhlmann, "Applications of thermoanalytical techniques to the study of crystallization kinetics in glass-forming liquids, part I: Theory", *J. Non. Cryst. Solids*, vol. 54, pp. 253–275, 1983.
- [196] W. A. Johnson and R. F. Mehl, "Reaction Kinetics in Processes of Nucleation and Growth", *Trans. Am. Inst. Min. Metall. Eng.*, vol. 135, pp. 416–458, 1939.
- [197] M. Avrami, "Kinetics of phase change. I general theory", *J. Chem. Phys.*, vol. 7, no. 12, pp. 1103–1112, 1939.
- [198] M. Avrami, "Kinetics of Phase Change. II Transformation-Time Relations for Random Distribution of Nuclei", *J. Chem. Phys.*, vol. 8, no. 2, pp. 212–224, 1940.
- [199] M. Avrami, "Granulation, Phase Change, and Microstructure Kinetics of Phase Change. III", *J. Chem. Phys.*, vol. 9, no. 2, pp. 177–184, 1941.
- [200] A. Kolmogorov, "On the Statistical Theory of Crystallization of Metals [in Russian]", *Izv. Akad. Nauk SSSR Ser. Mat.*, vol. 1, no. 3, pp. 355–359, 1937.
- [201] H. E. Kissinger, "Reaction Kinetics in Differential Thermal Analysis", *Anal. Chem.*, vol. 29, no. 11, pp. 1702–1706, 1957.
- [202] P. Boutron and A. Kaufmann, "Stability of the amorphous state in the system Water-Glycerol-Dimethylsulfoxide", *Cryobiology*, vol. 15, pp. 93–108, 1978.
- [203] J. A. Augis and J. E. Bennett, "Calculation of the Avrami parameters for heterogeneous solid state reactions using a modification of the Kissinger method", *J. Therm. Anal.*, vol. 13, pp. 283–292, 1978.
- [204] K. Matsushita and S. Sakka, "Kinetic Study on Non-Isothermal Crystallization of Glass by Thermal Analysis", *Bull. Inst. Chem. Res. Kyoto Univ.*, vol. 59, no. 3, pp. 159–171, 1981.
- [205] V. L. Bronshteyn and P. L. Steponkus, "Nucleation and growth of ice crystals in concentrated solutions of ethylene glycol", *Cryobiology*, vol. 32, pp. 1–22, 1995.
- [206] D. H. Rasmussen and A. P. MacKenzie, "Phase Diagram for the System Water-Dimethylsulphoxide", *Nature*, vol. 220, no. 5174, pp. 1315–1317, 1968.
- [207] B. Han, J. H. Choi, J. A. Dantzig, and J. C. Bischof, "A quantitative analysis on latent heat of an aqueous binary mixture", *Cryobiology*, vol. 52, pp. 146–151, 2006.

- [208] S. S. N. Murthy, "Some Insight into the Physical Basis of the Cryoprotective Action of Dimethyl Sulfoxide and Ethylene Glycol", *Cryobiology*, vol. 36, pp. 84–96, 1998.
- [209] D. R. Cordray, L. R. Kaplan, P. M. Woyciesjes, and T. F. Kozak, "Solid - liquid phase diagram for ethylene glycol + water", *Fluid Phase Equilib.*, vol. 117, pp. 146–152, 1996.
- [210] S. A. Schichman and R. L. Amey, "Viscosity and local liquid structure in dimethyl sulfoxide-water mixtures", *J. Phys. Chem.*, vol. 75, no. 1, pp. 98–102, 1971.
- [211] S. Zhang, X. Yu, Z. Chen, and G. Chen, "Viscosities of the ternary solution dimethyl sulfoxide/water/sodium chloride at subzero temperatures and their application in cryopreservation", *Cryobiology*, vol. 66, pp. 186–191, 2013.
- [212] G. Vajta and Z. P. Nagy, "Are programmable freezers still needed in the embryo laboratory? Review on vitrification", *Reprod. Biomed. Online*, vol. 12, no. 6, pp. 779–796, 2006.
- [213] G. D. Elliott, S. Wang, and B. J. Fuller, "Cryoprotectants: A review of the actions and applications of cryoprotective solutes that modulate cell recovery from ultra-low temperatures", *Cryobiology*, vol. 76, pp. 74–91, 2017.
- [214] R. V. Devireddy, D. Raha, and J. C. Bischof, "Measurement of Water Transport during Freezing in Cell Suspensions Using a Differential Scanning Calorimeter", *Cryobiology*, vol. 36, pp. 124–155, 1998.
- [215] "Webmineral.com," 2014. [Online]. Available: Webmineral.com/data/hydrohalite.shtml.